

AFIT/DS/ENP/95-03

OPTICAL CHARACTERIZATION OF  
INDIUM ARSENIDE ANTIMONIDE SEMICONDUCTORS  
GROWN BY MOLECULAR BEAM EPITAXY

DISSERTATION

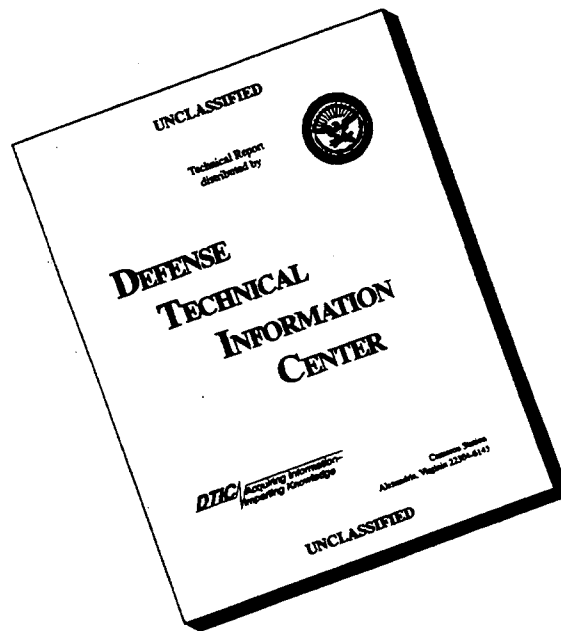
Michael A. Marciniak, Major, USAF

AFIT/DS/ENP/95-03

19960327 010

Approved for public release; distribution unlimited

# DISCLAIMER NOTICE



**THIS DOCUMENT IS BEST QUALITY AVAILABLE. THE COPY FURNISHED TO DTIC CONTAINED A SIGNIFICANT NUMBER OF PAGES WHICH DO NOT REPRODUCE LEGIBLY.**

AFIT/DS/ENP/95-03

OPTICAL CHARACTERIZATION OF INDIUM ARSENIDE ANTIMONIDE  
SEMICONDUCTORS GROWN BY MOLECULAR BEAM EPITAXY

DISSERTATION

Presented to the Faculty of the Graduate School of Engineering  
of the Air Force Institute of Technology

Air University

In Partial Fulfillment of the  
Requirements for the Degree of  
Doctor of Philosophy

Michael A. Marciniak, B.S., B.S.E.E., M.S.E.E.

Major, USAF

September 1995

Approved for public release; distribution unlimited

OPTICAL CHARACTERIZATION OF INDIUM ARSENIDE ANTIMONIDE  
SEMICONDUCTORS GROWN BY MOLECULAR BEAM EPITAXY

Michael A. Marciniak, B.S., B.S.E.E., M.S.E.E.  
Major, USAF

Approved:

Robert L. Hengehold 21 Aug '95  
Robert L. Hengehold  
Chairman, Advisory Committee

Yung Kee Yeo 21 Aug '95  
Yung Kee Yeo  
Member, Advisory Committee

Paul H. Ostdiek 21 Aug 95  
Paul H. Ostdiek, Major, USAF  
Member, Advisory Committee

Victor M. Bright 21 Aug 95  
Victor M. Bright  
Member, Advisory Committee

Mark E. Oxley 21 Aug 95  
Mark E. Oxley  
Dean's Representative

Accepted:

Robert A. Calico  
Robert A. Calico  
Dean, Graduate School of Engineering

## Preface

This has been, far and away, the most intense academic experience I've encountered and I certainly could not have made it through without the people that surrounded me for the last three years. At the top of the list are my advisors, Dr Robert Hengehold and Dr Yung Kee Yeo. Their genuine personal concern makes AFIT a truly unique place to earn a degree. I thank Dr George Turner of MIT-Lincoln Laboratory for providing me with all the samples I looked at under the guise that my work was helping him build a better laser - I know I got much more out of our many hours of discussions than he did! I thank Nick Pchelkin and Maj Mike Prairie of the Phillips Lab for encouraging George (their contractor) to collaborate with me, and for financial support. Without these, I'd have had a less well equipped lab and no samples - not a good way to do a dissertation! I thank Greg Smith for helping me set-up the lab and teaching me the experiment, and Belinda Johnson for being another pair of hands in the lab whenever I needed them.

Finally, I want to thank my wife, Melony, for encouraging me to find outside interests to distract me from the full time academics for a while, and for taking up a little more slack each time I was especially discouraged. The preface of my Master's thesis called Melony an AFIT widow - I know that had to be a picnic compared to this!

Michael A. Marciniak

Dedicated to my son, Noah.

## Table of Contents

	Page
Preface.....	iii
List of Figures.....	vi
List of Tables.....	xvi
List of Symbols.....	xviii
Abstract.....	xix
1. <u>Introduction</u> .....	1-1
Motivation.....	1-1
Objective.....	1-5
Approach.....	1-6
2. <u>Background</u> .....	2-1
Solid State Physics.....	2-1
Lattice Constant.....	2-4
Band Structure.....	2-8
Phonons.....	2-9
Semiconductor Diode Lasers.....	2-12
3. <u>Previous Work</u> .....	3-1
InAsSb Material Characterization.....	3-1
InAsSb Semiconductor Lasers.....	3-21
Summary.....	3-24
4. <u>Samples</u> .....	4-1
Molecular Beam Epitaxial Growth.....	4-2
Double Crystal X-Ray Diffraction.....	4-12
Undoped Samples.....	4-15
Doped Samples.....	4-26

5. <u>Characterization Techniques</u> .....	5-1
Absorption.....	5-1
Photoluminescence .....	5-7
Calibration.....	5-18
Fitting Software .....	5-20
6. <u>Results and Discussion: Absorption</u> .....	6-1
Experiment.....	6-1
Spectra.....	6-3
Fitting the Data .....	6-5
Temperature Dependence of the Energy Gap .....	6-19
Compositional Dependence of the Energy Gap: Low Temperatures.....	6-23
Compositional Dependence of the Energy Gap: Room Temperature.....	6-37
Varshni Parameters $\alpha$ and $\beta$ .....	6-42
Summary .....	6-47
7. <u>Results and Discussion: Photoluminescence</u> .....	7-1
InAs Homoepitaxy .....	7-2
InAs Heteroepitaxy on GaSb .....	7-15
Undoped InAs <sub>1-x</sub> Sb <sub>x</sub> : Single-Peaked Spectra.....	7-20
Undoped InAs <sub>1-x</sub> Sb <sub>x</sub> : Multiple-Peaked Spectra .....	7-55
Doped InAs <sub>1-x</sub> Sb <sub>x</sub> .....	7-59
Summary .....	7-71
8. <u>Conclusions and Recommendations</u> .....	8-1
Conclusions.....	8-1
Recommendations.....	8-6
<u>Bibliography</u> .....	Bib-1
<u>Vita</u> .....	V-1

## List of Figures

	Page
Figure 1-1. (Top) Atmospheric transmission in the mid-infrared (Wolfe, 1989:5-88). (Bottom) Lattice constant in Å versus energy gap diagram for the III-V semiconductors (Saleh, 1991:550).....	1-3
Figure 2-1. Schematic drawing of the energy bands of diamond as a function of atomic spacing (Kimball, 1935:560).....	2-2
Figure 2-2. Energy band diagrams for (a) insulator, (b) semiconductor at low temperature, (c) semiconductor at high temperature, and (d) metal (McKelvey, 1966:246).....	2-3
Figure 2-3. (a) FCC structure. (b) Interpenetrating FCCs. (c) Zincblende structure. (d) Tetrahedral bonds.....	2-5
Figure 2-4. Thermal expansion coefficients for InAs and InSb (Madelung, 1991:136).....	2-7
Figure 2-5. Variation of InAs <sub>1-x</sub> Sb <sub>x</sub> lattice constant with x-composition. Solid line - Woolley and Warner's measurements. Dotted line - Vegard's law. (Woolley, 1964a:1142).....	2-8
Figure 2-6. InAs band structure (Madelung, 1991:135).....	2-10
Figure 2-7. Phonon dispersion relations for InAs and InSb. The LO-phonon energies at the Γ-point are 29.6 meV and 24.8 meV for InAs and InSb, respectively. (Madelung, 1991:137).....	2-11
Figure 2-8. Energy band diagram of bulk intrinsic and extrinsic semiconductor material.....	2-13
Figure 2-9. Band diagram of a p-n junction in thermal equilibrium.....	2-14
Figure 2-10. (a) Band diagram of a heavily doped p-n junction. (b) Band-to-band radiative transitions under injection.....	2-15
Figure 2-11. (a) Band diagram of an ideal double heterojunction (DH). (b) p-n-n DH in thermal equilibrium. (c) p-n-n DH under forward bias with carrier injection. (d) Refractive indices of p-n-n DH which forms optical waveguide.....	2-16



Figure 2-12. (a) Calculated refractive indices of $\text{Ga}_x\text{In}_{1-x}\text{As}_y\text{Sb}_{1-y}/\text{GaSb}$ as a function of photon energy with x-composition increments of 0.1. (b) Calculated refractive indices of $\text{Al}_x\text{Ga}_{1-x}\text{As}_y\text{Sb}_{1-y}/\text{GaSb}$ as a function of photon energy with x-composition increments of 0.1. (Adachi, 1987:4869).....	2-19
Figure 2-13. Band offsets for $\text{AlGaAsSb}/\text{InGaAsSb}$ heterojunctions lattice-matched to $\text{GaSb}$ (Martinelli, 1991:13). .....	2-20
Figure 2-14. $\text{InAs}_{0.91}\text{Sb}_{0.09}/\text{AlAs}_{0.08}\text{Sb}_{0.92}$ lattice matched to $\text{GaSb}$ DH laser structure.....	2-21
Figure 3-1. Top: Variation of composition of cross sectional slice as a function of position in a directionally frozen ingot. Bottom: Variation of composition of cross sectional slice as a function of position in a zone recrystallized ingot (Woolley, 1964a:1142).....	3-3
Figure 3-2. Variation of optical energy gap with alloy composition: o = room temperature transmission measurements; + and I = room temperature diffuse reflectivity measurements; and • = transmission measurements extrapolated to 0 K (Woolley, 1964b:1879). .....	3-4
Figure 3-3. Variation of extrapolated absolute zero band gap of $\text{InAs}_{1-x}\text{Sb}_x$ with Sb composition, x: o = Coderre and Woolley results; × = extrapolated absolute zero band gap from Woolley and Warner (1964) data; and -- = Woolley and Warner (1964) room temperature optical band gap. (Coderre, 1968:1207).....	3-5
Figure 3-4. Compositional dependence of the room temperature energy gap of LPE-grown $\text{InAs}_{1-x}\text{Sb}_x$ on $\text{InAs}$ by Stringfellow and Greene. $E_g$ was assigned as the photon energy when $\alpha(E_g) = 300 \text{ cm}^{-1}$ in absorption measurements. (Stringfellow, 1971:805).....	3-7
Figure 3-5. PL spectra of $\text{InAs}_{0.85}\text{Sb}_{0.15}$ which the authors attributed to impurity state emission. The deep dips at $4.3 \mu\text{m}$ are due to $\text{CO}_2$ absorption in the optical path. (Mohammed, 1986:215).....	3-10
Figure 3-6. $\text{InAsSb}/\text{n-GaSb}$ heterojunction band diagram (Srivastava, 1986:41). .....	3-11
Figure 3-7. Compositional dependence of the room temperature energy gap of MBE-grown $\text{InAs}_{1-x}\text{Sb}_x$ on $\text{InAs}$ by Yen <i>et al.</i> $E_g$ was assigned as the photon energy when $\alpha(E_g) = 300 \text{ cm}^{-1}$ in FTIR absorption measurements. (Yen, 1987:927).....	3-12

Figure 3-8. PL spectra of MBE-grown $\text{InAs}_{0.96}\text{Sb}_{0.04}$ and $\text{InAs}_{0.87}\text{Sb}_{0.13}$ on InAs at various temperatures. B is associated with band edge transitions and I with impurity.....	3-13
Figure 3-9. Compositional dependence of the 10 K peak PL wavelength for MBE-grown $\text{InAs}_{1-x}\text{Sb}_x$ on InAs. Dashed curve shows room temperature energy gap of Fig. 5. (Yen, 1988a:489).....	3-15
Figure 3-10. Raman scattering spectra for $\text{InAs}_{1-x}\text{Sb}_x$ showing InAs- and InSb-like optical phonon modes (Cherng, 1988:886).....	3-17
Figure 3-11. Compositional dependence of the 10 K peak PL energies for MOCVD-grown $\text{InAs}_{1-x}\text{Sb}_x$ on InAs. Solid curve is least squares fit to PL data. $\Delta$ data is also shown in Fig. 3 and $\times$ data in Fig. 6. (Fang, 1990:7034).....	3-18
Figure 3-12. Room temperature electron effective mass in $\text{InAs}_{1-x}\text{Sb}_x$ calculated by Rogalski. Symbols are data points taken from Woolley <i>et al.</i> (Aubin, 1968:1191; van Tongerloo, 1968:1199; Thomas, 1971:2052). The solid line is calculated assuming conduction-valence band mixing; the broken line uses the Kane model. (Rogalski, 1989b:35).....	3-19
Figure 3-13. Linear compositional dependence of optical phonon peaks in MBE-grown $\text{InAs}_{1-x}\text{Sb}_x$ on GaAs as measured by Raman scattering (Li, 1992:567).....	3-20
Figure 4-1. Schematic of an MBE system (Sze, 1985:337).....	4-2
Figure 4-2. Schematic illustration of the effusion cell-substrate system showing polar coordinates to substrate surface point, P (Herman, 1989:7).....	4-4
Figure 4-3. Schematic illustration of the important surface processes in MBE growth (Herman, 1989:9).....	4-5
Figure 4-4. Schematic illustration of the RHEED intensity oscillations as a tool for characterizing MBE growth (Herman, 1989:21).....	4-6
Figure 4-5. Successive III-V (001) growth planes in III-V ternary. ....	4-8
Figure 4-6. TEM [110] cross-section micrograph of MBE-grown $\text{InAs}_{1-x}\text{Sb}_x$ at two growth temperatures: (a) $T_g = 430^\circ\text{C}$ , homogeneous $\text{InAs}_{0.5}\text{Sb}_{0.5}$ material; (b) $T_g = 370^\circ\text{C}$ , natural SLS of $\sim 285 \text{ \AA}$ $\text{InAs}_{0.33}\text{Sb}_{0.67}$ and $\sim 285 \text{ \AA}$ $\text{InAs}_{0.69}\text{Sb}_{0.31}$ . (Ferguson, 1991a:3324).....	4-11

Figure 4-7. Bragg reflection from a set of atomic planes separated by distance, $a$ , occurring at the Bragg angle, $\theta_B$ .	4-12
Figure 4-8. Schematic illustration of a double crystal spectrometer. When the two crystals are parallel, the reflected wavelength from crystal A is incident to crystal B at the correct angle for reflection. (Warren, 1969:328)	4-13
Figure 4-9. Energy level diagrams of the epilayer structure for the $\text{InAs}_{1-x}\text{Sb}_x$ samples studied.	4-17
Figure 4-10. DCXRD data taken on seven of the 13 undoped $\text{InAs}_{1-x}\text{Sb}_x$ samples listed in Table V-1. GaSb substrate peaks are at 0 sec; epilayer peaks are at $\Delta\theta \neq 0$ .	4-19
Figure 4-11. DCXRD data taken on six of the 13 undoped $\text{InAs}_{1-x}\text{Sb}_x$ samples listed in Table V-1. GaSb substrate peaks are at 0 sec; epilayer peaks are at $\Delta\theta \neq 0$ .	4-20
Figure 4-12. Critical pseudomorphic thickness in units of substrate lattice constant, $a_s$ , given by Eq (4.11) as a function of misfit given by Eq (4.12) for $60^\circ$ misfit dislocations on (111) glide planes in a (001) interface with a Poisson's ratio of 0.25 (Herman, 1989:223).	4-22
Figure 4-13. Schematic illustration of DCXRD experiment with Bragg reflection from (115) planes.	4-25
Figure 4-14. DCXRD results for epitaxially Be-doped sample 95-017. GaSb substrate peak is at 0 sec; the $\text{InAs}_{0.955}\text{Sb}_{0.045}$ epilayer peak is at $\Delta\theta = 356$ sec.	4-27
Figure 5-1. Schematic drawing of BioRad FTS-60A Fourier transform spectrometer infrared absorption experimental apparatus.	5-3
Figure 5-2. Michelson interferometer.	5-4
Figure 5-3. Fourier transform pairs of sinusoids at two different frequencies and their sum.	5-6
Figure 5-4. Spectral ranges of BioRad FTS absorption experiments.	5-8
Figure 5-5. Recombination processes for direct gap semiconductors: (a) band-to-band; (b) free exciton; (c) bound exciton; (d) donor-to-valence band; (e) conduction band-to-acceptor; and (f) donor-acceptor pair.	5-11

Figure 5-6. Schematic drawing of photoluminescence experiment.....	5-11
Figure 5-7. Geometric optical schematic diagram of 0.5 m grating spectrometer.....	5-15
Figure 5-8. PL spectra showing advantage of N <sub>2</sub> purge of luminescence light path in reducing CO <sub>2</sub> absorption at wavelengths of interest.....	5-19
Figure 5-9. Calibration of Spex 500M PL spectrometer and BioRad FTS-60A absorption spectrometer using OCLI bandpass filter #W03540-6.....	5-21
Figure 5-10. Calibration of Spex 500M PL spectrometer and BioRad FTS-60A absorption spectrometer using OCLI bandpass filter #W04018-4.....	5-22
Figure 6-1. Absorbance spectra of MBE-grown InAs <sub>0.905</sub> Sb <sub>0.095</sub> and InAs <sub>0.911</sub> Sb <sub>0.089</sub> as measured by FTS at three temperatures. The spectral range of sample InAs <sub>0.905</sub> Sb <sub>0.095</sub> is set by the FTS optics and ZnSe helitran windows, while that of sample InAs <sub>0.911</sub> Sb <sub>0.089</sub> is set by sapphire helitran windows. The dotted lines represent a least squares fit of the free carrier absorption below the band edge with exponent, p, is indicated. The minimum value is offset from zero by differences in the polished finishes of the sample and background substrates.....	6-4
Figure 6-2. Absorbance spectra of an epitaxial AlAs <sub>0.08</sub> Sb <sub>0.92</sub> /InAs <sub>0.903</sub> Sb <sub>0.097</sub> / AlAs <sub>0.08</sub> Sb <sub>0.92</sub> heterostructure grown on GaSb substrate as measured by Fourier transform spectroscopy (FTS) at several temperatures. The InAs <sub>0.903</sub> Sb <sub>0.097</sub> epilayer absorption data is masked by a strong etalon effect occurring between the AlAsSb/GaSb interface and the epilayer surface. The spacing between adjacent etalon fringes for this sample is approximately 80 meV.....	6-6
Figure 6-3. Absorbance spectra for epitaxial InAs <sub>0.911</sub> Sb <sub>0.089</sub> obtained from spectra of Figure 6-1 by removing free carrier and surface scatter absorbances. Dotted lines represent the least squares fit of the absorbance to a non-excitonic, band-to-band absorption form which includes density of states and carrier distribution considerations for each band.....	6-10
Figure 6-4. (a) The Fabry-Perot etalon and (b) resulting interference fringes.....	6-16
Figure 6-5. Depiction of self-referencing technique. a and b represent two spectra at different temperatures; thus, the band edge has moved. When one is subtracted from the other, information about both band edges is maintained in the difference spectrum.....	6-18
Figure 6-6. Absorbance spectra for epitaxial InAs <sub>0.903</sub> Sb <sub>0.097</sub> obtained from spectra of Figure 6-2 by referencing each against the 6 K spectrum.....	6-20

Figure 6-7. Temperature-dependence of the energy gap for five of the 13 epitaxial  $\text{InAs}_{1-x}\text{Sb}_x$  samples measured. The dashed lines are the least squares fit of the Varshni equation to the data. The error associated with each data point was determined by the absorption spectrometer resolution to be 0.5 meV for the  $\text{InAs}$ ,  $\text{InAs}_{0.969}\text{Sb}_{0.031}$  and  $\text{InAs}_{0.808}\text{Sb}_{0.192}$  samples, and 2.0 meV for the  $\text{InAs}_{0.905}\text{Sb}_{0.095}$  and  $\text{InAs}_{0.821}\text{Sb}_{0.179}$  samples. The other eight samples fit as well to the Varshni equation but are excluded here for clarity. .... 6-21

Figure 6-8. Least squares linear fit of the compositional dependence of the energy gap at 0 K ( $E_g(0\text{ K})$ ) for MBE-grown  $\text{InAsSb}$  samples on GaSb substrate ( $\bullet$ , solid line), compared to other low temperature  $E_g(x)$  relationships reported previously:  $\square$ , dotted line (Woolley, 1964b:1879);  $\Delta$ , dashed line (Coderre, 1968:1207);  $*$ , dash-dot line (Yen, 1988a:489); and  $\circ$ , dash-double dot line (Fang, 1990:7034). The error in determining the  $E_g(0)$  parameter from the fit of the Varshni equation to the temperature-dependent data is shown for each composition..... 6-25

Figure 6-9. Comparison of Woolley and Warner's temperature-dependent energy gap results for bulk, polycrystalline  $\text{InAs}_{1-x}\text{Sb}_x$  to the current results for MBE-grown  $\text{InAs}_{1-x}\text{Sb}_x$  on GaSb substrate. The solid symbols represent the bulk data; the open symbols the current data:  $\blacksquare$  -  $\text{InAs}$ ;  $\square$  -  $\text{InAs}$ ;  $\bullet$  -  $\text{InAs}_{0.96}\text{Sb}_{0.04}$ ;  $\circ$  -  $\text{InAs}_{0.955}\text{Sb}_{0.045}$ ;  $\blacktriangle$  -  $\text{InAs}_{0.92}\text{Sb}_{0.08}$ ;  $\Delta$  -  $\text{InAs}_{0.923}\text{Sb}_{0.077}$ ;  $\blacktriangledown$  -  $\text{InAs}_{0.89}\text{Sb}_{0.11}$ ;  $\nabla$  -  $\text{InAs}_{0.905}\text{Sb}_{0.095}$ ;  $\blacklozenge$  -  $\text{InAs}_{0.80}\text{Sb}_{0.20}$ ; and  $\diamond$  -  $\text{InAs}_{0.809}\text{Sb}_{0.191}$ . The dotted lines represent the linear extrapolations of the bulk data to lower temperatures. .... 6-27

Figure 6-10. Comparisons of PL peak positions for previously reported  $\text{InAs}_{0.8}\text{Sb}_{0.2}$  ( $\blacktriangle$ ) (Fang, 1990:7034) and the currently studied  $\text{InAs}_{0.808}\text{Sb}_{0.192}$  sample ( $\square$ ), and the energy gap assignments made from the  $\text{InAs}_{0.8}\text{Sb}_{0.2}$  PL data ( $\blacktriangledown$ , dashed line) and FTS absorption experiments on the currently studied sample ( $\circ$ , dotted line). .... 6-29

Figure 6-11. Compositional dependence of the energy gap at 0 K ( $E_g(0\text{ K})$ ) for MBE-grown InAsSb samples on GaSb substrate ( $\bullet$ , solid line), along with other low temperature  $E_g(x)$  relationships reported previously:  $\square$ , dotted line (Woolley, 1964b:1879);  $\Delta$ , dashed line (Coderre, 1968:1207);  $*$ , dash-dot line (Yen, 1988a:489); and  $\nabla$ , dash-double dot line (Fang, 1990:7034). The error in determining the  $E_g(0)$  parameter from the fit of the Varshni equation to the temperature-dependent data is shown for each composition. The solid line is the least squares fit of the bowing parameter equation (Eq (6.25)) to this data. The bowing parameters are given for each data set in the parentheses.  $\circ$  - Data point for MBE-grown InAs<sub>0.6</sub>Sb<sub>0.4</sub> on GaSb in which Cu-Pt ordering was observed (Kurtz, 1992:1909). ..... 6-31

Figure 6-12. Differences between the energy gaps at 0 K of MBE-grown InAs<sub>1-x</sub>Sb<sub>x</sub> on GaSb substrates and the bowing-parameter polynomial fit of this data as given by Eqs (6.25) and (6.26) are shown as square symbols,  $\Delta E_g(0)$ . Sample epilayer thicknesses in units of critical thickness as given by Eq (4.11) are shown as vertical bars. Samples are labeled by lattice-mismatched with the GaSb substrate here rather than composition. .... 6-34

Figure 6-13. Least squares linear fit of the compositional dependence of the room temperature energy gap,  $E_g(295\text{ K})$ , for MBE-grown InAsSb samples on GaSb substrate ( $\bullet$ , solid line) compared to other low temperature  $E_g(x)$  relationships which include a bowing parameter reported previously:  $\square$ , dotted line (Woolley, 1964b:1879);  $\nabla$ , dashed line (Stringfellow, 1971:805); and  $*$  (Yen, 1987:927). The error associated with each data point was determined by the absorption spectrometer resolution to be either 0.5 or 2.0 meV as listed in Table 6-1..... 6-39

Figure 6-14. Compositional dependence of the room temperature energy gap,  $E_g(295\text{ K})$ , for MBE-grown InAsSb samples on GaSb substrate ( $\bullet$ , solid line), along with other room temperature  $E_g(x)$  relationships previous reported:  $\square$ , dotted line (Woolley, 1964b:1879);  $\Delta$ , dashed line (Stringfellow, 1971:805); and  $*$  (Yen, 1987:927). The error associated with each data point was determined by the absorption spectrometer resolution to be either 0.5 or 2.0 meV as listed in Table 6-1. The solid line is the least squares fit of the bowing parameter equation (Eq (6.25)) to this data. The bowing parameters are given for each data set in the parentheses..... 6-41

Figure 6-15. Compositional dependence of the Varshni parameters, $\alpha$ (solid squares) and $\beta$ (open circles), for the 13 MBE-grown $\text{InAs}_{1-x}\text{Sb}_x$ on GaSb samples studied. The errors in determining these parameters from the fit of the Varshni equation to the temperature-dependent data are shown for each composition. ....	6-43
Figure 6-16. Plot of the Varshni parameters $\alpha$ and $\beta$ showing a fixed relationship exists between them for the $\text{InAs}_{1-x}\text{Sb}_x$ samples studied here (■) and for those previously reported ( $\Delta$ and $\nabla$ ). ....	6-46
Figure 7-1. Photoluminescence spectra of InAs homoepitaxial material. The PL spectrometer resolution is 0.8 meV. ....	7-3
Figure 7-2. Comparison of homoepitaxial InAs low temperature photoluminescence and absorption spectra. The PL spectrometer resolution is 0.8 meV; FTS absorption spectrometer resolution is 2.0 meV. ....	7-4
Figure 7-3. Low temperature PL spectra of peak $E_{D1}$ from InAs homoepitaxial sample at two laser excitation powers, 5 and 500 mW. This apparent single peak is actually a double peak as shown by the double Gaussian fit. The PL spectrometer resolution is 0.8 meV. ....	7-7
Figure 7-4. Schematic drawing of donor-acceptor pair radiative recombination. Donor-bound electrons and acceptor-bound holes are separated by some distance, $r$ , in the crystal lattice. (Pankove, 1971:143) ....	7-11
Figure 7-5. Photoluminescence peak positions as a function of temperature for homoepitaxial InAs. The PL spectrometer resolution is 0.8 meV. ....	7-13
Figure 7-6. Low temperature photoluminescence spectra of MBE-grown InAs on n-GaSb substrate. The PL spectrometer resolution is 1.6 meV. ....	7-16
Figure 7-7. Photoluminescence peak positions as a function of temperature for MBE-grown InAs on n-GaSb substrate. The PL spectrometer resolution is 1.6 meV. ....	7-19
Figure 7-8. Typical low temperature photoluminescence spectra for MBE-grown $\text{InAs}_{1-x}\text{Sb}_x$ on GaSb substrate. The LO-phonon replica appears in several samples at energies 27-29 meV below the main peak. The main peak shifts to higher energies with increased excitation. The PL spectrometer resolution is 0.5 meV. ....	7-22

- Figure 7-9. PL peak positions as a function of laser excitation power for 11 MBE-grown samples of  $\text{InAs}_{1-x}\text{Sb}_x$  on GaSb substrate at 4 K. The solid lines show the least squares linear fit to the data. The numbers in the legend show the magnitude of the peak shift for each sample in meV/decade of excitation power as given by the slope of the linear fit. .... 7-25
- Figure 7-10. Comparison of photoluminescence and absorption spectra for MBE-grown  $\text{InAs}_{0.911}\text{Sb}_{0.089}$  on GaSb substrate shows the radiative recombination to be band-to-band. The PL spectrometer resolution is 0.5 meV..... 7-27
- Figure 7-11. Effective carrier temperature,  $T_e$ , extracted from band-to-band PL peaks as shown. Dashed lines show the least squares linear fit to the high energy side of the peak.  $T_e$  is extracted from the slope of these lines using Eq (7.35). The PL spectrometer resolution is 0.5 meV..... 7-37
- Figure 7-12. Schematic drawing of electron cooling processes: 1. Carrier-carrier interaction (scattering); 2. Optical phonon emission; and 3. Acoustic phonon emission. .... 7-39
- Figure 7-13. Inverse carrier temperature,  $1/T_e$ , as a function of excitation intensity for GaAs. The solid line has a slope of  $-k_B/h\nu_{LO}$  where  $h\nu_{LO}$  is the LO-phonon energy (36.7 meV). (Shah, 1978:43)..... 7-42
- Figure 7-14. Inverse effective carrier temperatures,  $1/T_e$ , as a function of laser excitation power for several MBE-grown  $\text{InAs}_{1-x}\text{Sb}_x/\text{GaSb}$  samples. The lines show the least squares linear fit to the data. The energy of the carrier cooling mechanism,  $h\nu_{ph}$ , is extracted from the slopes of these lines using Eq (7.41). .... 7-44
- Figure 7-15. Theoretical band-to-band lineshape given by Eq (7.42), with (solid line) and without (dotted and dashed lines) Gaussian broadening. The broadening mechanism for the dotted line case has a narrower linewidth than that for the dashed line case. .... 7-49
- Figure 7-16. PL spectrum of sample  $\text{InAs}_{0.911}\text{Sb}_{0.089}$  showing effects of band tailing on the low energy side of the PL peak. The PL spectrometer resolution is 0.5 meV. .... 7-51
- Figure 7-17. Band tailing effect on the density of states for each band as a result of (a) coulombic attraction between inhomogeneously distributed defects or impurities and free carriers (Pankove, 1971:11), and (b) phase separation of the material..... 7-52



- Figure 7-18. Empirical parameter with dimensions of energy describing band tailing effects on density of states,  $E_0$ , extracted from band-to-band photoluminescence peaks as shown. Dashed lines show the least squares linear fit to the low energy side of the peak.  $E_0$  is extracted from the slope of these lines using Eq (7.44). The PL spectrometer resolution is 0.5 meV..... 7-54
- Figure 7-19. PL spectra of undoped  $\text{InAs}_{0.808}\text{Sb}_{0.192}$  sample showing three resolvable peaks. The PL spectrometer resolution is 0.6 meV..... 7-57
- Figure 7-20. Low temperature PL spectra of Be-implanted MBE-grown  $\text{InAs}_{0.905}\text{Sb}_{0.095}$  on GaSb substrate. The PL spectrometer resolution is 0.9 meV..... 7-62
- Figure 7-21. PL spectra for Be-implanted MBE-grown  $\text{InAs}_{0.905}\text{Sb}_{0.095}$  on GaSb substrate at several temperatures, showing the gradual ionization of the extrinsic peak. The PL spectrometer resolution is 0.9 meV. .... 7-64
- Figure 7-22. Low temperature PL spectra of p-type, Be-doped  $\text{InAs}_{0.955}\text{Sb}_{0.045}$  MBE-grown sample. The PL spectrometer resolution is 0.9 meV..... 7-66
- Figure 7-23. Comparison of PL (solid lines) and absorption (dashed lines) spectra for MBE-grown  $\text{InAs}_{0.955}\text{Sb}_{0.045}:\text{Be}$ . Peak  $E_{\text{band}}$  is due to band-to-band recombination. Peak  $E_{\text{DAP}}$  ionizes at  $\sim 96$  K. The PL spectrometer resolution is 0.9 meV; FTS absorption spectrometer resolution is 0.5 meV..... 7-67
- Figure 7-24. Double Gaussian fit of the higher energy peak of a low temperature  $\text{InAs}_{0.955}\text{Sb}_{0.045}:\text{Be}$  PL spectrum. The PL spectrometer resolution is 0.9 meV..... 7-69

## List of Tables

	Page
Table 4-1. MBE-growth characteristics of the $\text{InAs}_{1-x}\text{Sb}_x$ samples studied. (*InAs sample. **Thickness of top cladding layer included in this sample.).....	4-16
Table 4-2. DCXRD peak position, $\Delta\theta$ , for each $\text{InAs}_{1-x}\text{Sb}_x/\text{GaSb}$ sample with calculated lattice-mismatch, $\Delta a/a$ , and corresponding Sb composition, $x$ . Misfit, $f_0$ , and critical thickness, $t_c$ , were calculated using Eq (4.12) and Figure 4-10.....	4-21
Table 6-1. FTS absorption experimental conditions for MBE-grown $\text{InAs}_{1-x}\text{Sb}_x$ samples studied. The “p” column indicates the range of exponents obtained for that sample from the fit of the free carrier absorption equation to the data. The “ $\alpha_A$ ” column indicates the absorption coefficient as given by Eq (6.16). .....	6-2
Table 6-2. Comparison of measured and calculated Fabry-Perot interference fringe spacings, $v_{\text{FP}}$ and $hc/2n_{\text{eff}}d_{\text{eff}}$ , respectively, and fringe half widths, $\gamma_{\text{FP}}$ . The measured $\gamma_{\text{FP}}$ are approximately 0.5.....	6-17
Table 6-3. Varshni parameters for the temperature-dependence of the energy gap of MBE-grown $\text{InAs}_{1-x}\text{Sb}_x$ as determined by a least squares fit to the experimental data.....	6-23
Table 6-4. DCXRD linewidth, FWHM, along with Scherrer linewidth, $\beta_{1/2}$ , calculated using Eq (6.28) for each $\text{InAs}_{1-x}\text{Sb}_x$ GaSb sample. (* InAs sample).....	6-37
Table 7-1. Photoluminescence characteristics of 11 $\text{InAs}_{1-x}\text{Sb}_x$ samples grown by MBE on GaSb substrates. $h\nu_{\text{LO}}$ is the energy difference between the LO-phonon replica observed and the main PL peak. $\text{FWHM}_{\text{min}}$ is the minimum linewidth observed for the main PL peak for that sample. The magnitude of the PL peak shift to higher energies with increased excitation power is given in meV/decade of excitation power.....	7-23

Table 7-2. Photoluminescence characteristics of 11  $\text{InAs}_{1-x}\text{Sb}_x$  samples grown by MBE on GaSb substrates. The magnitude of the observed PL peak shift to higher energies with increased excitation power is given in meV/decade of excitation power.  $h\nu_{\text{ph}}$  is the quantized thermalization energy derived from the effective carrier temperatures. The magnitude of the PL peak shift to higher energies with increased excitation power calculated from the observed effective carrier temperatures is also given in meV/decade of excitation power.  $E_0$  refers to an empirical parameter having the dimensions of energy which describes band tailing effects..... 7-45

## List of Symbols

$a_0$	lattice constant	K	kelvin
Al	aluminum	LO	longitudinal optical (phonon)
As	arsenic	LPE	liquid phase epitaxy
Be	beryllium	$m_n$	electron effective mass
$c$	speed of light ( $299792458 \text{ m sec}^{-1}$ )	$m_p$	hole effective mass
cm	centimeter ( $10^{-2} \text{ m}$ )	meV	milli-electron volt ( $10^{-3} \text{ eV}$ )
Cu	copper	min	minute
$^{\circ}\text{C}$	degree Celsius	mW	milliwatt
DAP	donor-acceptor pair	MBE	molecular beam epitaxy
DCXRD	double crystal x-ray diffraction	MOCVD	metal organic chemical vapor deposition
<i>e.g.</i>	for example	N	nitrogen
eV	electron volt	Pt	platinum
$E_c$	conduction band energy	PL	photoluminescence
$E_{exc}$	exciton energy	sec	second
$E_g$	energy gap	Sb	antimony
$E_v$	valence band energy	Si	silicon
$E_0$	band tailing parameter	t	time
<i>et al.</i>	and others	T	temperature
<i>etc.</i>	<i>et cetera</i>	$T_e$	effective carrier temperature
$E_F$	fermi energy level	W	watt
$f(E)$	electron distribution function	x	mole fraction, typically of Sb
F-B	free-to-bound (radiative recombination)	$^{\circ}$	angular degree
FTS	Fourier transform spectroscopy	%	percent
$g(E)$	electronic density of states	Å	Angstrom ( $10^{-10} \text{ m}$ )
Ga	gallium	$\Gamma$	Brillouin zone center
GaSb	binary III-V semiconductor, gallium antimonide	$\lambda$	wavelength
h	Planck constant ( $4.1356692 \times 10^{-15} \text{ eV K}^{-1}$ )	$\mu\text{m}$	micron ( $10^{-6} \text{ m}$ )
<i>i.e.</i>	that is	$\nu$	frequency ( $\text{sec}^{-1}$ )
In	indium	$\theta_B$	Bragg angle
$\text{InAs}_{1-x}\text{Sb}_x$	ternary III-V semiconductor, indium arsenide antimonide	(###)	Miller index, plane
IR	infrared	{###}	Miller index, set of equivalent planes
$k_B$	Boltzmann constant ( $8.617385 \times 10^{-5} \text{ eV sec}$ )	[###]	Miller index, direction
		<###>	Miller index, set of equivalent directions

## Abstract

$\text{InAs}_{1-x}\text{Sb}_x$  is an attractive material for optoelectronic devices because it provides the lowest direct energy gap of the III-V semiconductors. Undoped, MBE-grown  $\text{InAs}_{1-x}\text{Sb}_x$  nearly lattice-matched to (100) GaSb substrates ( $-0.617\% \leq \Delta a/a \leq +0.708\%$ ) was studied by optical characterization to determine its material parameters and crystalline quality. Absorption measurements at temperatures between 6-295 K determined the energy gap and wavelength-dependent absorption coefficient for each sample. The resulting compositional dependence of the energy gap was anomalous when compared to previously reported data, suggesting that phase separation existed in this material. The samples were also studied by temperature- and excitation-dependent photoluminescence (PL), which resulted in single-peaked spectra for the majority of cases; this peak was identified as band-to-band recombination by comparison with absorption data. Linewidths as narrow as 4.3 meV and the observation of LO-phonon replicas both indicated high material quality, but the shift of the band edge peak to higher energies with increased excitation was much greater than expected from band filling alone and underscored the likelihood of phase separation. Additional extrinsic PL peaks were also observed from one of the undoped samples, and were identified as a free-to-bound transition at 4-7 meV and a donor-acceptor pair transition at 10-14 meV below the band edge. Characterization of ion implanted and epitaxially doped  $\text{InAs}_{1-x}\text{Sb}_x:\text{Be}$  identified the Be acceptor energy as  $>30$  meV above the valence band in this material.

# OPTICAL CHARACTERIZATION OF INDIUM ARSENIDE ANTIMONIDE SEMICONDUCTORS GROWN BY MOLECULAR BEAM EPITAXY

## I. Introduction

The ternary semiconductor  $\text{InAs}_{1-x}\text{Sb}_x$  is an attractive choice for the development of mid-infrared (IR) optoelectronics because it offers the lowest direct energy gap of the III-V semiconductors. It has been grown and characterized by various means since 1964, but after initial material characterization on a set of bulk-grown polycrystalline samples, much of the basic materials work gave way to more device-oriented research. Often the funding source dictates the emphasis on device development since that is where the profits lie. This current research complements the  $\text{InAs}_{1-x}\text{Sb}_x$  semiconductor laser development by providing the materials characterization which ultimately contribute to device performance in a less direct fashion.

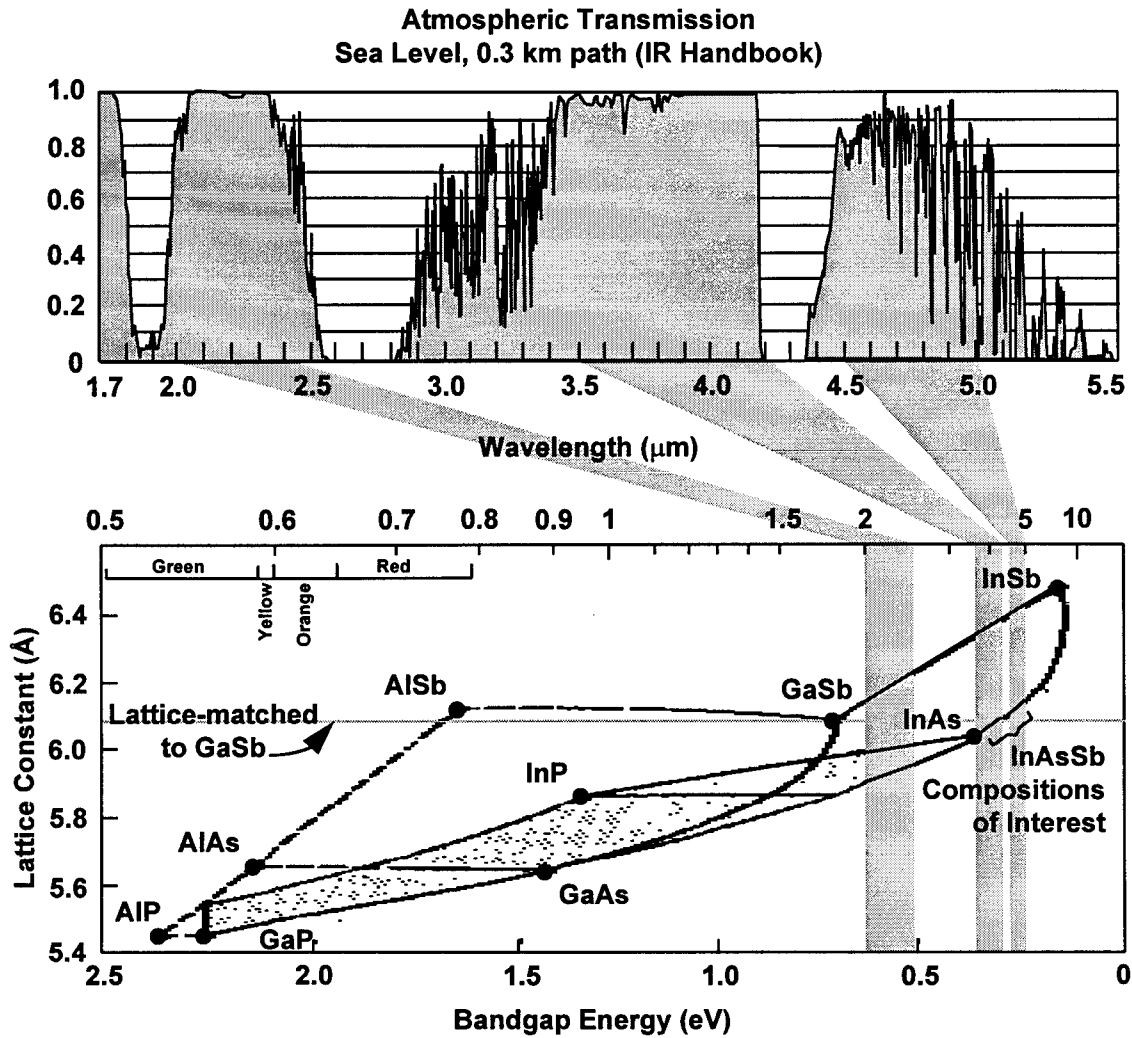
### **Motivation**

There has been considerable interest for some time, both by the government and commercially, in developing optoelectronic devices which exploit the atmospheric transmission windows in the mid-IR, i.e., at wavelengths of  $\sim 2.0\text{-}2.5\ \mu\text{m}$ ,  $\sim 3.5\text{-}4.2\ \mu\text{m}$  and  $\sim 4.5\text{-}5.0\ \mu\text{m}$  (Figure 1-1, top), for applications such as eye-safe laser radar and

communications, remote atmospheric gas detection, molecular spectroscopy and military countermeasures. With successful semiconductor detectors such as InAs, InSb, InAsSb, PtSi and HgCdTe existing to cover these bands, the need for companion sources at these wavelengths has become even more pressing.

Semiconductor lasers have the advantage of being more compact, rugged, and much more efficient than other types of lasers. This makes them very attractive for these applications. Several semiconductor systems have been considered for mid-IR lasers. Much effort has been put into developing the II-VI compositions such as HgCdTe for IR detection, so they are likely candidates for IR emission, as well. HgCdTe diode lasers have been demonstrated but are too immature for applications (Arias, 1993:S255; Le, 1994:810) A significant effort was also put into developing the Pb-salts (PbSe, PbTe, PbSSe, PbSeTe, PbEuSeS, PbEuSeTe) as diode lasers by General Motors for emissions monitoring, but device reliability is still in question for these materials (Partin, 1988:1716). The most mature semiconductor laser material system is the III-V GaAs/AlGaAs system. Development of a mid-IR laser in a III-V composition draws on the experience already developed for the GaAs devices.

The bottom of Figure 1-1 shows the lattice constant versus energy gap diagram for the group III-V semiconductors. In this figure, binary semiconductors (those with two elements) are shown as solid dots, ternaries (three elements) as lines connecting the binary endpoints, and quaternaries (four elements) as the area which is surrounded by the ternary lines.



**III-V Semiconductor Compound  
Lattice Constants, Bandgap Energies and Bandgap Wavelengths  
(Saleh and Teich)**

Figure 1-1. (Top) Atmospheric transmission in the mid-infrared (Wolfe, 1989:5-88). (Bottom) Lattice constant in Å versus energy gap diagram for the III-V semiconductors (Saleh, 1991:550).

The room temperature energy gap of the quaternary semiconductor,  $Ga_{1-y}In_yAs_{1-x}Sb_x$ , is shown in Figure 1-1 to cover the optical wavelength region of 2-12  $\mu m$  in the mid-IR spectrum. High quality semiconductor crystal structure is required for



optimum optoelectronic device performance and this requires that the epitaxial layers are grown lattice-matched (*i.e.*, near the same lattice constant) to high quality substrates. Similar lattice constants are shown in Figure 1-1 as horizontal lines. Since high quality ternary substrates are not readily available, binary substrates must be considered. For  $\text{Ga}_{1-y}\text{In}_y\text{As}_{1-x}\text{Sb}_x$ , GaSb and InAs are substrate candidates.

The gray bars extending from the top of Figure 1-1 show that wavelengths in the first two atmospheric transmission windows can be covered by  $\text{Ga}_{1-y}\text{In}_y\text{As}_{1-x}\text{Sb}_x$  compositions lattice matched to GaSb. The lattice matching conditions for  $\text{Ga}_{1-y}\text{In}_y\text{As}_{1-x}\text{Sb}_x$  to GaSb are given by Adachi as (Adachi, 1987: 4869):

$$y = \frac{0.3835 - 0.3835x}{0.421 + 0.216x} \quad (1.1)$$

The third atmospheric transmission window,  $\sim 4.5\text{-}5.0 \mu\text{m}$ , can be covered by the ternary semiconductor  $\text{InAs}_{1-x}\text{Sb}_x$  (actually a subset of the quaternary  $\text{Ga}_{1-y}\text{In}_y\text{As}_{1-x}\text{Sb}_x$ ) at compositions lattice matched ( $x \cong 9\%$ ) or slightly lattice-mismatched to GaSb substrates. High performance diode and optically-pumped semiconductor lasers in the  $4\text{-}5 \mu\text{m}$  spectral region have been developed at these  $\text{InAs}_{1-x}\text{Sb}_x$  compositions using the molecular beam epitaxial (MBE) growth technique (see Chapter II, Semiconductor Diode Lasers for details).

Although these lasers and other optoelectronic devices have been demonstrated in the  $\text{InAs}_{1-x}\text{Sb}_x$  material system in the past, good quality epitaxial material was not easily obtained. Therefore, there are few reports of the basic material characterization of

epitaxial  $\text{InAs}_{1-x}\text{Sb}_x$  in the literature (see Chapter III, InAsSb Material Characterization). Device modeling and design are intricate parts of the development process, and effective modeling requires accurate knowledge of the material parameters involved. To enhance the material parameter data base for  $\text{InAs}_{1-x}\text{Sb}_x$ , temperature-dependent optical absorption and the excitation- and temperature-dependent photoluminescence (PL) measurements of MBE-grown  $\text{InAs}_{1-x}\text{Sb}_x$  closely lattice-matched to GaSb substrates have been completed to provide empirical values for several material parameters not reported previously.

### **Objective**

The underlying objective of this research, in general, is to improve the performance of optically- and electrically-pumped  $\text{InAs}_{1-x}\text{Sb}_x$  mid-infrared semiconductor lasers. The specific contributions of this current research toward the achievement of this objective are: the determination of basic material parameters for MBE-grown  $\text{InAs}_{1-x}\text{Sb}_x$  not previously available in the literature; and the assessment of the quality of the material being used in these lasers. Although several optoelectronic devices in the  $\text{InAs}_{1-x}\text{Sb}_x$  material system have been reported in the past, surprisingly little basic material characterization of  $\text{InAs}_{1-x}\text{Sb}_x$  has been reported, especially for epitaxially-grown samples.

## Approach

To form a baseline for undoped  $\text{InAs}_{1-x}\text{Sb}_x$  characterization, undoped InAs grown by molecular beam epitaxy (MBE) on both InAs and GaSb substrates was studied. InAs provides a system which, first, is easier to grow and characterize because it is binary (composed of only two elements), and second, has been reported in more detail in the literature. Since the ternary  $\text{InAs}_{1-x}\text{Sb}_x$  samples ranged in Sb composition between  $0 < x < 20\%$ , knowledge of the band edge, defect, and impurity tendencies of InAs was useful.

Undoped, bulk (thicknesses greater than  $\sim 0.5 \mu\text{m}$ )  $\text{InAs}_{1-x}\text{Sb}_x$  samples nearly lattice-matched to GaSb substrates which were grown by MBE as calibrations for actual laser structure growth, were studied by optical characterization, namely absorption and photoluminescence (PL). The composition and strain relaxation of each sample was determined using double crystal x-ray diffraction (see Chapter IV, Samples).

Differences between reported band edge measurements for  $\text{InAs}_{1-x}\text{Sb}_x$  exist in the literature. Therefore, absorption experiments were performed primarily to determine accurate band edge positions for these samples. However, a secondary result of these measurements was the determination of absorption coefficients for  $\text{InAs}_{1-x}\text{Sb}_x$ . A description of the absorption experiment is included in Chapter V, with the experimental results in Chapter VI.

The samples were also studied in detail by temperature- and excitation-dependent PL to determine intrinsic linewidths, ascertain material quality, and determine extrinsic energy levels. Because relatively few  $\text{InAs}_{1-x}\text{Sb}_x$  characterization results have been

published (see Chapter III, Previous Work), identification of extrinsic energy levels observed in nominally undoped  $\text{InAs}_{1-x}\text{Sb}_x$  material was uncertain. Therefore, epitaxially Be-doped and Be-ion implanted samples were studied to identify the position of one specific impurity in the material. The PL experiment is described in Chapter V, with experimental results given in Chapter VII.

## II. Background

The physical principles underlying the various semiconductor phenomena observed in this research are outlined here. The reader is pointed toward more detailed references as applicable.

### **Solid State Physics**

Crystalline solids are a class of materials in which the constituent atoms are arranged in a periodic structure. Understanding the physical properties of such material has been simplified because of this periodicity. The discrete electronic levels of an isolated atom are predicted by quantum mechanics. As individual atoms are brought together in a solid, these discrete levels form into bands of energies (Figure 2-1) due to the overlap of the individual atomic wave functions.

These energy bands can overlap themselves at one atomic spacing, and separate into a new configuration at a closer atomic separation. This redistribution of electronic states results in solid bands which can be either completely filled, partially filled or completely empty. The classification of a solid as either an “insulator,” “semiconductor” or “metal” is dependent on its conductivity. Since no electrical conduction can occur in either completely filled or completely empty bands, this classification is dependent on the filling and energy separation of the bands.

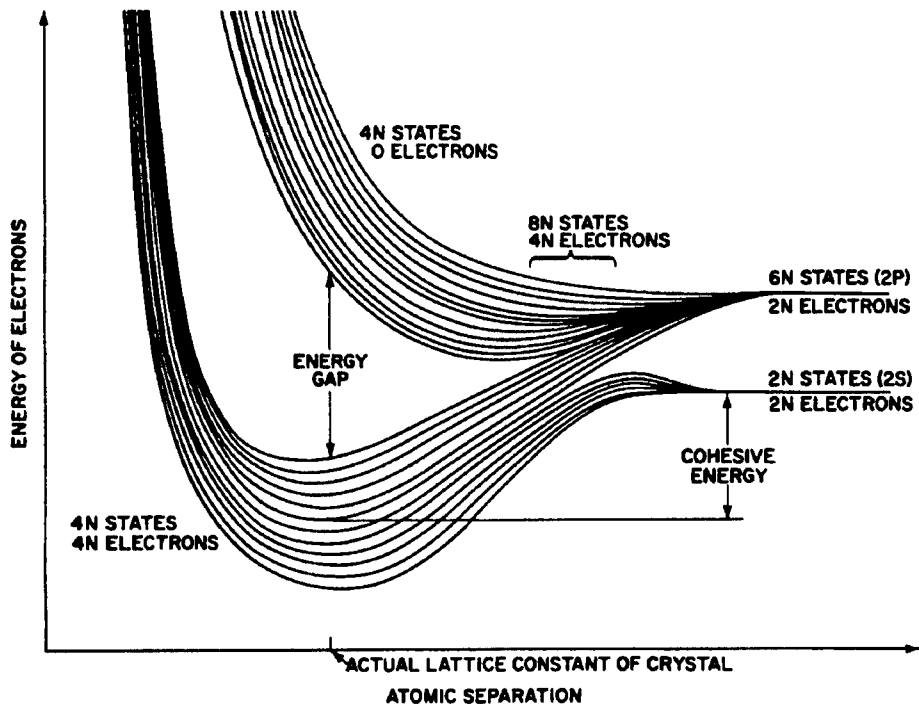


Figure 2-1. Schematic drawing of the energy bands of diamond as a function of atomic spacing (Kimball, 1935:560).

An insulator has completely filled lower energy bands and completely empty upper bands. Since by statistical physics, the occupation probability of an energy level,  $E$ , is given by the Fermi distribution,

$$f(E) = \frac{1}{1 + \exp\left(\frac{E - E_F}{k_B T}\right)}, \quad (2.1)$$

there is always some probability that an energy level is filled thermally ( $T$  is temperature and  $k_B$  is the Boltzmann constant). This probability decreases as the separation between that level and the Fermi energy level,  $E_F$ , increases. Therefore, the width of the forbidden energy gap (*i.e.*, between the highest filled band and the lowest empty band) in an

insulator is large enough that the probability of occupying a state in the upper band is minimal (Figure 2-2 (a)). In practice, the energy gap for insulators is generally larger than  $\sim 3$  eV (Pankove, 1971:3).

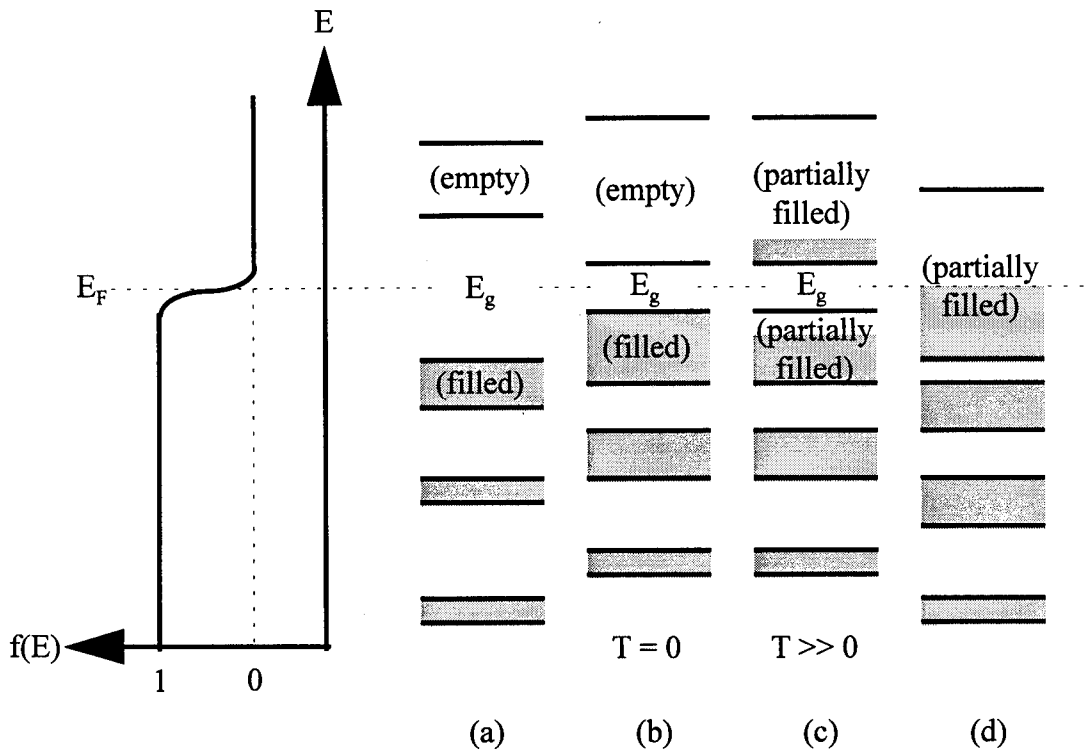


Figure 2-2. Energy band diagrams for (a) insulator, (b) semiconductor at low temperature, (c) semiconductor at high temperature, and (d) metal (McKelvey, 1966:246).

A semiconductor acts like an insulator at low temperatures (Figure 2-2 (b)). However, as temperature is increased, a significant number of electrons are excited thermally from the states near the top of the highest filled band to those near the bottom of the lowest empty band because the width of the forbidden energy gap is smaller (Figure 2-2 (c)). This creates partially filled bands and allows conduction to occur. In

practice, the energy gaps of semiconductors are generally less than  $\sim 3$  eV. The density of electrons in the upper band,  $N_c$ , (or holes in the lower band) is given by the Fermi distribution (Eq (2.1)) and the density of states for that band, *e.g.*,

$$g_c(E) = \frac{(2m_n)^{3/2}}{2\pi^2\hbar^3} \sqrt{E - E_c}, \quad (2.2)$$

where  $m_n$  is the effective mass of the upper (conduction) band electron and  $E_c$  is the energy at the bottom of the conduction band, to be

$$N_c = 4N \int_{E_c}^{\infty} g_c(E) f(E) dE, \quad (2.3)$$

where  $N$  is the number of atoms in the solid. In semiconductors, the density is generally less than  $10^{20} \text{ cm}^{-3}$  (Pankove, 1971:3).

Metals have partially filled upper bands, even at low temperatures (Figure 2-2 (d)). In practice, the electron concentration of the partially filled band is generally on the order of  $10^{23} \text{ cm}^{-3}$  (Pankove, 1971:3).

### **Lattice Constant**

The lattice constant for a periodic crystal structure gives a consistent quantifier by which atomic separations are measured. It is not the distance between nearest-neighbor atoms, but the length of a side of the conventional atomic unit cell. The lattice constant is important for this current research because it is used to calculate the exact ternary



compositions for the  $\text{InAs}_{1-x}\text{Sb}_x$  samples, and many of the results given are composition-dependent.

The atomic unit cell which repeats itself in the periodic crystalline structure of many semiconductors is that of two interpenetrating face-centered cubics (FCC, Figure 2-3 (a)), offset on the diagonal by one fourth a lattice constant,  $a_0$  (Figure 2-3 (b)). In a group IV elemental semiconductor such as Si, all the atoms of this unit cell are the same and the structure is called “diamond.” In the III-V semiconductors, including  $\text{InAs}_{1-x}\text{Sb}_x$ , the group III atoms occupy the lattice sites of one of the face-centered cubics and the group V atoms occupy the other (Figure 2-3 (c)). This structure is called “zincblende.”

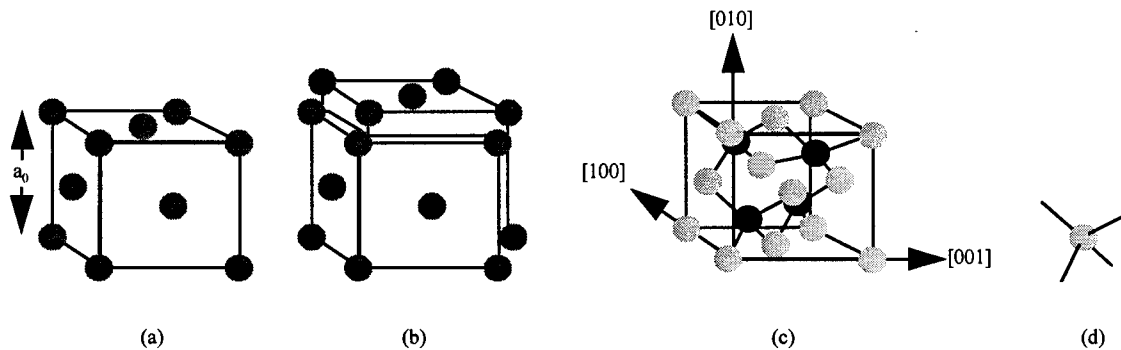


Figure 2-3. (a) FCC structure. (b) Interpenetrating FCCs. (c) Zincblende structure. (d) Tetrahedral bonds.

The atoms of the diamond and zincblende structures form tetrahedral bonds with their four nearest neighbors (Figure 2-3 (d)). In the case of the group IV atoms in the diamond structure, the four outer shell valence electrons are shared with the nearest neighbor atoms. The attractive force of the shared electron to both nuclei holds the atoms

together by covalent bonding. In the III-V semiconductors such as  $\text{InAs}_{1-x}\text{Sb}_x$ , since three valence electrons of the group III atoms are shared with five valence electrons of the group V atoms, the bonding is mainly covalent but also slightly ionic since the group III anion is electrostatically attracted to the group V cation as well.

The sizes and potentials of the atoms which make up the unit cell determine the size of the unit cell and the lattice constant,  $a_0$ . The lattice constants for the binary III-V semiconductors, InAs and InSb, are well known from x-ray measurements to be:

$$a_{0-\text{InAs}} = 6.0583 \text{ \AA} \quad (2.4a)$$

$$a_{0-\text{InSb}} = 6.47937 \text{ \AA} \quad (2.4b)$$

at 298.15 K with thermal expansion coefficients as shown in Figure 2-4 (Madelung, 1991:136).

The lattice constant of a ternary semiconductor,  $\text{AB}_{1-x}\text{C}_x$ , is determined by Vegard's law to be the linear interpolation between the binary endpoints:

$$a_{0-\text{ABC}} = a_{0-\text{AB}}(1-x) + a_{0-\text{AC}}x \quad (2.5)$$

Woolley and Warner showed a slight variance from Vegard's law for polycrystalline  $\text{InAs}_{1-x}\text{Sb}_x$  formed by six month anneals of compressed InAs-InSb powders near the solidus temperature (Figure 2-5) (Woolley, 1964a:1142). However, despite this small variance, Vegard's law is normally assumed to hold for single crystal  $\text{InAs}_{1-x}\text{Sb}_x$  compositions.

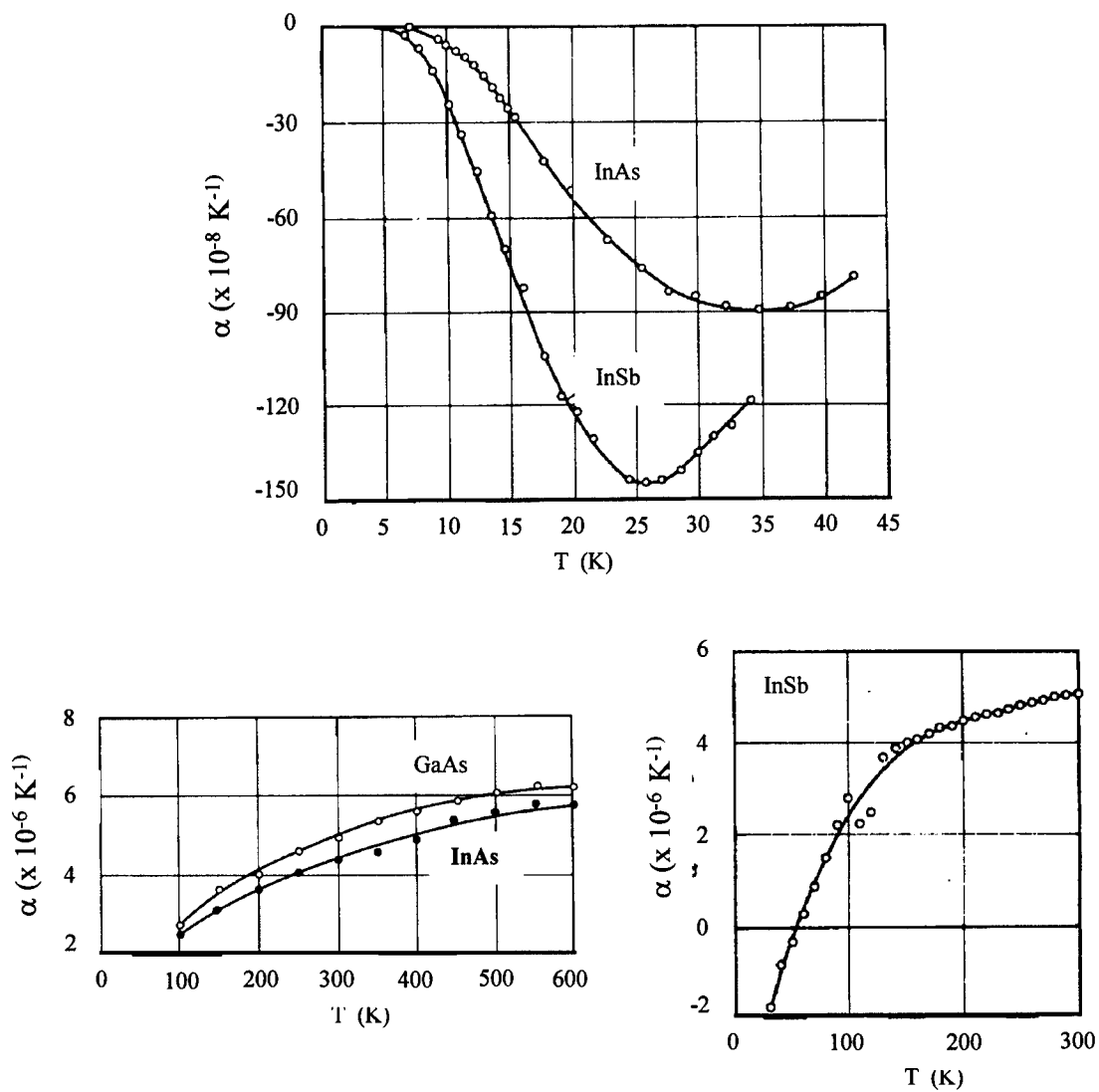


Figure 2-4. Thermal expansion coefficients for InAs and InSb (Madelung, 1991:136).

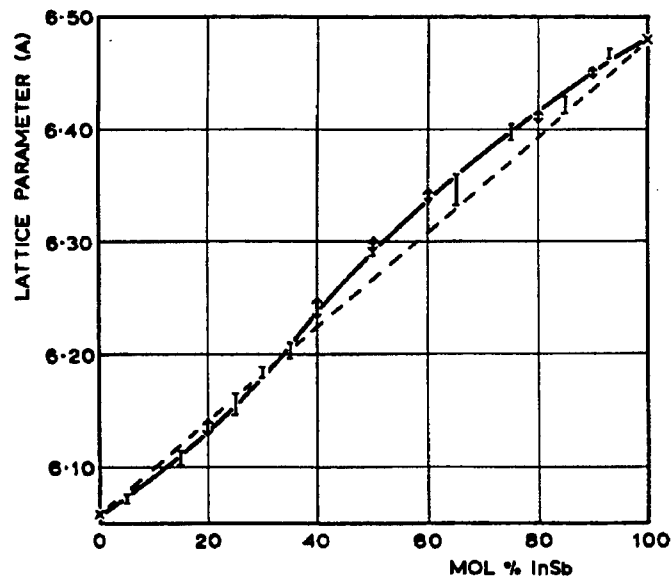


Figure 2-5. Variation of  $\text{InAs}_{1-x}\text{Sb}_x$  lattice constant with x-composition. Solid line - Woolley and Warner's measurements. Dotted line - Vegard's law. (Woolley, 1964a:1142)

### Band Structure

The band structure of a specific semiconductor is calculated quantum mechanically from the potentials and lattices constants of the constituent atoms in the crystalline structure using one of many models, *e.g.*, Weak Periodic Potential, Tight Binding, *etc.* (see Ashcroft and Mermin), but fundamental to these models is Bloch's theory that the wave function for an electron moving in a periodic potential such as a crystal lattice must also be periodic. The plane waves which compose this wave function for an electron moving through a family of lattice planes separated by a distance,  $d$ , are Bragg reflected by this periodic potential only for certain propagation vectors, namely  $k \cong$

$2\pi/d$ . This Bragg reflection leads to the notion of a reciprocal lattice where the lattice points are separated, not by the real-space dimensions corresponding to the lattice constant,  $a_0$ , but by momentum-space dimensions corresponding to the wave vector,  $2\pi/a_0$ .

A calculated band structure for  $\text{InAs}_{1-x}\text{Sb}_x$  was not available from the literature so the band structure for InAs is shown in Figure 2-6 (Madelung, 1991:135) with the assumption that it is similar to that of  $\text{InAs}_{1-x}\text{Sb}_x$  with  $x < 0.2$ . The momentum-space vectors labeled X, K, and L correspond to a real-space coordinate system with coordinates labeled (x,y,z) as  $X = 2\pi/a_0 (0,0,1)$ ,  $K = 2\pi/a_0 (3/4,3/4,0)$  and  $L = 2\pi/a_0 (1/2,1/2,1/2)$ .

The parabolic band shapes near the bottom of the conduction band,  $\Gamma_6$ , and the tops of the valence bands,  $\Gamma_8$ , are close to the free electron E versus k parabola,

$$E = \frac{\hbar^2 k^2}{2m}, \quad (2.6)$$

where the electron mass,  $m$ , is actually the electron effective mass,  $m_n$ , in the conduction band, or the heavy hole effective mass,  $m_{ph}$ , or the light hole effective mass,  $m_{pl}$ , in the valence bands.

## Phonons

Phonons are the harmonic modes of lattice vibration supported by the crystal lattice. The three dimensional phonon dispersion relations for InAs and InSb are shown

in Figure 2-7. The acoustic branches, labeled LA and TA in Figure 2-7, show the  $\omega = ck$  form characteristic of sound waves, where  $\omega$  is the frequency supported. The optical branches, labeled LO and TO in Figure 2-7, are less dependent on momentum, especially near the  $\Gamma$ -point, and more able to interact with electromagnetic radiation. (For a more detailed development of phonons, see Ashcroft and Mermin, pp. 430-443.)

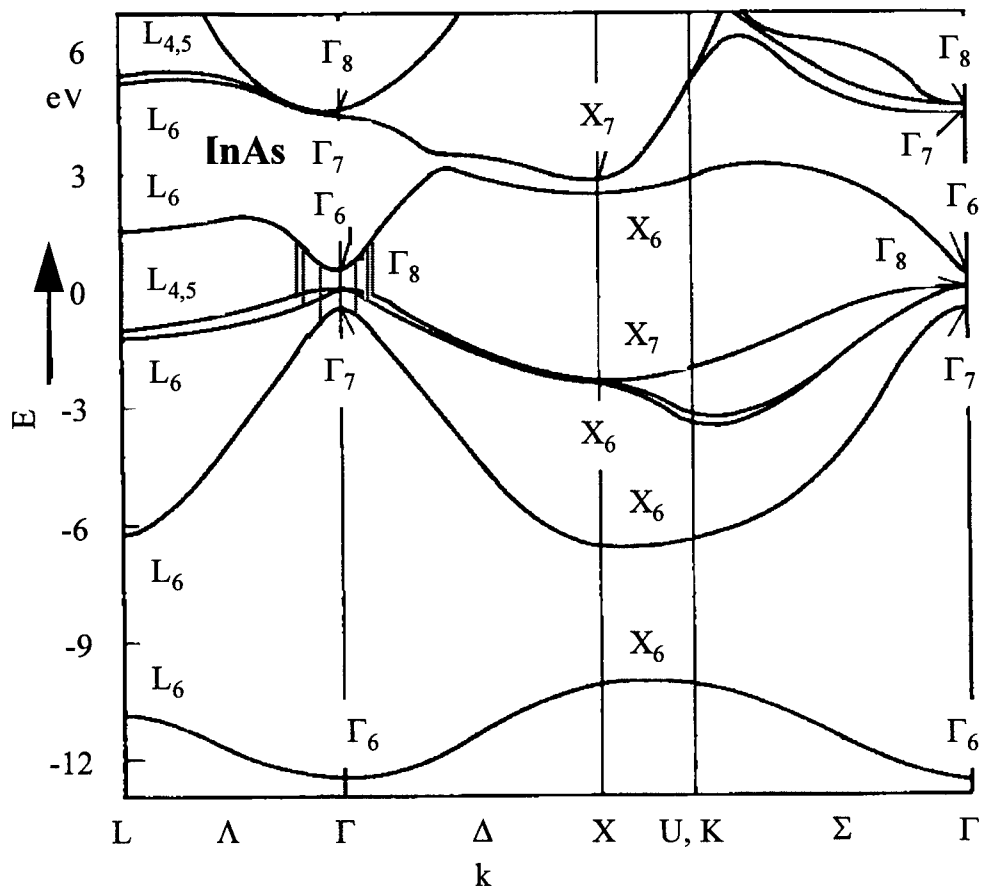


Figure 2-6. InAs band structure (Madelung, 1991:135).

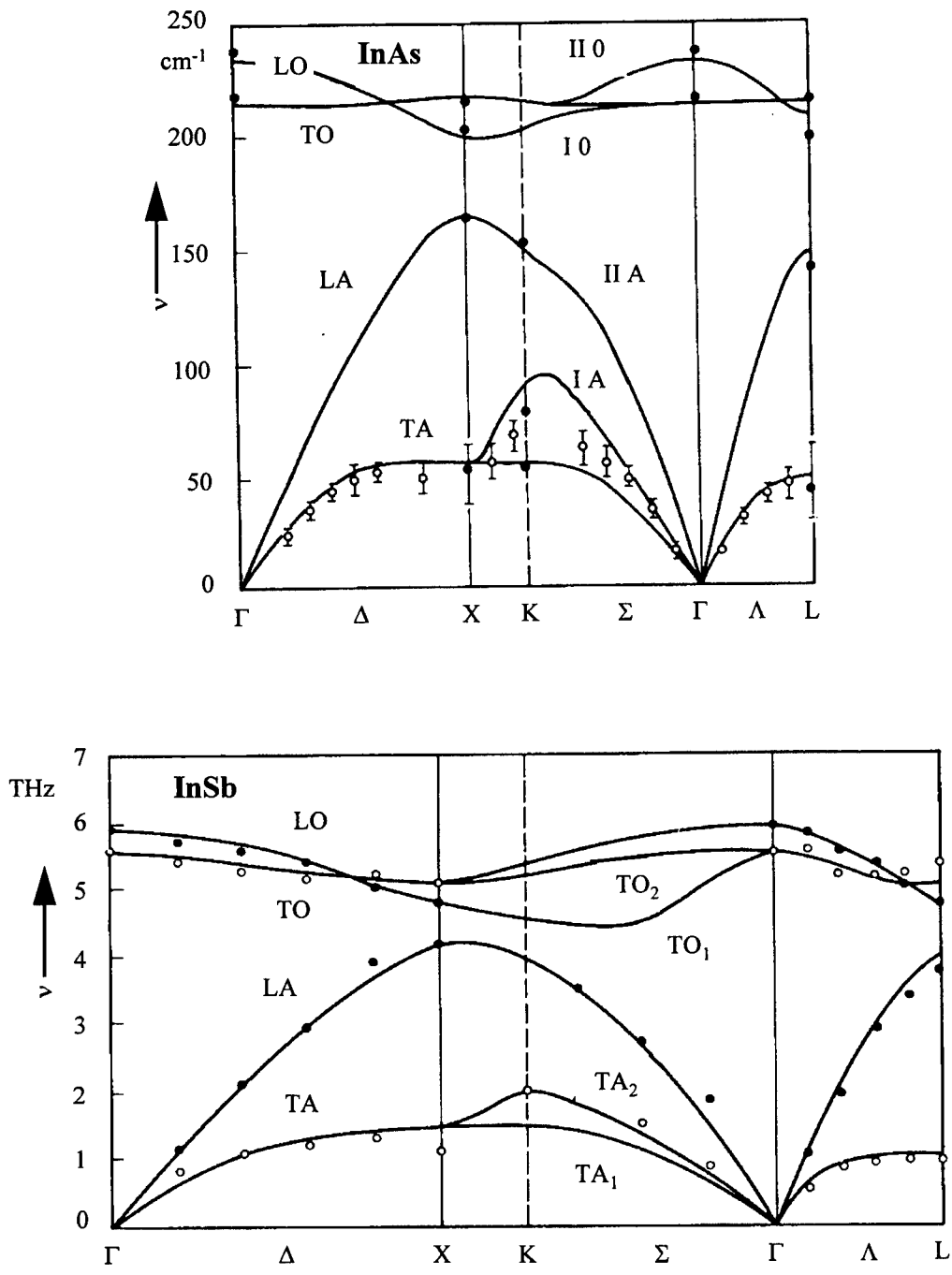


Figure 2-7. Phonon dispersion relations for InAs and InSb. The LO-phonon energies at the  $\Gamma$ -point are 29.6 meV and 24.8 meV for InAs and InSb, respectively. (Madelung, 1991:137)

The phonon dispersion for a ternary is generally taken to be the linear interpolation between those of the binary endpoints (Pavesi, 1994:4779). This was shown to hold for  $\text{InAs}_{1-x}\text{Sb}_x$  through Raman studies by Li *et al.* (Li, 1992:567) (see Chapter III, InAsSb Material Characterization, Figure 3-14). Knowledge of the phonon energies for the materials studied in this current research is important in identifying features which occur in the experimental spectra as will be explained in Chapters V, VI and VII.

### **Semiconductor Diode Lasers**

As was mentioned in Chapter I, the underlying objective of this research is to improve the performance of  $\text{InAs}_{1-x}\text{Sb}_x$  mid-infrared semiconductor lasers. The preceding sections of this chapter focused on the physical characteristics of semiconductor material. This section addresses the heterostructure (or a structure composed of layers of different materials), in particular, one required to make an efficient semiconductor laser.

The flat energy band for a bulk intrinsic semiconductor was shown in Figure 2-2. An intrinsic semiconductor is one in which all available electronic states are only in either the valence or conduction bands. The pure zincblende lattice described above may be altered from the intrinsic state by defects or impurities. Defects may occur in the form of vacancies (atoms missing at a lattice site allowing a neighboring site to be easily ionized), substitutionals (group III atoms at a group V site or *vice versa* which are easily doubly



ionized), or interstitials (atoms in the lattice but not at a lattice site). Impurities occur when atoms with a valence other than III or V occupy lattice sites and are easily ionized. Intentional placement of these atoms is called, “doping.”

These shallow ionization energies appear as energy levels inside the band gap but near the conduction band edge (n-type, donates an electron to the conduction band) or valence band edge (p-type, accepts an electron from the valence band). For an intrinsic semiconductor, the Fermi level is near the middle of the band gap (Figure 2-8 (a)), but when the semiconductor is doped, the addition of the donor levels near the conduction band moves the Fermi level up, nearer to the conduction band in bulk n-type material (Figure 2-8 (b)) and the addition of the acceptor levels near the valence band moves the Fermi level down, nearer to the valence band in bulk p-type materials (Figure 2-8 (c)).

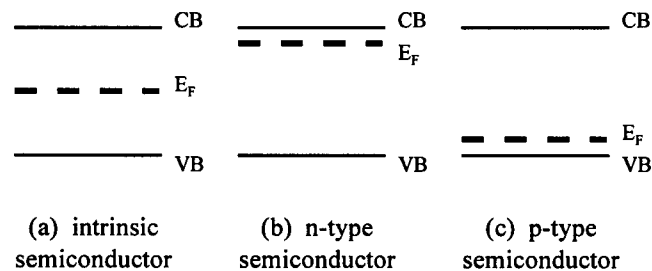


Figure 2-8. Energy band diagram of bulk intrinsic and extrinsic semiconductor material.

When similar p-type and n-type material are brought together (a p-n homojunction), holes from the p-side diffuse into the n-type material leaving negatively-charged acceptor ions fixed in their lattice sites near the junction. Likewise, electrons from the n-side diffuse into the p-type material leaving positively-charged donor ions

behind. This separation of space charge results in an electric field which, in turn, results in carrier movement opposite that of diffusion. When thermal equilibrium is achieved, net carrier movement is zero and the Fermi level is constant throughout the material (Figure 2-9).

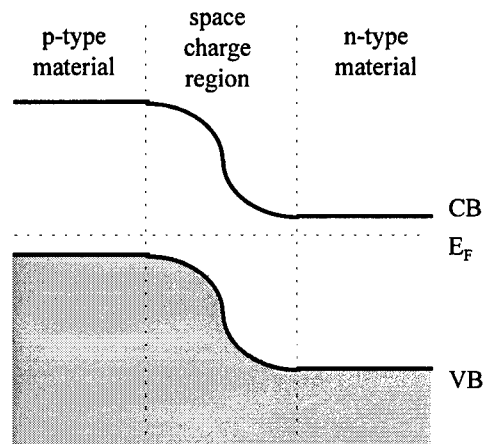


Figure 2-9. Band diagram of a p-n junction in thermal equilibrium.

For degenerately doped semiconductors at thermal equilibrium, the Fermi level is below the valence band maximum on the p-side and above the conduction band minimum on the n-side, (Figure 2-10 (a)). When a forward bias is applied to the junction, *i.e.*, a positive voltage to the p-side with respect to the n-side, the electro-static potential across the junction is decreased and electrons are injected into the space charge region from the n-side and holes from the p-side. At a large enough bias, the space charge region contains a large number of electrons in the conduction band and holes in the valence band with large spatial overlap allowing band-to-band radiative recombination to occur (Figure

2-10 (b)). The condition for population inversion is  $E_{Fn} - E_{Fp} > E_g$ . This type of p-n junction is the basis for a homojunction diode laser.

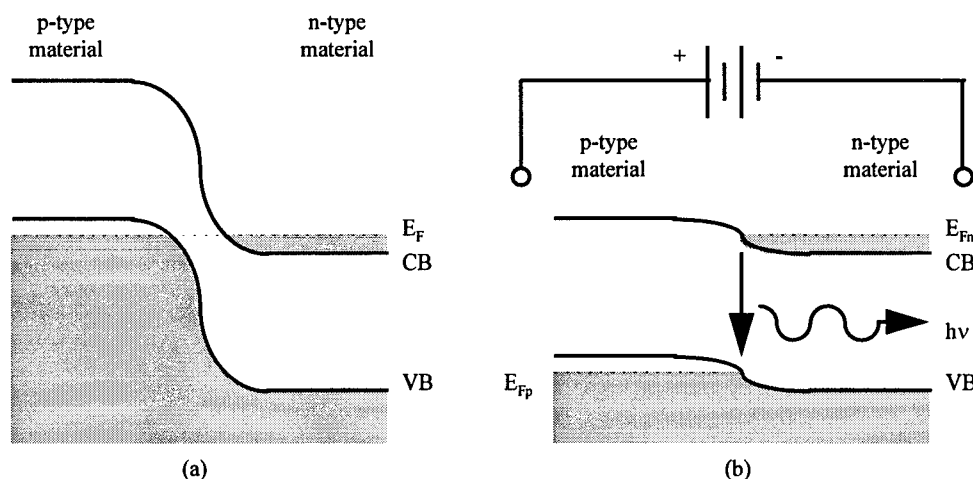


Figure 2-10. (a) Band diagram of a heavily doped p-n junction. (b) Band-to-band radiative transitions under injection.

The use of heterojunctions, *i.e.*, the bringing together of two different semiconductor materials, improved diode laser performance. One material, the active region, was surrounded by a wider band gap “cladding” material to provide better electrical confinement of the conduction band electrons and valence band holes in the active region (Figure 2-11 (a)); this resulted in more efficient radiative recombination. The term “double heterojunction (DH) diode laser” results from the two heterojunctions on either side of the active region in Figure 2-11 (a).

A p-n junction is still required for efficient injection, but here the band offsets between the active region and cladding materials affect the band banding at the interface (Figure 2-11 (b)). The conduction band offset is the difference between the electron

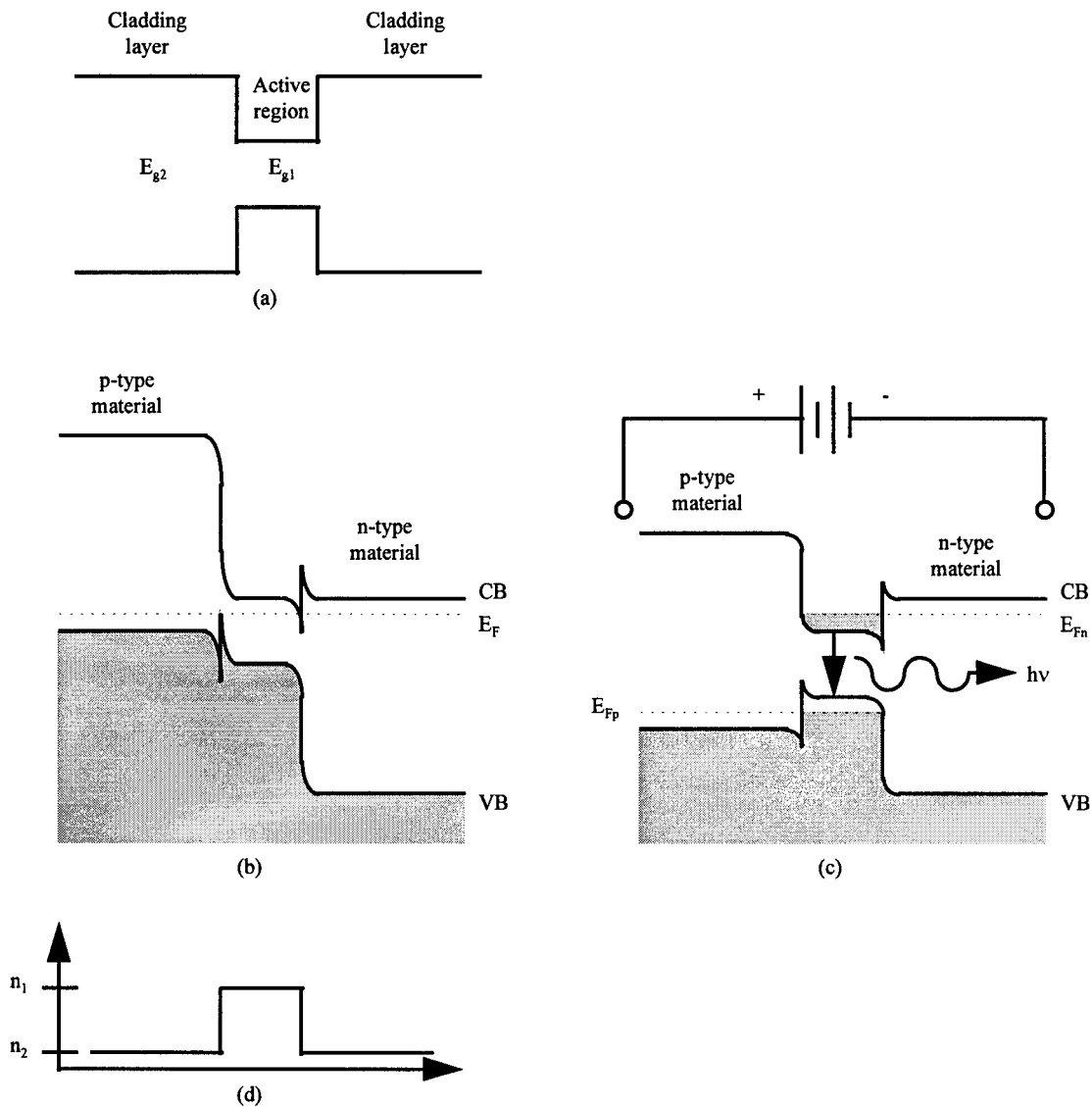


Figure 2-11. (a) Band diagram of an ideal double heterojunction (DH). (b) p-n-n DH in thermal equilibrium. (c) p-n-n DH under forward bias with carrier injection. (d) Refractive indices of p-n-n DH which forms optical waveguide.

affinities (the energy from the bottom of the conduction band to the vacuum level),  $\chi$ , of the two materials; and the valence band offset is the difference between the ionization potentials (the energy from the top of the valence band to the vacuum level),  $I_p = \chi + E_g$ , of the two materials. As in the case of the homojunction laser, a forward bias is applied

to inject electrons and holes into the active region for radiative recombination (Figure 2-11 (c)).

The efficiency improvement achieved by using a DH laser is also due to the confinement of the optical mode in the active region where gain extraction occurs. Another consideration in choosing the two semiconductor materials for the DH structure, then, is that an optical waveguide is formed. This is achieved when the index of the active region is greater than the index of the cladding layers (Figure 2-11 (d)). The optical confinement is defined by the decay rate of the active region mode as it penetrates into the cladding layers, or the "extinction coefficient" (Saleh, 1991:253),

$$\gamma = (n_1^2 k^2 \cos^2 \theta - n_2^2 k^2)^{1/2}, \quad (2.7)$$

where  $n_1$  is the refractive index of the active region,  $n_2$  is the refractive index of the clad,  $k$  is the wave vector propagating down the waveguide and  $\theta$  is the bounce angle of that mode.

Optimum DH semiconductor laser performance requires high quality crystalline structures. Misfit dislocations can occur at any heterojunction when the lattice constants of the two materials are significantly different. When one material is grown upon another material, the atomic lattice of the top layer is distorted (or "strained") to match that of the bottom layer. However, after a certain "critical thickness" of the top layer has been grown, misfit dislocations occur which allow the strain to be relieved, and allow the crystal to relax back to its natural lattice constant. High quality, defect-free materials in

the laser structure require that any thick layers grown must be closely lattice-matched, *i.e.*, have nearly the same lattice constant, to the material upon which it is grown to keep misfit dislocations to a minimum. High dislocation densities limit the laser device's performance and lifetime.

The III-V semiconductors required to develop a mid-IR DH diode laser structure were shown in Figure 1-1. The ternary  $\text{InAs}_{1-x}\text{Sb}_x$  provides the energy gap of  $\sim 0.3$  eV (or optical wavelengths of  $\sim 4$   $\mu\text{m}$  in the mid-IR) necessary for the active region. Since a lattice matched structure is required and high quality substrates are available only in binary materials, GaSb is a suitable choice of substrate. All compositions of  $\text{Ga}_x\text{In}_{1-x}\text{As}_y\text{Sb}_{1-y}$  lattice-matched to GaSb have energy gaps greater than  $\text{InAs}_{1-x}\text{Sb}_x$  to provide the necessary electrical confinement. (Lattice-matching conditions for  $\text{Ga}_x\text{In}_{1-x}\text{As}_y\text{Sb}_{1-y}$  to GaSb were given in Eq (1.1).) However, Figure 2-12 (a) shows that the refractive index increases for increasing Ga content in  $\text{Ga}_x\text{In}_{1-x}\text{As}_y\text{Sb}_{1-y}$  lattice-matched to GaSb so the necessary optical confinement is not provided by these compositions (Adachi, 1987:4869).

Figure 1-1 also shows another quaternary alloy with a wider band gap than  $\text{InAs}_{1-x}\text{Sb}_x$  and lattice-matched to GaSb is  $\text{Al}_x\text{Ga}_{1-x}\text{As}_y\text{Sb}_{1-y}$ . The lattice matching condition is given by (Adachi, 1987:4869) as

$$y = \frac{0.0396x}{0.4426 + 0.0318x} \quad (2.8)$$

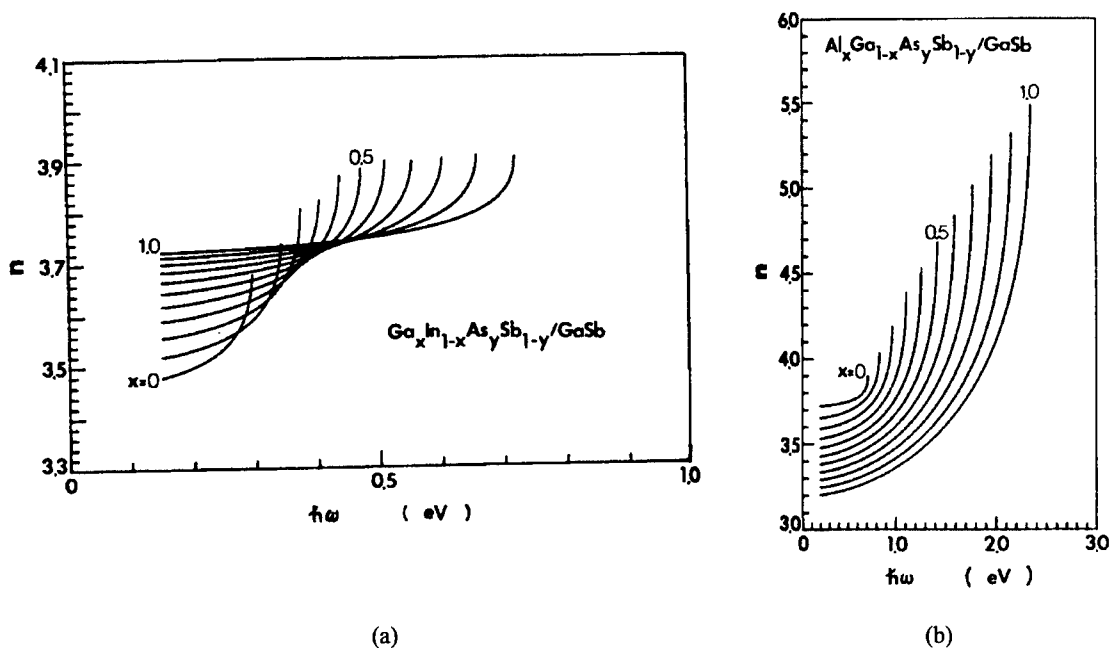


Figure 2-12. (a) Calculated refractive indices of  $\text{Ga}_x\text{In}_{1-x}\text{As}_y\text{Sb}_{1-y}/\text{GaSb}$  as a function of photon energy with  $x$ -composition increments of 0.1. (b) Calculated refractive indices of  $\text{Al}_x\text{Ga}_{1-x}\text{As}_y\text{Sb}_{1-y}/\text{GaSb}$  as a function of photon energy with  $x$ -composition increments of 0.1. (Adachi, 1987:4869)

Figure 2-12 (b) shows the refractive indices for  $x$ -compositions of  $\text{Al}_x\text{Ga}_{1-x}\text{As}_y\text{Sb}_{1-y}$  greater than  $\sim 20\%$  are below that of  $\text{InAs}_{1-x}\text{Sb}_x$ , so they do provide the necessary optical confinement.

The band offsets between the  $\text{InAs}_{1-x}\text{Sb}_x$  and  $\text{Al}_x\text{Ga}_{1-x}\text{As}_y\text{Sb}_{1-y}$  compositions, and the GaSb substrate are still uncertain. However, one estimate based on experimental ionization potentials of the AlAs, AlSb, GaSb, InAs and InSb binaries, linear interpolations between binary ionization potentials for the ternary ionization potentials, and linear interpolations between these ternary ionization potentials and the GaSb ionization potential is shown in Figure 2-13 (Martinelli, 1991:13). Using the band offsets

of Figure 2-13, the band diagram of the  $\text{InAs}_{0.91}\text{Sb}_{0.09}/\text{AlAs}_{0.08}\text{Sb}_{0.92}/\text{GaSb}$  DH laser structure is shown in Figure 2-14. The laser structure shown in Figure 2-14 leads directly to the structures of the samples studied in this current research as described in Chapter IV, Undoped Samples.

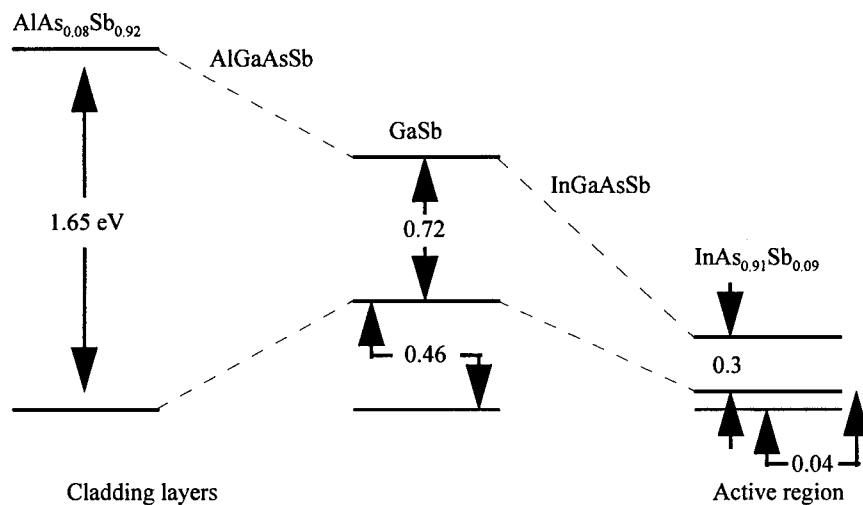


Figure 2-13. Band offsets for AlGaAsSb/InGaAsSb heterojunctions lattice-matched to GaSb (Martinelli, 1991:13).



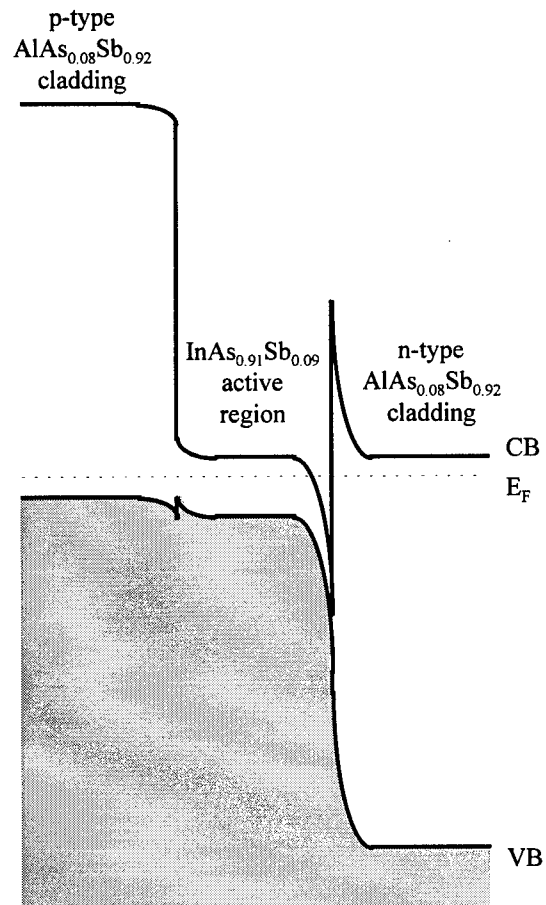


Figure 2-14.  $\text{InAs}_{0.91}\text{Sb}_{0.09}/\text{AlAs}_{0.08}\text{Sb}_{0.92}$  lattice matched to GaSb DH laser structure.

### III. Previous Work

Although the diode and optically-pumped semiconductor lasers described in Chapter II and other optoelectronic devices have been reported in the  $\text{InAs}_{1-x}\text{Sb}_x$  material system in the past, high quality  $\text{InAs}_{1-x}\text{Sb}_x$  epitaxial material has been readily available only recently. Therefore, there are few reports of its basic material characterization in the literature. This chapter begins with a synopsis of previously reported  $\text{InAs}_{1-x}\text{Sb}_x$  material characterization work, and concludes with a brief history of the  $\text{InAs}_{1-x}\text{Sb}_x$  semiconductor laser development, to inform the reader as to the rationale in studying these current  $\text{InAs}_{1-x}\text{Sb}_x$  compositions and structures.

#### **InAsSb Material Characterization**

The study of the optical properties of  $\text{InAs}_y\text{Sb}_{1-y}$  began in 1964 with Potter and Kretschmar of the US Naval Ordinance Laboratory in Corona, CA. They performed transmission measurements of polycrystalline n-type films with compositions of  $0 \leq y \leq 1$  thermally evaporated onto glass substrates. These bulk alloys were then annealed for eight weeks at 500 °C to approach single phase from the InAs-InSb solid solution. The 1-6  $\mu\text{m}$  IR transmittance and reflectance of the  $\text{InAs}_{0.7}\text{Sb}_{0.3}$  film was measured. From the transmission and reflection maxima and minima, the dispersion of these curves was calculated. Then, the effective mass of an electron at the conduction band minimum was calculated to be 0.044 times the electronic mass (Potter, 1964:57).

The bulk of the reported  $\text{InAs}_{1-x}\text{Sb}_x$  characterization work between 1964-1971 was co-authored by J.C. Woolley, first at the University of Nottingham, UK, then at the University of Ottawa. Homogeneous but polycrystalline ingots with Sb composition between 3 and 12% were produced from high purity n-InAs and n-InSb which were melted together and cooled in a temperature gradient of 7 °C/cm with a rate of cooling of 4 °C/day over a six month period to form 15-20 cm long ingots. Each end of these ingots was in single phase with the cross sectional compositional variation shown at the top of Figure 3-1. Specimens out to 20% Sb content were produced by zone recrystallization in which a background furnace kept the ingot at a temperature of 550 °C while a 5 cm molten zone produced by heater rods and cooled copper plates was moved along the ingot at 0.5 cm/day. Again, each end was in single phase with the cross sectional compositional variation shown in Figure 3-1 (Woolley, 1964a:1142).

The energy gap of  $\text{InAs}_{1-x}\text{Sb}_x$  was first measured by infrared transmission by Woolley and Warner at the University of Nottingham, UK, (Woolley, 1964b:1879). Specimens from these ingots were studied by infrared transmission at temperatures between 90 and 360 K. The method of obtaining  $E_g$  from transmission data on polycrystalline samples of unknown reflectivity was somewhat arbitrary (Woolley, 1961:354). Using the absorption formula,

$$I(h\nu) = I_0(h\nu) \exp[-\alpha(h\nu)d] \quad (3.1)$$

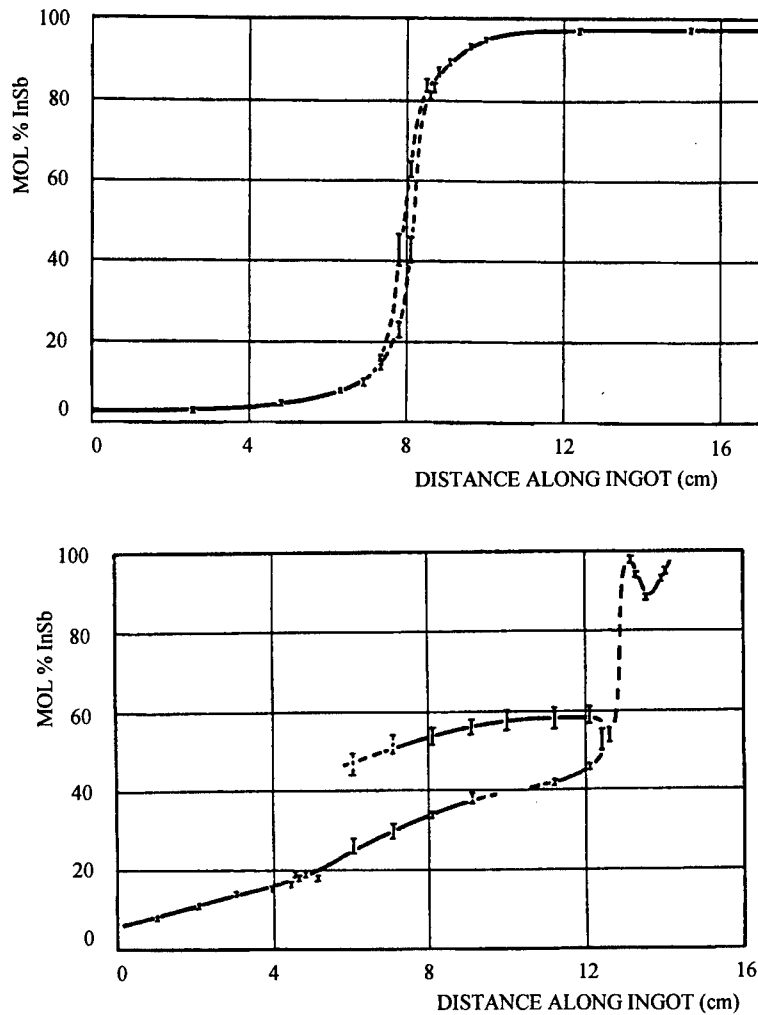


Figure 3-1. Top: Variation of composition of cross sectional slice as a function of position in a directionally frozen ingot. Bottom: Variation of composition of cross sectional slice as a function of position in a zone recrystallized ingot (Woolley, 1964a:1142).

the energy gap was assigned by choosing a constant value of  $\alpha(h\nu)$  ( $300 \text{ cm}^{-1}$  in their case) at which  $h\nu$  equaled the accepted values for the energy gaps of the binary endpoints, InAs and InSb.  $E_g$  for each ternary was then assigned to correspond to  $\alpha(E_g) = 300 \text{ cm}^{-1}$ .

(This methodology is addressed again in Chapter VI.) The energy gap is plotted as a function of molar fraction of InAs-InSb in Figure 3-2. The energy gap at a temperature of 0 K,  $E_g(0)$ , shown in Figure 3-2 were linearly extrapolated from the high temperature data. (This linear extrapolation is also addressed again in Chapter VI.) Woolley and Thompson at the University of Ottawa then calculated the effective mass of an electron at the  $\Gamma$ -point using this data (Woolley, 1964c:2030).

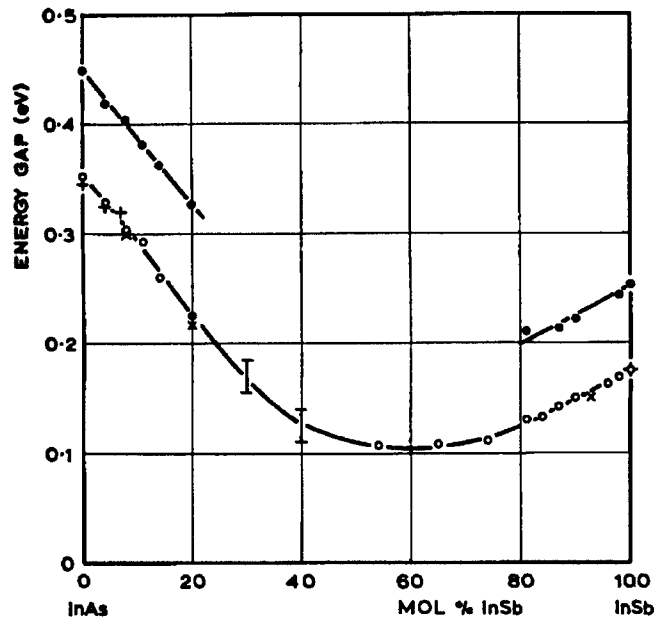


Figure 3-2. Variation of optical energy gap with alloy composition: ○ = room temperature transmission measurements; + and I = room temperature diffuse reflectivity measurements; and ● = transmission measurements extrapolated to 0 K (Woolley, 1964b:1879).

The  $E_g(0)$  values for the entire x-composition range were also extrapolated by Coderre and Woolley from Hall coefficient measurements at temperatures between 123 and 773 K. These samples were prepared as described above or by a horizontal

Bridgman technique. Once again, a linear extrapolation from the higher temperature data was done. Figure 3-3 shows the variation of extrapolated band gap with composition (Coderre, 1968:1191).

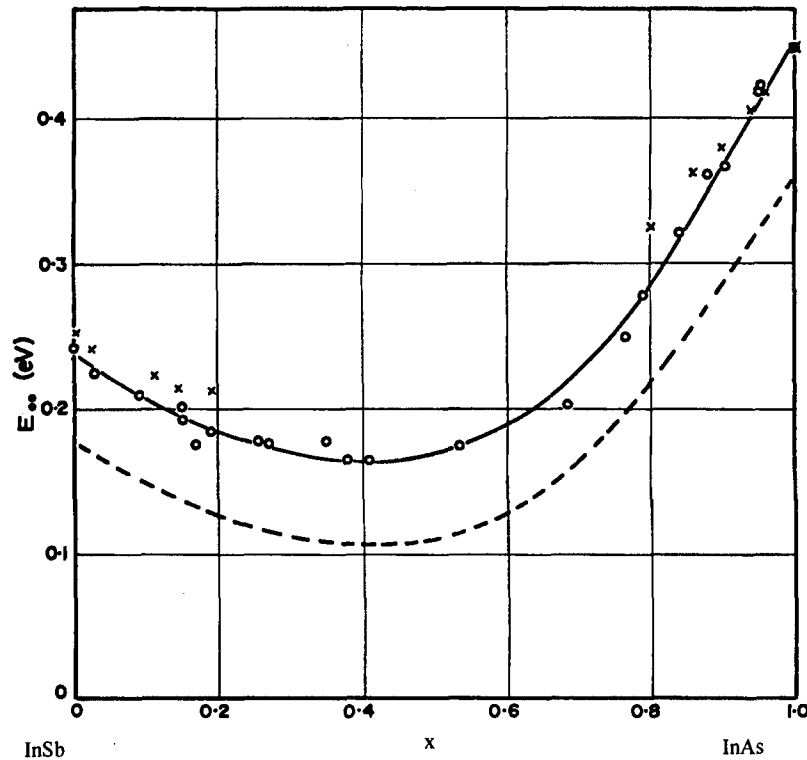


Figure 3-3. Variation of extrapolated absolute zero band gap of  $\text{InAs}_{1-x}\text{Sb}_x$  with Sb composition,  $x$ :  $\circ$  = Coderre and Woolley results;  $\times$  = extrapolated absolute zero band gap from Woolley and Warner (1964) data; and  $--$  = Woolley and Warner (1964) room temperature optical band gap. (Coderre, 1968:1207)

Aubin and Woolley measured thermoelectric power and Hall coefficient as a function of magnetic field on the same material to determine the scattering mechanisms for this material. The scattering parameter,  $s$ , was determined from the variation of the

relaxation time with energy as  $\tau \propto E^s$ . Since  $s$  was near  $+1/2$  in all cases, acoustic or optical phonons were possible, but since the measurements were made at 296 K, a temperature not considerably greater than  $\hbar\omega_0/2\pi k_B$  where  $\omega_0$  is the optical phonon frequency, optical phonons were ruled out and the scattering was attributed to acoustic phonons. The electronic effective mass at the  $\Gamma$ -point was then calculated (Aubin, 1968:1191).

Free carrier Faraday rotation was measured by van Tongerlo and Woolley on the same material, again to determine the electron effective mass at the  $\Gamma$ -point. To avoid interband transitions, Faraday rotation measurements were made at photon energies considerably less than  $E_g$  (van Tongerlo, 1968:1199). Vishnubhatla and Woolley performed electroreflectance measurements on the same material to determine disorder in the alloy lattice (Vishnubhatla, 1969:1661).

Far IR reflectivity studies of the  $\text{InAs}_{1-x}\text{Sb}_x$  samples from Woolley *et al.* were performed by Lucovsky and Chen at the University of Rochester. They observed one TO phonon reflectance band in the  $x = 0.15$  samples at  $\sim 230 \text{ cm}^{-1}$  ( $\sim 29 \text{ meV}$ ) and two TO phonon bands in the higher Sb-content samples ( $x = 0.75$  and  $0.80$ ) at  $\sim 185\text{-}200 \text{ cm}^{-1}$  ( $\sim 23\text{-}25 \text{ meV}$ ) (Lucovsky, 1970:1397). Finally, the electric susceptibility effective mass was investigated using IR plasma reflectance on the same samples by Thomas and Woolley (Thomas, 1971:2052).

The first epitaxial growth technique of  $\text{InAs}_{1-x}\text{Sb}_x$  was reported in 1971 by Stringfellow and Greene of Hewlett-Packard (Stringfellow, 1971:805). They reported

liquid phase epitaxial (LPE) growth of  $\text{InAs}_{1-x}\text{Sb}_x$  on (111) InAs substrates and determined the room temperature energy gap as Woolley and Warner had done previously by assigning  $E_g$  at the energy when the absorption coefficient was  $\alpha(E_g) = 300 \text{ cm}^{-1}$ , and found the following expression for the compositional dependence (Figure 3-4):

$$E_g = 0.35 - 0.771x + 0.596x^2 \text{ eV} \quad (3.2)$$

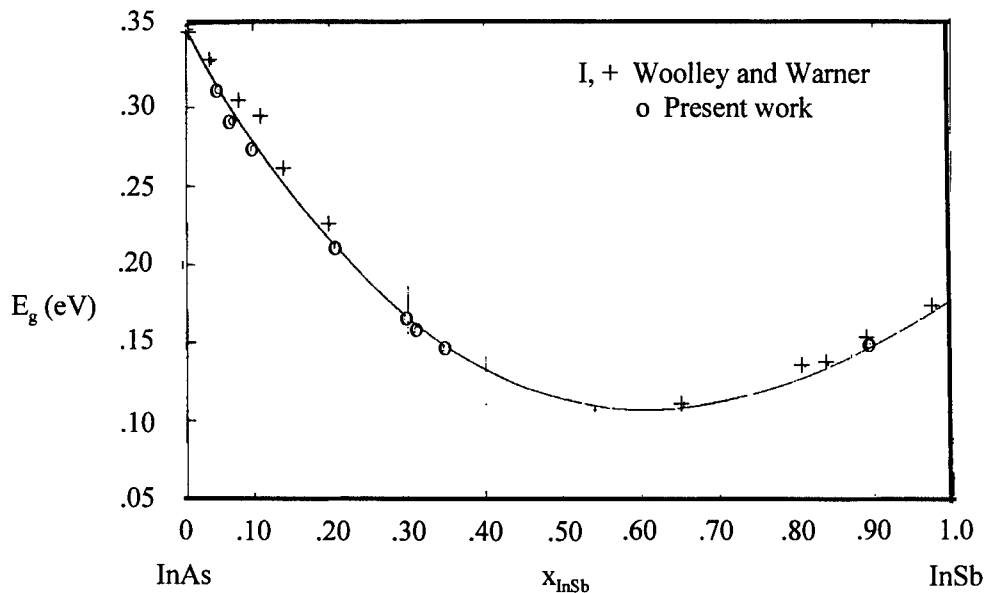


Figure 3-4. Compositional dependence of the room temperature energy gap of LPE-grown  $\text{InAs}_{1-x}\text{Sb}_x$  on InAs by Stringfellow and Greene.  $E_g$  was assigned as the photon energy when  $\alpha(E_g) = 300 \text{ cm}^{-1}$  in absorption measurements. (Stringfellow, 1971:805)

A.M. Andrews of Rockwell co-authored a number of papers on LPE-grown  $\text{InAs}_{1-x}\text{Sb}_x$  between 1976 and 1980. Andrews *et al.* reported growth on (100) InAs



substrates and referred to the crystal synthesis problems of Woolley *et al.* as preventing the development of high quality  $\text{InAs}_{1-x}\text{Sb}_x$  alloys for IR applications (Andrews, 1976:961).

Bubulac and Andrews reported on Be-ion implantation of LPE-grown  $\text{InAs}_{0.89}\text{Sb}_{0.11}$  on (100) GaSb. They focused on the Be concentration profiles determined by secondary ion mass spectroscopy (SIMS) before and after annealing. No mention was made of any optical characterization of the implanted samples (Bubulac, 1979:519). Bubulac and Andrews also reported an IR detector from  $\text{InAs}_{0.86}\text{Sb}_{0.14}$  lattice-matched to (100) GaSb substrate with spectral response between  $\sim 1.8\text{-}4.0\ \mu\text{m}$  (Bubulac, 1980:734).

A few Russian papers on LPE-grown  $\text{InAs}_{1-x}\text{Sb}_x$  were published between 1978 and 1982. Esina *et al.* of the Ioffe Institute, Leningrad, reported the first PL measurements of LPE-grown single crystal,  $60\ \mu\text{m}$  epilayers of  $\text{InAs}_{1-x}\text{Sb}_x$  at  $77\ \text{°K}$ . They attributed the reduced PL intensity to Auger recombination similar to that of InAs. They also verified the Sb-composition with previous bandgap versus composition theory (Esina, 1978:342). Bondar *et al.* of the Institute of Electronic Material, Moscow, reported Hall measurements of  $\text{InAs}_y\text{Sb}_{1-y}$  grown on p-type GaSb substrates (Bondar, 1982:215).

The first successful epitaxial growth of  $\text{InAs}_x\text{Sb}_{1-x}$  epilayers and  $\text{p}^+\text{-n}$  junctions by metal organic chemical vapor deposition (MOCVD) was reported by Chiang and Bedair of the North Carolina State University in 1985. Their compositions were  $0.4 < x < 0.7$  and grown on (100) InAs or (100) InSb substrates, as they were interested in materials for  $8\text{-}12\ \mu\text{m}$  detectors (Chiang, 1985:383). Lee and Bedair (1985) also reported molecular

beam epitaxial (MBE) growth of InSb/InAsSb superlattices on GaAs and InSb substrates (Lee, 1985:1219).

Aside from the MOCVD and MBE firsts at North Carolina State, the majority of  $\text{InAs}_{1-x}\text{Sb}_x$  research reported between 1985 and 1988 was done at AT&T Bell Labs. VanderZiel *et al.* reported optically-pumped laser oscillation from LPE-grown  $\text{InAs}_{0.87}\text{Sb}_{0.13}/\text{InAs}$  DHs on (100) InAs substrates. The PL peak shifted from 4.05  $\mu\text{m}$  to 4.2  $\mu\text{m}$  with temperature (77-300 K) and showed deep dips at 4.3  $\mu\text{m}$  are due to  $\text{CO}_2$  absorption in the optical path (VanderZiel, 1985:1827).

Mohammed and VanderZiel reported operation of an  $\text{InAs}_{0.85}\text{Sb}_{0.15}$  p-n junction photodetector grown on (100) InAs by LPE. A shift in the PL peak to longer wavelengths was smaller than expected for the bandgap, and was nonlinear with temperature. Therefore, the authors attributed the emission to impurity states rather than the band edge (Figure 3-5) (Mohammed, 1986:215).

The first MBE growth of  $\text{In}_{1-x}\text{Ga}_x\text{As}_{1-y}\text{Sb}_y$  and  $\text{InAs}_{0.92}\text{Sb}_{0.08}$  lattice-matched to (100) GaSb was reported by Tsang *et al.* in 1986. PL of the quaternary alloys with compositions near the GaSb binary was reported, but PL of the ternary could not be accomplished because they were limited in wavelength by their quartz optics (Tsang, 1985:283; Chiu, 1986:600).

Capacitance-voltage (C-V) and current-voltage (I-V) measurements were made by Srivastava *et al.* on n-type  $\text{InAs}_{0.95}\text{Sb}_{0.05}$  heterojunctions grown by MOCVD on n-type

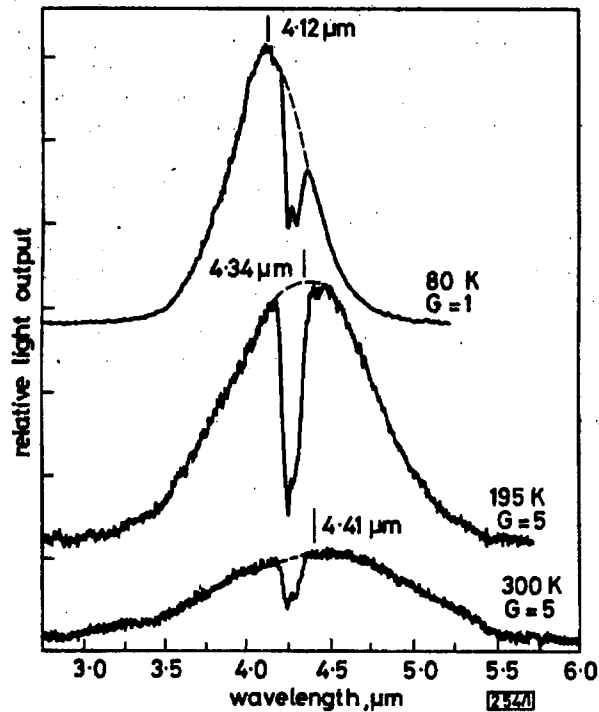


Figure 3-5. PL spectra of  $\text{InAs}_{0.85}\text{Sb}_{0.15}$  which the authors attributed to impurity state emission. The deep dips at  $4.3 \mu\text{m}$  are due to  $\text{CO}_2$  absorption in the optical path. (Mohammed, 1986:215).

(100) GaSb:Te substrates. The valence band offset,  $\Delta E_v$ , was determined by:

$$\Delta E_v = (V_{d2} - \xi_2 - E_{g2}) + (V_{d1} + \xi_1 + E_{g1}) \quad (3.3)$$

where: the GaSb band bending,  $V_{d2} = 0.8 \text{ eV}$ , was determined from the V-intercept of the C-V curve;  $\xi_2 = 0.01 \text{ eV}$  was determined from Fermi-Dirac statistics and the GaSb carrier concentration which was determined by the slope of the C-V curve;  $E_{g2}$  is the GaSb energy gap,  $0.73 \text{ eV}$ ; the InAsSb band bending calculated solving Poisson's equation in the InAsSb accumulation region,  $V_{d1} = 0.25 \text{ eV}$ ,  $\xi_1 = 0.03 \text{ eV}$  was determined from

Fermi-Dirac statistics and the InAsSb carrier concentration; and  $E_{g1}$  is the InAsSb energy gap, 0.32 eV (Figure 3-6) (Srivastava, 1986:41).

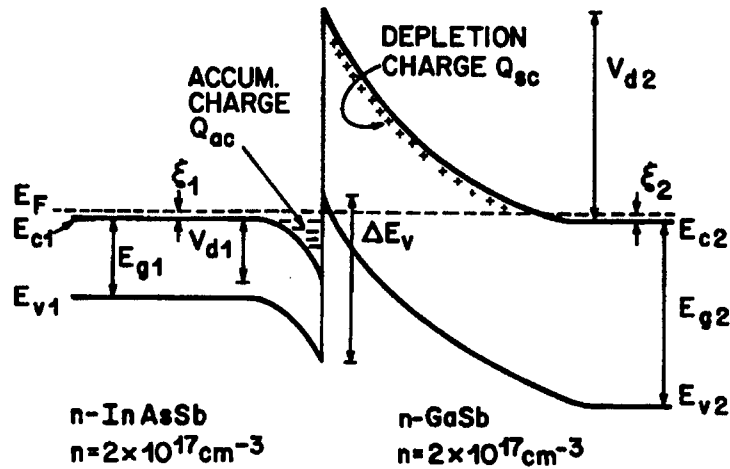


Figure 3-6. InAsSb/n-GaSb heterojunction band diagram (Srivastava, 1986:41).

Yen *et al.* performed Fourier Transform IR (FTIR) absorption measurements of 2.5  $\mu\text{m}$  epilayers of  $\text{InAs}_{1-x}\text{Sb}_x$  grown on (100) InAs substrates by MBE. They also determined the room temperature energy gap by assigning  $E_g$  when  $\alpha(E_g) = 300 \text{ cm}^{-1}$  as previously described, and found the bandgap to be in agreement with Woolley and Warner's for the entire  $0 < x < 1$  range (Figure 3-7). The compositional dependence of the energy gap they determined was (Yen, 1987:927):

$$E_g = 0.35 - 0.771x + 0.596x^2 \text{ eV} \quad (3.4)$$

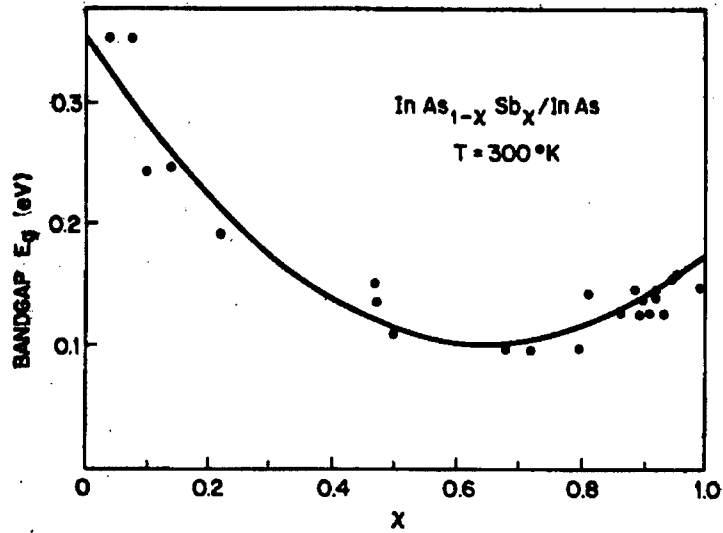


Figure 3-7. Compositional dependence of the room temperature energy gap of MBE-grown  $\text{InAs}_{1-x}\text{Sb}_x$  on InAs by Yen *et al.*  $E_g$  was assigned as the photon energy when  $\alpha(E_g) = 300 \text{ cm}^{-1}$  in FTIR absorption measurements. (Yen, 1987:927)

Bethea and Yen reported  $\text{InAs}_{0.02}\text{Sb}_{0.98}/\text{GaAs}$  photoconducting detectors grown by MBE (Bethea, 1987:1431) and the optical transmission of  $\text{InAs}_{0.22}\text{Sb}_{0.78}$  grown by MBE on a (100) SI-GaAs (Bethea, 1988:291). Yen then investigated the Hall properties of  $\text{InAs}_{1-x}\text{Sb}_x$  ( $x > 0.5$ ) grown on (100) GaAs by MBE (Yen, 1988b:3306).

PL of  $\text{InAs}_{1-x}\text{Sb}_x$  grown by MBE on (100) InAs was also reported by Yen *et al.* in 1988. Luminescence peaks at wavelengths as long as  $8 \mu\text{m}$  were reported for the first time in a III-V semiconductor. Figure 3-8 shows the PL spectra of  $\text{InAs}_{0.96}\text{Sb}_{0.04}$  and  $\text{InAs}_{0.87}\text{Sb}_{0.13}$  at various temperatures. Peaks denoted by B were assigned as band-edge transitions since they shifted to longer wavelengths with increasing temperature; they had linewidths as narrow as  $5.76 \text{ meV}$ . Peaks denoted by I were assigned as impurity-related transitions since they were sharp, appeared only at low temperatures, and shifted to

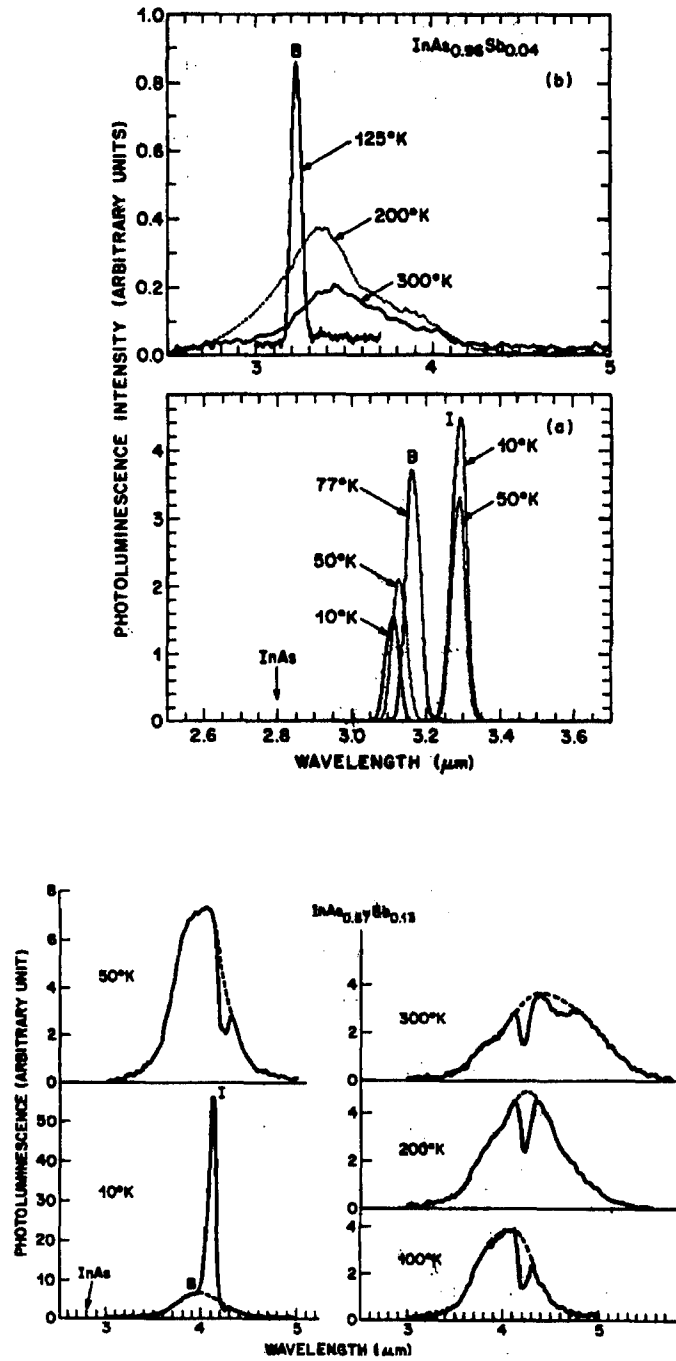


Figure 3-8. PL spectra of MBE-grown  $\text{InAs}_{0.96}\text{Sb}_{0.04}$  and  $\text{InAs}_{0.87}\text{Sb}_{0.13}$  on InAs at various temperatures. B is associated with band edge transitions and I with impurity transitions. The linewidths are as narrow as 5.15 meV for the  $\text{InAs}_{0.96}\text{Sb}_{0.04}$  I peak at 10 K. (Yen, 1988a:489)

shorter wavelengths with increasing temperature. The impurity linewidth was as narrow as 5.15 meV. The dips in the spectra at 4.2 and 4.6  $\mu\text{m}$  are due to absorption by  $\text{CO}_2$  in the optical path. The difference in energy between the B and I peaks differs between the two compositions, indicating the acceptor impurity level moves closer to the valence band with increasing Sb content. (The difference is  $\sim 22$  meV for  $\text{InAs}_{0.96}\text{Sb}_{0.04}$  at low temperature, a composition comparable to those studied in this current research.) Yen also developed an expression for the compositional dependence of the peak luminescence wavelength of the  $\text{InAs}_{1-x}\text{Sb}_x$  samples at 10 K (Figure 3-9) (Yen, 1988a:489):

$$E_g(10 \text{ K}) = 0.4324 - 0.8831x + 0.6853x^2 \text{ eV} \quad (3.5)$$

Yen *et al.* also reported the longest PL wavelength (4.58  $\mu\text{m}$ ) at that time for  $\text{InAs}_{1-x}\text{Sb}_x$  grown by MBE, this time on (100) GaAs substrates (Yen, 1988c:952).

Beginning in 1988, the volume of  $\text{InAs}_{1-x}\text{Sb}_x$  research from places other than AT&T Bell Labs began to increase. Lone publications from a person or institute include: the growth and Hall measurement of  $\text{InAs}_{0.33}\text{Sb}_{0.67}$  grown on (100) GaAs by MBE at the University of Illinois (Chyi, 1988:1092); room temperature transmission of  $\text{InAs}_{1-x}\text{Sb}_x$  grown by MBE on (100) GaAs and GaAs-coated (100) Si substrates at the Interuniversity Micro-Electronics Center, Leuven, Belgium (Dobbelaere, 1989:1856); and the first metal organic molecular beam epitaxy (MOMBE) growth of InAsSb at Osaka University (Kaneko, 1991:638).

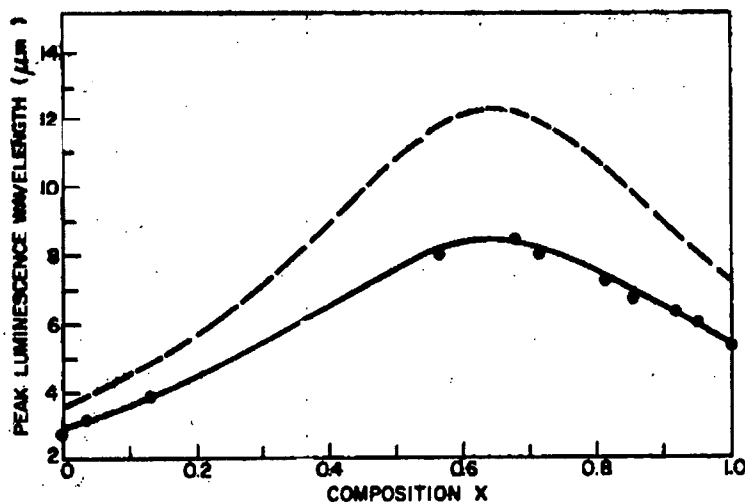


Figure 3-9. Compositional dependence of the 10 K peak PL wavelength for MBE-grown  $\text{InAs}_{1-x}\text{Sb}_x$  on InAs. Dashed curve shows room temperature energy gap of Fig. 5. (Yen, 1988a:489)

S.R. Kurtz of Sandia National Labs co-authored a number of  $\text{InAs}_{1-x}\text{Sb}_x$  papers between 1988 and the present. In 1988, PL and IR absorption measurements from an  $\text{InAs}_{0.13}\text{Sb}_{0.87}/\text{InSb}$  strained layer superlattice (SLS) grown by MOCVD on an InSb substrate were reported by Kurtz *et al.* The PL spectra proved conclusively that a Type II superlattice existed since the PL peak occurred at energies lower than the  $\text{InAs}_{0.13}\text{Sb}_{0.87}$  energy gap. IR absorption confirmed the position of these peaks (Kurtz, 1988:216). Dawson, also of Sandia, reported MBE growth and FTIR measurements of  $\text{InAsSb}/\text{InGaSb}$  SLS on (100) InSb substrates (Dawson, 1989:220).

Kurtz *et al.* first reported on the optical properties of ordered  $\text{InAs}_{0.60}\text{Sb}_{0.40}$ , MBE-grown on a strain-relief buffer of  $\text{Al}_{0.7}\text{In}_{0.3}\text{Sb}/\text{AlSb}$  strained-layer SL (SLS) on a (001)



GaSb substrate, in 1992. The ordering was attributed to a lower growth temperature (425 °C) than that previously reported by Yen for MBE-grown  $\text{InAs}_{1-x}\text{Sb}_x$  (480 °C). PL at 15 K and photoconductivity response at 77 K showed an energy gap reduction of 45 meV compared to Yen's previously reported values (Kurtz, 1992:1909).

Kurtz *et al.* again reported the energy gap at 77 K of unstrained  $\text{InAs}_{0.9}\text{Sb}_{0.1}$  grown by MOCVD on InAs at 475 °C to be 0.270 eV, well below the accepted value of 0.330 eV from the melt-grown data. They also reported the energy gaps of MBE- and MOCVD-grown  $\text{InAs}_{1-x}\text{Sb}_x$  alloys,  $0.05 \leq x \leq 0.50$ , (unreported growth temperatures) were consistently below the accepted values. TEM results indicated ordering may have been occurring in these samples, as well, to reduce these energy gaps (Kurtz, 1994:812).

G.B. Stringfellow of the University of Utah co-authored several papers on MOCVD-grown  $\text{InAs}_{1-x}\text{Sb}_x$  between 1988 and 1990. Cherng and Stringfellow investigated the optical phonon modes in  $\text{InAs}_{1-x}\text{Sb}_x$  grown on (100) InAs and (100) InSb substrates by Raman scattering in 1988. The optical modes shown in Figure 3-10 are InAs-LO ( $242 \text{ cm}^{-1}$  or 30 meV), InAs-TO ( $220 \text{ cm}^{-1}$  or 27 meV), InSb-LO ( $195 \text{ cm}^{-1}$  or 24 meV), InSb-TO ( $185 \text{ cm}^{-1}$  or 23 meV), and a broad band identified as DALA (disorder-activated longitudinal acoustic) (Cherng, 1988:886).

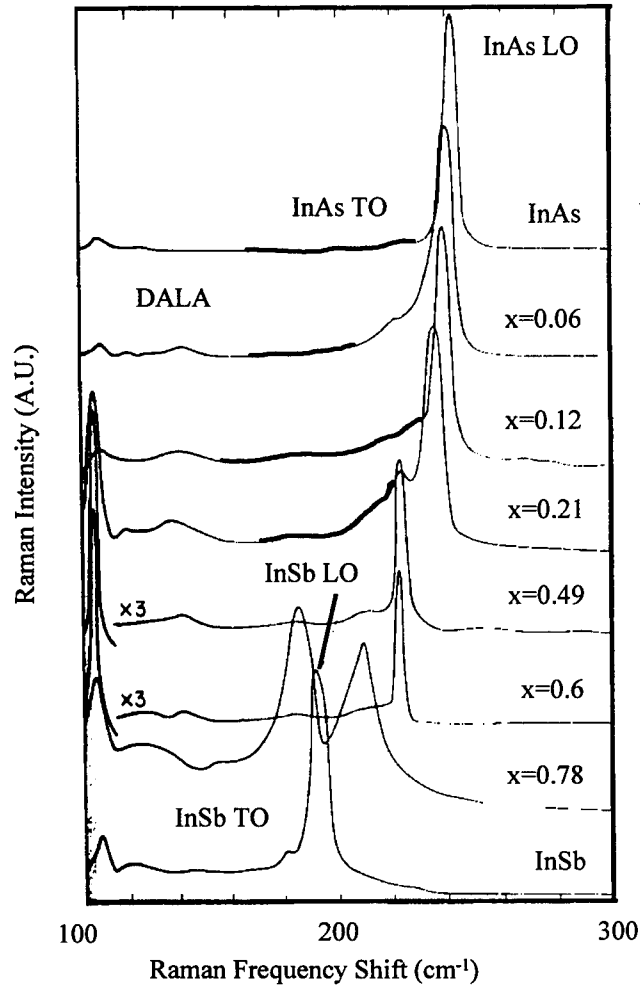


Figure 3-10. Raman scattering spectra for InAs<sub>1-x</sub>Sb<sub>x</sub> showing InAs- and InSb-like optical phonon modes (Cherng, 1988:886).

Fang and Stringfellow reported 10 K PL results for InAs<sub>1-x</sub>Sb<sub>x</sub> ( $x < 0.3$ ) grown on (100) InAs. As Yen had earlier, Fang developed an expression for the compositional dependence of the peak luminescence wavelength of the InAs<sub>1-x</sub>Sb<sub>x</sub> samples at 10 K (Figure 3-11) (Fang, 1990:7034):

$$E_g(10 \text{ K}) = 415(1 - x) - 672x(1-x) + 235x \text{ meV} \quad (3.6)$$

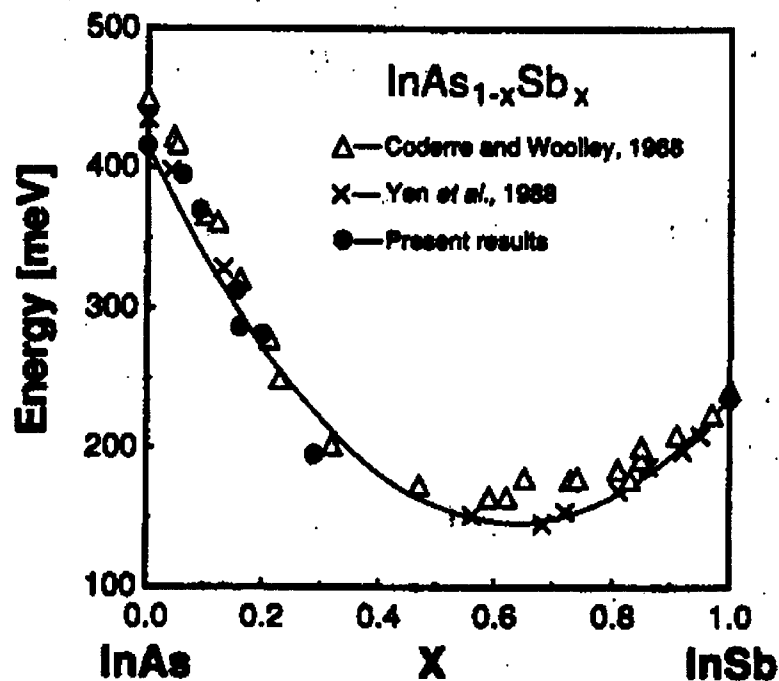


Figure 3-11. Compositional dependence of the 10 K peak PL energies for MOCVD-grown  $\text{InAs}_{1-x}\text{Sb}_x$  on InAs. Solid curve is least squares fit to PL data.  $\Delta$  data is also shown in Fig. 3 and  $\times$  data in Fig. 6. (Fang, 1990:7034)

A. Rogalski of the Institute of Technical Physics, Warsaw, Poland published two papers in 1989. The first calculated the room temperature electron effective mass using  $\mathbf{k}\cdot\mathbf{p}$  theory (Rogalski, 1989b:35). The results are shown in Figure 3-12. The second was a review of previous  $\text{InAs}_{1-x}\text{Sb}_x$  work as it applied to  $\text{InAs}_{1-x}\text{Sb}_x$  IR detectors (Rogalski, 1989a:191).

R.A. Stradling of London University co-authored two papers on MBE-grown  $\text{InAs}_{1-x}\text{Sb}_x$  GaAs substrates in 1991 and 1992. The first was on Hall measurements where the Hall mobility was shown to drop by as much as three orders of magnitude in the mid-range compositions. Since contamination of the MBE machine was believed to be very

unlikely, this drop was attributed to structural problems in the  $\text{InAs}_{1-x}\text{Sb}_x$  alloy, itself (Stradling, 1991:C52). Li and Stradling also studied the phonon energies of these  $\text{InAs}_{1-x}\text{Sb}_x$  alloys by Raman scattering. The range of the Raman spectra covered the zone-center transverse optical (TO) and longitudinal optical (LO) phonon frequencies for InAs and InSb. The LO peaks occurred throughout the composition range and their energies were shown to vary linearly with composition (Figure 3-13) (Li, 1992:567). (This data is used in Chapter VII in interpreting the current data.)

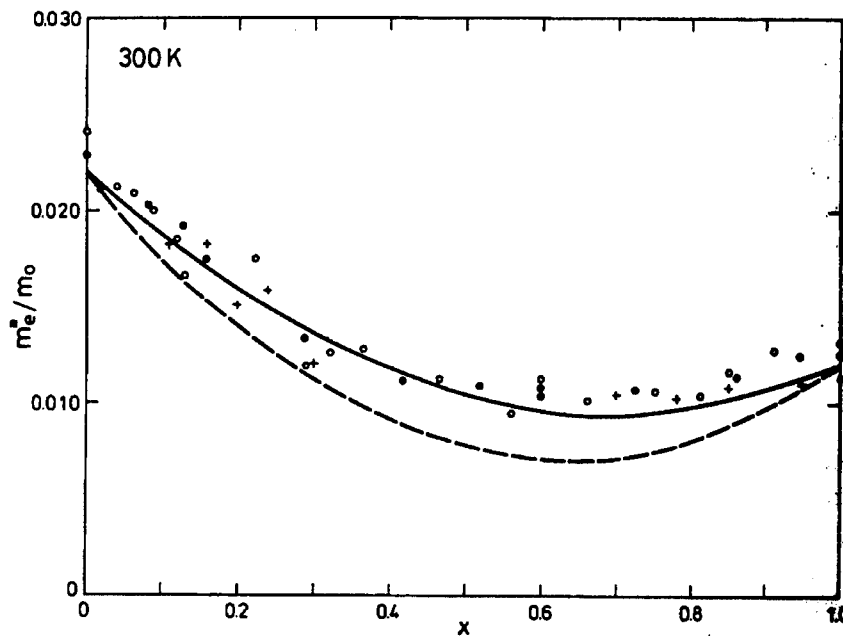


Figure 3-12. Room temperature electron effective mass in  $\text{InAs}_{1-x}\text{Sb}_x$  calculated by Rogalski. Symbols are data points taken from Woolley *et al.* (Aubin, 1968:1191; van Tongerlo, 1968:1199; Thomas, 1971:2052). The solid line is calculated assuming conduction-valence band mixing; the broken line uses the Kane model. (Rogalski, 1989b:35)

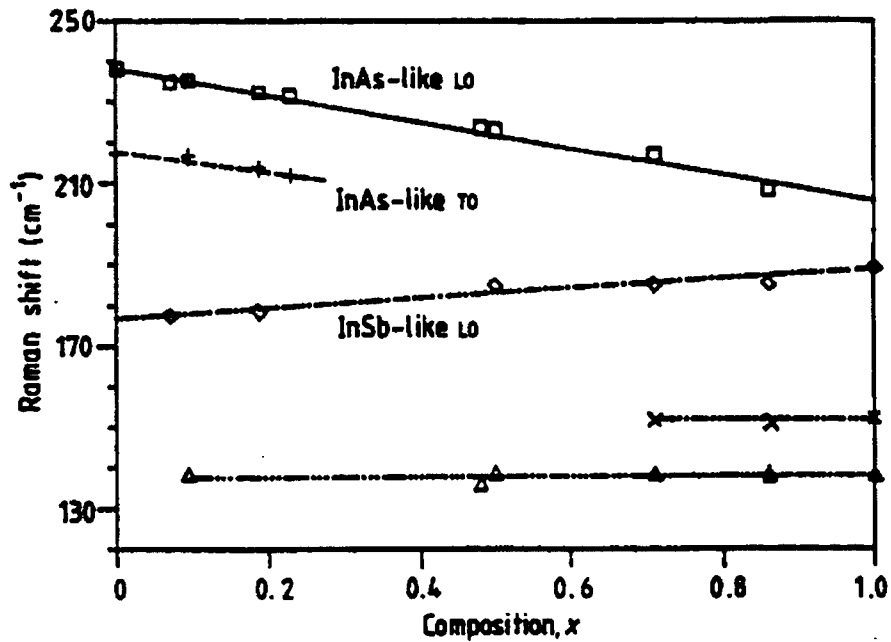


Figure 3-13. Linear compositional dependence of optical phonon peaks in MBE-grown  $\text{InAs}_{1-x}\text{Sb}_x$  on GaAs as measured by Raman scattering (Li, 1992:567).

The most current publications on the optical characterization of  $\text{InAs}_{1-x}\text{Sb}_x$  have been made by researchers at the University of Lancaster, UK. Elies *et al.* investigated PL emissions at temperatures greater than 77 K of  $\text{InAs}_{0.91}\text{Sb}_{0.09}$  lattice-matched to GaSb, grown by MBE. (This material is similar to that studied in the current research, and Elies' paper is the only published research on the type of material.) For the first time, the temperature dependence of the energy gap in the form of Varshni's equation (Varshni, 1967:149),

$$E_g(T) = E_g(0) - \frac{\alpha T^2}{T + \beta} \quad (3.7)$$

where  $E_g(0)$  is the band gap energy at 0 K,  $\alpha$  is a fitting parameter with units of eV/K and  $\beta$  is related to the Debye temperature (*i.e.*, the temperature at which vibrational modes of the crystal begin to be excited), which is the form used in this current research, was presented, but the energy values fit were from PL peaks which may differ from the actual  $E_g$  (see Chapter VI, The Temperature and Compositional Dependencies of the Energy Gap). Elies' value for  $E_g(0)$  was 0.349 eV. However, since the measurements were made only at temperatures above 77 K, the accuracy of this value is uncertain. The values for  $\alpha$  and  $\beta$  were  $3.064 \times 10^{-4}$  eV/K and 254 K, respectively. The temperature dependence of the PL intensity was also fit to an Arrhenius equation which resulted in an activation energy of 30 meV (Elies, 1993:159).

Mao and Krier reported PL measurements at temperatures above 77 K for LPE-grown  $\text{InAs}_{1-x}\text{Sb}_x$  on GaSb with  $x = 0.095, 0.102, 0.110, 0.117$  and  $0.124$ . The Varshni parameters they found ranged as:  $0.318 \leq E_g(0) \leq 0.331$  eV;  $0.198 \leq \alpha \leq 0.265$  meV/K; and  $100 \leq \beta \leq 269$  K. The activation energy they reported from the Arrhenius analysis on the  $x = 0.095$  sample was 57 meV (Mao, 1993:108).

### **InAsSb Semiconductor Lasers**

Although this current research is material oriented, the need for it is heavily driven by laser device development. Therefore, this section reviews published mid-IR semiconductor laser development in  $\text{InAs}_{1-x}\text{Sb}_x$ -related materials. Chapter II outlined the rationale in selecting the materials for these lasers. In general, the longer the lasing

wavelength that was desired, the more difficult an efficient device was to develop. The following chronology is by no means complete, but is organized to show how the lasing wavelength was progressively pushed to longer wavelengths through the  $\text{In}_y\text{Ga}_{1-y}\text{As}_{1-x}\text{Sb}_x$  compositions and finally to  $\sim 4 \mu\text{m}$  with the  $\text{InAs}_{1-x}\text{Sb}_x$  compositions.

**Homojunction Laser.** The first p-n homojunction lasers in the  $\text{InAs}_{1-x}\text{Sb}_x$  system were reported by Basov *et al.* in 1966.  $\text{InAs}_{0.98}\text{Sb}_{0.02}$  crystals were grown by the Czochralski method, diffused with Zn to form the p-n junction, and cleaved to form the Fabry-Perot cavity. The laser was operated at 77 K, produced a wavelength of  $3.19 \mu\text{m}$ , and had a best threshold current density,  $J_{\text{th}}$ , of  $800 \text{ A/cm}^2$  (Basov, 1966:847).

**Double Heterojunction Lasers.** The first  $\text{In}_{0.05}\text{Ga}_{0.95}\text{As}_{0.04}\text{Sb}_{0.96}/\text{Al}_{0.20}\text{Ga}_{0.80}\text{As}_{0.02}\text{Sb}_{0.98}$  double heterojunction (DH) injection lasers were reported by Kobayashi *et al.* in 1980. The structure was grown by LPE, emitted light at  $1.8 \mu\text{m}$  when operated at room temperature, and had a threshold of  $5 \text{ kA/cm}^2$  (Kobayashi, 1980:L30).

In 1985, the lasing wavelength was increased, first to  $2.2 \mu\text{m}$  by Caneau *et al.* ( $\text{In}_{0.14}\text{Ga}_{0.86}\text{As}_{0.12}\text{Sb}_{0.88}/\text{Al}_{0.27}\text{Ga}_{0.73}\text{As}_{0.04}\text{Sb}_{0.96}$  by LPE,  $J_{\text{th}} = 6.9 \text{ kA/cm}^2$ ) (Caneau, 1985:815), then to  $2.29 \mu\text{m}$  by Bochkarev *et al.* ( $\text{In}_{0.19}\text{Ga}_{0.81}\text{As}_{0.17}\text{Sb}_{0.83}/\text{Al}_{0.15}\text{Ga}_{0.85}\text{As}_{0.02}\text{Sb}_{0.98}$  by LPE,  $J_{\text{th}} = 20 \text{ kA/cm}^2$ ) (Bochkarev, 1985:869). In 1988, Akimova and Bochkarev increased the lasing wavelength to  $2.4 \mu\text{m}$  ( $\text{InGaAsSb}/\text{AlGaAsSb}$  by LPE,  $J_{\text{th}} = 7.5 \text{ kA/cm}^2$ ) (Akimova, 1988:429) and Mani *et al.* to  $3.2 \mu\text{m}$

(InAs<sub>0.95</sub>Sb<sub>0.05</sub>/InAs<sub>0.50</sub>Sb<sub>0.19</sub>P<sub>0.31</sub> by LPE, 78 K operation,  $J_{th} = 4.5 \text{ kA/cm}^2$ ) (Mani, 1988:1542).

DH diode lasers emitting at 4  $\mu\text{m}$  were reported by Eglash and Choi of the Lincoln Laboratory, Massachusetts Institute of Technology (MIT/LL) in 1994. The InAs<sub>0.91</sub>Sb<sub>0.09</sub>/AlAs<sub>0.08</sub>Sb<sub>0.92</sub> structure was grown by MBE, and operated in continuous wave (CW) mode up to 80 K and pulsed to 155 K with threshold current densities as low as 33 A/cm<sup>2</sup> (Eglash, 1994:833). Later in 1994, the performance of this structure was improved by Choi *et al.* to operating temperatures of 105 K CW and 170 K pulsed (Choi, 1994:2251).

**Quantum Well Lasers.** Multiple quantum well devices with ten 15 nm InAs<sub>0.86</sub>Sb<sub>0.14</sub> wells, 30 nm In<sub>0.85</sub>Al<sub>0.15</sub>As<sub>0.86</sub>Sb<sub>0.14</sub> barriers and AlAs<sub>0.08</sub>Sb<sub>0.92</sub> cladding layers were reported by G.W. Turner *et al.* of MIT/LL in 1995. (Dr Turner is also responsible for the MBE growth of the samples studied in this current research.) These devices were grown by MBE with emission wavelengths of 3.9  $\mu\text{m}$ ; operating temperatures were improved to 123 K for CW operation (Turner, 1995:699).

**Optically-Pumped Lasers.** Optically-pumped lasing of DH InAsSb and GaInAsSb active regions with AlGaSb or AlGaAsSb cladding layers was reported by Le *et al.*, also of MIT/LL, in 1994. Emission wavelengths were 4  $\mu\text{m}$  and 3  $\mu\text{m}$ , operating temperatures reached 150 K and 210 K, and peak output powers reached 1.5 W and 0.8 W per facet for the ternary and quaternary, respectively (Le, 1994:152). Optical pumping



of  $\text{InAs}_{0.9}\text{Sb}_{0.1}/\text{In}_{0.9}\text{Ga}_{0.1}\text{As}$  strained layer superlattice lasers emitting at  $3.9 \mu\text{m}$  at a temperature of 100 K was also reported by Kurtz *et al.* of Sandia in 1994 (Kurtz, 1994:812).

## Summary

Development of a III-V semiconductor laser based on the GaSb substrate has historically moved toward lasing wavelengths deeper in the IR. The result of this is that optoelectronic device interests now focus on the  $\text{InAs}_{1-x}\text{Sb}_x$  materials which have energy gaps corresponding to wavelengths of  $\sim 4 \mu\text{m}$ . High quality device structures demand the use of modern epitaxial growth techniques, but only recently has  $\text{InAs}_{1-x}\text{Sb}_x$  been grown by such techniques (1985 for MOCVD and 1986 for MBE). Therefore, since relatively little  $\text{InAs}_{1-x}\text{Sb}_x$  material characterization has been published overall, an even smaller amount has been reported for epitaxially grown material.

These limited publications have left deficiencies in the  $\text{InAs}_{1-x}\text{Sb}_x$  data available to device developers. Basic intrinsic parameters such as the temperature and compositional dependencies of the energy gap for epitaxially grown material have not been accurately determined, and extrinsic parameters such as defect and impurity energy levels for  $\text{InAs}_{1-x}\text{Sb}_x$  are still not readily available. Also, assessments of  $\text{InAs}_{1-x}\text{Sb}_x$  material and its impact on device performance have not been completed, but would be beneficial to device developers. These issues have been addressed in this current research, and the results are reported in succeeding chapters.

#### IV. Samples

Chapters I and II established the motive for selecting the  $\text{InAs}_{1-x}\text{Sb}_x$  semiconductor system for use as the active region in a mid-infrared (IR) semiconductor laser. Immiscibility regions for these compositions were established by Stringfellow for equilibrium growth techniques such as liquid phase epitaxy (Stringfellow, 1969:1779). In these regions, the ternary or quaternary alloys of interest are immiscible, *i.e.*, two phase, polycrystalline growth occurs, rather than single crystal growth, and are useless as a laser material. Therefore, nonequilibrium growth, such as metal-organic chemical vapor deposition (MOCVD) or molecular beam epitaxy (MBE) is required.

MOCVD is not without its problems, however. Carbon incorporation is severe when trimethyl aluminum (Al) is used as the MOCVD source material for the growth of the Al alloys necessary for the cladding layers (Kuech, 1987:632). Therefore, MBE is the growth technique of choice for growing these laser structures. Since the goal of this research was to assist in the improvement of mid-IR semiconductor lasers, all the samples studied were grown by MBE by Dr George Turner of the Lincoln Laboratory, Massachusetts Institute of Technology, Lexington, MA (Turner, 1994:1266; Turner, 1995:699).

## Molecular Beam Epitaxial Growth

MBE is an epitaxial growth process involving the reaction of one or more thermal beams of atoms or molecules with a crystal surface under ultra-high vacuum conditions. A schematic of an example MBE growth system for AlGaAs growth is shown in Figure 4-1.

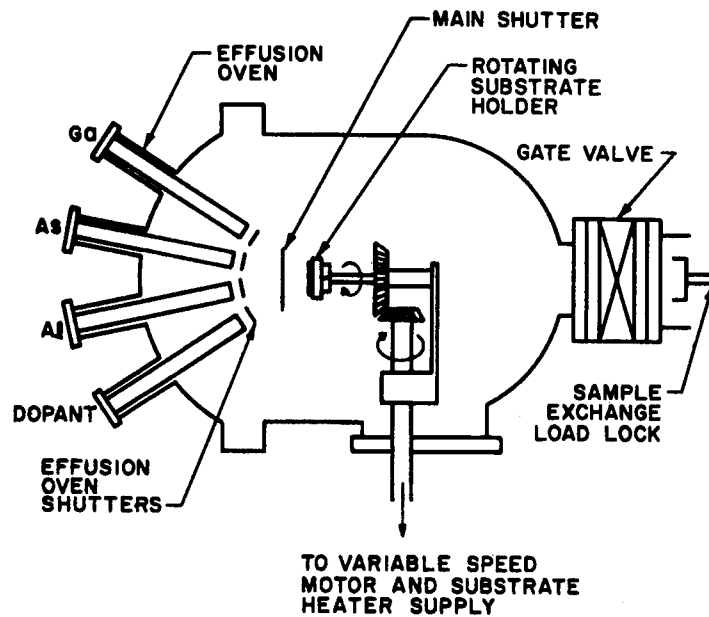


Figure 4-1. Schematic of an MBE system (Sze, 1985:337).

Separate effusion ovens are used for the elemental sources and housed in an ultra-high vacuum chamber ( $\sim 10^{-10}$  Torr). The rate of evaporation of each source is controlled

by the temperature of each oven and is given by the Hertz-Knudsen equation (Herman, 1989:31),

$$\frac{dN_e}{A_e dt} = a_v (p_{eq} - p) \left( \frac{N_A}{2\pi M k_B T} \right)^{1/2} m^{-2} s^{-1}, \quad (4.1)$$

where  $dN_e$  molecules evaporate from a surface of area  $A_e$  in time  $dt$ ,  $a_v$  is the evaporation coefficient,  $p_{eq}$  is the equilibrium pressure,  $p$  is the hydrostatic pressure of the evaporant in the gas phase,  $M$  is the molecular weight of the evaporating species,  $T$  is the temperature, and  $k_B$  and  $N_A$  are the Boltzmann and Avogadro constants, respectively. Often, growth must be interrupted between different epilayers while the effusion oven temperatures are reset. The beam of evaporated atoms or molecules heading for the substrate is started and stopped by the effusion oven shutters shown in Figure 4-1.

The number of atoms or molecules impinging on the surface per unit area and unit time at point, P, as shown in Figure 4-2 is given by (Herman, 1989:7):

$$N_P = I_A \left( \frac{r}{r_P} \right)^2 \cos \vartheta \cos (\vartheta + \Phi) \cos \delta, \quad (4.2)$$

where  $I_A$  is the beam flux at substrate center, A (Herman, 1989:34), such that:

$$I_A = \frac{dN_e / dt}{\pi r^2}, \quad (4.3)$$

and distances,  $r$  and  $r_P$ , and angles,  $\vartheta$ ,  $\Phi$  and  $\delta$ , are shown in Figure 4-2. Since these distances and angles are unique for each point on the substrate surface and for each

effusion cell, the substrate is rotated as shown in Figure 4-1 to achieve more uniform growth.

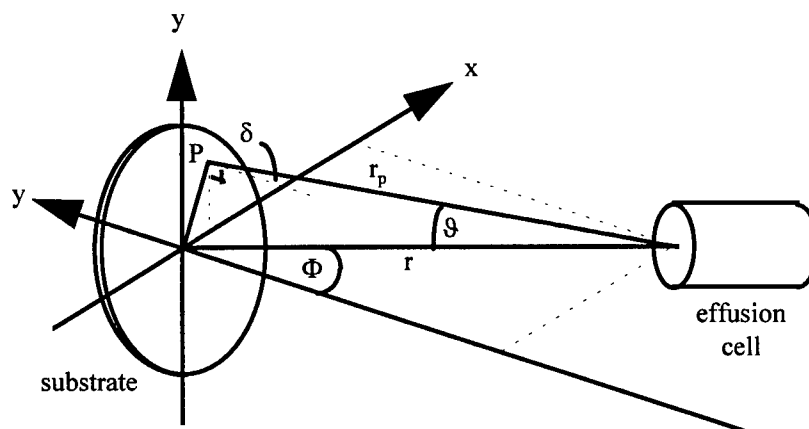


Figure 4-2. Schematic illustration of the effusion cell-substrate system showing polar coordinates to substrate surface point, P (Herman, 1989:7).

The surface processes important in MBE growth are (Figure 4-3) (Herman, 1989:9): (1) adsorption of the constituent atoms or molecules impinging on the surface; (2) surface migration and dissociation of adsorbed molecules; (3) incorporation of the constituent atoms into the substrate or epilayer crystal lattice; and (4) thermal desorption of the atoms not incorporated. (For much more detail on these processes, see Herman and Sitter.) Each of these processes is affected by the substrate temperature so control of the substrate temperature by the substrate heater as shown in Figure 4-1 is required.

An *in-situ* measurement of the surface growth is provided by reflection high-energy electron diffraction (RHEED). Figure 4-4 shows a schematic representation of

how the RHEED intensity can grow and decay depending on the stage of completeness of a particular epitaxial monolayer. Monolayer control of MBE growth is possible.

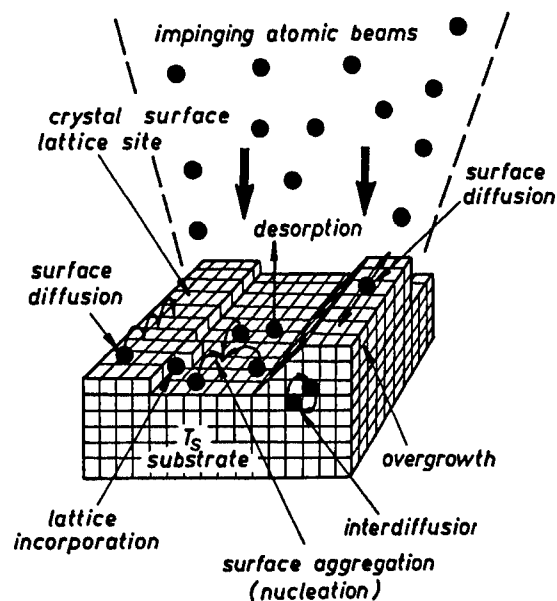


Figure 4-3. Schematic illustration of the important surface processes in MBE growth (Herman, 1989:9).

The particular MBE system used for growth of the samples studied here was an EPI Gen II 3-in. MBE system. Effusion cells to provide fluxes of Al, Ga and In atoms, and uncracked  $Sb_4$  (*i.e.*,  $Sb_4$  molecules impinge upon the surface rather than being thermally split into  $Sb_2$  molecules at the source) were used along with an EPI valved As source to provide uncracked  $As_4$  fluxes. To achieve the necessary III-V ratio for each alloy, two  $Sb_4$  effusion cells were used (Turner, 1994:1266).

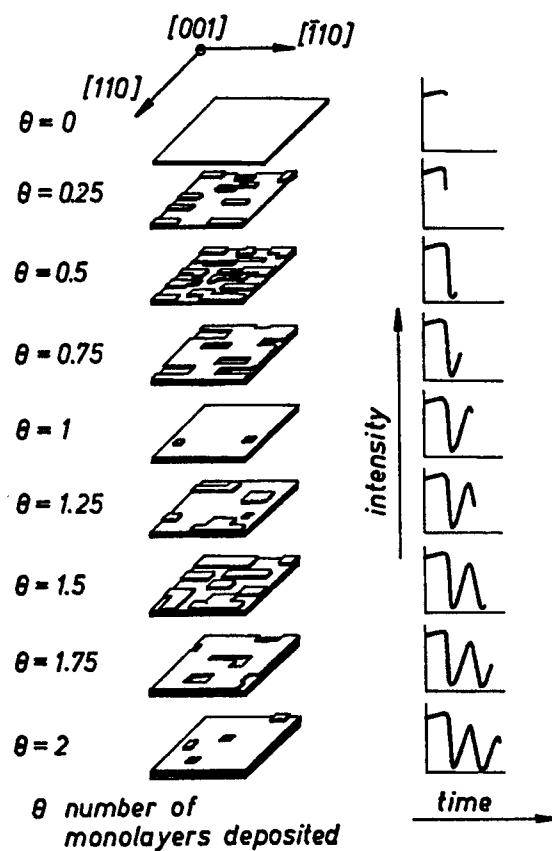


Figure 4-4. Schematic illustration of the RHEED intensity oscillations as a tool for characterizing MBE growth (Herman, 1989:21).

The Te-doped n-type and undoped p-type (100) GaSb substrates were obtained from Sumitomo. They were prepared by solvent cleaning and chemical etching with a  $\text{Br}_2$ -based etch and mounted with In on Mo substrate holders. Outgassing and surface oxide desorption of the substrate was accomplished under ultrahigh vacuum conditions in an  $\text{Sb}_4$  flux (Turner, 1994:1266).

**Ordering.** Certain phenomena can occur when a semiconductor crystal is grown in successive monolayers as in the MBE growth process. The successive monolayers for a III-V composition grown in the [001] direction (see zincblende unit cell, Figure 2-3) are alternating planes of group III and group V atoms as shown in Figure 4-5. For a ternary alloy such as  $\text{InAs}_{1-x}\text{Sb}_x$ , either of the group V cations may occupy any of the group V lattice sites. However, many III-V ternaries demonstrate a particular order as to which cations occupy which sites. When this occurs, a monolayer superlattice (SL) is formed in the  $\langle 111 \rangle$  directions, especially for cation compositions near 50%, which is known as "Cu-Pt ordering."

Although in the zincblende structure there are four equivalent  $\{111\}$  planes, this SL formation is not invariant among them. SLs along  $(11\bar{1})$  and  $(\bar{1}\bar{1}\bar{1})$  are never formed, and those in either  $(\bar{1}11)$  or  $(1\bar{1}1)$  are dominant dependent on substrate growth orientation. This indicates SL formation is not governed by bulk thermodynamics (Suzuki, 1988:396) and that the symmetry between the four is broken by a boundary effect; the substrate surface has been postulated as this boundary (Gomyo, 1988:2645).

Cu-Pt ordering in  $\text{InAs}_{1-x}\text{Sb}_x$  was first observed by Jen and Stringfellow of the University of Utah in 1989 in  $\text{InAs}_{1-x}\text{Sb}_x$  grown by metal-organic chemical vapor deposition (MOCVD) on (001) InAs and (001) InSb substrates, with  $0.22 \leq x \leq 0.88$ . The degree of ordering has been shown to be maximized by certain epitaxial growth temperatures. The substrate growth temperatures used here were either 450 or 480 °C for



the ordered samples, and one  $\text{InAs}_{0.94}\text{Sb}_{0.06}$  sample grown at 375 °C showed no ordering (Jen, 1989:1154).

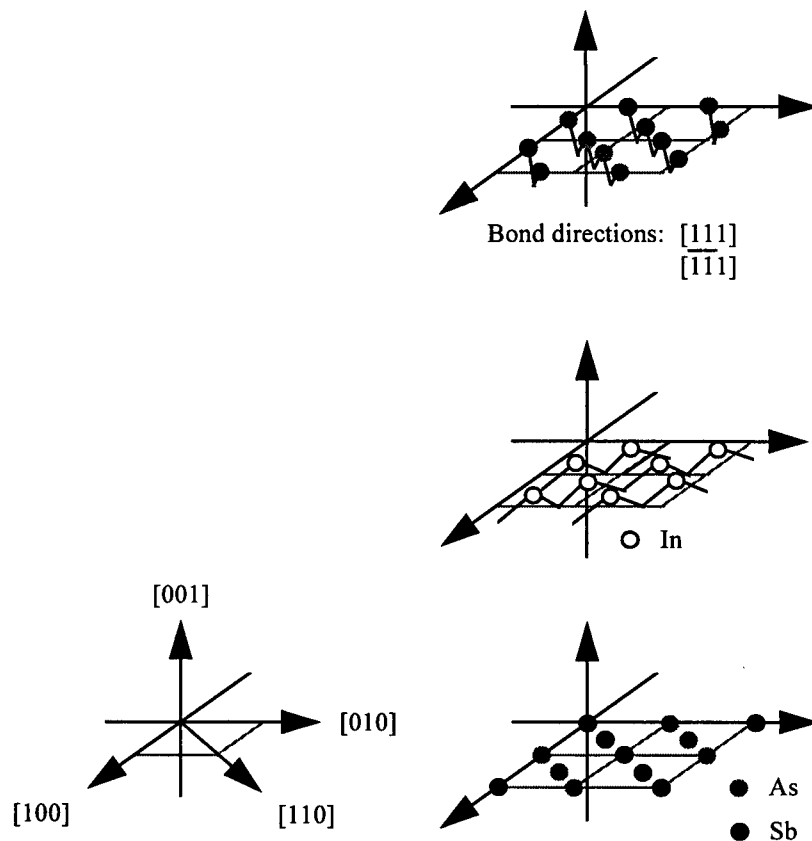


Figure 4-5. Successive III-V (001) growth planes in III-V ternary.

S.R. Kurtz *et al.* of Sandia National Laboratories first reported on the optical properties of MBE-grown ordered  $\text{InAs}_{0.60}\text{Sb}_{0.40}$  on a (001) GaSb substrate in 1992. The ordering was attributed to a lower growth temperature (425 °C) than usually reported (480 °C), and PL at 15 K and photoconductivity response at 77 K showed an energy gap

reduction of 45 meV compared to the previously reported values (Kurtz, 1992:1909). Kurtz *et al.* again reported the energy gap at 77 K of unstrained  $\text{InAs}_{0.9}\text{Sb}_{0.1}$  grown by MOCVD on InAs at 475 °C to be ~60 meV below the accepted values from melt-grown samples, and the energy gaps of MBE- and MOCVD-grown  $\text{InAs}_{1-x}\text{Sb}_x$  alloys,  $0.05 \leq x \leq 0.50$  (unreported growth temperatures) also to be consistently below the accepted values. Transmission electron microscope results indicated ordering may have been occurring to reduce these energy gaps (Kurtz, 1994:812).

The theory for energy gap reduction due to ordering in III-V alloys is given by Wei and Zunger of the Solar Research Institute, Golden, CO. Cu-Pt ordering effectively doubles the size of the unit cell, and accordingly shrinks the first Brillouin zone. The L-point of the zincblende Brillouin zone (see Figure 2-6) is essentially folded back to zone center where the conduction band  $\Gamma$ - and folded L-states are mutually repelled, as are the valence band states, which leads to a reduction of the direct energy gap (Wei, 1991:2684).

**Phase Separation.** Phase separation is another phenomenon which is observed in semiconductors grown by a successive monolayer growth process. It is the decomposition of a ternary or quaternary semiconductor alloy into a mixture of two phases, and has been attributed to the presence of an immiscibility gap in the alloy at low growth temperatures.

An immiscibility gap is the range of semiconductor alloy compositions over which crystal growth below a certain temperature results in the decomposition of the material into two polycrystalline phases. Although it is normally associated with an

equilibrium growth process such as liquid phase epitaxy, it can occur in non-equilibrium growth processes such as MOCVD or MBE, as well. Alloy systems with a large difference in lattice constant between the constituent binaries have a large positive enthalpy of mixing. Below the critical growth temperature, this large enthalpy overcomes the negative entropy of mixing and the material can no longer be grown as a single crystal (Stringfellow, 1989:108).

The observation of phase separation in MBE-grown  $\text{InAs}_{0.5}\text{Sb}_{0.5}$  on (001) Si-GaAs was reported by I.T. Ferguson *et al.* of the Imperial College, London, UK in 1991. A "natural" strained-layer superlattice of  $\text{InAs}_{0.69}\text{Sb}_{0.31}$  and  $\text{InAs}_{0.33}\text{Sb}_{0.67}$  platelets with periodicity of 1000-2000 Å occurred at growth temperatures,  $295 \leq T_g \leq 430$  °C (Figure 4-6). For  $430 \leq T_g \leq 480$  °C, the material was homogeneous with {111} ordering as described above. Two results indicated the platelet structure is generated at or near the growth surface, most likely by a surface diffusion process: (1) as the growth temperature was increased from 340 to 400 °C, platelet morphology extended in size laterally in both <110> directions; and (2) homogeneous material grown at 430 °C, but subsequently annealed at 370 °C, showed no phase separation (Seong, 1991:485; Ferguson, 1991a:3324; Ferguson, 1991b:395).

An apparent reduction in the energy gap measured by optical characterization of phase separated materials is possible when the observed absorption or recombination occurs in the region of lower energy gap, *e.g.*, in a region of higher Sb content in

InAs<sub>1-x</sub>Sb<sub>x</sub> material. If these results are then attributed to the nominal composition of the material, an apparent shift to lower energies occurs.

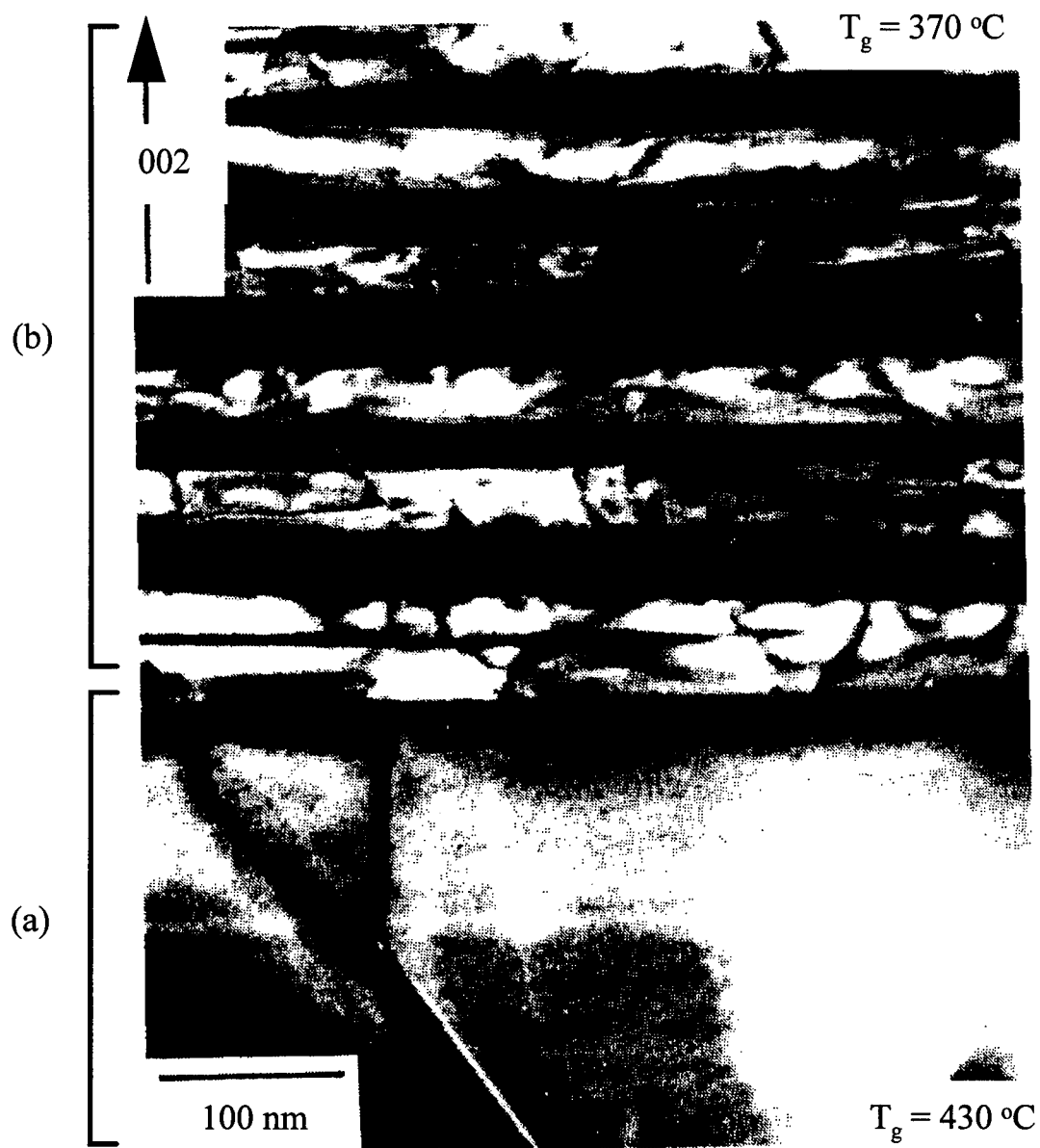


Figure 4-6. TEM [110] cross-section micrograph of MBE-grown InAs<sub>1-x</sub>Sb<sub>x</sub> at two growth temperatures: (a)  $T_g = 430\text{ }^\circ\text{C}$ , homogeneous InAs<sub>0.5</sub>Sb<sub>0.5</sub> material; (b)  $T_g = 370\text{ }^\circ\text{C}$ , natural SLS of  $\sim 285\text{ \AA}$  InAs<sub>0.33</sub>Sb<sub>0.67</sub> and  $\sim 285\text{ \AA}$  InAs<sub>0.69</sub>Sb<sub>0.31</sub>. (Ferguson, 1991a:3324)

## Double Crystal X-Ray Diffraction

The lattice mismatch between the sample epilayer and the substrate was determined by double crystal x-ray diffraction (DCXRD). The DCXRD characterizations were performed at Lincoln Laboratory and at the Solid State Electronics Directorate, Wright Laboratory, Wright-Patterson AFB, OH. The diffraction angle,  $\theta_B$ , between an incident beam of electromagnetic radiation of wavelength,  $\lambda$ , and a set of atomic planes separated by distance,  $a$ , which results in the constructive interference of the beams reflected from each plane as illustrated in Figure 4-7 is given by Bragg's law,

$$m\lambda = 2a \sin \theta_B, \quad (4.4)$$

where  $m$  is the order.

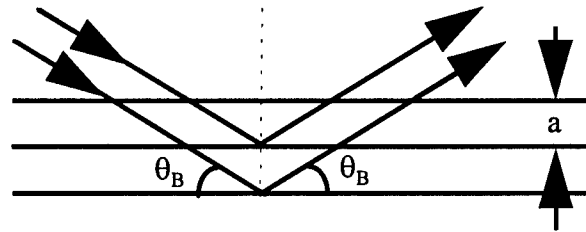


Figure 4-7. Bragg reflection from a set of atomic planes separated by distance,  $a$ , occurring at the Bragg angle,  $\theta_B$ .

In a practical diffraction experiment, the Bragg's law assumption of a parallel, monochromatic incident beam may not be accurate; the usual beam produced by an x-ray tube contains only a small fraction of intensity which is closely monochromatic and parallel to within a few seconds of arc. The double crystal spectrometer approaches this assumption, however, by placing a perfect crystal in a reflecting position (A in Figure 4-8) and using the reflected beam as the incident beam for the test sample (B in Figure 4-8) (Warren, 1969:327).

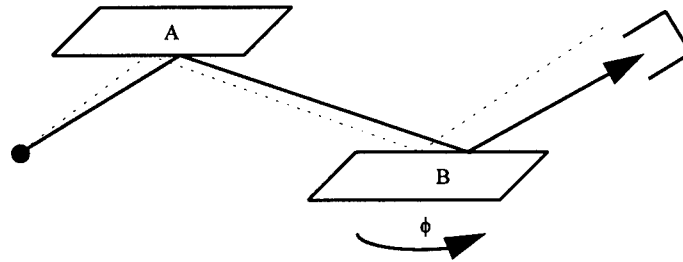


Figure 4-8. Schematic illustration of a double crystal spectrometer. When the two crystals are parallel, the reflected wavelength from crystal A is incident to crystal B at the correct angle for reflection. (Warren, 1969:328)

Rearranging Bragg's law to be equal to  $a$ , then differentiating with respect to  $\theta$  results in:

$$\frac{\Delta a}{a} = - \cot \theta_B \Delta \theta. \quad (4.5)$$

When multiple diffraction peaks are seen in the DCXRD experiment, it is because diffraction has occurred at both the substrate atomic planes and the epilayer atomic planes

which have a lattice constant different than that of the substrate. The unknown lattice constant of the epilayer can be obtained from Eq (4.5) where  $\theta_B$  is the Bragg angle for the substrate and  $\Delta\theta$  is the angular separation of the DCXRD peaks.

The lattice constant for GaSb, the substrate material used here, is:

$$a_{0-\text{GaSb}} = 6.09593 \text{ \AA} \quad (4.6)$$

at 298.15 °C (Madelung, 1991:116). For (400) GaSb reflections of 1.540 Å Cu-K $_{\alpha 1}$  radiation, the Bragg angle in Eq (4.4) is:

$$\begin{aligned} \theta_B &= \sin^{-1} \frac{0.1540}{2 \times 0.609593 / 4} \\ &= 30.36^\circ \end{aligned} \quad (4.7)$$

The lattice constants of InAs and InSb were given in Chapter II as:

$$a_{0-\text{InAs}} = 6.0583 \text{ \AA} \quad (2.4a)$$

$$a_{0-\text{InSb}} = 6.47937 \text{ \AA}. \quad (2.4b)$$

Vegard's law, given generically by Eq (2.5), becomes:

$$a_{\text{InAsSb}} = a_{\text{InAs}}(1 - x) + a_{\text{InSb}}x \quad (4.8)$$

and the left side of Eq (4.5) becomes:

$$\begin{aligned} \frac{\Delta a}{a} &= \frac{a_{\text{InAsSb}} - a_{\text{GaSb}}}{a_{\text{GaSb}}} \\ &= \frac{a_{\text{InAs}}(1 - x) + a_{\text{InSb}}x}{a_{\text{GaSb}}} - 1 \end{aligned} \quad (4.9)$$

Using Eq (2.4) and solving Eq (4.9) to find the Sb composition, x, from the DCXRD data results in:

$$x = 0.089291 + 14.465 \Delta a/a. \quad (4.10)$$

### Undoped Samples

Thirteen MBE-grown, nominally undoped  $\text{InAs}_{1-x}\text{Sb}_x$  samples were investigated as listed in Table 4-1. The code listed in the "Sample" column of Table 4-1 was given to that MBE-growth run by Lincoln Lab personnel. The substrate temperatures during growth for these samples mainly ranged from 467-489 °C with one exception, 94-035, at 430 °C. All but one of the samples were grown on Te-doped (100) n-GaSb substrates; the remaining sample, 93-030, was grown undoped on an undoped (100) p-GaSb substrate.

The samples' structures differed slightly, reflecting the nature of these samples as test growths for eventual diode laser structure growth. Nine of the 13 samples'  $\text{InAs}_{1-x}\text{Sb}_x$  epilayers were grown directly on top of a nominally undoped p-GaSb buffer layer. Three of the remaining four included a nominally undoped lattice-matched p-



AlAs<sub>0.08</sub>Sb<sub>0.92</sub> layer between the GaSb buffer and InAs<sub>1-x</sub>Sb<sub>x</sub> epilayer which represents the cladding layer in the laser structure. The remaining sample, 93-120, also included another lattice-matched nominally undoped 1.02 μm p-AlAs<sub>0.08</sub>Sb<sub>0.92</sub> layer with a 100 Å GaSb cap on top of the InAs<sub>1-x</sub>Sb<sub>x</sub> layer representing the top cladding layer in the laser structure. Using the band offsets of Figure 2-13, energy level diagrams of the samples' structures are shown in Figure 4-9.

Table 4-1. MBE-growth characteristics of the InAs<sub>1-x</sub>Sb<sub>x</sub> samples studied. (\*InAs sample. \*\*Thickness of top cladding layer included in this sample.)

Sample	T <sub>growth</sub> (°C)	Substrate	GaSb buffer (μm)	AlAsSb clad (μm)	InAsSb epilayer (μm)
95-007*	472	n-GaSb	2.20	n/a	1.40
93-044	489	n-GaSb	1.10	n/a	0.82
93-114	485	n-GaSb	0.73	0.88	0.75
93-030	482	p-GaSb	0.96	n/a	0.65
93-113	486	n-GaSb	1.23	1.48	0.68
93-112	479	n-GaSb	1.30	0.87	1.02
93-048	479	n-GaSb	0.73	n/a	0.77
93-045	480	n-GaSb	0.82	n/a	0.78
93-068	477	n-GaSb	0.80	n/a	1.06
93-092	480	n-GaSb	0.36	n/a	1.38
93-120	475	n-GaSb	-	0.56/1.02**	0.40
94-035	430	n-GaSb	0.71	n/a	0.49
93-151	467	n-GaSb	0.53	n/a	0.78

[004] DCXRD. To determine the room temperature lattice mismatch, Δa/a, between the epitaxial InAs<sub>1-x</sub>Sb<sub>x</sub> layer and the GaSb substrate, DCXRD measurements were made by Lincoln Lab personnel for diffraction from the (004) planes. Results are

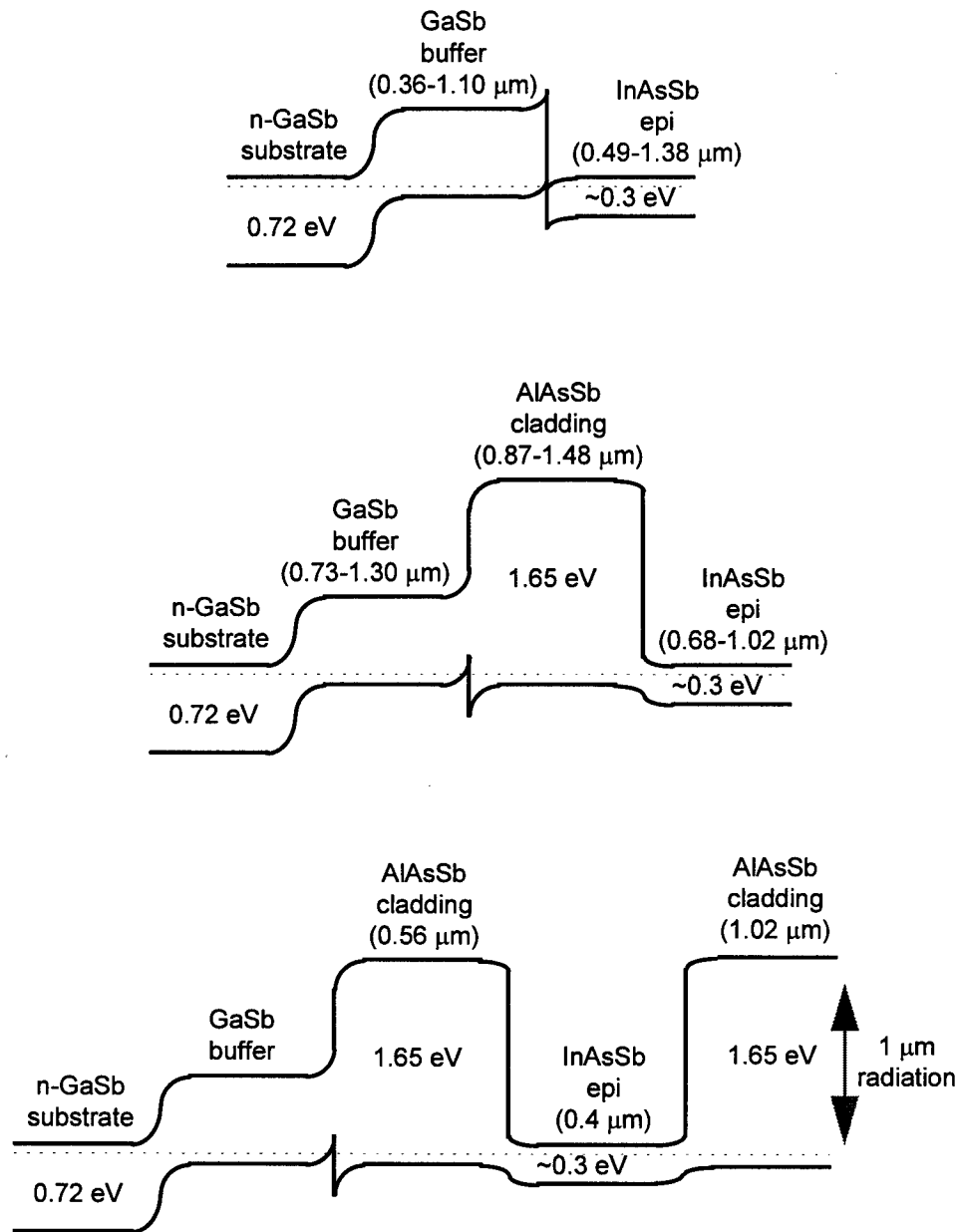


Figure 4-9. Energy level diagrams of the epilayer structure for the  $\text{InAs}_{1-x}\text{Sb}_x$  samples studied.

shown in Figures 4-10 and 4-11. Each spectrum shows at least two peaks as a function of angle. The angles have been normalized to show the GaSb substrate peak at 0 sec. In this manner, the angle then shows the  $\Delta\theta$  value as derived in Eq (4.5). The additional peaks in the spectra with more than two peaks are due to the  $\text{AlAs}_{1-x}\text{Sb}_x$  cladding epilayers which are also slightly lattice-mismatched to the GaSb substrate.

The peak position and full width at half maximum (FWHM) linewidth of each  $\text{InAs}_{1-x}\text{Sb}_x$  epilayer peak shown in Figures 4-10 and 4-11 are listed in Tables 4-2. The lattice mismatch of the  $\text{InAs}_{1-x}\text{Sb}_x$  epilayer with the GaSb substrate,  $\Delta a/a$ , was determined using Eq (4.5). These results ranged from -0.617 % for the InAs epilayer sample, 95-007, to +0.708 % for sample 93-151, and are listed in Table 4-2.

The Sb composition,  $x$ , of each sample was calculated assuming full strain relaxation of the  $\text{InAs}_{1-x}\text{Sb}_x$  epilayer and Eq (4.10). The resulting compositions ranged  $0 \leq x \leq 0.192$  as listed in Table 4-2. To determine whether full relaxation is a good assumption for these cases, a comparison of the epilayer thickness to the critical pseudomorphic thickness was made.

When an epitaxial layer is grown upon a substrate with a different lattice constant, the atomic lattice of that epilayer is strained to match that of the substrate. The critical thickness,  $t_c$ , of the lattice-mismatched epilayer is an epitaxial growth thickness above which misfit dislocations are introduced into the crystal lattice which allow this strain to be relieved, and allow a relaxation of the epitaxial crystal back to its natural lattice

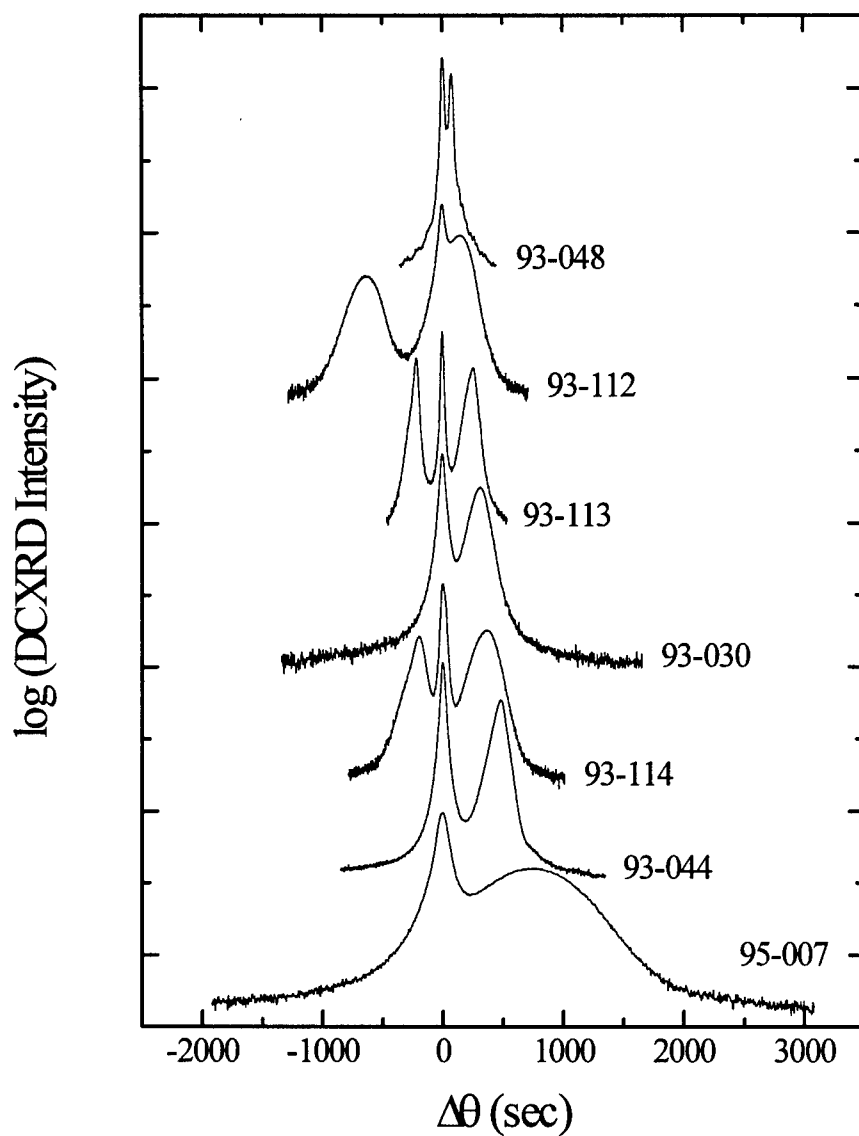


Figure 4-10. DCXRD data taken on seven of the 13 undoped  $\text{InAs}_{1-x}\text{Sb}_x$  samples listed in Table V-1. GaSb substrate peaks are at 0 sec; epilayer peaks are at  $\Delta\theta \neq 0$ .

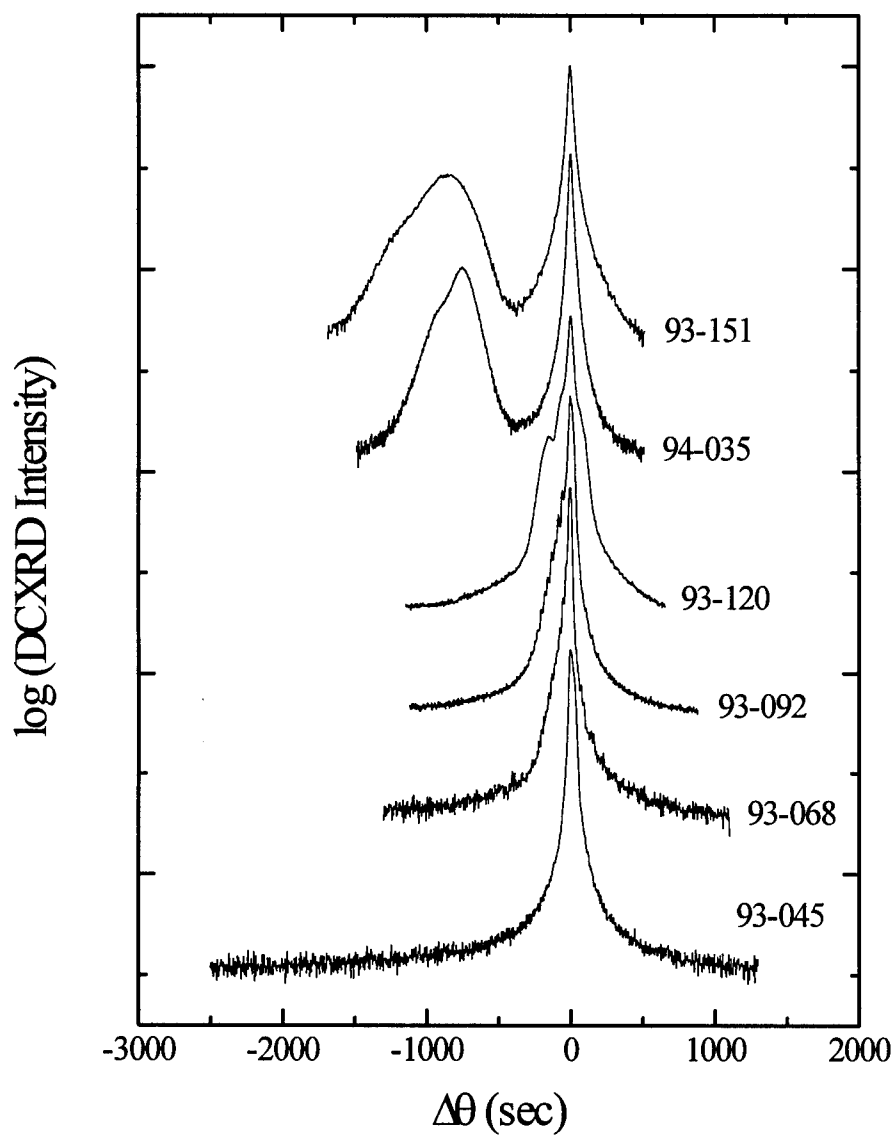


Figure 4-11. DCXRD data taken on six of the 13 undoped  $\text{InAs}_{1-x}\text{Sb}_x$  samples listed in Table V-1. GaSb substrate peaks are at 0 sec; epilayer peaks are at  $\Delta\theta \neq 0$ .

Table 4-2. DCXRD peak position,  $\Delta\theta$ , for each  $\text{InAs}_{1-x}\text{Sb}_x/\text{GaSb}$  sample with calculated lattice-mismatch,  $\Delta a/a$ , and corresponding Sb composition,  $x$ . Misfit,  $f_0$ , and critical thickness,  $t_c$ , were calculated using Eq (4.12) and Figure 4-10.

Sample	$\Delta\theta$ (sec)	FWHM (sec)	$\Delta a/a$ (%)	$x$	$f_0$ ( $\times 10^{-3}$ )	$t_c$ ( $\mu\text{m}$ )	$d$ ( $\mu\text{m}$ )	$d/t_c$
95-007	760	795	-0.629	0	6.2	0.040	1.40	40
93-044	484	95	-0.401	0.031	4.0	0.060	0.82	10
93-114	368	197	-0.305	0.045	3.1	0.100	0.75	6
93-030	315	135	-0.261	0.052	2.6	0.100	0.65	5
93-113	256	77	-0.212	0.059	2.1	0.100	0.68	6
93-112	148	291	-0.123	0.071	1.3	0.200	1.02	6
93-048	100	28	-0.083	0.077	0.9	0.200	0.77	4
93-045	0	39	0	0.089	0	-	0.78	-
93-068	-51	92	+0.042	0.095	-0.4	1.0	1.06	1
93-092	-58	112	+0.048	0.096	-0.5	1.0	1.38	1
93-120	-68	-	+0.056	0.097	-0.5	1.0	0.40	0.4
94-035	-753	194	+0.623	0.179	-6.2	0.040	0.49	10
93-151	-855	365	+0.708	0.192	-7.1	0.040	0.78	20

constant. A theoretical estimate of the critical thickness is given by (Herman, 1989:222):

$$t_c = \frac{b(1 - \nu \cos^2 \beta)}{8\pi |f_0|(1 + \nu) \sin \beta \cos \gamma} \ln \left( \frac{\zeta t_c}{b} \right), \quad (4.11)$$

where  $b$  is the Burger's vector,  $\nu$  is Poisson's ratio,  $\beta$  is the angle between Burger's vector and the dislocation line,  $\gamma$  is the angle between the glide plane of the dislocation and the substrate/epilayer interface,  $\zeta$  is a numerical factor which accounts for the energy of dislocation ( $\zeta \cong 4$ ), and  $f_0$  is the misfit given by (Herman, 1989:221):

$$f_0 = 2 \frac{a_{\text{substr}} - a_{\text{epi}}}{a_{\text{substr}} + a_{\text{epi}}} \quad (4.12)$$

where  $a_{\text{substr}}$  and  $a_{\text{epi}}$  are the lattice constants of the substrate and epilayer, respectively.

A plot of the critical thickness as a function of misfit,  $f_0$ , is shown in Figure 4-12 for  $60^\circ$  misfit dislocations on (111) glide planes in a (001) interface with a Poisson's ratio of 0.25 (Herman, 1989:223). The misfits,  $f_0$ , for the  $\text{InAs}_{1-x}\text{Sb}_x$  samples on GaSb substrate were calculated using Eqs (4.8) and (4.12), and are listed in Table 4-2. From these values and Figure 4-12, the critical thicknesses for these samples were estimated and are also listed in Table 4-2, along with each ratio of epilayer thickness to the estimated critical thickness.

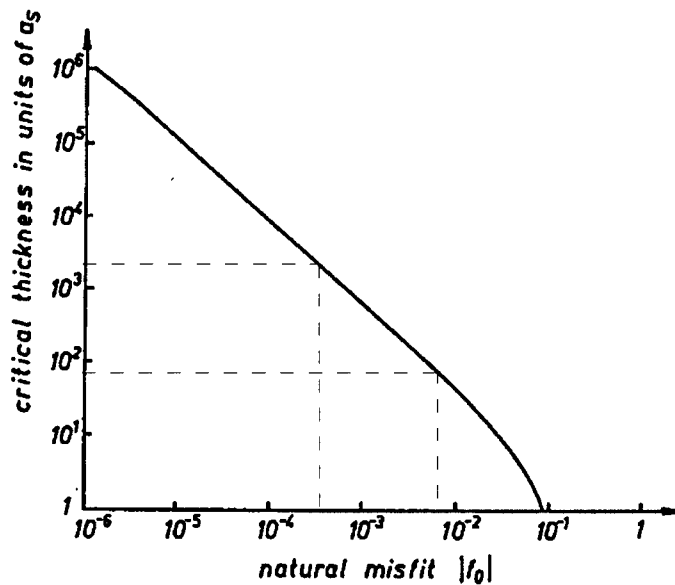


Figure 4-12. Critical pseudomorphic thickness in units of substrate lattice constant,  $a_s$ , given by Eq (4.11) as a function of misfit given by Eq (4.12) for  $60^\circ$  misfit dislocations on (111) glide planes in a (001) interface with a Poisson's ratio of 0.25 (Herman, 1989:223).

**[115] DCXRD.** As a complement to the theoretical analysis of critical thickness, DCXRD experiments were also performed on these samples at Wright Laboratory, but for diffraction from the (115) planes. Whereas diffraction from the (004) planes (which are the growth planes) results in calculation of the lattice constant normal to the growth planes, diffraction from another family of planes, along with knowledge of the normal lattice constant, results in a calculation of the lattice constant in a direction parallel to the growth planes, *i.e.*, the “in-plane lattice constant”.

Since one kind of strain in the in-plane lattice directions, *e.g.*, compressive strain if the natural lattice constant of the epilayer is larger than that of the substrate, results in the opposite strain in the normal direction by Poisson’s ratio, *i.e.*, tensile strain for this example, knowledge of both the normal and in-plane lattice constants results in a conclusive statement as to the amount of strain existing in an epilayer.

For DCXRD from the (115) planes, the angle between the (115) planes and the (004) planes,  $\phi$ , is  $15.793^\circ$  as shown in Figure 4-13. Strain in the epilayer results in a slight change in this angle,  $\Delta\phi$ , because of the difference between the normal and in-plane lattice constants. When the incident beam is at an angle  $\theta_B - \phi$ , where  $\theta_B$  is the Bragg angle for the substrate (115) planes as shown in Figure 4-13, the substrate reflection is at an angle  $\theta_B + \phi$ . The Bragg reflected beam for the epilayer is at an angle of  $\theta_B - \Delta\theta_B + \phi + \Delta\phi$ , where  $\theta_B - \Delta\theta_B$  is the Bragg angle for the epilayer (115) planes. The



DCXRD peak separation, then, is  $\Delta\phi - \Delta\theta_B$ , and the normal and in-plane components of the lattice constant are given by (Herman, 1989:179):

$$\frac{\Delta a_{\perp}}{a_0} = \Delta\phi \cot \phi - \Delta\theta_B \cot \theta_B \quad (4.13a)$$

$$\frac{\Delta a_{\parallel}}{a_0} = \Delta\phi \tan \phi - \Delta\theta_B \cot \theta_B \quad (4.13b)$$

where  $\Delta a_{\perp}$  and  $\Delta a_{\parallel}$  are the differences between the normal and in-plane lattice constants, and the unstrained lattice constant, respectively.

DCXRD from the (115) planes was performed on sample 93-151 which had a  $\Delta\theta$  peak from the (004) planes at -855 arcsec as listed in Table 4-2. Using Eqs (4.5) and (4.9), this results in a normal lattice constant of 6.13853 Å. From the relationships given in Eqs 4.13, the in-plane lattice constant was calculated to be 6.14099 Å. From these normal and in-plane lattice constants, the fully relaxed lattice constant is calculated to be 6.13965 Å. Using this value and Eqs (2.4) and (4.8), the Sb composition,  $x$ , of sample 93-151 is still calculated to be 0.192, the same value as calculated from the normal lattice constant, only.

The ratio of the epilayer thickness to the calculated critical thickness for sample 93-151 given in Table 4-2 was 21. From this ratio, it was expected that the epilayer was fully relaxed, and that no change in the calculated Sb composition would be found using the (115) DCXRD results for the experimental in-plane lattice constant. However,

because some of the other ratios listed in Table 4-2 are closer to unity, the full strain relaxation assumption may not be a good assumption for all the samples.

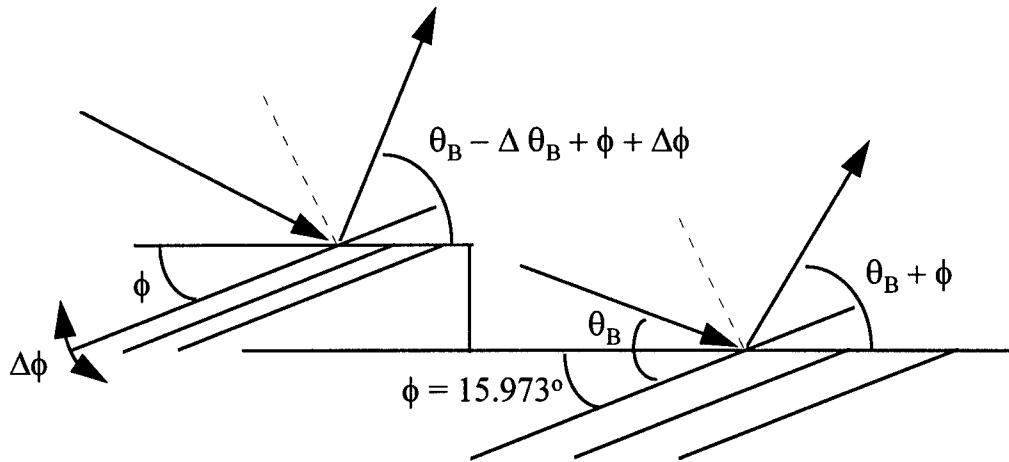


Figure 4-13. Schematic illustration of DCXRD experiment with Bragg reflection from (115) planes.

**Conductivity.** Since semi-insulating (SI) GaSb substrates (which have a lattice constant near that of the  $\text{InAs}_{1-x}\text{Sb}_x$  material considered) are not available, the  $\text{InAs}_{1-x}\text{Sb}_x$  conductivity could only be determined by Hall measurements made on MBE-grown  $\text{InAs}_{1-x}\text{Sb}_x$  layers grown under similar growth conditions to those grown on the n- or p-GaSb substrates, but grown on SI-GaAs. The lattice mismatch between the  $\text{InAs}_{1-x}\text{Sb}_x$  epilayers and the GaAs substrate is quite large ( $\Delta a/a \cong -8\%$  for  $x \cong 10\%$ ) resulting in a high misfit dislocation density. Therefore, it is believed that a close correlation between the results of the Hall experiments, *i.e.*, carrier concentrations and mobilities, for the epitaxial material grown nearly lattice-matched on GaSb and that grown highly lattice-

mismatched on GaAs would not exist. However, in general, the conductivity of the  $\text{InAs}_{1-x}\text{Sb}_x$  samples was measured as n-type.

### **Doped Samples**

The conductivity of  $\text{InAs}_{1-x}\text{Sb}_x$  can be changed to p-type by doping with Be. As mentioned in Chapter III, Bubulac reported Be-doping of  $\text{InAs}_{1-x}\text{Sb}_x$  by Be ion implantation in 1979, but reported no optical measurements, concentrating on SIMS measurements of Be ion cross sectional profiles (Bubulac, 1979:519). A portion of sample 93-068 was implanted with Be ions using the parameters from Bubulac as a reference: a 970 Å  $\text{Si}_3\text{N}_4$  implantation cap was used (Bubulac - 1000 Å  $\text{SiO}_2$ ); the dose was  $5 \times 10^{14} \text{ cm}^{-2}$  (Bubulac -  $5 \times 10^{15} \text{ cm}^{-2}$ ); the implantation energy was 50 keV (Bubulac - 100 keV); and the ion beam was directed at  $7^\circ$  from any low index axial direction to minimize channeling (same as Bubulac).

Bubulac used conventional annealing at a temperature of 550 °C for times of 15, 30 and 45 min. Both conventional and Rapid thermal annealing (RTA) were available for this study. The RTA time was fixed at 10 sec. with RTA temperatures of 450, 550 and 650 °C. The conventional annealing was performed using a BioRad alloy furnace under an argon-hydrogen forming gas atmosphere. The temperature was fixed at 550 °C, with annealing times of 4, 10 and 20 min. The  $\text{Si}_3\text{N}_4$  cap was removed before any optical measurements were made.

Another sample, 95-017, was epitaxially doped with Be. The DCXRD spectrum of this sample is shown in Figure 4-14. The DCXRD peak position is at  $\Delta\theta = 356$  sec, corresponding to a lattice-mismatch with the GaSb substrate of  $\Delta a/a = -0.295\%$  and a composition of  $\text{InAs}_{0.955}\text{Sb}_{0.045}$  assuming full strain relaxation. Another MBE growth under similar conditions as for this sample but on SI-GaAs allowed Hall measurements to be made which resulted in a hole concentration of  $4\text{-}5 \times 10^{18} \text{ cm}^{-3}$ . Electron concentrations of  $2\text{-}6 \times 10^{16} \text{ cm}^{-3}$  were typical for undoped samples.

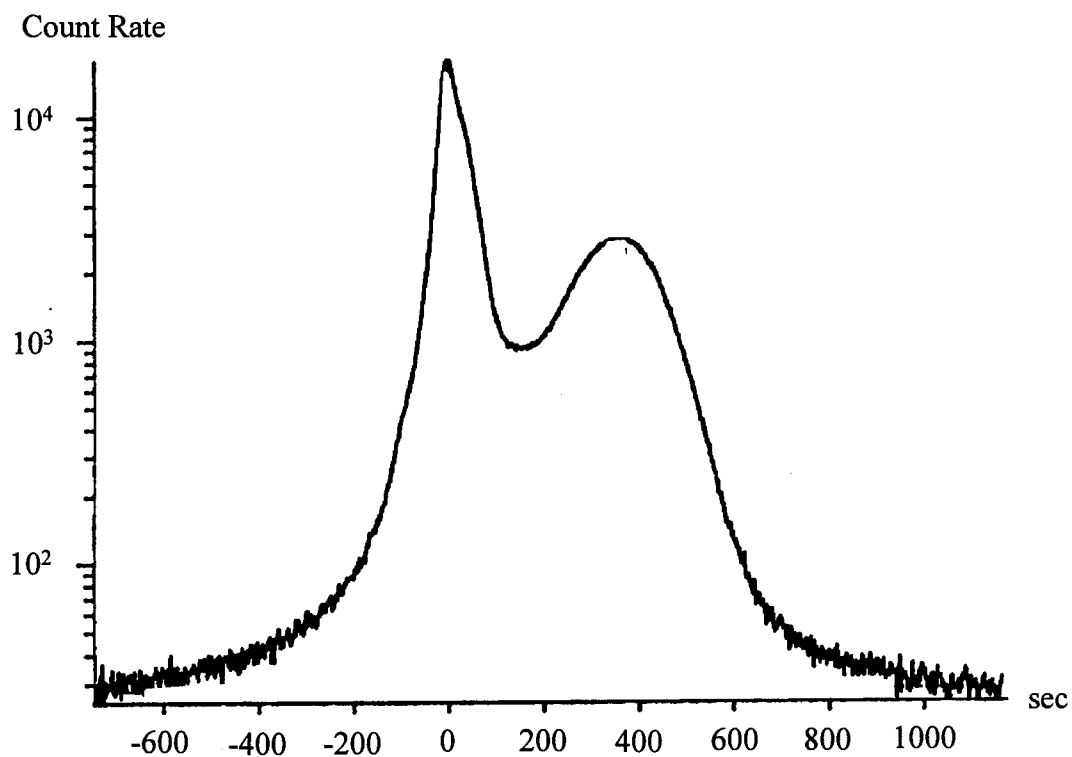


Figure 4-14. DCXRD results for epitaxially Be-doped sample 95-017. GaSb substrate peak is at 0 sec; the  $\text{InAs}_{0.955}\text{Sb}_{0.045}$  epilayer peak is at  $\Delta\theta = 356$  sec.

## V. Characterization Techniques

The two primary methods of optical semiconductor characterization used in this study were absorption and photoluminescence (PL). Infrared (IR) absorption was used mainly to determine the band edge energy of the samples. This provided a baseline against which the PL results were compared. The absorption measurements also provided an estimate of the absorption coefficients for these samples, a number which is not available from the literature. PL was used to either characterize the material quality or to identify extrinsic energy levels which existed. Since the spectral data from the absorption and PL experiments were often compared, a calibration between the different spectrometers used for each experiment was necessary. Finally, much of the data was analyzed by fitting experimental results to known physical relationships. Therefore, an understanding of the limitations of the fitting routines is essential. The optical characterization experiments and analyses were performed in the laboratories of the Engineering Physics Department of the Air Force Institute of Technology, Bldg 640, Wright-Patterson AFB, OH.

### **Absorption**

An optical absorption experiment is a very simple way to measure the band structure of semiconductors. By imparting the known energy from an incident photon to an electron of the material, the electron is caused to transition from a lower to a higher

energy state. Thus, by illuminating the sample with a broad spectrum of incident photons, all possible transitions are excited and knowledge of the energy levels of the material is obtained (Pankove, 1971:34). Because the momentum of a photon,  $h/\lambda$  where  $h$  is Planck's constant and  $\lambda$  is the wavelength of the light, is small ( $1.7 \times 10^{-28}$  kg-m/sec for a 4  $\mu\text{m}$  photon) in comparison to the crystal momentum,  $h/a_0$  ( $1.1 \times 10^{-24}$  kg-m/sec for lattice constant,  $a_0$ , of 6  $\text{\AA}$ ), nearly vertical transitions are expected, *i.e.*, the momenta of the electron and hole created by the transition are approximately the same (Saleh, 1991:578).

Optical absorption, mainly to determine the band edge position of the  $\text{InAs}_{1-x}\text{Sb}_x$  epitaxial layers, was performed using a BioRad FTS-60A Fourier transform spectroscopy (FTS) system. A schematic diagram of the BioRad FTS system is shown in Figure 5-1.

FTS works on the principle of the Michelson interferometer (Figure 5-2). Light from the source is split by the beam splitter into two separate paths. One path travels to a fixed mirror and back to the beamsplitter; the other path travels to the translating mirror and back. Light from the two paths is recombined at the beamsplitter and travels to the detector.

For any monochromatic light, a constructive interference fringe occurs at the detector whenever the two path lengths are equal. As the translating mirror is moved, alternating destructive and constructive interference fringes are observed at the detector as the path lengths differ by odd and even multiples of half a wavelength, respectively.

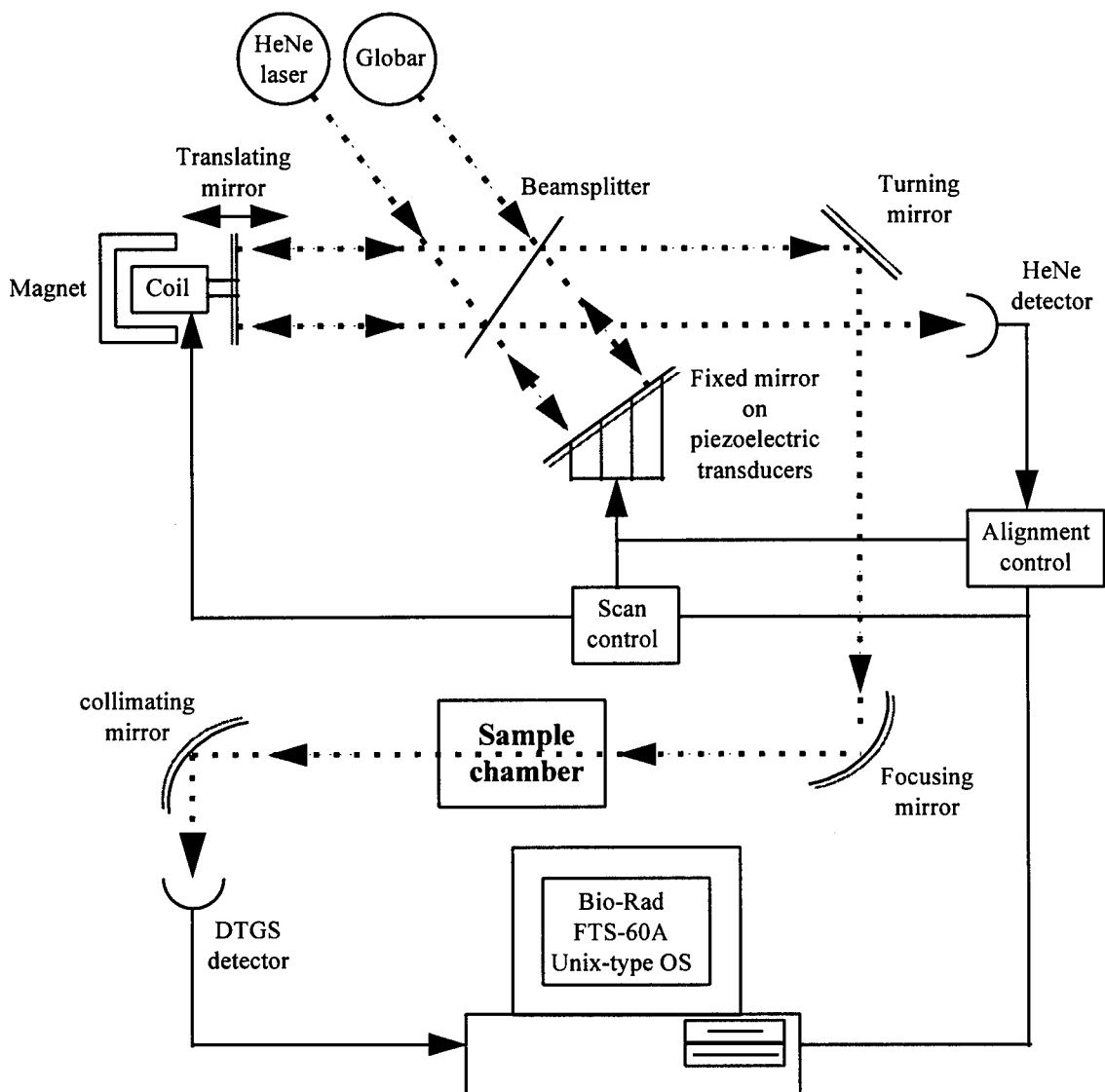


Figure 5-1. Schematic drawing of BioRad FTS-60A Fourier transform spectrometer infrared absorption experimental apparatus.

These multiples of half wavelengths correspond to mirror translations of one quarter wavelength. The intensity of the signal at the detector is given by:

$$I(\lambda_1, x) = I_1(\lambda_1) + I_2(\lambda_1) + 2 [I_1(\lambda_1) I_2(\lambda_1)]^{1/2} \cos\left(\frac{4\pi x}{\lambda_1}\right), \quad (5.1)$$

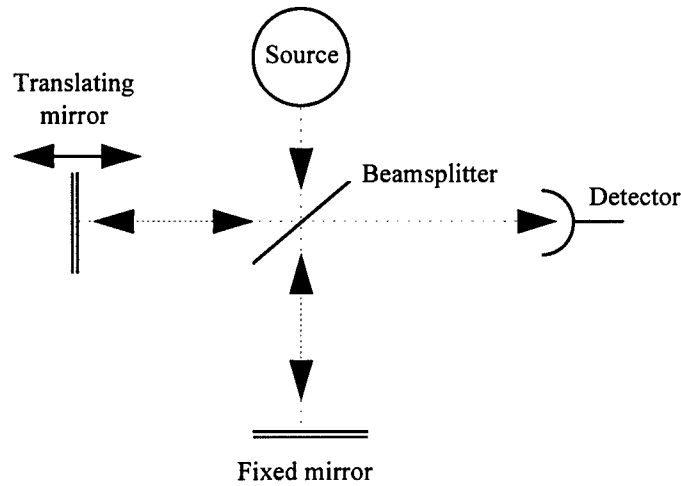


Figure 5-2. Michelson interferometer.

where  $\lambda_1$  is wavelength of the monochromatic light,  $x$  is the mirror translation, and  $I_1$  and  $I_2$  are the intensities along the individual paths. The Fourier transform of this signal becomes:

$$\begin{aligned} \mathcal{F}\{I(\lambda_1, x)\} &= \mathcal{F}\{I_1(\lambda_1) + I_2(\lambda_1)\} + I_0(\lambda_1) \int_{-\infty}^{\infty} \cos\left(\frac{4\pi x}{\lambda_1}\right) \exp(-i\xi x) dx \\ &= A(\lambda_1) \delta(\xi) + \pi I_0(\lambda_1) [\delta(\xi - 4\pi/\lambda_1) + \delta(\xi + 4\pi/\lambda_1)], \end{aligned} \quad (5.2)$$

where  $\xi$  is the spatial frequency in the Fourier transform pair with spatial position,  $x$ , and  $\delta(\xi)$  is the Dirac delta or impulse function. The transform, then, yields impulses at the origin (dc) and at  $\xi_1 = \pm 4\pi/\lambda_1$  in spatial frequency space. This spatial frequency is related to the optical frequency by:

$$\xi_1 = \frac{4\pi\nu_1}{c}, \quad (5.3)$$



where  $\nu_1$  is the optical frequency corresponding to the optical wavelength,  $\lambda_1$ , and  $c$  is the speed of light.

For polychromatic light, a constructive interference fringe occurs when the two path lengths are equal. However, when the mirror is translated to any other position, a superposition of the interference for all the wavelengths corresponding to that mirror position is observed at the detector:

$$I(x) = \sum_{i=1}^{\infty} [I_1(\lambda_i) + I_2(\lambda_i) + 2\sqrt{I_1(\lambda_i)I_2(\lambda_i)} \cos(\frac{4\pi x}{\lambda_i})]. \quad (5.4)$$

The limit of this summation, of course, is the integration over all wavelengths. The Fourier transform of Eq (5.4) is:

$$\mathcal{F}\{I(x)\} = \sum_{i=1}^{\infty} \{A_i(\lambda_i)\delta(\xi) + \pi I_0(\lambda_i) [\delta(\xi - \frac{4\pi}{\lambda_i}) + \delta(\xi + \frac{4\pi}{\lambda_i})]\}. \quad (5.5)$$

This spectrum is depicted in Figure 5-3. Spectral attenuation of this polychromatic signal by the sample can be viewed as individual adjustments of the coefficients at each frequency:

$$I_0'(\lambda_i) = I_0(\lambda_i) \exp[-\alpha(\lambda_i) d], \quad (5.6)$$

where  $\alpha(\lambda_1)$  is the absorption coefficient of the sample at wavelength,  $\lambda_1$ , and  $d$  is the sample thickness.

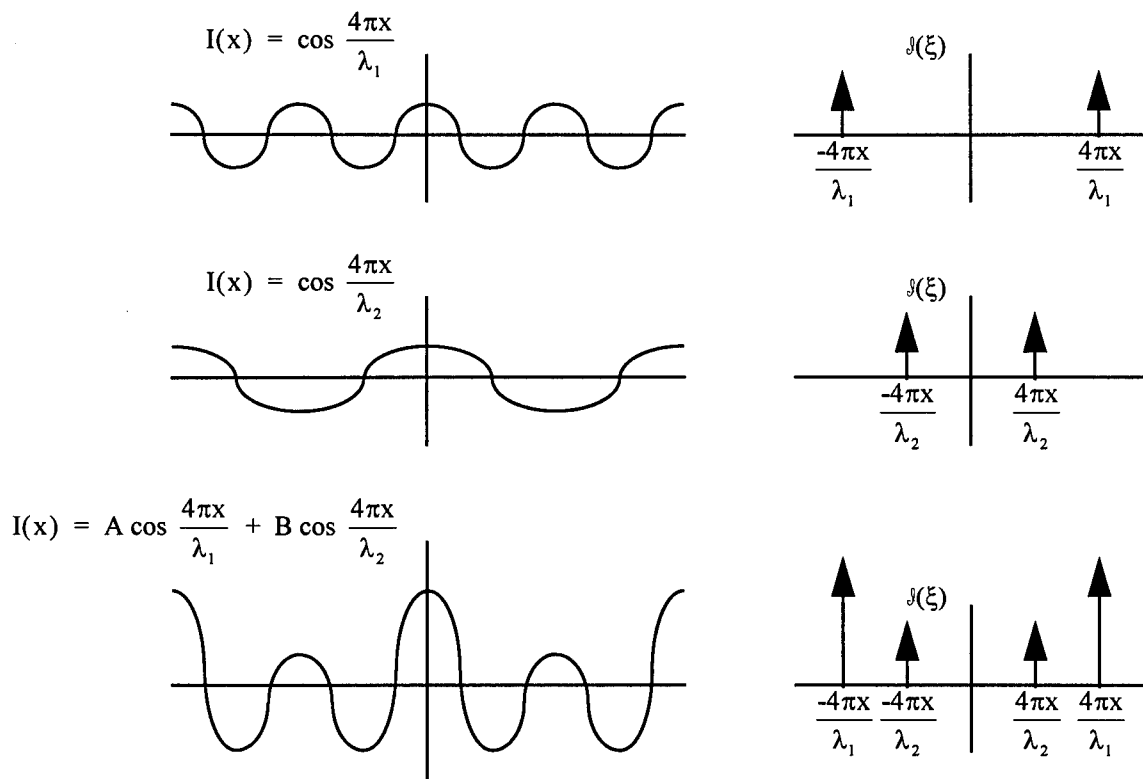


Figure 5-3. Fourier transform pairs of sinusoids at two different frequencies and their sum.

The “absorbance” is defined as:

$$\text{Absorbance} = \log_{10} \frac{I_{\text{Background}}}{I_{\text{Sample}}}, \quad (5.7)$$

where  $I_{\text{Background}}$  is the BioRad FTS single-beam spectrum of the substrate or open aperture, whichever was used as the background, and  $I_{\text{Sample}}$  is the single-beam spectrum of the combination of the epitaxial layer and the substrate on which it was grown. Calculating absorbances of the epitaxial layers using the substrates as the background minimized inclusion of intraband absorption effects from the substrate in the spectral region of interest.

The spectral coverage of the BioRad FTS system was determined, initially, by the deuterated triglycine sulfate (DTGS) detector used; this is  $>200\text{ cm}^{-1}$  ( $<50\text{ }\mu\text{m}$  or  $>0.025\text{ eV}$ ). The range of the spectrometer was then reduced to  $400\text{-}4000\text{ cm}^{-1}$  ( $25\text{-}2.5\text{ }\mu\text{m}$  or  $0.05\text{-}0.5\text{ eV}$ ) by the Ge/Sb<sub>2</sub>S<sub>3</sub>-coated KBr beamsplitter used.

The BioRad sample chamber was modified with an Air Products helitran which allowed absorption measurements to be made over sample temperatures of  $6\text{-}300\text{ K}$  while maintaining a high quality nitrogen purge of the remainder of the beam path to avoid extraneous atmospheric absorption. The system spectral range was reduced farther to  $1450\text{-}4000\text{ cm}^{-1}$  ( $6.9\text{-}2.5\text{ }\mu\text{m}$  or  $0.18\text{-}0.5\text{ eV}$ ) by the transmission of the helitran sapphire windows or to  $500\text{-}4000\text{ cm}^{-1}$  ( $20\text{-}2.5\text{ }\mu\text{m}$  or  $0.06\text{-}0.5\text{ eV}$ ) by ZnSe windows. Figure 5-4 shows a summary of the spectral range of the individual components of the BioRad FTS system. Thus, for these absorption experiments on InAs<sub>1-x</sub>Sb<sub>x</sub> epitaxial layers, the spectral range covered was either  $500\text{-}4000\text{ cm}^{-1}$  ( $20\text{-}2.5\text{ }\mu\text{m}$  or  $0.06\text{-}0.5\text{ eV}$ ) or  $1450\text{-}4000\text{ cm}^{-1}$  ( $6.9\text{-}2.5\text{ }\mu\text{m}$  or  $0.18\text{-}0.5\text{ eV}$ ), depending on the equipment used for a particular experiment.

### **Photoluminescence**

Luminescence is the result of a transition of an electron from an energy state higher than it would occupy under equilibrium conditions to an empty lower energy state. The energy difference between the two states is emitted as electromagnetic radiation. The electron, then, must first be excited by some means to the higher energy state. PL is

the optical excitation of the electron, *i.e.*, absorption of an incident photon, and subsequent radiative transition, *i.e.*, emission of a photon at the same or lower energy.

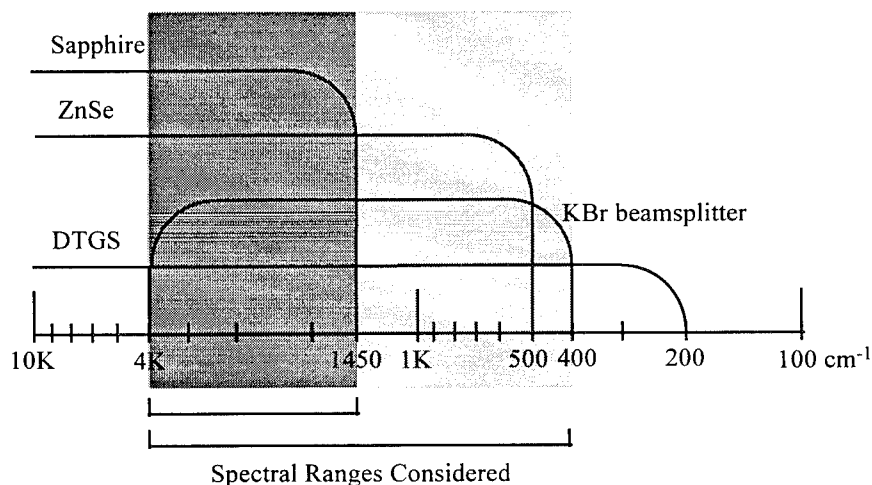


Figure 5-4. Spectral ranges of BioRad FTS absorption experiments.

PL can be a powerful semiconductor characterization tool because it provides direct observation of the energy levels that exist in the material. Since the objective of this research was to characterize the quality of  $\text{InAs}_{1-x}\text{Sb}_x$  material for use as the active region of a semiconductor laser, an even greater interest is given to the PL experiment since often the luminescence efficiency observed in this experiment is an indication of the performance that can be expected once this material is processed into the laser device.

PL has the advantage of being able to excite materials in which electrical contact or junction technology has not been developed, and it offers the flexibility to select a particular region of the semiconductor crystal to be excited making it readily adaptable to device structures as well as bulk materials (Pankove, 1971:249). It is a rather simple

characterization experiment, requiring only a source for optical excitation (usually a laser), a spectrometer and a suitable detector for the emitted radiation.

Basic characterization of the semiconductor usually requires the sample to be cooled to low temperatures. Two primary reasons for this cooling are: information about the electronic levels, *e.g.*, excitons, donors, and acceptors, can only be obtained when these levels are not thermally ionized; and cooling reduces the spectral broadening of PL peaks due to thermal vibrations (Dean, 1982:89).

Although absorption and PL initially appear to be the inverse processes of each other, different information can be learned from each. Absorption couples any occupied lower energy state with any empty higher energy state, providing energy and momentum are conserved. Therefore, the observed spectrum is broad. PL, on the other hand, is a nonequilibrium process which couples a narrow band of occupied higher energy states with a narrow band of empty lower energy states. Therefore, the emission spectrum is often narrower (Pankove, 1971:107).

The van Roosbroeck-Shockley equation gives a relationship between the absorption coefficient,  $\alpha(\nu)$ , and the radiative recombination rate,  $R(\nu)$ , at equilibrium:

$$R(\nu)d\nu = \alpha(\nu) \frac{8\pi\nu^2 n^2}{c^2 [\exp(\frac{h\nu}{k_B T}) - 1]} d\nu, \quad (5.8)$$

where  $n$  is the refractive index. For nonequilibrium (as in PL), the recombination rate becomes:

$$R_{\text{noneq}} = \frac{np}{n_i^2} R, \quad (5.9)$$

where  $n$  and  $p$  are the nonequilibrium concentrations of electrons and holes, respectively,  $n_i$  is the intrinsic carrier concentration, and  $R = \int R(\nu) d\nu$ . Eq (5.9) assumes all excited electrons recombine radiatively. However, in practice, other recombination mechanisms participate, reducing  $R_{\text{noneq}}$  farther (Pankove, 1971:110).

Radiative transitions may occur from an upper state to a lower state through many paths. Figure 5-5 depicts several recombination mechanisms for direct gap semiconductors.

**Laboratory Equipment.** The PL spectra of the MBE-grown  $\text{InAs}_{1-x}\text{Sb}_x$  samples were measured as a function of temperature and excitation power. Figure 5-6 shows a schematic of the PL experiment. The samples were mounted inside a liquid helium cooled Janis cryostat. Vacuum pumping on the sample chamber allowed a temperature range of 2-300 K to be studied.

The samples were excited using a fiber-coupled Applied Optronics 1.2 W CW, 1  $\mu\text{m}$  InGaAs diode laser, but excitation was limited to 500 mW by the DC power supply used. A 1  $\mu\text{m}$  radiation source was chosen so the upper cladding layer of the laser structure being studied would be transparent, and all excitation would occur in the

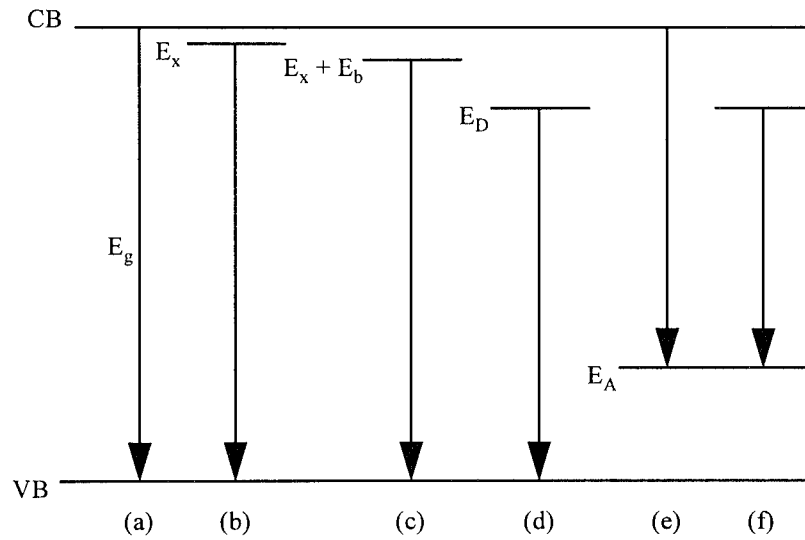


Figure 5-5. Recombination processes for direct gap semiconductors: (a) band-to-band; (b) free exciton; (c) bound exciton; (d) donor-to-valence band; (e) conduction band-to-acceptor; and (f) donor-acceptor pair.

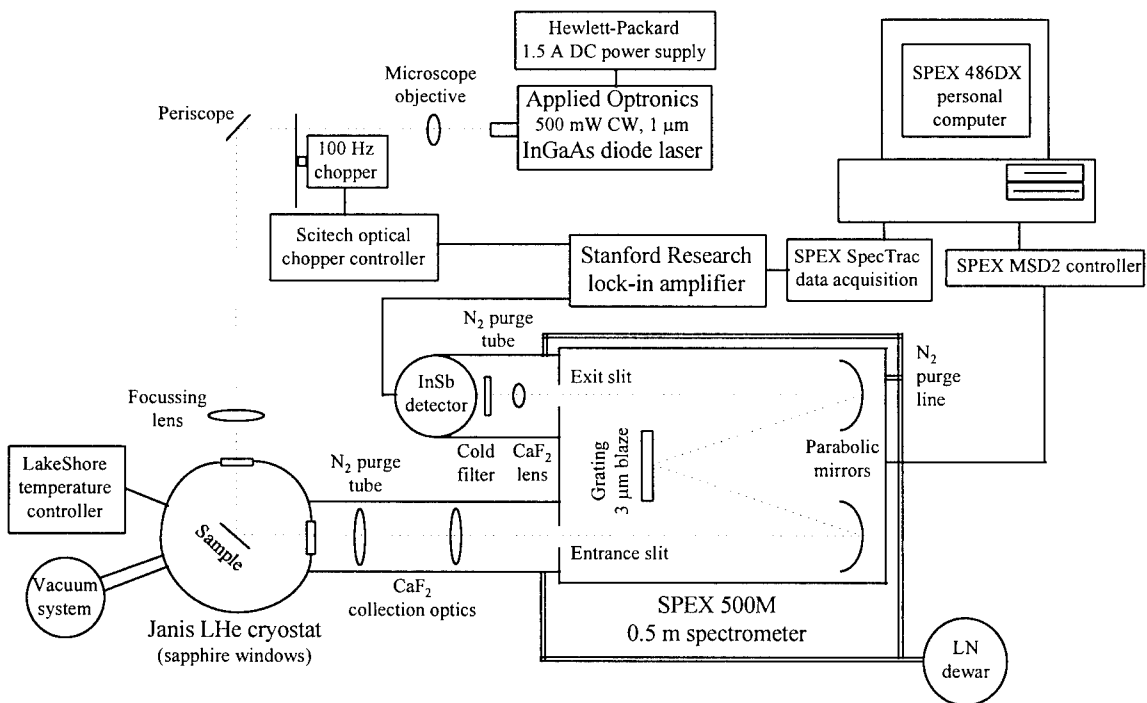


Figure 5-6. Schematic drawing of photoluminescence experiment.

InAs<sub>1-x</sub>Sb<sub>x</sub> active region (see Figure 4-7). The fiber output of the diode laser was collimated using a microscope objective and reimaged onto the sample using a 150 mm focal length, 2 inch diameter CaF<sub>2</sub> lens.

The laser spot on the sample was measured using a Beamcode imaging system. At low powers (5 mW), the beam shape was top-hat shaped with a spot diameter of 3.03 mm at the 86.5% power points. As the power was increased, the intensity at the center of the beam began to be reduced relative to the outer edges, and the diameter of the beam increased. The spot was clearly donut-shaped at 40 mW, with a measured outer diameter of 6.39 mm; the measured outer diameter at 320 mW was 7.38 mm. Since the excitation diode laser must be a broad area device to achieve these high output powers, the increase in spot size is expected as the coherence of a broad area laser decreases with increased output power. The ring shape of the spot is due to the optical mode selected in the 200 μm fiber. Because the homogeneity and size of the spot changed with the laser power, it was difficult to calculate the exact power density on the sample. However, the average densities were estimated to range from 0.035-3.5 W/cm<sup>2</sup> for laser powers of 5-500 mW, respectively.

The luminescence was collected and collimated by 100 mm focal length, 2 inch diameter CaF<sub>2</sub> lenses, and focused by a 250 mm focal length, 2 inch diameter CaF<sub>2</sub> lens into the Spex 500M 0.5 m spectrometer. The spectrometer grating was ruled to 300 grooves/mm, with the grating teeth blazed for 3 μm radiation.



**Resolution.** The grating dispersion may be derived from the grating equation,

$$a(\sin \theta_i + \sin \theta_m) = m\lambda, \quad (5.10)$$

where  $a$  is the grating groove spacing,  $\theta_i$  is the angle of incidence and  $\theta_m$  is the diffraction angle for the  $m^{\text{th}}$  order. Using the small angle approximation ( $\sin \theta \cong \theta$ ), the angular separation,  $\Delta\theta_1$ , of two first order wavelengths incident at the same angle is given by:

$$\Delta\theta_1 = \frac{\Delta\lambda}{a}, \quad (5.11)$$

where  $\Delta\lambda$  is the difference between these wavelengths. When this light is focused onto the exit slit plane by the spectrometer optics, the spatial separation of these two wavelengths becomes:

$$\Delta r = f \Delta\theta_1, \quad (5.12)$$

where  $f$  is the focal length of the optic. From Eqs (5.11) and (5.12), the spatial dispersion is given by:

$$\frac{\Delta\lambda}{\Delta r} = \frac{a}{f}. \quad (5.13)$$

Using this equation with a grating ruled to 300 grooves/mm and a 0.5 m focal length spectrometer, the grating dispersion for this experiment is 6.7 nm/mm at the exit slit plane.

Before the spectrometer resolution can be calculated, the coherence of the luminescence light must be established. Clearly, the emitting sample is not expected to be a coherent source. However, the light could be considered as quasimonochromatic if two conditions are met (Goodman, 1985:180):

$$\Delta\lambda \ll \lambda \quad (5.14a)$$

$$d \ll \frac{\lambda^2}{\Delta\lambda} \quad (5.14b)$$

where  $\Delta\lambda$  is the resolution expected from the experiment,  $\lambda$  is the typical wavelength of the experiment and  $d$  is the maximum pathlength difference encountered by light rays passing from the entrance slit of the spectrometer to the exit slit. Using the grating dispersion calculated above and the largest slit width used in these experiments, 2 mm, the resolution is expected to be  $\sim 13.4$  nm. Therefore, for wavelengths  $> 3$   $\mu\text{m}$  as in this experiment, the condition of Eq (5.14a) is met.

However, since the narrowest slit widths were  $< 1$  mm and the wavelengths as large as  $\sim 4.5$   $\mu\text{m}$ , the pathlength difference of Eq (5.14b) must be  $\ll 3.0$  mm, at largest. The actual pathlength difference for the 0.5 m spectrometer with 10 cm diameter lenses is  $\sim 5.0$  mm as depicted in Figure 5-7. Therefore, the quasimonochromatic conditions of Eq (5.14) are not met.

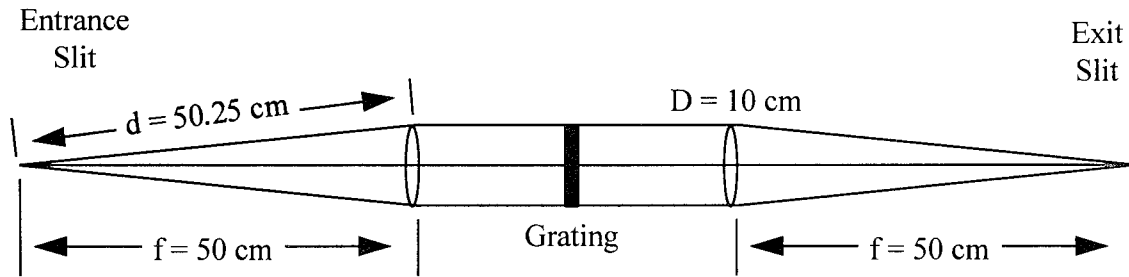


Figure 5-7. Geometric optical schematic diagram of 0.5 m grating spectrometer.

An incoherent source may also be regarded as coherent if the entrance slit is narrow enough that the source approaches a point source. This coherence condition is given by (Mielenz, 1967:66):

$$w \ll \frac{\lambda f}{D} \quad (5.15)$$

where  $w$  is the slit width and  $D$  is the diameter of the spectrometer optics. Again using the experimental conditions described above, the entrance slit width must be  $\ll 22.5 \mu\text{m}$  for this condition to hold. No slit widths this narrow were used in this experiments.

Therefore, the luminescence light may be regarded as both temporally and spatially incoherent, and the spectrometer resolution may be analyzed using geometric optics. Since the spectrometer is a one-to-one imaging system (Figure 5-7), the entrance slit is reimaged at the exit slit with unity magnification. First considering monochromatic light, as the grating turns during the experiment, the image of the entrance slit passes the exit slit so that the optical signal detected through the exit slit is the convolution of the entrance slit image and the exit slit. Since the linewidth of the convoluted signal is

determined by the greater of the two slit widths, the optimum configuration for this experiment is when the entrance and exit slit widths are set equal. This achieves maximum throughput. All PL experiments performed here were configured in this manner.

When this argument is expanded to the polychromatic case, separate wavelengths are only resolved when they cannot pass through the exit slit simultaneously. Therefore, using the spatial grating dispersion at the exit slit (Eq (5.13)), the spectrometer's wavelength resolution is:

$$\Delta\lambda = \frac{a w}{f}, \quad (5.16)$$

and its resolution in terms of photon energy is:

$$\Delta E = \frac{c h a w}{f \lambda^2} \quad (5.17)$$

where  $c$  is the speed of light,  $h$  is Planck's constant,  $a$  is the grating groove spacing,  $w$  is the slit width,  $f$  is the focal length of the spectrometer, and  $\lambda$  is the wavelength of light.

The spectrometer slit widths were typically 1-2 mm. Therefore, the resolutions were <0.6-1.2 meV over the spectral range studied. This calculated resolution was used to set the scan rate when the spectrometer was used in the continuous scan mode, or the wavelength step size in the step-and-integrate mode. In the continuous mode, the total wavelength range of the scan divided by the number of data points gives the wavelength

range covered per point. This was matched to the spectrometer resolution since including additional data points did not increase the physical resolution but did increase the volume of data to be handled. In the step-and-integrate mode, the step size was matched to the resolution for similar reasons.

**Lock-in Detection.** The signal was collected by a Cincinnati Electronics InSb photovoltaic detector with interchangeable 2.8-4.2  $\mu\text{m}$  or 3.1-4.9  $\mu\text{m}$  cold filters, depending on the sample studied. Since the diode laser excitation beam was chopped at 100 Hz by a SciTech Instruments optical chopper, the signal-to-noise ratio could be increased by standard lock-in techniques using a Stanford Research model SR850 DSP lock-in amplifier.

The basic premise of the lock-in technique is that a small signal of interest normally obscured by noise can be modulated at a specific reference frequency, then extracted from the noise by phase-sensitive detection. When the signal frequency and the reference frequency are compared, the difference is a DC signal proportional to the signal amplitude. Other (noise) signals, at frequencies different than the reference, produce AC signals when compared to the reference, and are easily removed by a low pass filter.

The bandwidth of the low pass filter is set by a time constant. The time constant is equal to  $1/2\pi f$ , where  $f$  is the -3 dB frequency of the filter. The notion of a time constant is used since the output signal is DC. Any noise at the input can be averaged out by increasing the time constant (*i.e.*,  $f$  is reduced to filter out more unwanted frequencies). PL data taking is optimized by setting the resolution/scan rate in the continuous scan

mode or the integration time of the spectrometer in step-and-integrate mode greater than or equal to the time constant.

**N<sub>2</sub> Purge.** As can be seen in Figure 1-1, there is significant CO<sub>2</sub> absorption in this spectral region of interest (~4.2-4.35 μm). To avoid interference of this absorption with a luminescence signal being measured, the luminescence light path from the sample to the detector was purged with N<sub>2</sub> as shown schematically in Figure 5-6. Figure 5-8 shows the significant reduction in CO<sub>2</sub> absorption achieved by the addition of this N<sub>2</sub> purge tube.

### **Calibration**

Since the samples were studied by both absorption and PL techniques, and the data from one technique was directly compared to the other, it was paramount to ensure that the calibration of each spectrometer was the same. Since it is difficult to find a gas lamp source with well known calibration lines at the mid-IR wavelengths of interest for this experiment (~4 μm), the two spectrometers, the Spex 500M and the BioRad FTS-60A, were calibrated to one another using the OCLI band-pass filters normally used as cold filters in the Cincinnati Electronics InSb detector. The quarter-wavelength dielectric stacks of these filters produce very spectrally sharp transitions between transmission and absorption regions which were used as calibration lines.

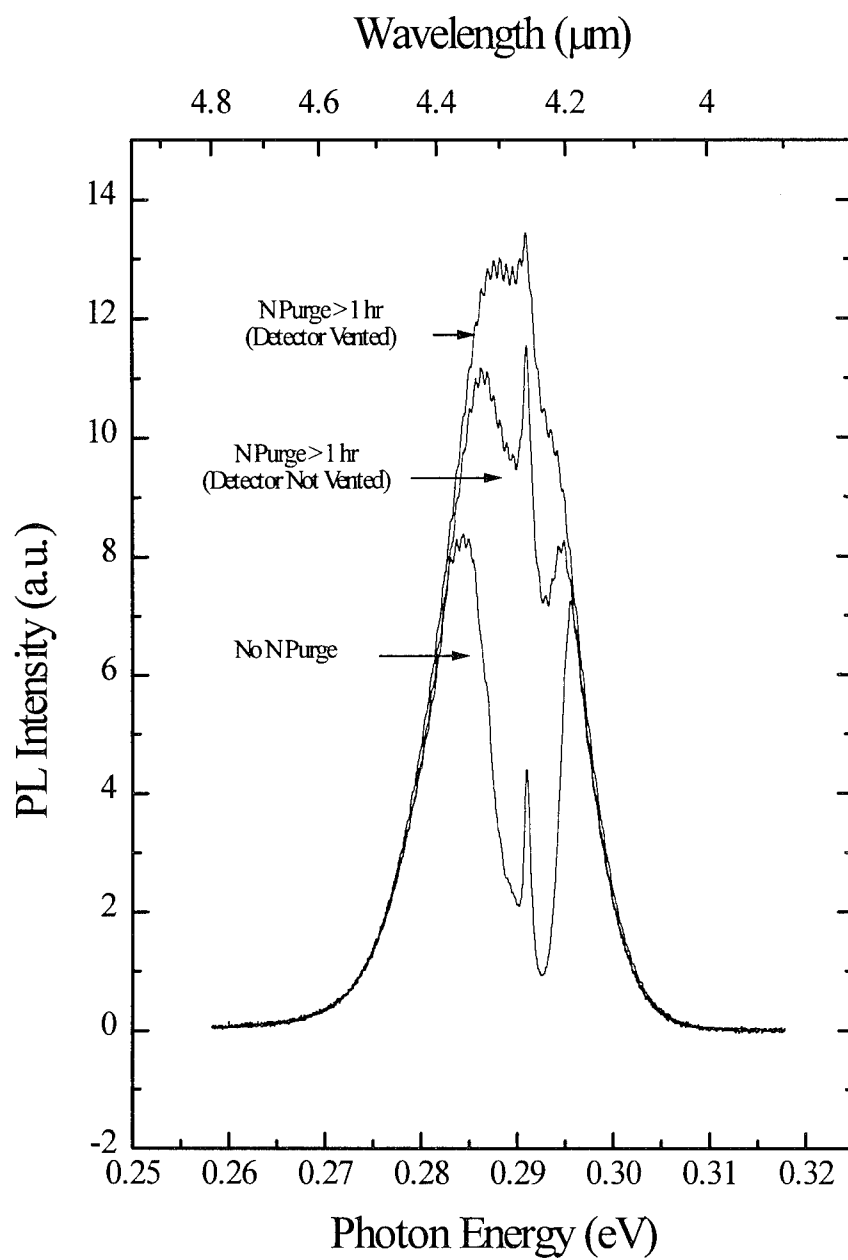


Figure 5-8. PL spectra showing advantage of  $\text{N}_2$  purge of luminescence light path in reducing  $\text{CO}_2$  absorption at wavelengths of interest.

The results of the calibration are shown in Figures 5-9 and 5-10. The roll-off at higher wavelengths for the Spex 500M is due to the blackbody curve of the quartz globalbar used for the experiment. The resolution of the Spex 500M for these experiments was  $\leq 6$  nm. The resolution of the BioRad FTS-60A was 10 nm. As can be seen in the two figures, the spectral feature size for the quarter-wave dielectric stack of the filters was  $\sim 50$  nm. Except for a few excursions of  $\leq 20$  nm, the agreement between the spectrometers at a particular filter feature was  $< 10$  nm, the resolution of the BioRad FTS-60A; this corresponds to  $< 2$  meV in the energy domain.

### **Fitting Software**

Much of the data measured during the absorption and PL experiments behaved as expected from known physical principles and could often be fit to a known physical relationship (a fitting function). The software application used for plotting such data was



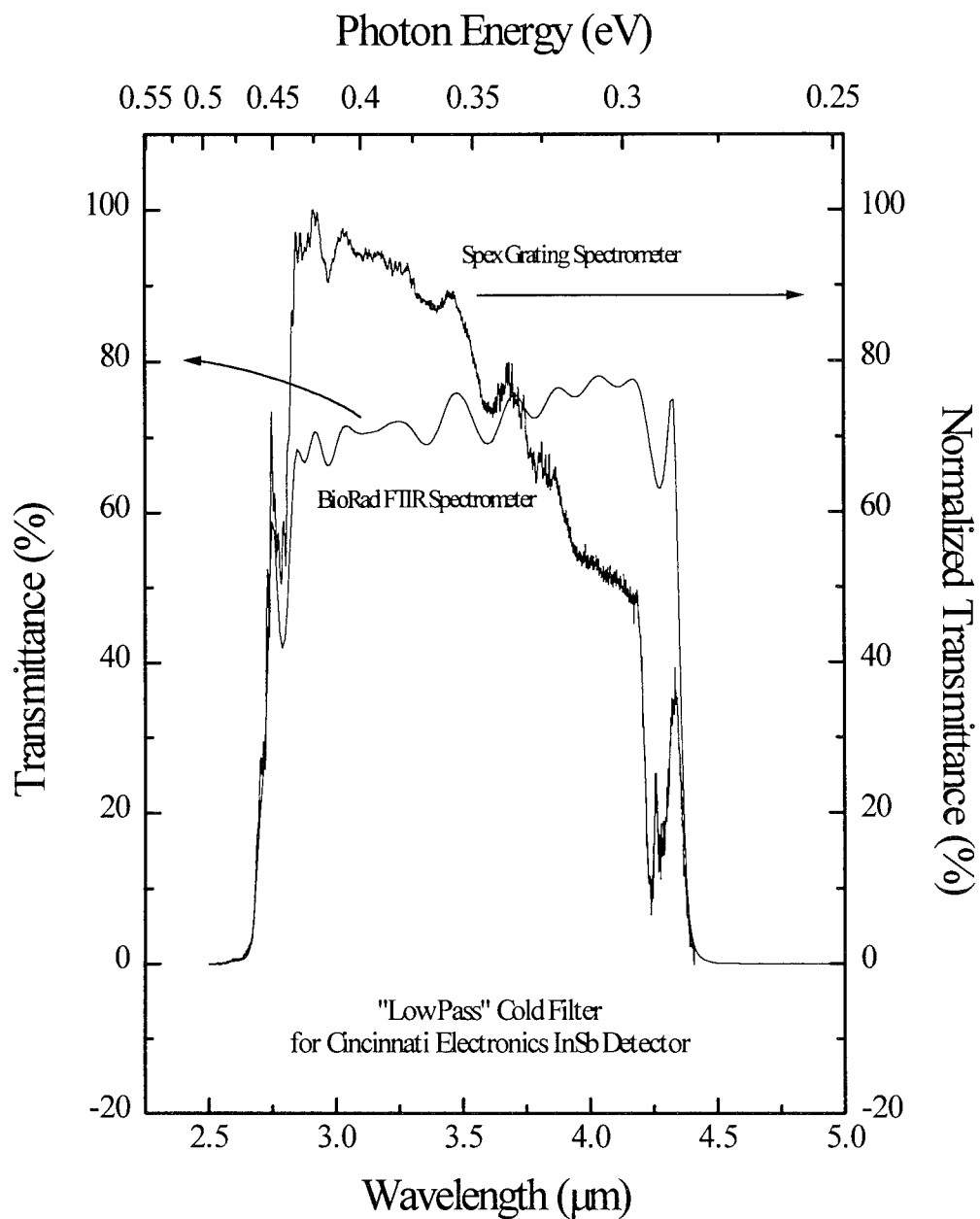


Figure 5-9. Calibration of Spex 500M PL spectrometer and BioRad FTS-60A absorption spectrometer using OCLI bandpass filter #W03540-6.

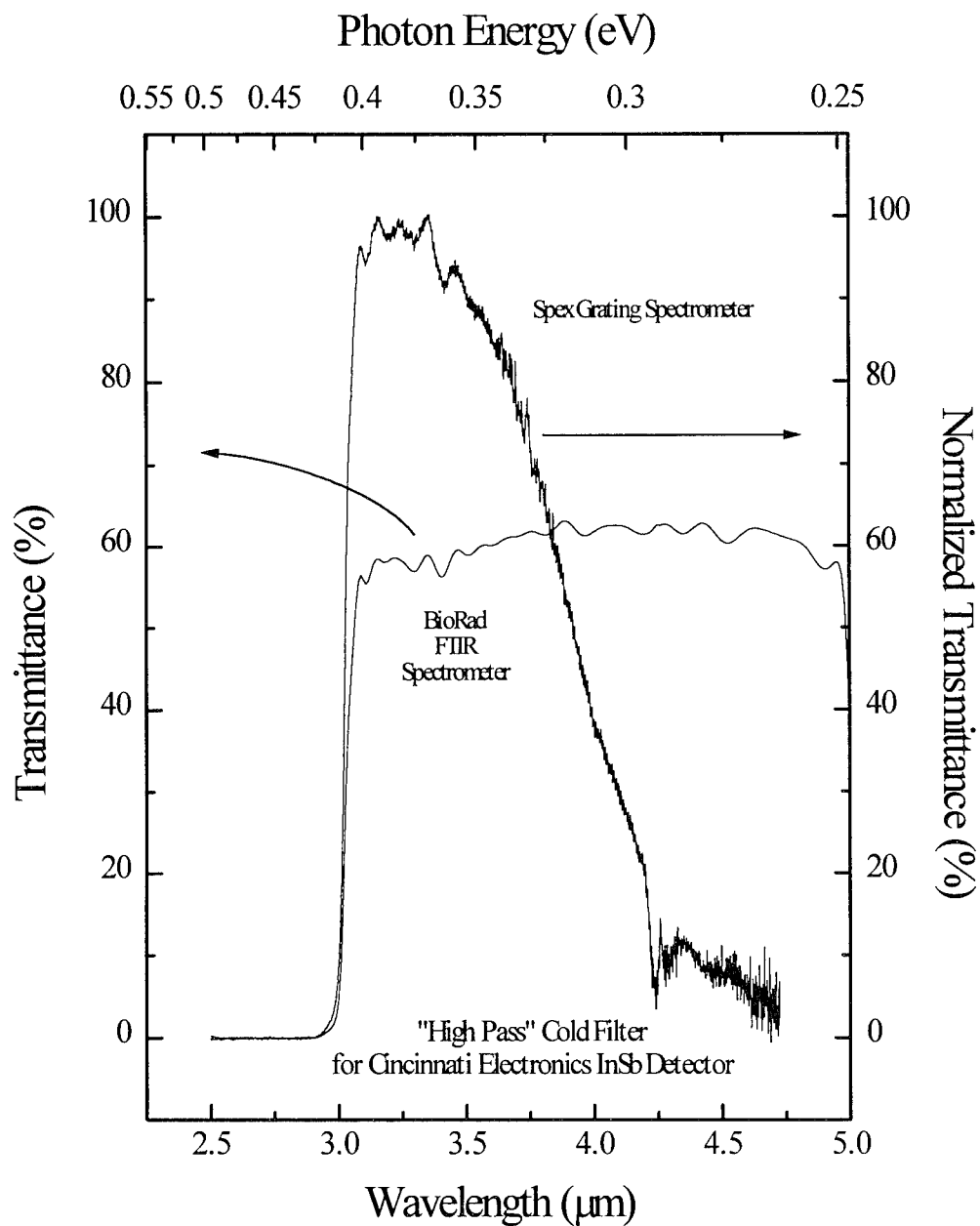


Figure 5-10. Calibration of Spex 500M PL spectrometer and BioRad FTS-60A absorption spectrometer using OCLI bandpass filter #W04018-4.

Microcal Origin, version 3.5. The basic approach used is explained by the following excerpt from the Microcal handbook:

Nonlinear curve fitting is a standard method for fitting data to user-provided models to estimate parameters. In Origin, this is achieved by minimizing the Chi-square value using the Levenberg-Marquardt algorithm...

The Levenberg-Marquardt algorithm... finds its solution iteratively, varying smoothly between the Hessian method and the steepest-descent method. This is achieved by magnifying the diagonal elements of the curvature matrix, and by adjusting the magnification factor dynamically. When the Chi-square is far from the minimum, the steepest-descent method is used with a larger magnification factor. As the minimum is approached, the routine gradually switches to the inverse-Hessian method with smaller magnification factor for better accuracy. Refer to Press et al. (Press, 1988) for an excellent description of this method. (Microcal:185)

All the parameters together form a parameter vector,  $\mathbf{p}$ . The “Sum of Squares” function is given by (Microcal:187):

$$S(\mathbf{p}) = \sum_{i=i^{\text{begin}}}^{i^{\text{end}}} w_i (f_i - y_i)^2 \quad (5.18)$$

where  $i^{\text{begin}}$  is the index of the first data point,  $i^{\text{end}}$  is the index of the last,  $w_i$  is a weighting factor (may be set to unity and often is),  $f_i$  is the fitting function value evaluated for the  $i^{\text{th}}$  data point, and  $y_i$  is the data. The Chi-Square value is given by (Microcal:188):

$$\chi^2(\mathbf{p}) = \frac{S(\mathbf{p})}{d} \quad (5.19)$$

where  $d$  is the degree of freedom given by (Microcal:187):

$$d = n - p \quad (5.20)$$

where  $n$  is the number of data points and  $p$  is the number of parameters. The parameters are modified in the fitting iterations ( $S_j(\mathbf{p})$ ,  $S_{j+1}(\mathbf{p})$ , ...) until a vector is found which minimizes the Chi-square value to within a preset tolerance (Microcal:188):

$$T = \frac{|S_{j+1}(\mathbf{p}) - S_j(\mathbf{p})|}{|S_{j+1}(\mathbf{p}) + S_j(\mathbf{p})|} \quad (5.21)$$

## VI. Results and Discussion: Absorption

The primary reason that infrared absorption experiments were performed on these MBE-grown  $\text{InAs}_{1-x}\text{Sb}_x$  epitaxial layers on GaSb substrates was to accurately determine the energy gap at a variety of temperatures for each sample. The first two sections of this chapter describe the samples and present the raw data from the absorption experiments. The third section describes the analyses performed on the absorption spectra which revealed the energy gap positions.

The remainder of the chapter focuses on the energy gap values, themselves. For any one composition, the absorption measurements were made over a variety of temperatures between 6 and 295 K, so the temperature dependencies of the energy gaps for the  $\text{InAs}_{1-x}\text{Sb}_x$  compositions,  $0 < x < 0.192$ , were determined. At two particular temperatures, very low temperature ( $\sim 0$  K) and room temperature, the compositional dependencies of the energy gaps in this compositional range were also analyzed. Finally, a brief analysis of the parameters that shape the temperature dependence of energy gaps is included.

### **Experiment**

The absorption data was obtained from the Fourier transform spectroscopic (FTS) absorption experiment detailed in Chapter V using the MBE-grown  $\text{InAs}_{1-x}\text{Sb}_x$  samples on GaSb substrates described in Chapter IV. Tables 4-1 and 4-2 list the structure and composition for the 13 undoped samples. The FTS resolution used for these experiments

was either 4 or 16  $\text{cm}^{-1}$  (0.5 or 2.0 meV). Table 6-1 lists the experimental absorption conditions for each sample studied, including the helitran windows which limited the spectral range (Figure (5-4) and the FTS resolution.

Table 6-1. FTS absorption experimental conditions for MBE-grown  $\text{InAs}_{1-x}\text{Sb}_x$  samples studied. The "p" column indicates the range of exponents obtained for that sample from the fit of the free carrier absorption equation to the data. The " $\alpha_A$ " column indicates the absorption coefficient as given by Eq (6.16).

Sample	x	Helitran Windows	FTS Resolution ( $\text{cm}^{-1}$ )	Background Reference	p	$\alpha_A$ ( $\text{cm}^{-1} \text{eV}^{-1/2}$ )
95-007	0	ZnSe	4	open	2.4-2.7	17,700
93-044	0.031	Sapphire	4	n-GaSb	1.5-3.4	54,000
93-114	0.045	Sapphire	4	n-GaSb	-	-
93-030	0.052	Sapphire	4	p-GaSb	-	29,200
93-113	0.059	Sapphire	4	n-GaSb	-	-
93-112	0.071	Sapphire	4	n-GaSb	2.9-3.5	49,800
93-048	0.077	Sapphire	4	n-GaSb	2.3-3.5	30,300
93-045	0.089	Sapphire	4	n-GaSb	3.4-3.5	25,600
93-068	0.095	ZnSe	16	open	2.4-2.5	15,500
93-092	0.096	Sapphire	4	n-GaSb	1.5-2.5	18,200
93-120	0.097	Sapphire	4	n-GaSb	-	-
94-035	0.179	ZnSe	16	open	3.4-3.5	2,600
93-151	0.192	Sapphire	4	n-GaSb	1.5-2.4	25,400
n-GaSb	n/a	Sapphire	4	n/a	n/a	-
p-GaSb	n/a	Sapphire	4	n/a	n/a	-

Single-beam spectra of the n- and p-GaSb substrates which were used as background references were recorded at the same temperatures as the epitaxial samples. The absorbance was defined in Eq (5.7).  $I_{\text{Background}}$  is the BioRad FTS single-beam spectrum of the substrate or open aperture, whichever was used as the background, and  $I_{\text{Sample}}$  is the single-beam spectrum of the combination of the epitaxial layer and the

substrate on which it was grown. Calculating absorbances of the epitaxial layers using the substrates as the background minimized inclusion of intraband absorption effects from the GaSb substrate in the spectral region of interest (2-6.25  $\mu\text{m}$  or 0.2-0.6 eV).

Five of the 13 samples studied, as indicated in Table 6-1, were referenced against the open aperture rather than the substrate either because a suitable background substrate was not available or because the substrate absorption was recorded under experimental conditions different than those of the epilayer. In any open-aperture case, the substrate added only simple free carrier absorption to the total absorption spectrum.

## **Spectra**

**Samples without AlAsSb cladding layers.** Typical absorbance spectra obtained from the samples without AlAsSb cladding layers are shown in Figure 6-1. The spectra are characterized by a parabolic-shaped band edge and free carrier absorption at energies below the band gap. The absorbance minima are offset from zero due to differences in the polished finishes of the substrate on which the epilayer was grown and the reference substrate; this surface scatter difference appears as additional absorbance in the experiment. The spectra of Figure 6-1 are very representative in behavior of the raw absorption data for all the samples without AlAsSb cladding layers.

**Samples with AlAsSb cladding layers.** Absorption measurements on samples which did include AlAsSb cladding epilayers resulted in an absorbance spectra dominated by an etalon effect between the AlAsSb/GaSb interface and the epilayer

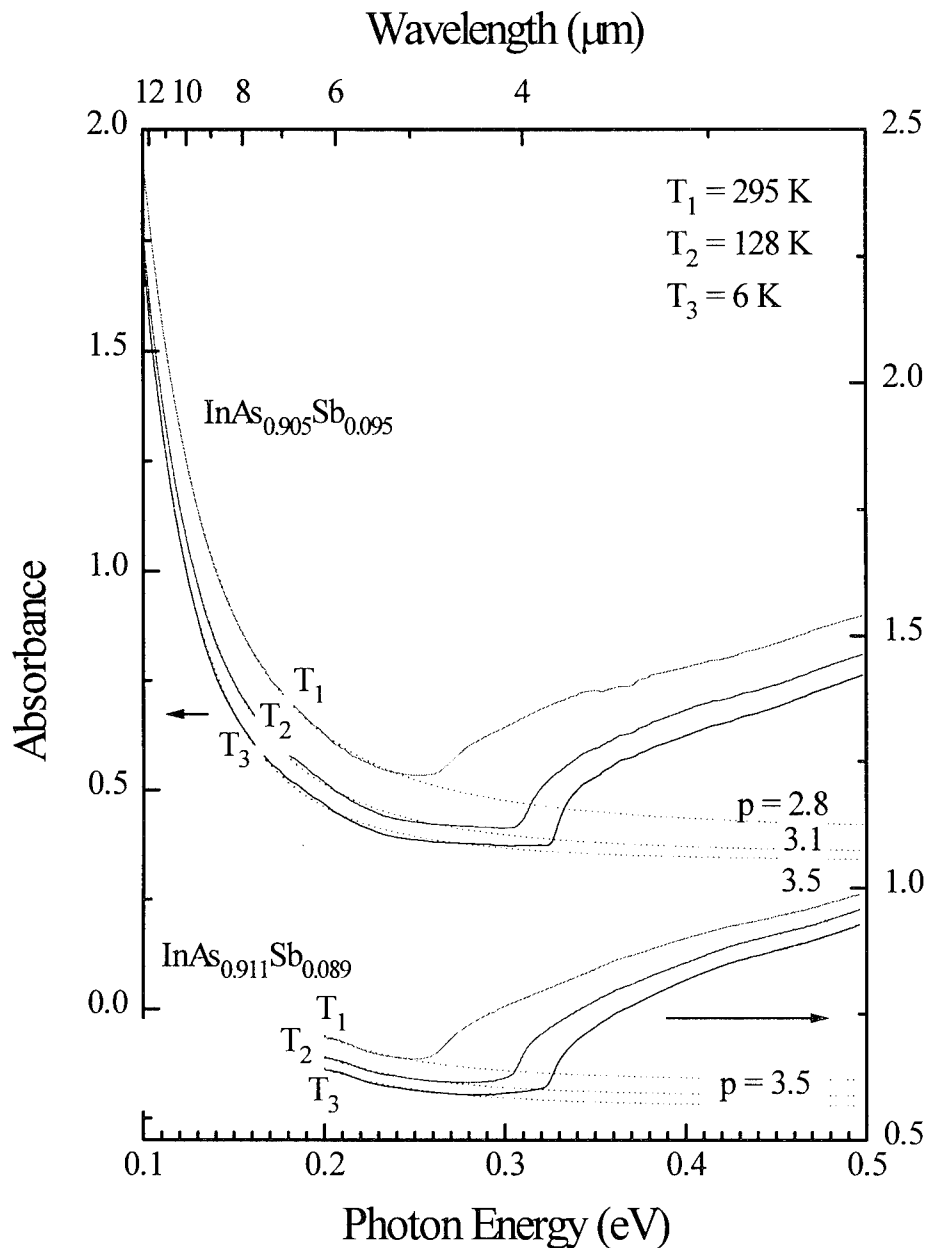


Figure 6-1. Absorbance spectra of MBE-grown  $\text{InAs}_{0.905}\text{Sb}_{0.095}$  and  $\text{InAs}_{0.911}\text{Sb}_{0.089}$  as measured by FTS at three temperatures. The spectral range of sample  $\text{InAs}_{0.905}\text{Sb}_{0.095}$  is set by the FTS optics and ZnSe helitran windows, while that of sample  $\text{InAs}_{0.911}\text{Sb}_{0.089}$  is set by sapphire helitran windows. The dotted lines represent a least squares fit of the free carrier absorption below the band edge with exponent,  $p$ , is indicated. The minimum value is offset from zero by differences in the polished finishes of the sample and background substrates.



surface (Figure 6-2). The  $\text{InAs}_{1-x}\text{Sb}_x$  band edge is less obvious in these spectra and extracting it is less straight forward than from the data of the samples without the AlAsSb layers. Figure 6-2 is very representative in behavior of the raw absorption data for all the samples with AlAsSb cladding layers.

### **Fitting the Data**

**Previous work.** Determining the energy gap position from experimental absorption data is not always straight forward. Because of this, several procedures for assigning the band gap energy have been described in the literature. Two examples follow:

Shah *et al.* were concerned with the absorption edge becoming less steep as the temperature was increased and the difficulty this presented in determining the band gap energy. They assigned the band gap as the midpoint between the threshold energy at which the band edge absorption starts to rise,  $E_0$ , and the energy at the top of the band edge absorption,  $E_1$ , *i.e.*,  $E_g = (E_0 + E_1)/2$  (Shah, 1994:449).

As mentioned in Chapter III, Woolley and Warner reported some of the first absorption experiments on  $\text{InAs}_{1-x}\text{Sb}_x$  in 1964. Their method of assigning the band gap energy for these ternaries was to first perform absorption experiments on the binary endpoint samples, InAs and InSb, in which the band gap energy had been previously established in the literature. They then determined the absorption level in their experiments with the binaries which corresponded to a previously established band gap energy ( $\sim 300 \text{ cm}^{-1}$  in their case). Finally, they assigned the energy gap in the ternary

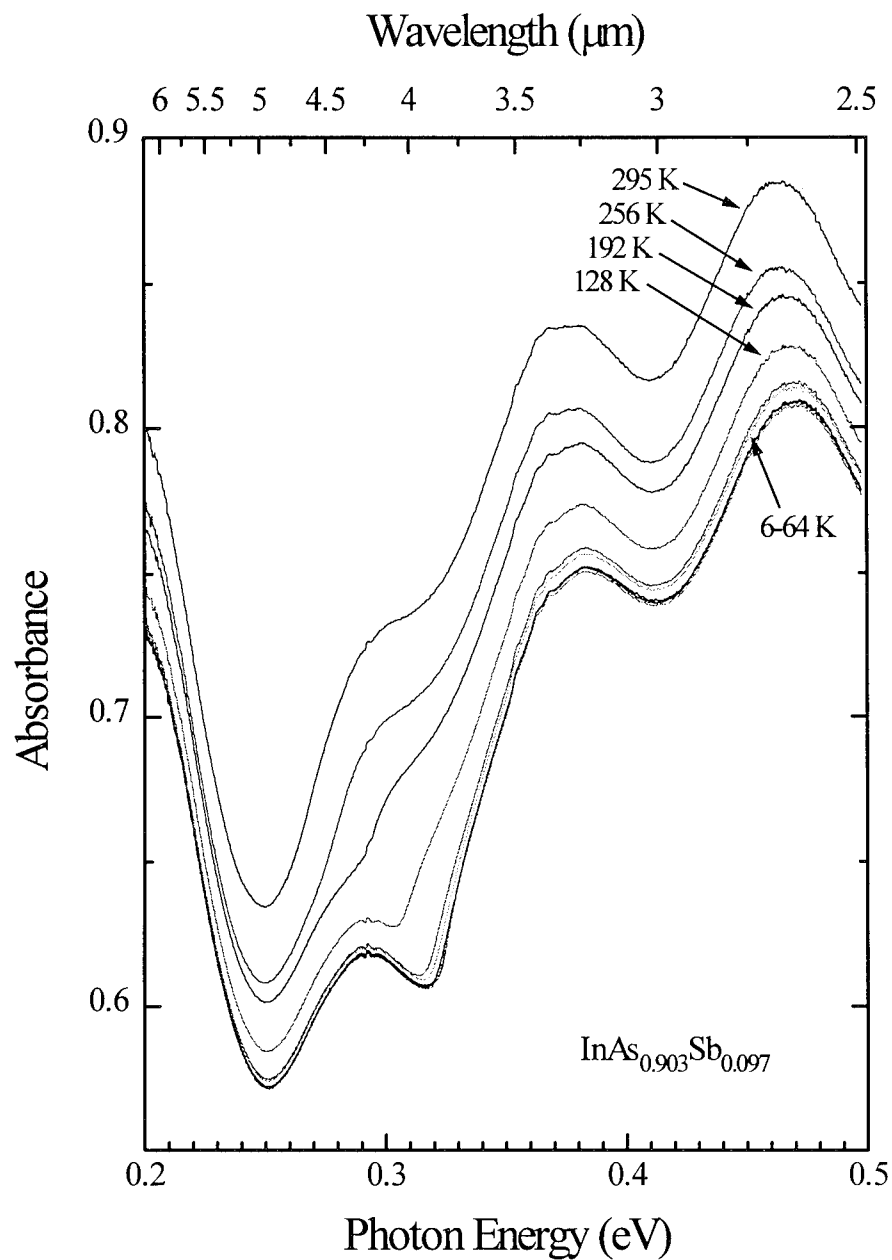


Figure 6-2. Absorbance spectra of an epitaxial  $\text{AlAs}_{0.08}\text{Sb}_{0.92}/\text{InAs}_{0.903}\text{Sb}_{0.097}/\text{AlAs}_{0.08}\text{Sb}_{0.92}$  heterostructure grown on GaSb substrate as measured by Fourier transform spectroscopy (FTS) at several temperatures. The  $\text{InAs}_{0.903}\text{Sb}_{0.097}$  epilayer absorption data is masked by a strong etalon effect occurring between the AlAsSb/GaSb interface and the epilayer surface. The spacing between adjacent etalon fringes for this sample is approximately 80 meV.

samples at the energy where the absorption was equal to this constant absorption level (Woolley, 1964b:1879). Other researchers have also reported this methodology (Stringfellow, 1971:805; Yen, 1987:927).

Fortunately, in the present work, the absorption data measured for the MBE-grown  $\text{InAs}_{1-x}\text{Sb}_x$  samples fit very well to established physical relationships. Therefore, interpretation of the data was performed by fitting the measured results to these established relationships.

**Samples without AlAsSb cladding layers.** Since the individual absorbances are linearly additive, the absorbance from the epitaxial layer alone was determined by subtracting the free carrier and surface scatter absorbances from the total absorbance. The large magnitude of free carrier absorption for the sample at the top of Figure 6-1 is due to absorption by the GaSb substrate. In the samples which were referenced against the substrate (*e.g.*, the lower set of spectra in Figure 6-1), the free carrier absorption was reduced.

The portion of the spectrum below the band edge was fit to an equation of the form,

$$\text{Absorbance}_{\text{Background}}(h\nu) = A + B (h\nu)^{-p} \quad (6.1)$$

where A represents the surface scatter and the remainder of the expression represents the free carrier absorption. The dotted lines in Figure 6-1 show the fits of Eq (6.1) to the data. The values for p obtained for the free carrier absorption fits ranged from 1.5-3.5

depending on the sample, which are within the suggested range (Pankove, 1971:74). The range of  $p$  for each sample is listed in Table 6-1.

The classical formula for free carrier absorption is given by (Pankove, 1971:75):

$$\alpha_f = \frac{Nq^2}{8\pi^2 m^* n c^3 \tau} \lambda^2, \quad (6.2)$$

where  $N$  is the carrier concentration. The intrinsic carrier concentration is expressed as (McKelvey, 1966:266):

$$N_i(T) = 2 \left( \frac{2\pi(m_n m_p)^{1/2} k_B T}{h^2} \right)^{3/2} \exp\left[ \frac{-E_g(T)}{2k_B T} \right], \quad (6.3)$$

where  $T$  is the temperature,  $m_n$  and  $m_p$  are the effective masses of free electrons and holes, respectively, and  $E_g$  is energy gap. The extrinsic carrier concentration,  $n_D(T)$ , *e.g.*, for a donor impurity, is expressed as (McKelvey, 1966:271):

$$n_D(T) = \frac{N_D}{1 + \frac{1}{2} \exp[(E_D - E_F)/k_B T]}, \quad (6.4)$$

where  $N_D$  is the concentration of donor impurity atoms,  $E_D$  is the energy of the donor level and  $E_F$  is the Fermi level. From Eqs (6.2)-(6.4), the temperature dependence of the  $B$  coefficient of Eq (6.1) should be either in the intrinsic form,

$$B_i(T) \propto T^{3/2} \exp\left[ \frac{-E_g(T)}{k_B T} \right], \quad (6.5)$$

or in the extrinsic form,

$$B_D(T) \propto \frac{1}{1 + \frac{1}{2} \exp[(E_D - E_F)/k_B T]}. \quad (6.6)$$

The intrinsic form,  $B_i(T)$ , results in an increase of many orders of magnitude in the B coefficient over the experimental temperature range, 6-295 K. On the other hand, the extrinsic form,  $B_D(T)$ , suggests a sharp increase in the magnitude of the B coefficient at some lower temperature, depending on the donor energy,  $E_D$ , then only a gradual increase beyond this. In the experiments, the B coefficient obtained from the fit of Eq (6.1) to the data increased rather slowly with temperature, and the overall increase never exceeded an order of magnitude, which is indicative of the extrinsic form.

For the samples which were referenced against the open aperture, the majority of the free carrier absorption occurred in the n-GaSb substrate, so the extrinsic form of the B coefficient was expected. However, for the samples which were referenced against a piece of the substrate, the free carrier absorption should have occurred in the epitaxial material, which was expected to be intrinsic. Since the B coefficient for these samples was in the extrinsic form, as well, the existence of native or unintentional defect and impurity levels in this material is possible.

The background fits using Eq (6.1) were subtracted from the original spectra. A typical set of  $\text{InAs}_{1-x}\text{Sb}_x$  epilayer absorbance spectra which remained after this subtraction is shown in Figure 6-3. The spectra in Figure 6-3 were derived from the  $\text{InAs}_{0.911}\text{Sb}_{0.089}$  epilayer sample shown at the bottom of Figure 6-1. The  $\text{InAs}_{1-x}\text{Sb}_x$

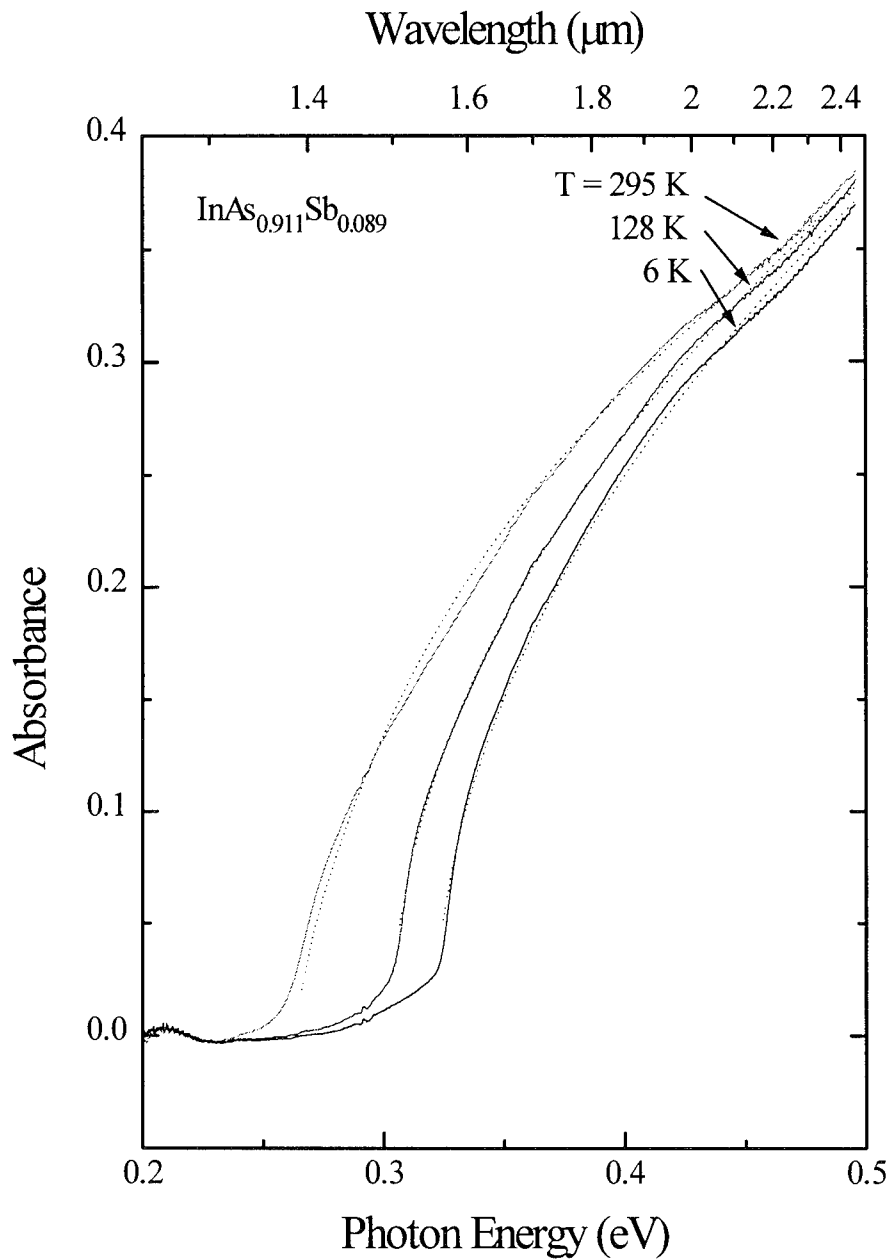


Figure 6-3. Absorbance spectra for epitaxial  $\text{InAs}_{0.911}\text{Sb}_{0.089}$  obtained from spectra of Figure 6-1 by removing free carrier and surface scatter absorbances. Dotted lines represent the least squares fit of the absorbance to a non-excitonic, band-to-band absorption form which includes density of states and carrier distribution considerations for each band.

epilayer absorbance spectra for all 9 samples without AlAsSb cladding layers are very similar in behavior to those shown for one sample in Figure 6-3.

The functionality of band-to-band, non-excitonic absorption is determined by the density of states and carrier occupation probability of each band. Assuming only direct transitions between parabolic bands, the joint density of states has the form,

$$g(h\nu) d(h\nu) = \frac{(2 m_r)^{3/2}}{2\pi^2 \hbar^3} (h\nu - E_g)^{1/2} d(h\nu), \quad (6.7)$$

where  $h\nu$  is the transition energy ( $h\nu = E_c - E_v$ ),  $E_g$  is the gap energy and  $m_r$  is the reduced effective mass. The absorbance then takes the form,

$$\text{Absorbance}(h\nu) \propto (h\nu - E_g)^{1/2} [1 - f_n(E_c)] f_p(E_v), \quad (6.8)$$

where  $f_n(E_c)$  and  $f_p(E_v)$  are the electron occupation probabilities of the conduction and valence bands, respectively. If the Fermi energy lies within the energy gap and several  $k_B T$  away from the band edges, then  $f_n(E_c) \cong 0$  and  $f_p(E_v) \cong 1$ . Therefore, the spectra were fit with an equation of the form,

$$\text{Absorbance}(h\nu) = A (h\nu - E_g)^{1/2}. \quad (6.9)$$

The validity of this equation assumes the occupation probability of electrons in the conduction band and holes in the valence band is nearly zero. This condition can be violated under high temperature conditions, and the high-temperature parabolic fits reflected this. When the Fermi energy level is within the energy gap but an appreciable

portion of the exponential tail of the carrier distribution function is inside either band, the Boltzmann approximation of the occupation probabilities can be used. Therefore, at temperatures approaching room temperature where the simple parabolic fit broke down, the spectra were fit with an equation in a form that includes a Boltzmann-like absorption probability:

$$\text{Absorbance}(h\nu) = A \sqrt{h\nu - E_g} \left\{ 1 - B \exp\left[-\frac{(h\nu - E_g)}{k_B T}\right] \right\}. \quad (6.10)$$

This fit is consistent with Urbach's rule, *i.e.*, the slope of  $\ln(\alpha)$ , where  $\alpha$  is the absorption coefficient, as a function of energy at the absorption edge is  $\sim 1/k_B T$  for many intrinsic semiconductors (Urbach, 1953:1324). Examples of the fits of Eqs (6.9) and (6.10) to the spectra are shown as dotted lines in Figure 6-3.

The absorption coefficient,  $\alpha$ , may be extracted from the experimental absorbance data. If surface reflection in the experiment is not considered, then:

$$\alpha = \frac{\text{Absorbance}}{d \log e}, \quad (6.11)$$

where  $d$  is the sample thickness. However, if surface reflection is considered,  $\alpha$  is related to absorbance by:

$$\alpha = \frac{\ln[(1 - R_f)(1 - R_b)] + \text{Absorbance} \ln 10}{d}, \quad (6.12)$$



where  $R_f$  and  $R_b$  are the reflectances for the front and back surfaces (Pankove, 1971:93) given by:

$$R = \left( \frac{n - 1}{n + 1} \right)^2 \quad (6.13)$$

where  $n$  is the index of the material and the index of air is taken to be unity.

The indices for the  $\text{InAs}_{1-x}\text{Sb}_x$  ternaries are not well known. However, for the purpose of these calculations, the indices used for the ternaries were:

$$n_{\text{InAsSb}} = 3.87 \quad (6.14a)$$

$$n_{\text{AlAsSb}} = 3.17 \quad (6.14b)$$

as interpolated from those of the binaries ( $n_{\text{InAs}} = 3.714$ ,  $n_{\text{InSb}} = 5.26$ ,  $n_{\text{AlAs}} = 3.03$  and  $n_{\text{AlSb}} = 3.182$  (Madelung, 1991:79)) for compositions of  $\text{InAs}_{0.9}\text{Sb}_{0.1}$  and  $\text{AlAs}_{0.08}\text{Sb}_{0.92}$ , and are considered dispersionless over the range of wavelengths at which the absorption experiment was conducted. The refractive index of GaSb is:

$$n_{\text{GaSb}} \cong 4.39 \quad (6.15)$$

(Madelung, 1991:120). The reflectance for the epilayer/substrate interface was not included in Eq (6.12) since it is very small,  $\sim 0.004$  using Eqs (6.14 (a)) and (6.15).

For these current experiments, Eq (6.11) should apply to those cases when the substrate was used as the background reference since the front surface reflectance,  $R_f$ , is approximately equal for the epilayer and the GaSb substrate ( $R_{\text{Air/InAsSb}} \cong 0.35$  and  $R_{\text{Air/GaSb}} \cong 0.40$  using Eqs (6.14 (a)) and (6.15)), and the rear reflectance,  $R_b$ , has already

been included by referencing the sample against the substrate. Eq (6.12) is applicable for those cases when the open aperture was used as the background reference.

Since the absorbances are in the form of Eq (6.9), the absorption coefficient also takes the form:

$$\alpha(h\nu) = \alpha_A (h\nu - E_g)^{1/2}. \quad (6.16)$$

The coefficient,  $\alpha_A$ , calculated from the low temperature absorbance data is listed for each sample in Table 6-1. Absorption coefficient values for  $\text{InAs}_{1-x}\text{Sb}_x$  compositions are not available in the literature. However, the room temperature absorption coefficient of InAs was reported by Dixon and Ellis in 1961 (Dixon, 1961:1560). As a comparison, the absorption coefficients they reported for 2.5  $\mu\text{m}$  radiation, the short wavelength limit of the spectral range of this current absorption experiment, ranged from 300-7,000  $\text{cm}^{-1}$ , depending on the carrier concentration. The absorption coefficient for 2.5  $\mu\text{m}$  radiation calculated from the value in Table 6-1 for InAs is  $\sim 5,100 \text{ cm}^{-1}$ , showing good agreement with the published values.

**Samples with AlAsSb cladding layers.** Absorption measurements on samples which included AlAsSb cladding epilayers resulted in absorbance spectra dominated by an etalon effect between the AlAsSb/GaSb interface and the epilayer surface as shown above in Figure 6-2. A Fabry-Perot etalon is a multiple beam interferometer which consists of two parallel, reflecting planar surfaces separated by a distance,  $d$ , as depicted in Figure 6-4 (a). Light entering the etalon is multiply reflected within the cavity so that

rays exiting on successive reflections interfere either constructively or destructively, depending on their frequency and the planar separation,  $d$ . The frequency separation of the adjacent constructive modes, as depicted in Figure 6-4 (b), is given by:

$$\nu_{\text{FP}} = \frac{c}{2n_2d}, \quad (6.17)$$

where  $c$  is the speed of light and  $n_2$  is the refractive index within the cavity. The spectral half width of the resonator mode, also depicted in Figure 6-4 (b), is given as a fraction of the separation between adjacent modes as:

$$\gamma_{\text{FP}} = \frac{2}{\pi\sqrt{F}}, \quad (6.18)$$

where  $F$  is the coefficient of finesse of the cavity:

$$F = \left(\frac{2\sqrt{R}}{1-R}\right)^2, \quad (6.19)$$

and  $R$  is the reflectance of the cavity for normal incidence when the separation,  $d$ , is equal to an odd integer number of quarter wavelengths (*i.e.*, constructive interference upon transmission):

$$R = \left(\frac{n_1n_3 - n_2^2}{n_1n_3 + n_2^2}\right)^2. \quad (6.20)$$

Here,  $n_1$ ,  $n_2$  and  $n_3$  are the refractive indices of each region as shown in Figure 6-4 (a).

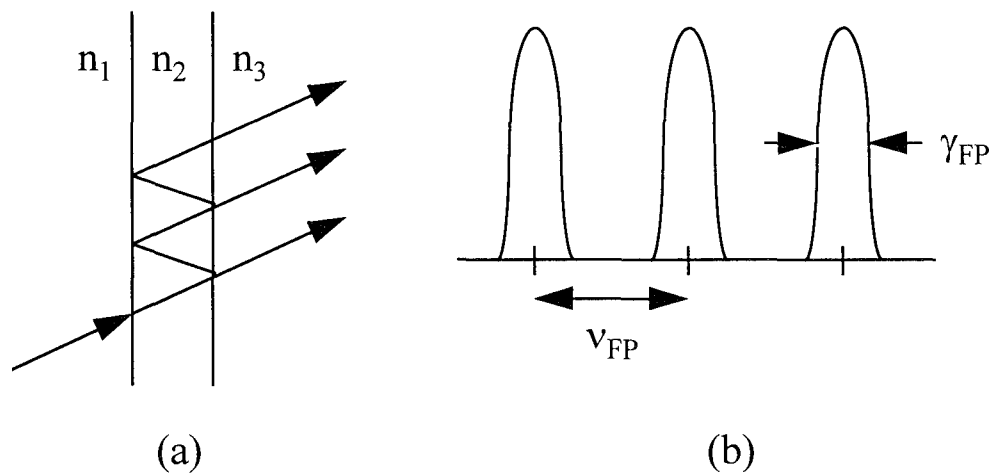


Figure 6-4. (a) The Fabry-Perot etalon and (b) resulting interference fringes.

Analyses using Eqs (6.17)-(6.20) indicate the etalon occurred between the AlAsSb/GaSb interface and the InAs<sub>1-x</sub>Sb<sub>x</sub> epilayer surface in these samples. It did not occur for the samples without the AlAsSb epilayer because the refractive index difference between the InAs<sub>1-x</sub>Sb<sub>x</sub> and the GaSb substrate is small. Eqs (6.17) and (6.20) become:

$$v_{FP} = \frac{c}{2n_{eff}d_{eff}} \quad (6.21)$$

and

$$R = \left( \frac{n_{air}n_{GaSb} - n_{eff}^2}{n_{air}n_{GaSb} + n_{eff}^2} \right)^2, \quad (6.22)$$

respectively, where  $n_{\text{eff}}$  is given by the thicknesses and indices of the InAsSb and AlAsSb epilayers as:

$$n_{\text{eff}} = \frac{d_{\text{InAsSb}} n_{\text{InAsSb}} + d_{\text{AlAsSb}} n_{\text{AlAsSb}}}{d_{\text{eff}}} \quad (6.23)$$

and  $d_{\text{eff}}$  is the sum of the epilayer thicknesses (as given in Table 4-1).

A comparison of the  $v_{\text{FP}}$  and  $\gamma_{\text{FP}}$  values measured experimentally, and those calculated using Eqs (6.18), (6.19), (6.21) and (6.22) are given in Table 6-2. As shown in Figure 6-2, the etalon peaks are not sharp and clearly separated; rather, they are quite broad, giving the spectrum a sinusoidal appearance. This indicates  $\gamma_{\text{FP}}$  is approximately 0.5 for these samples. The numbers calculated for  $\gamma_{\text{FP}}$  and given in Table 6-2 agree favorably with this.

Table 6-2. Comparison of measured and calculated Fabry-Perot interference fringe spacings,  $v_{\text{FP}}$  and  $hc/2n_{\text{eff}}d_{\text{eff}}$ , respectively, and fringe half widths,  $\gamma_{\text{FP}}$ . The measured  $\gamma_{\text{FP}}$  are approximately 0.5.

Sample	x	$d_{\text{eff}}$ ( $\mu\text{m}$ )	$n_{\text{eff}}$	Measured $h\nu_{\text{FP}}$ (meV)	$hc/2n_{\text{eff}}d_{\text{eff}}$ (meV)	Calculated $\gamma_{\text{FP}}$
93-114	0.045	1.63	3.49	120	110	0.5
93-113	0.059	2.16	3.39	90	90	0.6
93-112	0.071	1.89	3.55	110	90	0.5
93-120	0.097	1.98	3.31	80	90	0.6

The band edge in the samples having AlAsSb layers was determined by referencing an absorption spectrum at one temperature against another spectrum from the same sample at a different temperature. Figure 6-5 shows this technique schematically

using two simplified absorption spectra. Spectrum “a” represents an absorption spectrum for a sample at high temperature. Spectrum “b” represents an absorption spectrum for the same sample at a lower temperature. Thus, the band edge of spectrum “b” is at a higher energy than that of spectrum “a.” When the difference between the two spectra is taken, spectrum “a-b” in Figure 6-5, the band edge positions of both spectra “a” and “b” are maintained. Also, if the backgrounds of the individual spectra are comparable, the shape of spectrum “a” above the band edge is maintained up to the band edge position of spectrum “b.”

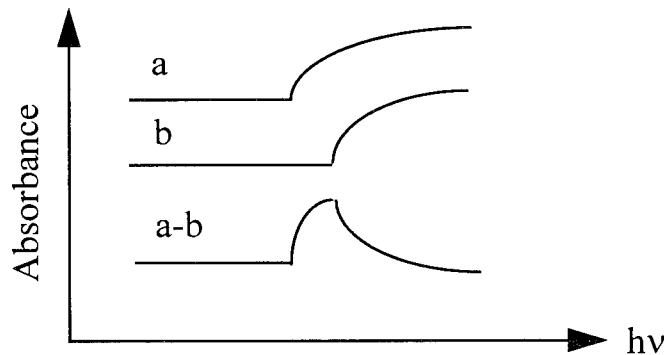


Figure 6-5. Depiction of self-referencing technique. a and b represent two spectra at different temperatures; thus, the band edge has moved. When one is subtracted from the other, information about both band edges is maintained in the difference spectrum.

In the experimental case, the absorption data is superimposed on the large etalon background, but the technique is the same. The implicit assumption in this procedure is that the etalon effect is relatively unchanged between the two temperatures. Figure 6-6 shows the how the etalon background has been subtracted out leaving a difference

spectrum similar to that in Figure 6-5. In Figure 6-6, the 6 K spectrum was used as the reference. The band edge of the 6 K spectrum is the top point of all the spectra in Figure 6-6. The absorption spectra for the other temperatures are now apparent for energies below the 6 K band edge. From these difference spectra, the energy gaps at each temperature were assigned using Eq (6.9) in a manner similar to that used for the samples without the AlAsSb epilayer. The resulting absorbance spectra for all the samples that included AlAsSb cladding layers and were reduced in this manner were very similar to those shown for the one sample in Figure 6-6.

### **Temperature Dependence of the Energy Gap**

The primary reason for doing these absorption experiments was to determine the energy gap for these MBE-grown  $\text{InAs}_{1-x}\text{Sb}_x/\text{GaSb}$  samples. To this end, the energy gap values for each composition at several temperatures between 6-295 K were determined from the absorption data as described above. Figure 6-7 shows the behavior of the energy gap as a function of temperature for five of the samples. Only five were included here for clarity of the figure. However, the temperature-dependent behavior of the eight samples not shown in Figure 6-7 was very similar.

The temperature dependence of the experimental energy gaps,  $E_g(T)$ , was determined for each composition using the semi-empirical Varshni equation (Varshni, 1967:149). Several empirical relationships for  $E_g(T)$  can be found in the literature (Logothetidis, 1991:11950; O'Donnell, 1991:2924), but the Varshni equation is most

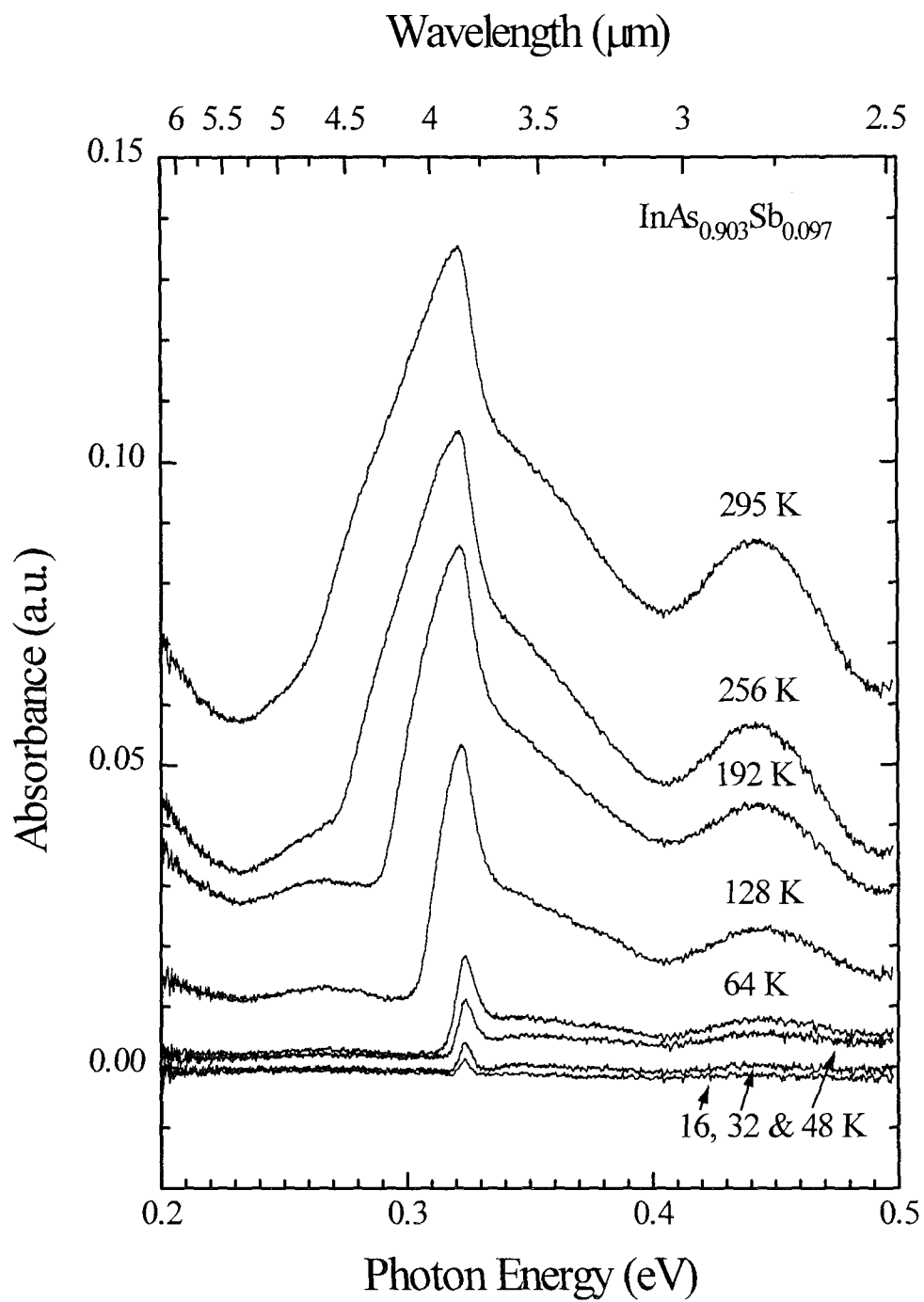


Figure 6-6. Absorbance spectra for epitaxial  $\text{InAs}_{0.903}\text{Sb}_{0.097}$  obtained from spectra of Figure 6-2 by referencing each against the 6 K spectrum.



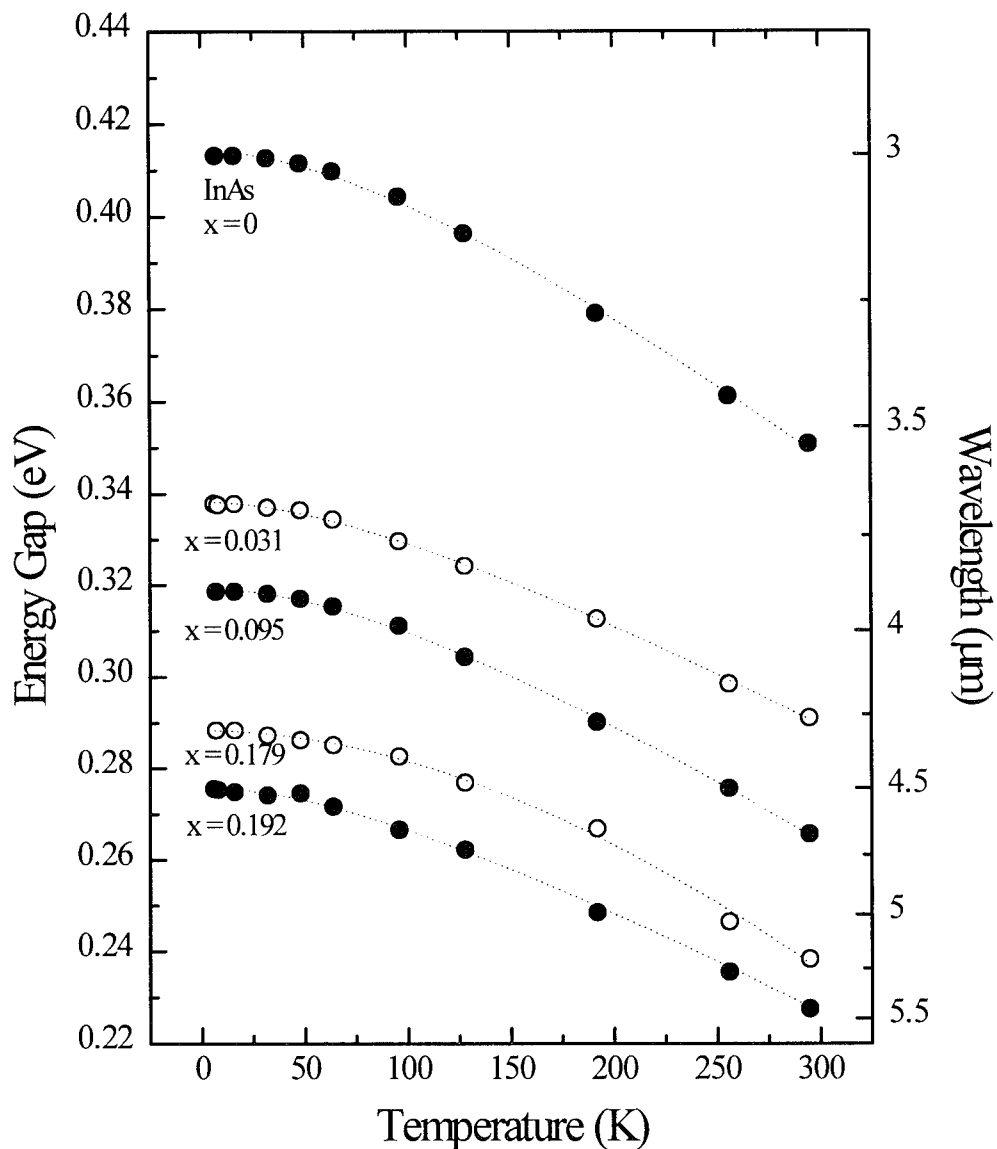


Figure 6-7. Temperature-dependence of the energy gap for five of the 13 epitaxial  $\text{InAs}_{1-x}\text{Sb}_x$  samples measured. The dashed lines are the least squares fit of the Varshni equation to the data. The error associated with each data point was determined by the absorption spectrometer resolution to be 0.5 meV for the  $\text{InAs}$ ,  $\text{InAs}_{0.969}\text{Sb}_{0.031}$  and  $\text{InAs}_{0.808}\text{Sb}_{0.192}$  samples, and 2.0 meV for the  $\text{InAs}_{0.905}\text{Sb}_{0.095}$  and  $\text{InAs}_{0.821}\text{Sb}_{0.179}$  samples. The other eight samples fit as well to the Varshni equation but are excluded here for clarity.

commonly used and has been shown to be representative of the temperature dependencies of the energy gaps for many semiconductors. It is given by:

$$E_g(T) = E_g(0) - \frac{\alpha T^2}{T + \beta} \quad (6.24)$$

where  $E_g(0)$  is the energy gap at 0 K,  $\alpha$  is a fitting parameter with units eV/K, and  $\beta$  is another fitting parameter with units of K. It is shown in Figure 6-7 that  $E_g(T)$  is essentially linear above some temperature. Since lattice vibrations and thermal expansion of the crystal lattice are the two main sources of the temperature dependence of the energy gap,  $\beta$  is related to the Debye temperature or the temperature at which vibrational modes of the crystal begin to be excited, thus influencing the linear and nonlinear portions of the curve.

Typical fits of Eq (6.24) are shown as dotted lines in Figure 6-7. It is shown by these fits that the Varshni equation is representative of  $E_g(T)$  for these samples, as well. The  $E_g(0)$ ,  $\alpha$  and  $\beta$  parameters which resulted from these fits for all the samples studied are tabulated in Table 6-3.

The energy gap values obtained for the InAs epilayer sample (top curve in Figure 6-7) are in agreement with the accepted InAs values found in the literature (Madelung, 1991:134). This agreement is a good corroboration of the methodology used to determine the energy gap for the ternary  $\text{InAs}_{1-x}\text{Sb}_x$  samples.

Table 6-3. Varshni parameters for the temperature-dependence of the energy gap of MBE-grown  $\text{InAs}_{1-x}\text{Sb}_x$  as determined by a least squares fit to the experimental data.

Sample	$\Delta a/a$ (%)	x	$E_g(0)$ (eV)	$\alpha$ ( $\times 10^{-4}$ eV/K)	$\beta$ (K)
95-007	-0.617	0	0.4143	3.8	215
93-044	-0.401	0.031	0.3382	2.6	180
93-114	-0.305	0.045	0.3357	3.3	205
93-030	-0.261	0.052	0.3370	8.2	1080
93-113	-0.212	0.059	0.3311	3.3	246
93-112	-0.123	0.071	0.3239	4.7	523
93-048	-0.083	0.077	0.3246	4.5	376
93-045	0	0.089	0.3216	2.6	113
93-068	+0.042	0.095	0.3193	3.3	236
93-092	+0.048	0.096	0.3210	4.8	431
93-120	+0.056	0.097	0.3194	13	1670
94-035	+0.623	0.179	0.2883	8.4	1140
93-151	+0.708	0.192	0.2758	2.6	177

### Compositional Dependence of the Energy Gap: Low Temperatures

Along with the temperature dependence of the energy gap for these MBE-grown  $\text{InAs}_{1-x}\text{Sb}_x$  samples, the compositional dependence of the energy gap at any fixed temperature can be assessed from the absorption data. The very low temperature range, *i.e.*,  $<2$  K, is important since many of the photoluminescence (PL) measurements made on these samples and reported in Chapter VII were performed there. It was shown above that the Varshni equation fit the experimental data very well. Therefore, the compositional dependence of the low temperature energy gaps will be studied using the Varshni parameter,  $E_g(0)$ , obtained from each sample.

The  $E_g(0)$  values are shown as a function of composition as solid round symbols in Figure 6-8. There are few reports of the measurement of the low temperature energy

gap for  $\text{InAs}_{1-x}\text{Sb}_x$  in the literature (see Chapter III, InAsSb Material Characterization), but four are also shown by the other symbols in Figure 6-8. An initial comparison of these current  $E_g(0)$  values from the 13 MBE-grown  $\text{InAs}_{1-x}\text{Sb}_x$  samples and those previously reported shows that the current values are at lower energies for similar compositions. For example, the  $E_g(0)$  value measured here is 15-60 meV lower than those previously reported at the lattice-matched composition,  $x = 0.089$ . Since this difference exists, an examination of the experimental techniques used to obtain the previously reported low temperature energy gap results is in order to attempt to explain this difference.

The energy gap of  $\text{InAs}_{1-x}\text{Sb}_x$  was first measured using infrared transmission at temperatures greater than 90 K on bulk-grown, polycrystalline material (Woolley, 1964b:1879) as described in Chapter III, InAsSb Material Characterization. Since the energy gap results for each composition had a linear temperature dependence between 90-360 K as shown by the solid symbols in Figure 6-9, the values for  $E_g(0)$  were linearly extrapolated from this data as shown by the dotted lines in Figure 6-9. Also shown by the open symbols in Figure 6-9 are the energy gap values obtained from some of the MBE-grown  $\text{InAs}_{1-x}\text{Sb}_x$  samples studied here. This current data not only shows the linear temperature dependence at higher temperatures, but also shows the nonlinear behavior at lower temperatures which reduces the energy gap values well below those which a linear extrapolation would produce. The failure of these early researchers to consider the nonlinearity of the temperature dependence of the energy gap at low temperatures artificially increases their  $E_g(0)$  values by approximately 30 meV. Thus, the difference

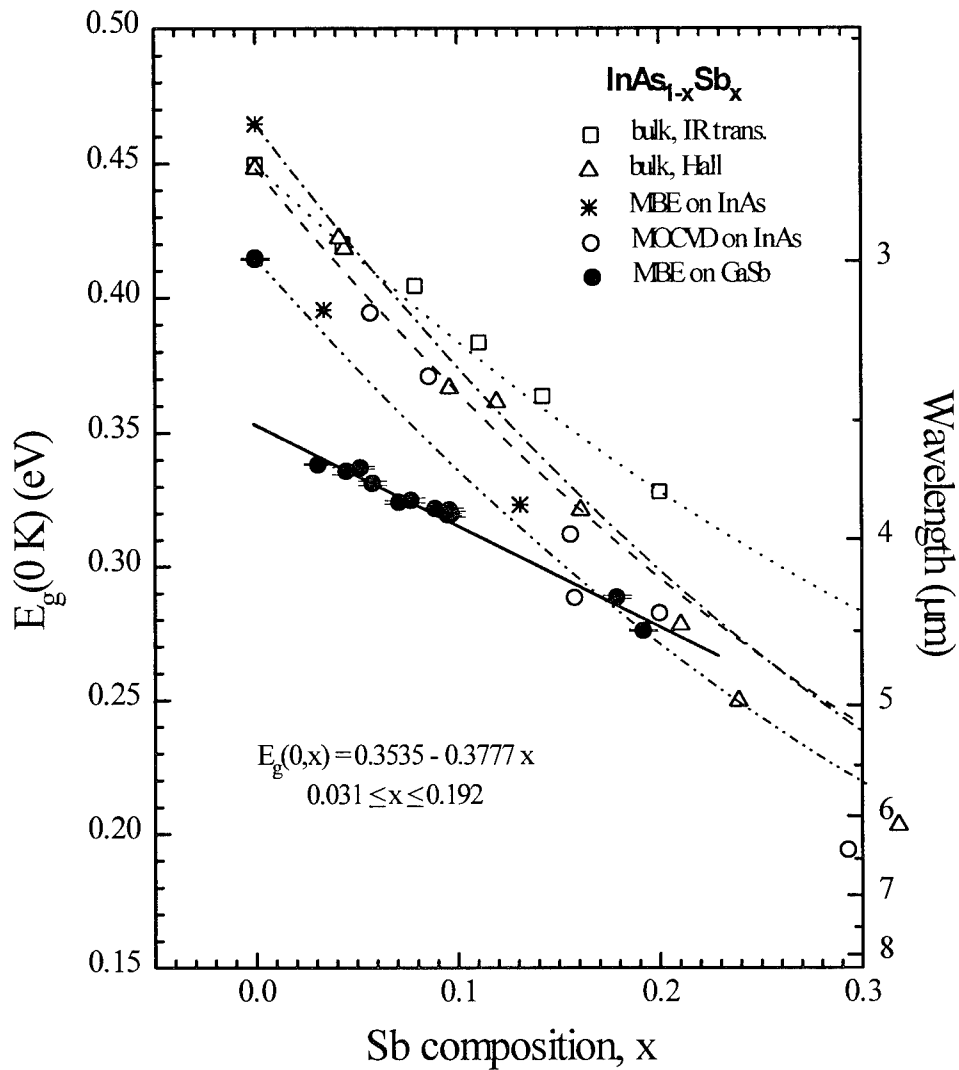


Figure 6-8. Least squares linear fit of the compositional dependence of the energy gap at 0 K ( $E_g(0\text{ K})$ ) for MBE-grown InAsSb samples on GaSb substrate ( $\bullet$ , solid line), compared to other low temperature  $E_g(x)$  relationships reported previously:  $\square$ , dotted line (Woolley, 1964b:1879);  $\Delta$ , dashed line (Coderre, 1968:1207);  $*$ , dash-dot line (Yen, 1988a:489); and  $\circ$ , dash-double dot line (Fang, 1990:7034). The error in determining the  $E_g(0)$  parameter from the fit of the Varshni equation to the temperature-dependent data is shown for each composition.

between the data represented by the open square symbols in Figure 6-8 and the  $E_g(0)$  values from this current study may be partially explained by the analysis technique used.

Similarly, the  $E_g(0)$  values represented by the open upward triangles in Figure 6-8 were also linearly extrapolated from Hall coefficient measurements at temperatures between 123 and 773 K (Coderre, 1968:1207) (see Chapter III, InAsSb Material Characterization). Once again, a linear extrapolation from the higher temperature data increased the reported  $E_g(0)$  well above actual levels.

The open downward triangular symbols in Figure 6-8 represent the peak energy positions from PL experiments performed at a lattice temperature of 10 K on  $\text{InAs}_{1-x}\text{Sb}_x$  ( $x < 0.3$ ) grown by metal-organic chemical vapor deposition (MOCVD) on (100) InAs substrates (Fang, 1990:7034). Since the PL peak position may be  $k_B T_e/2$  to  $2k_B T_e$  above the band gap for band-to-band transitions, where  $T_e$  is the effective carrier temperature which is close to the lattice temperature (10 K) only under very low excitation conditions, these peak positions may be above the actual band gap by a significant amount depending on the laser excitation intensity used. Also, Fang's PL peak positions for the  $\text{InAs}_{0.8}\text{Sb}_{0.2}$  sample over a range of temperatures are shown as open upward triangles in Figure 6-10, along with the PL peaks from the currently studied MBE-grown  $\text{InAs}_{0.808}\text{Sb}_{0.192}$  sample, shown as solid squares, and the energy gap values of this sample as measured by absorption, shown as solid dots. Fang determined the energy gap position from his PL data by subtracting  $2k_B T$  from the PL peak position as shown by the open downward triangles in Figure 6-10. Although the PL peak positions for the two samples agree reasonably well with one another, Fang's method of determining the energy gap results in

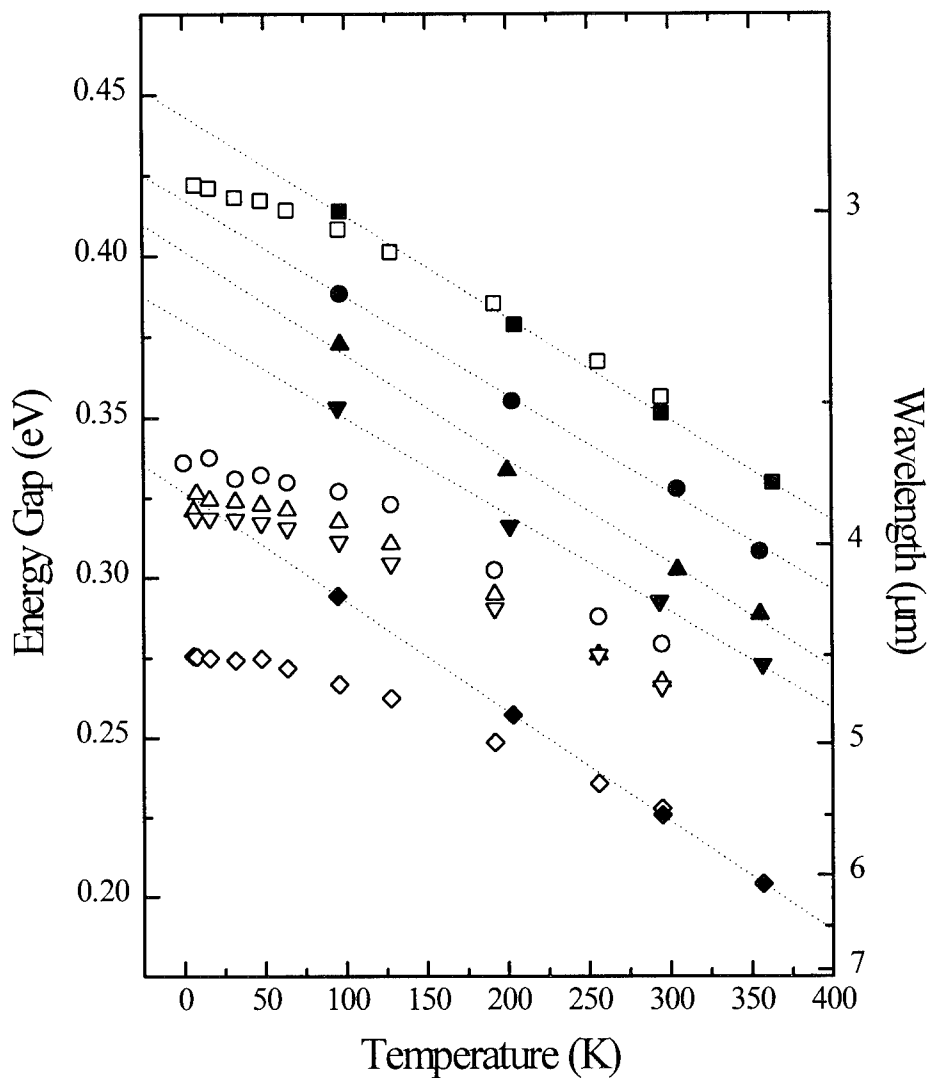


Figure 6-9. Comparison of Woolley and Warner's temperature-dependent energy gap results for bulk, polycrystalline  $\text{InAs}_{1-x}\text{Sb}_x$  to the current results for MBE-grown  $\text{InAs}_{1-x}\text{Sb}_x$  on GaSb substrate. The solid symbols represent the bulk data; the open symbols the current data:  $\blacksquare$  -  $\text{InAs}$ ;  $\square$  -  $\text{InAs}$ ;  $\bullet$  -  $\text{InAs}_{0.96}\text{Sb}_{0.04}$ ;  $\circ$  -  $\text{InAs}_{0.955}\text{Sb}_{0.045}$ ;  $\blacktriangle$  -  $\text{InAs}_{0.92}\text{Sb}_{0.08}$ ;  $\triangle$  -  $\text{InAs}_{0.923}\text{Sb}_{0.077}$ ;  $\blacktriangledown$  -  $\text{InAs}_{0.89}\text{Sb}_{0.11}$ ;  $\triangledown$  -  $\text{InAs}_{0.905}\text{Sb}_{0.095}$ ;  $\blacklozenge$  -  $\text{InAs}_{0.80}\text{Sb}_{0.20}$ ; and  $\diamond$  -  $\text{InAs}_{0.809}\text{Sb}_{0.191}$ . The dotted lines represent the linear extrapolations of the bulk data to lower temperatures.

a linear  $E_g(T)$ , even to low temperatures. This indicates there may be a problem in assigning the energy gap from PL data in this manner.

The star symbols in Figure 6-8 also represent PL peak positions performed at a lattice temperature of 10 K, but on  $\text{InAs}_{1-x}\text{Sb}_x$  ( $0 < x < 1$ ) grown by MBE on (100) InAs substrates (Yen, 1988a:489). Once again, the PL peak position for band-to-band transitions is above the actual energy gap position by some amount depending on the laser excitation intensity used, and the accuracy of assigning the energy gap from PL data is unclear.

Since the energy gap values for ternary III-V semiconductors of the form  $\text{AB}_{1-x}\text{C}_x$  are rarely given by a linear interpolation with respect to composition between those of the binary constituents, AB and AC, the most common form of the compositional dependence of the energy gap for ternaries is a second order polynomial such as:

$$E_g(x) = E_g(1)x + b(1-x)x + E_g(0)(1-x). \quad (6.25)$$

The coefficient,  $b$ , is known as the “bowing parameter” and represents the magnitude of the deviation from linearity.

The  $E_g(0)$  values for the currently studied MBE-grown  $\text{InAs}_{1-x}\text{Sb}_x$  samples were fit to an equation of the form of Eq (6.25) as shown by the solid line in Figure 6-11. The standard method of obtaining a bowing parameter for ternary alloys is to fix the energy gap values for the binary endpoints, with the assumption that the highest confidence is in these values, then to fit the second order polynomial to the ternary data. This method was used here. The  $E_g(0)$  value for the InAs endpoint was 0.4143 eV taken from the data,



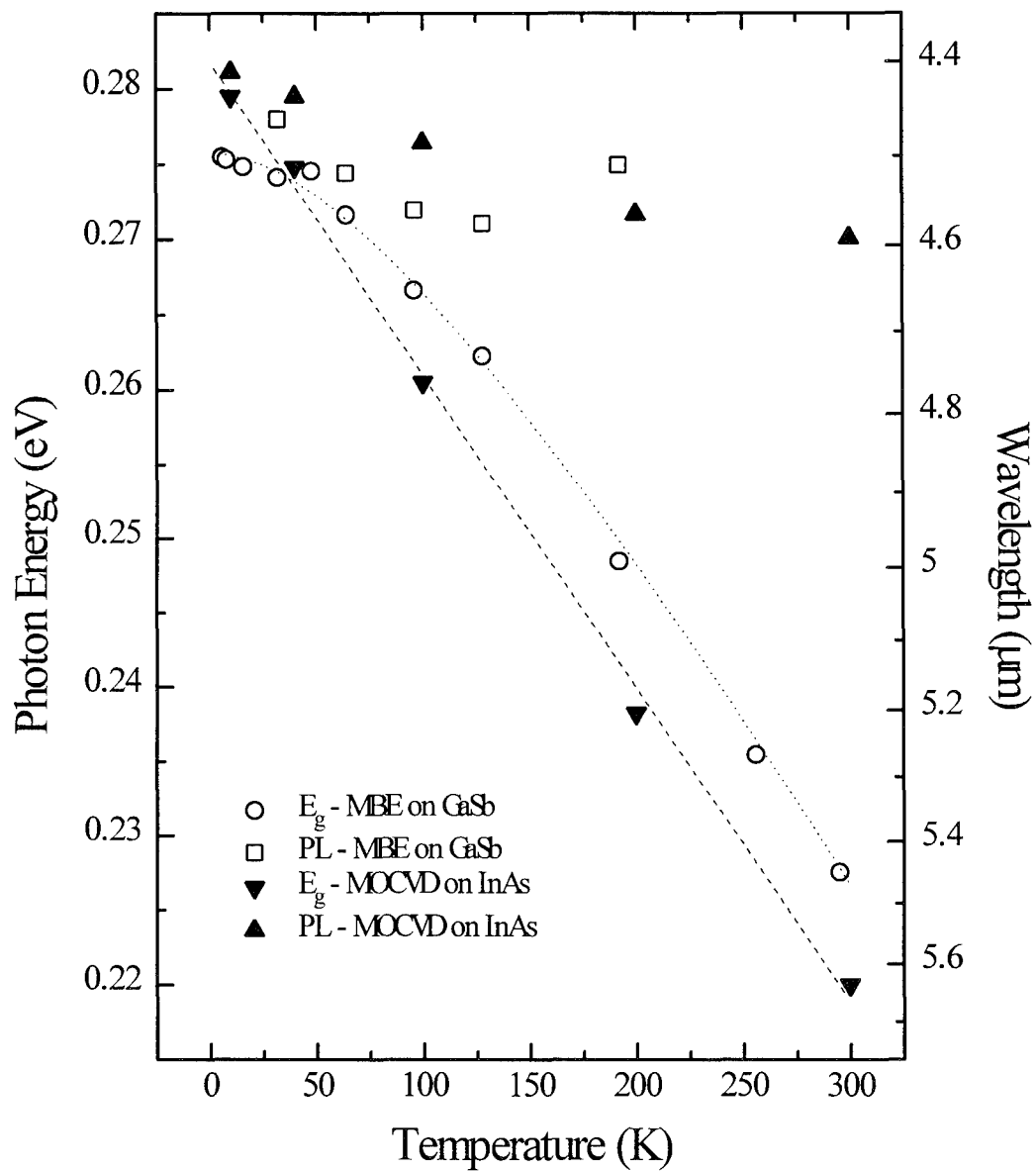


Figure 6-10. Comparisons of PL peak positions for previously reported  $\text{InAs}_{0.8}\text{Sb}_{0.2}$  (▲) (Fang, 1990:7034) and the currently studied  $\text{InAs}_{0.808}\text{Sb}_{0.192}$  sample (□), and the energy gap assignments made from the  $\text{InAs}_{0.8}\text{Sb}_{0.2}$  PL data (▼, dashed line) and FTS absorption experiments on the currently studied sample (○, dotted line).

while that for the InSb endpoint was obtained from the literature to be 0.2352 eV (Madelung, 1991:142). The low temperature bowing parameter obtained in this fashion was

$$b_{\text{InAsSb}} = 858 \text{ meV}. \quad (6.26)$$

The previously reported low temperature energy gap values shown on Figure 6-8 are also shown on Figure 6-11 for the entire  $\text{InAs}_{1-x}\text{Sb}_x$  composition range. The bowing parameters obtained from these results are listed in the legend of Figure 6-11. The value of 858 meV for these currently studied MBE-grown samples is 14% higher than any of the four previously reported values ( $b_{\text{Woolley}} = 515 \text{ meV}$ ,  $b_{\text{Corderre}} = 706 \text{ meV}$ ,  $b_{\text{Yen}} = 751 \text{ meV}$ , and  $b_{\text{Fang}} = 672 \text{ meV}$ ), and results in minimum energy gap values at  $x \cong 0.6$  which are  $> 40 \text{ meV}$  lower than any of the other four.

However, another data point from the literature, shown by the open circular symbol in Figure 6-11, agrees very well with this polynomial fit obtained for the currently studied material. This data point was reported for  $\text{InAs}_{0.6}\text{Sb}_{0.4}$  grown by MBE on GaSb with a growth temperature of 425 °C (Kurtz, 1992:1909) which is similar to the 430-489 °C growth temperatures for these current MBE-grown samples (see Table 4-1). The polynomial fit of Eqs (6.25) and (6.26) results in a value of 0.137 eV for the 40% Sb composition, while Kurtz' value for this composition measured at 15 K was 0.132 eV.

Cu-Pt ordering was observed in Kurtz' sample as discussed in Chapter IV, Molecular Beam Epitaxial Growth. Because MBE growth temperatures affect the degree of ordering that results, and similar growth temperatures were used for Kurtz' sample and

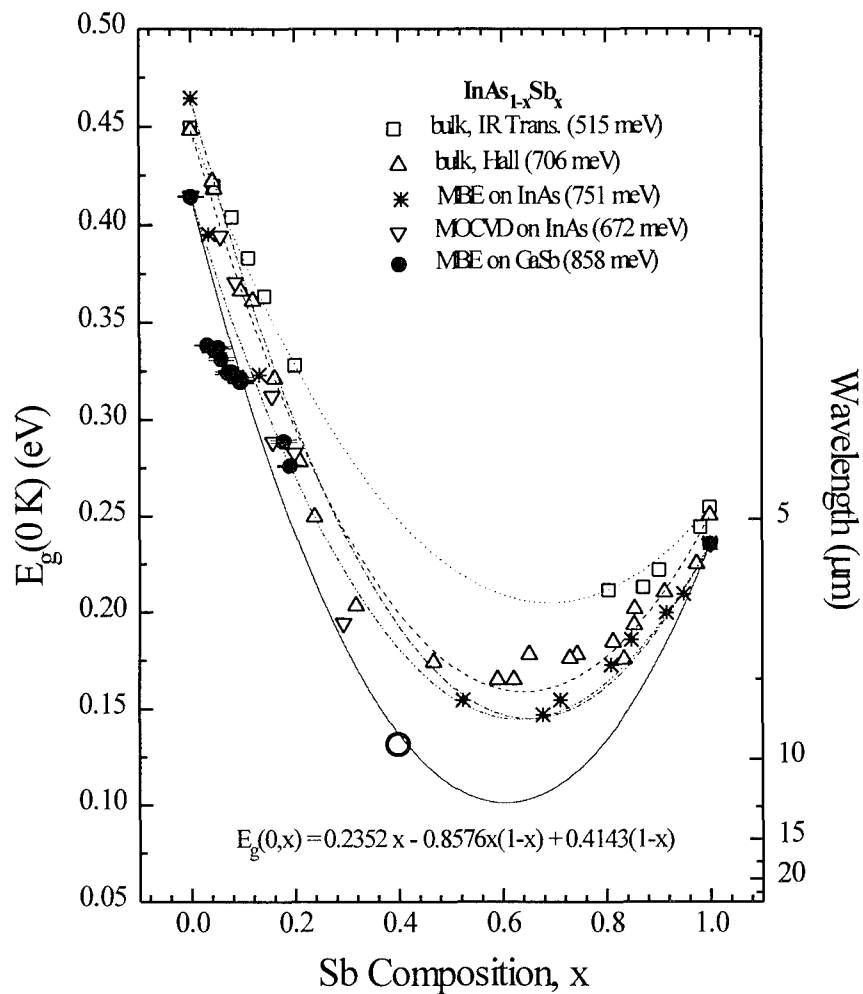


Figure 6-11. Compositional dependence of the energy gap at 0 K ( $E_g(0\text{ K})$ ) for MBE-grown InAsSb samples on GaSb substrate ( $\bullet$ , solid line), along with other low temperature  $E_g(x)$  relationships reported previously:  $\square$ , dotted line (Woolley, 1964b:1879);  $\Delta$ , dashed line (Coderre, 1968:1207);  $*$ , dash-dot line (Yen, 1988a:489); and  $\nabla$ , dash-double dot line (Fang, 1990:7034). The error in determining the  $E_g(0)$  parameter from the fit of the Varshni equation to the temperature-dependent data is shown for each composition. The solid line is the least squares fit of the bowing parameter equation (Eq (6.25)) to this data. The bowing parameters are given for each data set in the parentheses.  $\circ$  - Data point for MBE-grown  $\text{InAs}_{0.6}\text{Sb}_{0.4}$  on GaSb in which Cu-Pt ordering was observed (Kurtz, 1992:1909).

for the 13 samples studied here, it is possible that some degree of ordering exists in the current samples, as well. However, the likelihood of ordering decreases for materials with compositions away from the  $x = 50\%$  point. The compositions of the currently studied samples are near the InAs binary endpoint. Also discussed in Chapter IV is the potential for ordering to reduce the energy gap of a material. If ordering does exist in this material, this is another reason for the energy gaps of Figures 6-8 and 6-11 to be at values below those previously reported.

As can be seen in Figure 6-11, the second order polynomial which includes the bowing parameter does not fit well to the ternary data for the currently studied MBE-grown  $\text{InAs}_{1-x}\text{Sb}_x$  samples. A much better fit for the compositional dependence of  $E_g(0)$  for the ternary samples is shown in Figure 6-8 and given by:

$$E_g(0,x) = 0.3535 - 0.3777 x \quad (0.031 \leq x \leq 0.191) \quad (6.27)$$

However, the slope,  $dE_g(0)/dx$ , of this linear fit does not behave as expected, *i.e.*, it is not comparable to that of the polynomial fits over this composition range. Three possible explanations for this are considered: (1) a residual strain effect if these epilayers are not fully relaxed, as was assumed when interpreting the double crystal x-ray diffraction data (see Chapter IV, Undoped Samples); (2) ordering, as mentioned above; and (3) phase separation as described in Chapter IV, Molecular Beam Epitaxial Growth.

The possibility for the existence of residual strain in these samples was addressed in Chapter IV, Undoped Samples. The degree of strain relaxation in an epitaxial layer lattice-mismatched with the substrate upon which it was grown depends on its thickness

relative to the critical pseudomorphic thickness for the degree of lattice-mismatch that exists. An epilayer grown many times the critical thickness has a higher probability of being fully relaxed than one grown close to or below the critical thickness.

Table 4-2 listed the epilayer thickness in units of critical thickness for each sample; these relative thicknesses are also shown graphically as bars in Figure 6-12. The square symbols in Figure 6-12 show the differences,  $\Delta E_g(0)$ , between the measured energy gaps (*i.e.*, the solid dots in Figure 6-11) and the polynomial fit given by Eqs (6.25) and (6.26) (the solid line in figure 6-11), which is the deviation of the  $dE_g(0)/dx$  slope given by Eq (6.27) from that expected (Eqs (6.25) and (6.26)). As shown in Figure 6-12, the magnitude of this deviation increases as the composition of the sample departs from the lattice-matched condition.

If this deviation is due to residual strain effects, two contradictions occur: (1) the samples for which  $\Delta E_g(0)$  is largest are also the ones which are mostly likely to be fully relaxed because they are many times their critical thicknesses; and (2) the samples which are most likely to be partially strained, *i.e.*, those grown near their critical thicknesses, are the ones whose energy gaps would be effected least by the strain since the lattice-mismatch is so small. Also, the double crystal x-ray diffraction from the [115] planes of the  $\text{InAs}_{0.808}\text{Sb}_{0.192}$  sample described in Chapter IV found this sample to be fully relaxed, which it cannot be if residual strain is responsible for the anomalous  $dE_g(0)/dx$  behavior of the data. Therefore, the first possibility, residual strain, affecting the energy gap positions of these samples is highly unlikely.

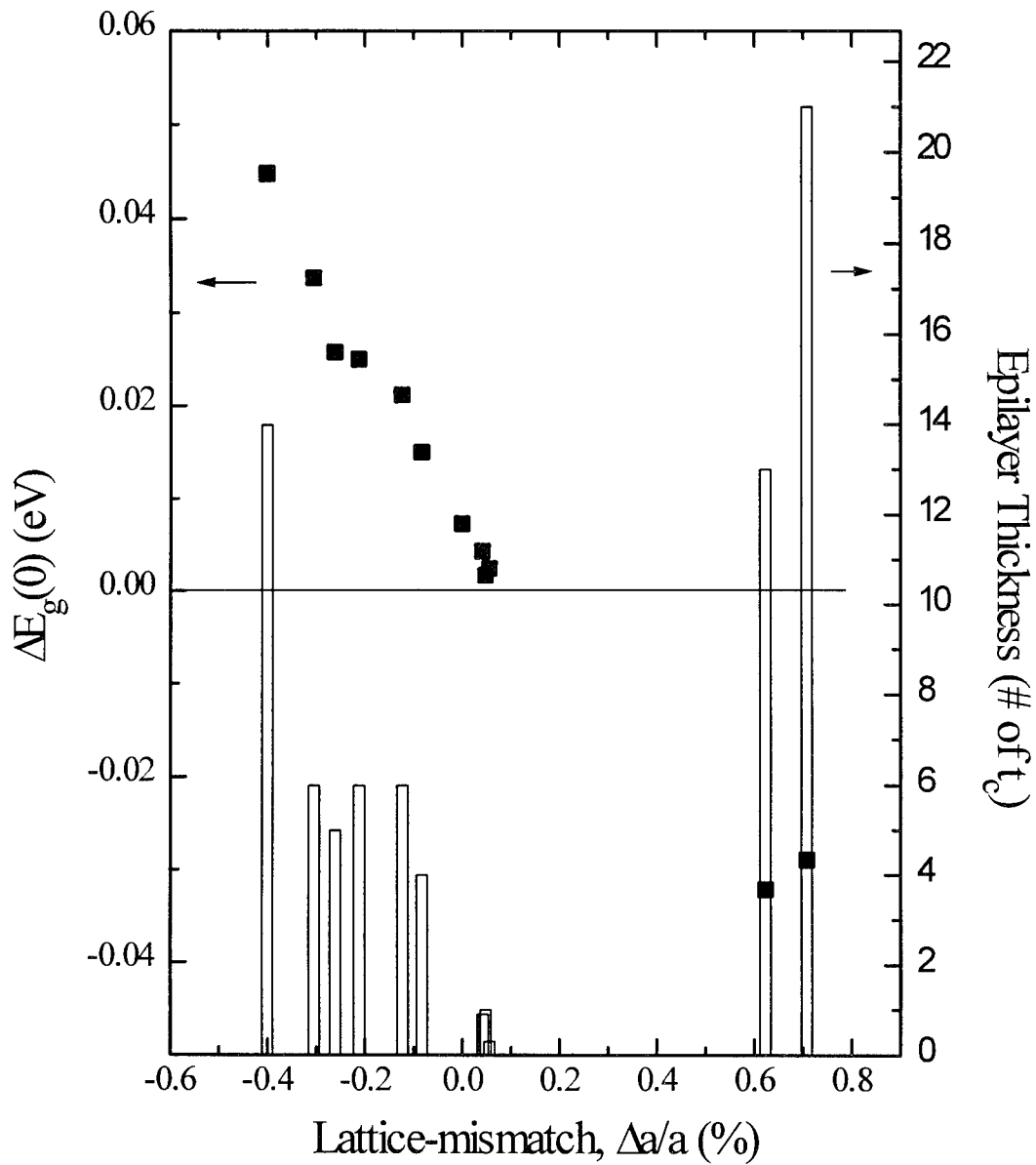


Figure 6-12. Differences between the energy gaps at 0 K of MBE-grown  $\text{InAs}_{1-x}\text{Sb}_x$  on GaSb substrates and the bowing-parameter polynomial fit of this data as given by Eqs (6.25) and (6.26) are shown as square symbols,  $\Delta E_g(0)$ . Sample epilayer thicknesses in units of critical thickness as given by Eq (4.11) are shown as vertical bars. Samples are labeled by lattice-mismatched with the GaSb substrate here rather than composition.

The second possibility for explaining the anomalous  $dE_g(0)/dx$  slope of the MBE-grown  $\text{InAs}_{1-x}\text{Sb}_x$   $E_g(0)$  data is the existence of Cu-Pt ordering in this material. However, Figure 6-8 shows that the difference between the measured and expected energy gaps increases as the  $\text{InAs}_{1-x}\text{Sb}_x$  compositions approach the InAs binary endpoint. This implies that the degree of ordering, which lowers the energy gap, increases as the compositions approach the InAs binary endpoint. This contradicts the statement made above that the probability and degree of ordering decrease as a material's composition departs the  $x = 50\%$  point. It is concluded that this contradiction is especially valid for these samples since their compositions are  $x < 20\%$ . Therefore, ordering in these samples is also believed to be unlikely.

The third possibility being considered as a phenomenon existing in these samples which affects  $E_g(0)$  is phase separation. As discussed in Chapter IV, strong phase separation has been observed in  $\text{InAs}_{0.5}\text{Sb}_{0.5}$  material in which this nominal composition was separated into  $\text{InAs}_{0.69}\text{Sb}_{0.31}/\text{InAs}_{0.33}\text{Sb}_{0.67}$  platelets forming a natural strained layer superlattice. These MBE growth temperatures were  $< 430^\circ\text{C}$  (Seong, 1991:485; Ferguson, 1991a:3324; Ferguson, 1991b:395). As listed in Table 4-1, the growth temperatures for the currently studied MBE-grown  $\text{InAs}_{1-x}\text{Sb}_x$  samples were between  $430\text{-}489^\circ\text{C}$ . However, MBE growth temperatures may be calibrated differently between different MBE growers and machines, depending on how the substrate temperature is measured and the thermal conductivity between the substrate and the mount. Also, the degree of phase separation which exists in the currently studied samples may not be as obvious as that which produced the platelet formation.

One way of assessing if a distribution of compositions about the nominal composition exists in a semiconductor material is by studying the linewidths of the double crystal x-ray diffraction (DCXRD) peaks. The Bragg's law development for DCXRD peak position given in Chapter IV assumed Bragg reflection from an infinite number of lattice planes. In practice, the finite epitaxial layer thickness broadens the peak to some minimum linewidth. A theoretical estimation for this minimum full width at half maximum (FWHM) linewidth is given by the Scherrer formula as (Herman, 1991:177):

$$\beta_{1/2} = \frac{0.9 \lambda}{d \cos \theta_B}, \quad (6.28)$$

where  $\lambda$  is the wavelength of the incident radiation,  $d$  is the epilayer thickness and  $\theta_B$  is the Bragg angle. The FWHM linewidths measured from the DCXRD experiments are listed in Tables 4-2 and 6-4. (The DCXRD peak for  $\text{InAs}_{0.903}\text{Sb}_{0.097}$  sample, 93-120, appeared as a shoulder on the GaSb substrate peak (Figure 4-11). For this reason, it was not possible to get an accurate measurement of its FWHM linewidth.) The theoretical minimum linewidth,  $\beta_{1/2}$ , was calculated for each sample along with the ratio,  $\text{FWHM}/\beta_{1/2}$ , and are also listed in Table 6-4.

Although most of the DCXRD peaks for these samples are broadened well beyond their theoretical minima, this method is inconclusive in making a definitive statement about the existence of phase separation in this material. Because these  $\text{InAs}_{1-x}\text{Sb}_x$  samples are lattice-mismatched with their GaSb substrates, a significant concentration of



misfit dislocations exist. Crystalline defects such as these also broaden the DCXRD linewidth. Another characterization method, such as transmission electron microscopy which was unavailable for this research, is necessary to draw a conclusion about the composition of this material. However, the existence of phase separation in this material has not been disproved, and the possibility of it is addressed again in the PL results of Chapter VII.

Table 6-4. DCXRD linewidth, FWHM, along with Scherrer linewidth,  $\beta_{1/2}$ , calculated using Eq (6.28) for each  $\text{InAs}_{1-x}\text{Sb}_x$  GaSb sample. (\* InAs sample)

Sample	FWHM (sec)	InAsSb epilayer ( $\mu\text{m}$ )	$\beta_{1/2}$ (sec)	FWHM/ $\beta_{1/2}$
95-007*	795	1.40	24	33
93-044	95	0.82	40	2.4
93-114	197	0.75	44	4.5
93-030	135	0.65	51	2.6
93-113	77	0.68	49	1.6
93-112	291	1.02	32	9.1
93-048	28	0.77	43	0.7
93-045	39	0.78	42	0.9
93-068	92	1.06	31	3.0
93-092	112	1.38	24	4.7
93-120	-	0.40	83	-
94-035	194	0.49	68	2.9
93-151	365	0.78	42	8.7

### Compositional Dependence of the Energy Gap: Room Temperature

The second important temperature at which to analyze the compositional dependence of the energy gap for the MBE-grown  $\text{InAs}_{1-x}\text{Sb}_x$  material on GaSb substrates

is room temperature since the goal of many device developers, especially semiconductor laser developers, is to eventually achieve efficient room temperature operation. Also, the measurement of the room temperature energy gap of  $\text{InAs}_{1-x}\text{Sb}_x$  is more common in the literature than those at low temperature described above. Thus, comparisons of the current results to other previously reported  $\text{InAs}_{1-x}\text{Sb}_x$  research can be made.

The energy gap positions measured at room temperature from the FTS absorption experiments are shown in Figures 6-13 as solid dots along with previously reported values from the literature. The open square symbols in Figures 6-13 represent infrared transmission data from the bulk polycrystalline samples measured by Woolley and Warner as described for the low temperature case. The open triangular symbols represent optical absorption data from single-crystal liquid phase epitaxial 4  $\mu\text{m}$ -thick layers of  $\text{InAs}_{1-x}\text{Sb}_x$ ,  $x < 0.35$  grown on (111) InAs and  $x > 0.89$  grown on (111) InSb (Stringfellow, 1971:805). These energy gap assignments were also made by choosing an absorption coefficient ( $\alpha(E_g) = 300 \text{ cm}^{-1}$ ) which gave the accepted values of energy gap for the binary endpoints, InAs and InSb, as Woolley and Warner had. The star symbols represent the room temperature FTS absorption measurements, again using  $\alpha(E_g) = 300 \text{ cm}^{-1}$  to determine the energy gap position, for MBE-grown  $\text{InAs}_{1-x}\text{Sb}_x$  on (100) InAs over the complete compositional range,  $0 < x < 1$  (Yen, 1987:927).

Similar to the low temperature results described above, the room temperature energy gap values measured here were lower for the currently studied MBE-grown  $\text{InAs}_{1-x}\text{Sb}_x$  material than those previously reported, but the difference has decreased to 6-15 meV at room temperature from 15-60 meV at 0 K for the lattice matched composition,

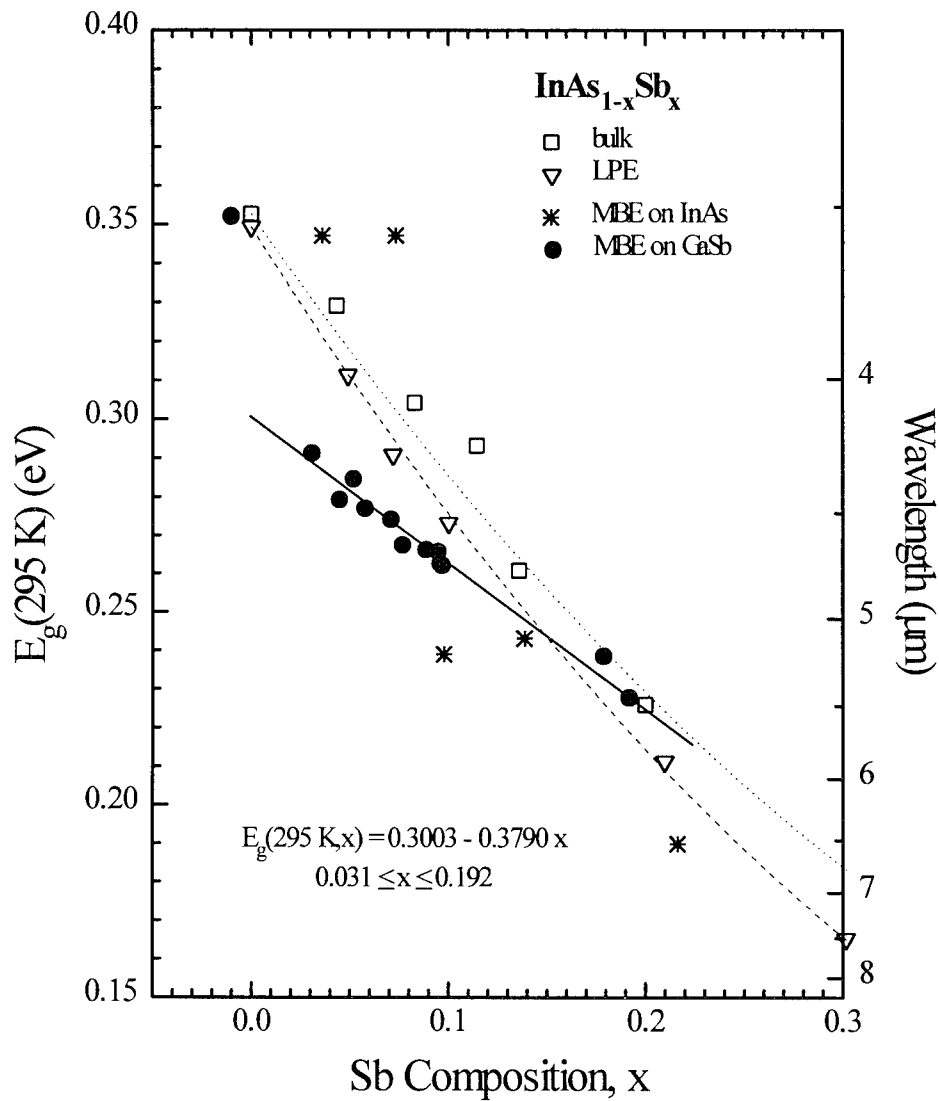


Figure 6-13. Least squares linear fit of the compositional dependence of the room temperature energy gap,  $E_g(295 \text{ K})$ , for MBE-grown InAsSb samples on GaSb substrate (●, solid line) compared to other low temperature  $E_g(x)$  relationships which include a bowing parameter reported previously: □, dotted line (Woolley, 1964b:1879); ▽, dashed line (Stringfellow, 1971:805); and \* (Yen, 1987:927). The error associated with each data point was determined by the absorption spectrometer resolution to be either 0.5 or 2.0 meV as listed in Table 6-1.

InAs<sub>0.911</sub>Sb<sub>0.089</sub>. Whereas arguments were made that perhaps the previously reported low temperature energy gap values were artificially high because of experimental or analysis techniques, such an argument cannot be made for the room temperature data.

The fit of the room temperature energy gap data for these currently studied ternary samples is shown in Figure 6-13 as the solid line and given by:

$$E_g(295 \text{ K}, x) = 0.3003 - 0.3790 x \quad (0.031 \leq x \leq 0.191) \quad (6.28)$$

for these compositions. As for the low temperature data, the  $dE_g(295 \text{ K})/dx$  slope of this linear fit does not behave as expected when compared to slopes of the previously reported data over this composition range. The bowing parameter fit of this current data is shown by the solid line in Figure 6-14. It was determined using Eq (6.25) with the room temperature energy gap of the InAs endpoint as measured at 0.3520 eV, and that of the InSb endpoint taken from the literature to be 0.1695 eV (Madelung, 1991:42), and is given by;

$$E_g(295 \text{ K}, x) = 0.1695x - 0.723(1-x)x + 0.3520(1-x) \quad (6.29)$$

The room temperature bowing parameter of 723 meV is 16% larger than any of the previously reported values ( $b_{\text{Woolley}} = 550 \text{ meV}$  and  $b_{\text{Stringfellow}} = 625 \text{ meV}$ ;  $b_{\text{Yen}}$  was unavailable); the low temperature bowing parameter determined for these samples was 14% larger than any previously reported.

As with low temperature energy gap data for these currently studied MBE-grown InAs<sub>1-x</sub>Sb<sub>x</sub> samples, an analysis of the overall reduction in energy gap position and the

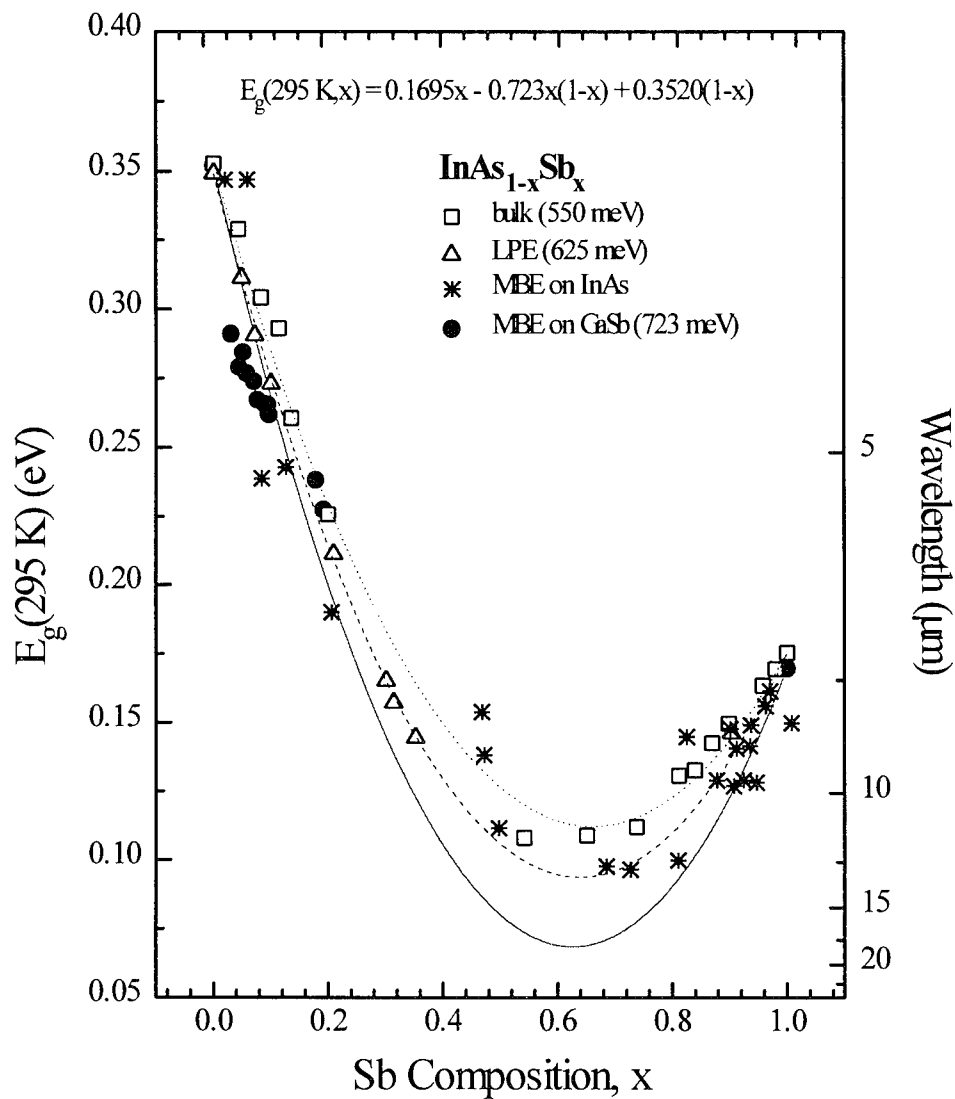


Figure 6-14. Compositional dependence of the room temperature energy gap,  $E_g(295 K)$ , for MBE-grown InAsSb samples on GaSb substrate (●, solid line), along with other room temperature  $E_g(x)$  relationships previously reported: □, dotted line (Woolley, 1964b:1879); △, dashed line (Stringfellow, 1971:805); and \* (Yen, 1987:927). The error associated with each data point was determined by the absorption spectrometer resolution to be either 0.5 or 2.0 meV as listed in Table 6-1. The solid line is the least squares fit of the bowing parameter equation (Eq (6.25)) to this data. The bowing parameters are given for each data set in the parentheses.

anomalous  $dE_g(295\text{ K})/dx$  slope over the ternary compositions studied must be made. However, the same arguments as given above are used. Again, those conclusions were that the existences of either residual strain or ordering in this material is unlikely, but the possibility of phase separation in this material cannot be definitively disproved by the available characterization techniques.

### **Varshni Parameters $\alpha$ and $\beta$**

As given by Eq (6.24), there are three Varshni fitting parameters,  $E_g(0)$ ,  $\alpha$  and  $\beta$ .  $E_g(0)$  was analyzed above in the Compositional Dependence of the Energy Gap: Low Temperatures section. The other Varshni parameters,  $\alpha$  and  $\beta$ , were listed in Table 6-3 and are plotted as a function of composition in Figure 6-15, along with the error calculated in determining them from the absorption data. Because the data for both parameters shown in Figure 6-15 shows no clear pattern and contains a large amount of scatter, no compositional dependence for  $\alpha$  or  $\beta$  was determined. This problem with determining a precise compositional dependence of the Varshni parameters has been shown to exist for other semiconductor alloys, as well (El Allali, 1993:4398).

The failure to accurately determine compositional dependencies for  $\alpha$  and  $\beta$  in  $\text{Al}_x\text{Ga}_{1-x}\text{As}$  compositions was addressed by analyzing the Varshni equation itself (El Allali, 1993:4398). The Varshni equation (Eq (6.24)) was differentiated with respect to  $\alpha$

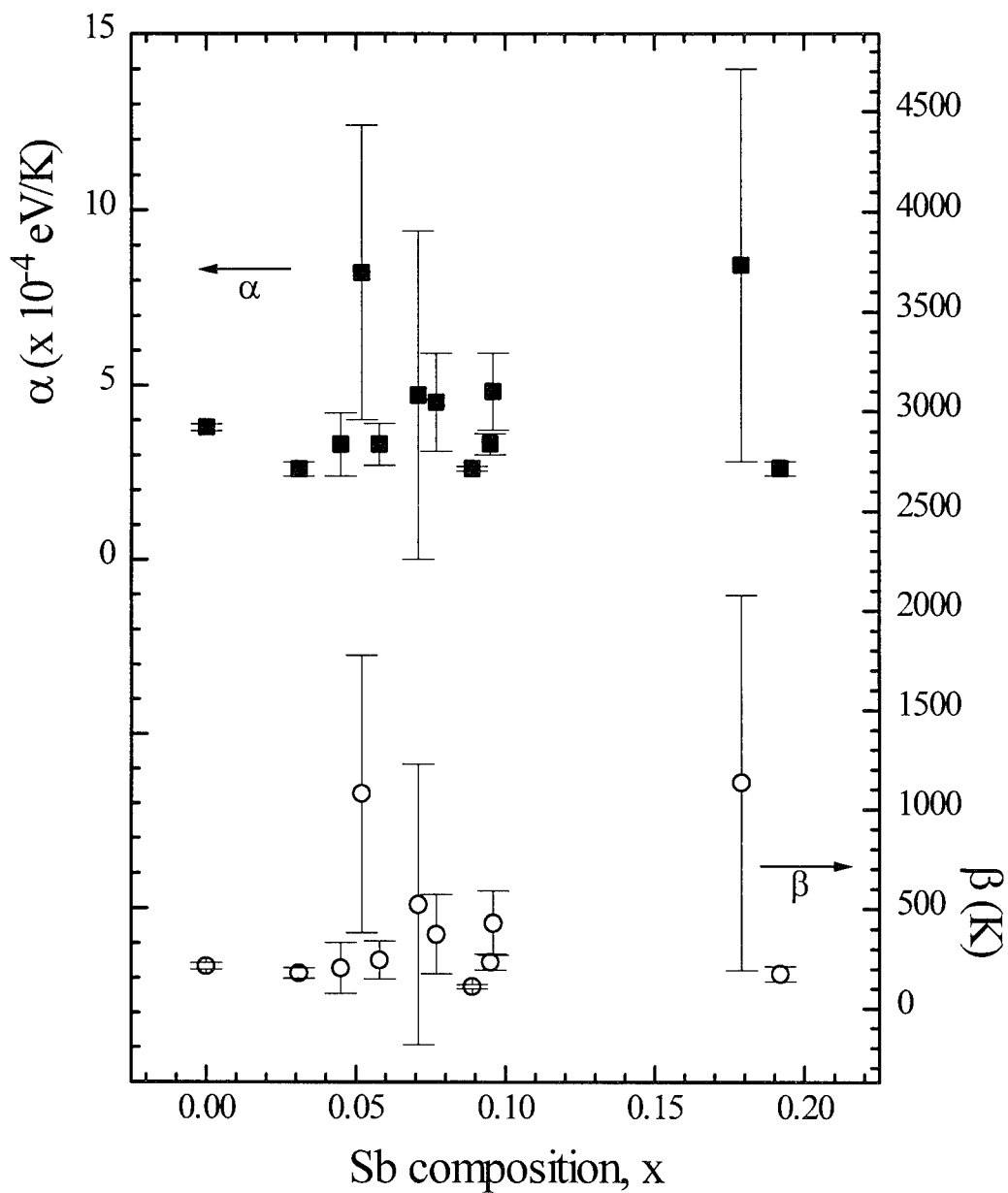


Figure 6-15. Compositional dependence of the Varshni parameters,  $\alpha$  (solid squares) and  $\beta$  (open circles), for the 13 MBE-grown  $\text{InAs}_{1-x}\text{Sb}_x$  on GaSb samples studied. The errors in determining these parameters from the fit of the Varshni equation to the temperature-dependent data are shown for each composition.

and  $\beta$  to determine the affect of small changes in either on the energy gap:

$$dE_g(T) = \frac{-T^2}{\beta + T} d\alpha + \frac{\alpha T^2}{(\beta + T)^2} d\beta. \quad (6.30)$$

Measurements made at low temperatures, *i.e.*,  $T \ll \beta$ , assuming any change in  $\alpha$  is proportional to a change in  $\beta$ , *i.e.*,  $d\alpha/\alpha = d\beta/\beta$ , result in no change in  $E_g(T)$  due to changes in  $\alpha$  and  $\beta$ . This shows that for low temperature measurements,  $\alpha$  and  $\beta$  by themselves are not given precisely, but a fixed relationship between  $\alpha$  and  $\beta$  exists (El Allali, 1993:4398).

At higher temperatures, if a fixed relationship is again assumed between  $\alpha$  and  $\beta$ , but this time:

$$\frac{\alpha}{\beta + T_0} = \text{constant} \quad (6.31)$$

so that  $d\alpha/\alpha = d\beta/(\beta + T_0)$ , measurements made around any one temperature,  $T_0$ , again result in no change in  $E_g(T)$  due to changes in  $\alpha$  and  $\beta$ . Again, this shows that  $\alpha$  and  $\beta$  by themselves may not be given precisely, but that a fixed relationship between them may exist. Also, from this result it was suggested that precise measurements of  $\alpha$  and  $\beta$ , independently, might require a temperature range larger than physically realizable in most experiments (El Allali, 1993:4398).

The  $\alpha$  and  $\beta$  parameters given for each  $\text{InAs}_{1-x}\text{Sb}_x$  composition in Table 6-3 are plotted with  $\beta$  as a function of  $\alpha$  in Figure 6-16. It is shown in Figure 6-16 that a linear relationship exists between  $\alpha$  and  $\beta$  for these MBE-grown samples as was suggested with



Eq (6.31). Therefore, it is concluded that the irregular changes in  $\alpha$  and  $\beta$  parameters measured here are real and sample-dependent rather than material dependent. It has been suggested that these observed variations in other material systems may be due to sample-dependent features such as strain or defects (El Allali, 1993:4398; Shah, 1994:449).

There are only a few previously reported  $E_g(T)$  relationships for  $\text{InAs}_{1-x}\text{Sb}_x$  material in the literature. The one reported in the form of the Varshni equation (Eq (6.24)) was based on PL measurements at temperatures between 78 and 295 K for MBE-grown  $\text{InAs}_{0.93}\text{Sb}_{0.07}$  on GaSb substrate. (The lattice mismatch was measured by DCXRD as  $\Delta a/a = -0.044\%$ .) The Varshni parameters given for this material are  $E_g(0) = 0.349$  eV,  $\alpha = 3.064 \times 10^{-4}$  eV/K and  $\beta = 254$  K (Elies, 1993:159).

Another  $E_g(T)$  relationship for  $\text{InAs}_{1-x}\text{Sb}_x$  was formulated from data from a variety of sources to also include the compositional dependence as (Rogalski, 1989:191):

$$E_g(T, x) = 0.411 - \frac{3.4 \times 10^{-4} T^2}{T + 210} - 0.876x + 0.70x^2 + 3.4 \times 10^{-4} T x(1 - x). \quad (6.32)$$

Here, the first two terms have the form of the Varshni equation with the remaining terms added for the compositional dependence. In this case, the equivalent Varshni parameters  $\alpha$  and  $\beta$  are  $\alpha = 3.4 \times 10^{-4}$  eV/K and  $\beta = 210$  K.

Both of these previously reported sets of Varshni parameters are also plotted as open symbols on Figure 6-16 along with those from the currently studied samples. The relationship between  $\alpha$  and  $\beta$  established for the current material holds for these previously reported samples, as well. This lends credibility to the suggestion that, while

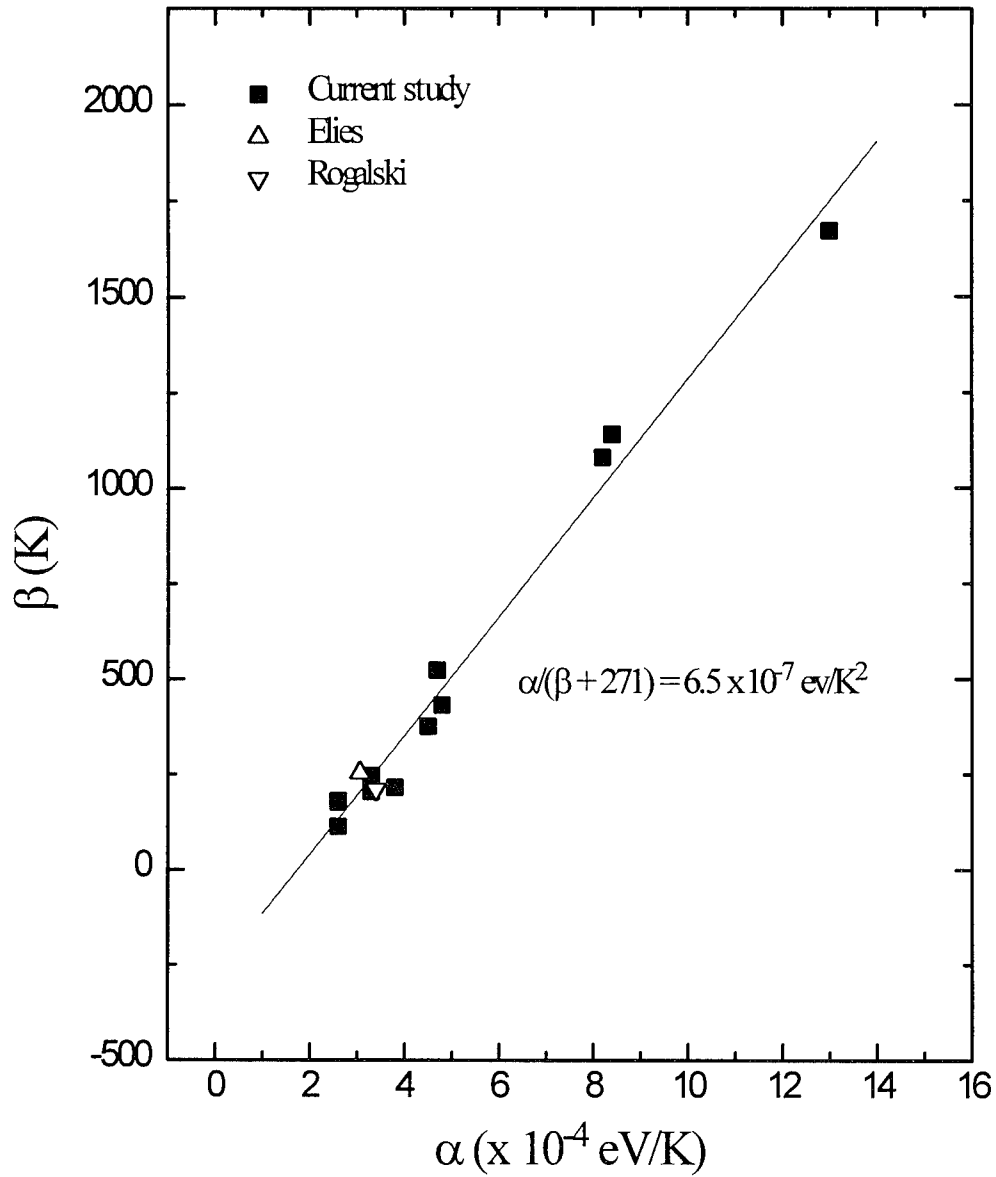


Figure 6-16. Plot of the Varshni parameters  $\alpha$  and  $\beta$  showing a fixed relationship exists between them for the  $\text{InAs}_{1-x}\text{Sb}_x$  samples studied here (■) and for those previously reported ( $\Delta$  and  $\nabla$ ).

precise measurements of  $\alpha$  and  $\beta$  individually may not be possible, the measurement of a fixed relationship between them for a certain material might be.

## Summary

Although the primary reason for performing FTS absorption measurements on these MBE-grown  $\text{InAs}_{1-x}\text{Sb}_x$  samples on GaSb substrates was to determine their energy gap positions at a variety of temperatures, other conclusions were drawn from the absorption data, as well. The absorption spectra showed strong free carrier absorption at energies below the band edge. From the change in the magnitude of this free carrier absorption with increased temperature, as given by the B coefficient of Eq (6.1), it was determined that a significant concentration of native or unintentional defects or impurities probably exists in this nominally undoped epitaxial material.

The absorption coefficients for  $\text{InAs}_{1-x}\text{Sb}_x$  compositions have not been previously reported in the literature. These coefficients for compositions over the range  $0 \leq x \leq 0.192$  were derived from the absorption data and the coefficient for the ( $x = 0$ ) InAs sample agreed well with values previously reported for bulk InAs.

Once the energy gap was determined for each sample over a range of temperatures, it was found that the temperature dependence of these values for any composition fit well to an established relationship, the Varshni equation (Eq. 6.24). The compositional dependence of the  $\text{InAs}_{1-x}\text{Sb}_x$  energy gap for these samples was also studied closely at two important temperatures: near 0 K, which is important since other

experiments such as the PL reported in Chapter VII are most effective at low temperatures; and room temperature, since it is desirable for optoelectronic devices to operate efficiently here.

At both these temperatures, two trends were evident in the energy gap data. First, the energy gap values determined in this current study are considerably lower than those reported previously for  $\text{InAs}_{1-x}\text{Sb}_x$  material; and second, the compositional dependence of the energy gap does not behave as expected from the previously reported results in that the slope,  $dE_g/dx$ , is different. An analysis of possible reasons for both of these anomalies determined that the existence of residual strain or ordering effects in this material is unlikely. A third possibility, phase separation, could not be definitively proven or disproved by the characterization techniques available.

## VII. Results and Discussion: Photoluminescence

Photoluminescence (PL) was used to characterize the quality of the MBE-grown  $\text{InAs}_{1-x}\text{Sb}_x$  samples on GaSb substrates described in Chapter IV, and to identify any defect or impurity levels which exist in these materials. Using the PL experiment detailed in Chapter V, these samples, as well as some complementary samples, were studied. Tables 4-1 and 4-2 listed the structure and composition for the 13 undoped samples.

The first two sections of this chapter discuss the PL results for the binary InAs samples used to baseline the ternary  $\text{InAs}_{1-x}\text{Sb}_x$  PL results. One InAs sample was grown on InAs (*i.e.*, InAs homoepitaxy), while the other was grown on GaSb and is the  $x = 0$  sample described in Tables 4-1 and 4-2.

The middle two sections describe the PL results for the  $\text{InAs}_{1-x}\text{Sb}_x$  ternary samples. Although multiple-peaked spectra was expected, the majority of these samples produced only single-peaked spectra. However, once the recombination mechanism responsible for this peak was identified, additional information about the material was obtained from this peak. One of the 12 undoped samples did produce multiple-peaked PL spectra. This allowed identification of extrinsic levels in  $\text{InAs}_{1-x}\text{Sb}_x$  by PL for the first time.

The remaining section describes work done to identify the energy levels associated with an intentional dopant, Be, since extrinsic levels in  $\text{InAs}_{1-x}\text{Sb}_x$  have not

been reported previously. Two forms of doping were studied: Be-ion implantation and epitaxial Be doping.

### **InAs Homoepitaxy**

In order to provide a point of reference for the  $\text{InAs}_{1-x}\text{Sb}_x$  ternary PL spectra, undoped homoepitaxial InAs was first studied by PL since it is a relatively well characterized material (Allaberenov, 1972a:2050; Allaberenov, 1972b:330; Guseva, 1975:591; Grober, 1989:4079; Fang, 1990:7034; Lacroix, 1995:1101). The PL spectra for the homoepitaxial InAs sample is shown for several temperatures between 4 and 128 K in Figure 7-1. Six distinct PL peaks were apparent from these spectra as labeled  $E_{\text{exc}}$ ,  $E_{\text{band}}$ ,  $E_{\text{D1}}$ ,  $E_{\text{DAP1}}$ ,  $E_{\text{D2}}$  and  $E_{\text{DAP2}}$  in Figure 7-1.

Identification of these peaks was facilitated by comparison of the PL spectra with absorption spectra at similar temperatures as shown for the 7 and 8 K data in Figure 7-2. The strong excitonic absorption at the band edge also identifies the exciton in the PL spectrum. Identification of additional energy levels in the PL spectrum were then made in reference to the exciton peak. The position of the band edge was calculated from the exciton peak using the hydrogenic model to determine the excitonic binding energy in InAs. The excitonic binding energy is given by:

$$E_{\text{exc}} = \frac{m_r q^3}{8h^2 \epsilon_r^2 \epsilon_0}, \quad (7.1)$$

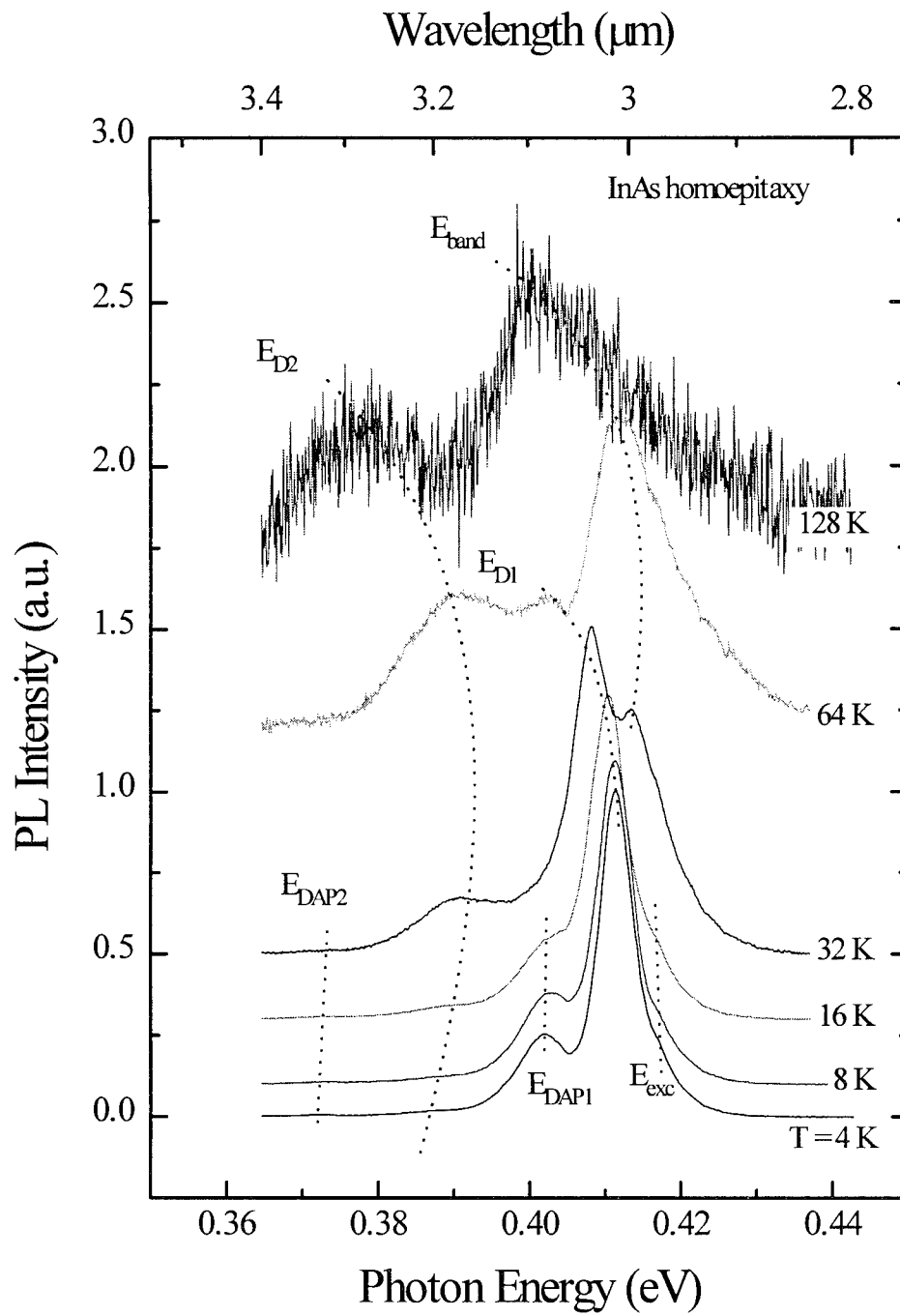


Figure 7-1. Photoluminescence spectra of InAs homoepitaxial material. The PL spectrometer resolution is 0.8 meV.

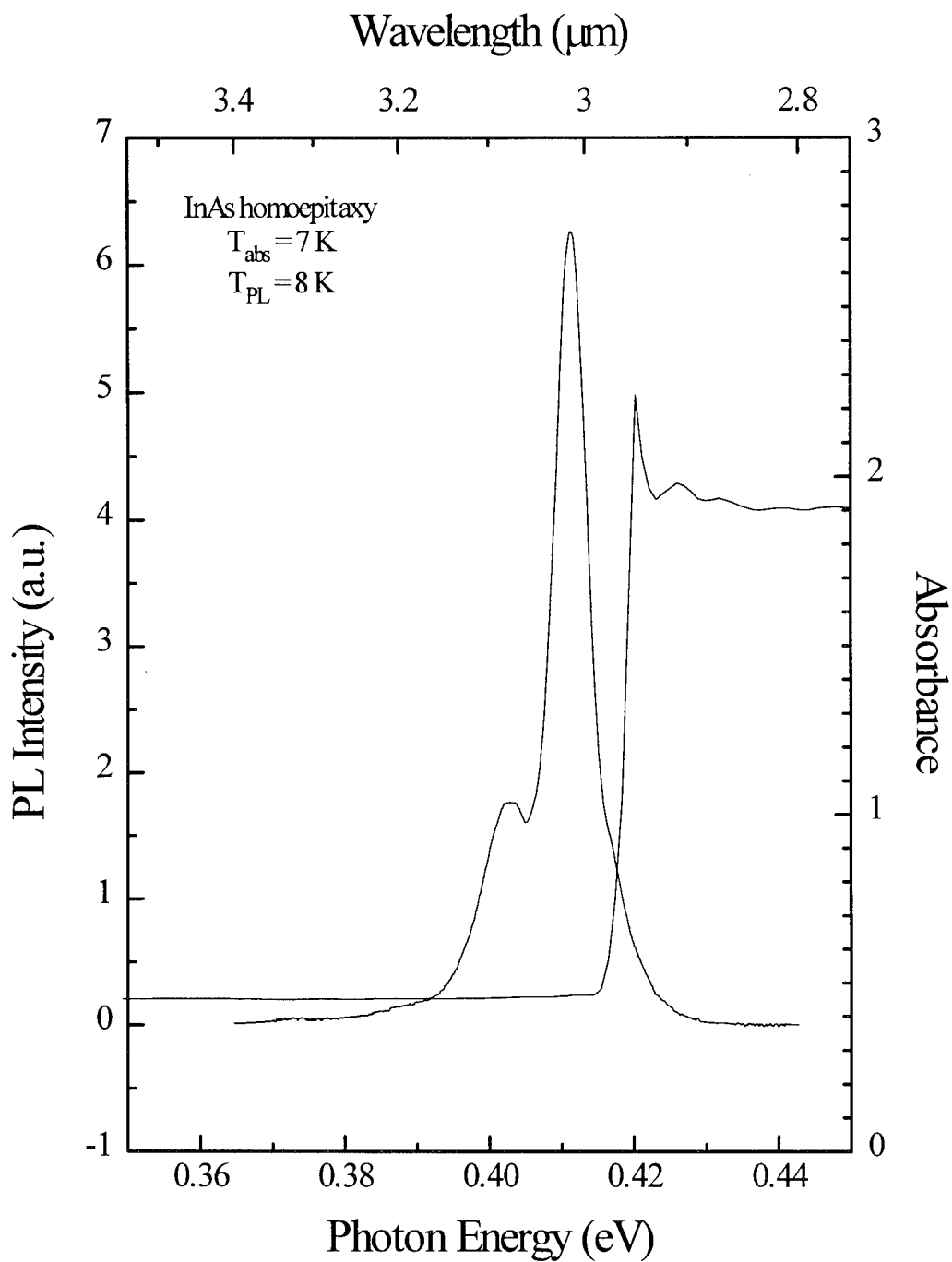


Figure 7-2. Comparison of homoepitaxial InAs low temperature photoluminescence and absorption spectra. The PL spectrometer resolution is 0.8 meV; FTS absorption spectrometer resolution is 2.0 meV.



where  $q$  is the electronic elementary charge,  $h$  is Planck's constant,  $\epsilon_0$  is the permittivity of a vacuum,  $\epsilon_r$  is the relative dielectric constant (Madelung, 1991:138),

$$\epsilon_r = 12.25, \quad (7.2)$$

and  $m_r$  is the reduced effective mass. The conduction band electron effective mass,  $m_n$ , is (Madelung, 1991:134):

$$m_n = 0.0239. \quad (7.3)$$

The equivalent valence band hole effective mass,  $m_p$ , is derived from the heavy hole effective masses in the [111] and [100] directions (Madelung, 1991:134),

$$m_{ph111} = 0.43 \quad (7.4a)$$

$$m_{ph100} = 0.35, \quad (7.4b)$$

respectively, such that the equivalent heavy hole effective mass becomes (McKelvey, 1986:301):

$$\begin{aligned} m_{ph} &= (m_{ph111} m_{ph100})^{1/2} \\ &= 0.39 \end{aligned} \quad (7.5)$$

This result, along with the light hole effective mass (Madelung, 1991:134),

$$m_{pl} = 0.026, \quad (7.6)$$

yields the equivalent valence band hole effective mass as (McKelvey, 1986:300):

$$\begin{aligned} m_p &= (m_{pl}^{3/2} + m_{ph}^{3/2})^{2/3} \\ &= 0.39 \end{aligned} \quad (7.8)$$

Then the reduced effective mass becomes:

$$\begin{aligned} m_r &= (1/m_n + 1/m_p)^{-1} \\ &= 0.023 \end{aligned} \quad (7.9)$$

and the calculated excitonic binding energy for InAs from Eq (7.1) is:

$$E_{exc} = 2.0 \text{ meV}. \quad (7.10)$$

The excitonic band gap energy observed from the PL spectrum at 4 K is  $417 \pm 0.8$  meV, comparable to the  $415.28 \pm 0.02$  meV recently reported in the literature (Lacroix, 1995:1101).

As is shown in Figure 7-1, the peak labeled  $E_{D1}$  is the most pronounced peak in the PL spectrum at temperatures between 4 and 32 K. At low temperatures, this peak appears to move to lower energies with increased excitation as is shown in Figure 7-3, but it is believed this peak is actually the superposition of two subpeaks as shown in the 5 mW spectrum of Figure 7-3. The 5 mW spectrum is shown to be asymmetric and is fit well by the superposition of two Gaussian curves as shown by the dotted lines in Figure 7-3. At low excitations, the lower energy subpeak, labeled  $E_{D1L}$  in Figure 7-3, is

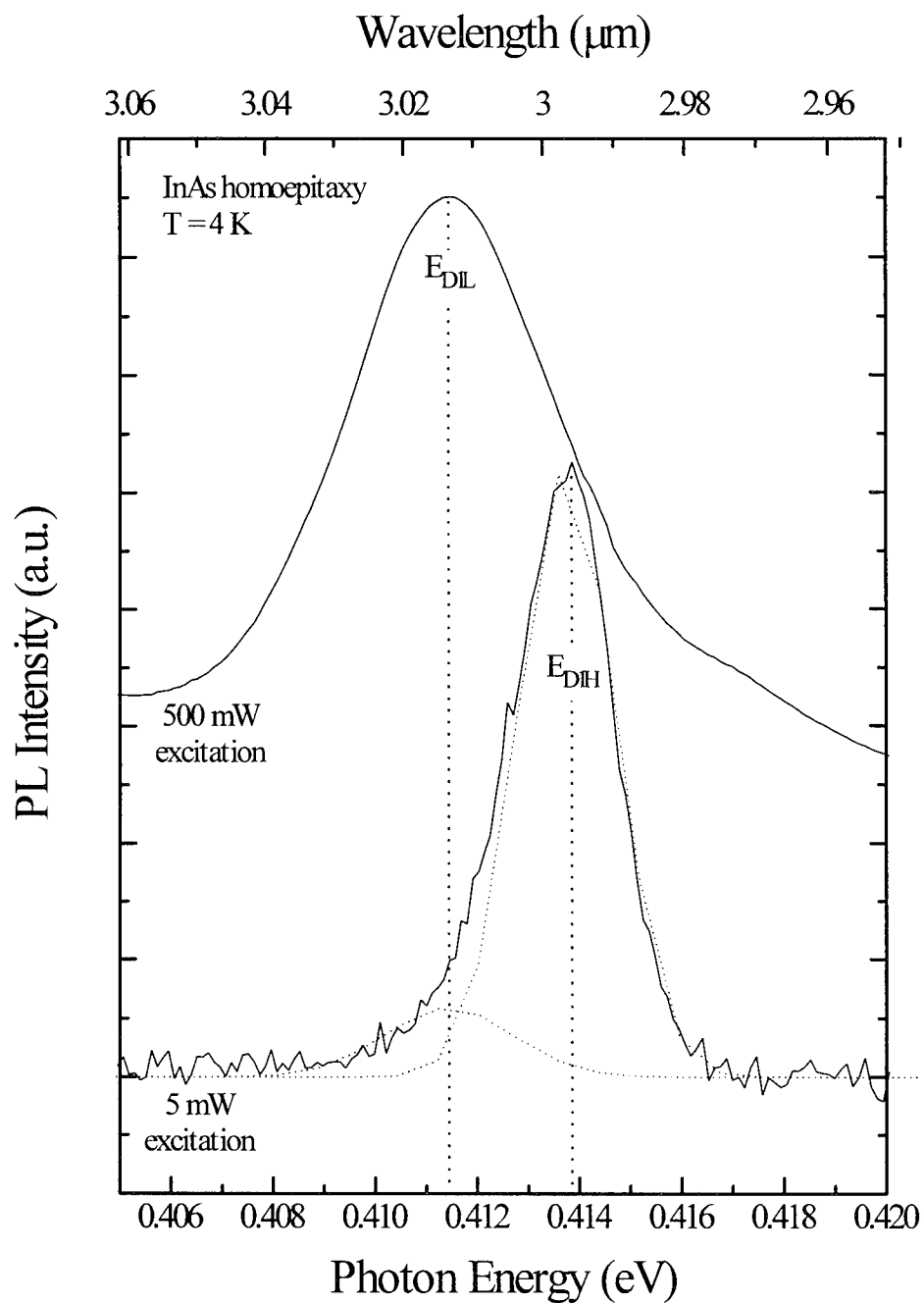


Figure 7-3. Low temperature PL spectra of peak  $E_{D1}$  from InAs homoepitaxial sample at two laser excitation powers, 5 and 500 mW. This apparent single peak is actually a double peak as shown by the double Gaussian fit. The PL spectrometer resolution is 0.8 meV.

dominated by the higher energy subpeak, labeled  $E_{D1H}$ . However, as excitation is increased, subpeak  $E_{D1L}$  dominates the apparent single peak spectrum.

The position of subpeak  $E_{D1H}$  is at  $414 \pm 0.8$  meV at 4 K. At low excitation powers ( $< 20$  mW), it is the dominant subpeak under the main peak with the lower energy subpeak appearing as a shoulder. The lower energy subpeak  $E_{D1L}$  is located at  $412 \pm 0.8$  meV at 4 K, and dominates the apparent single peak at excitation powers above 160 mW.

Both subpeaks  $E_{D1H}$  and  $E_{D1L}$  are believed to be due to free-to-bound (F-B) recombinations. Since the main peak  $E_{D1}$  no longer shifts to lower energies with increased excitation at temperatures above 32 K, it is believed that the impurity level associated with subpeak  $E_{D1H}$  is ionized at these temperatures. Since the position of this level is  $\sim 3$  meV from the band edge, ionization is reasonable ( $k_B T$  for 32 K is 2.8 meV).

The band edge peak also increases significantly in relative intensity at 32 K, from the excitonic peak being a small shoulder of the main peak, to where the band edge peak is an obviously resolvable peak. This implies that carriers, which at lower temperatures relaxed through the impurity level associated with subpeak  $E_{D1H}$  before radiatively recombining with a carrier in the opposite band, are more likely to combine directly from band-to-band at higher temperatures where the impurity level becomes thermally ionized.

At a temperature of 16 K and low excitation levels ( $< 40$  mW), peak  $E_{D1}$  is comparable in intensity to the lower energy peak labeled  $E_{DAP1}$  in Figure 7-1 as the main peaks in the 16 K spectra. However, as the excitation is increased above 40 mW, peak  $E_{D1}$  grows in intensity at a much faster rate than peak  $E_{DAP1}$  to become the dominant

peak. Similarly at 32 K, peak  $E_{D1}$  and the band edge peak are comparable in intensity at low excitations (again,  $< 40$  mW) as the main peaks in the 32 K spectra, but peak  $E_{D1}$  again grows in intensity with increased excitation at a much faster rate to become the dominant peak. By 64 K, the band edge peak is clearly the dominant peak in the spectrum.

Because subpeak  $E_{D1L}$  dominates the main peak  $E_{D1}$  at higher excitations, and because peak  $E_{D1}$  increases in PL intensity at a much faster rate than the other peaks, it is concluded that either the radiative lifetime of the transition associated with subpeak  $E_{D1L}$  is shorter than those of subpeak  $E_{D1H}$ , peak  $E_{DAP1}$  and the band edge peak, or that the concentration of impurity states associated with subpeak  $E_{D1L}$  is greater than those associated with subpeak  $E_{D1H}$  and peak  $E_{DAP1}$  such that saturation of the  $E_{D1L}$  transition does not occur until higher excitation powers.

The subpeak  $E_{D1L}$  is located 5-7 meV from the band edge; this is corroborated by the significant reduction in the relative intensity of the main peak  $E_{D1}$  at 64 K ( $k_B T$  for 64 K is 5.5 meV). Subpeak  $E_{D1H}$  is located  $\sim 3$  meV from the band edge. The energy levels associated with both of these F-B subpeaks are less than the minimum impurity level of 10 meV previously reported for InAs. These previous F-B recombinations were assigned as: free electron to bound acceptor in Sn-doped epitaxy (Guseva, 1975:591); bound donor to free hole in undoped epitaxy on Si substrate (Grober, 1989:4079); and bound donor to free hole in bulk InAs (Fang, 1990:7034).

The peak labeled  $E_{\text{DAP1}}$  in Figures 7-1 is positioned at an energy of  $402 \pm 0.8$  meV at 4 K which is  $\sim 15$  meV from the band edge. It is the second strongest peak in the low temperature spectrum, but is no longer observed at temperatures above 32 K ( $k_{\text{B}}T$  for 32 K is 2.8 meV). Recall that 32 K is the temperature at which subpeak  $E_{\text{DIH}}$  disappeared due to ionization. Peak  $E_{\text{DAP1}}$  was also observed to shift to higher energies with increased laser excitation power at a rate of 1 meV/decade of excitation. From these two observations, it is concluded that peak  $E_{\text{DAP1}}$  is due to donor-acceptor pair (DAP) recombination, and the impurity level associated with subpeak  $E_{\text{DIH}}$  is one of the impurity levels involved.

Unlike the recombination of free carriers, the DAP transition occurs between carriers associated with specific sites in the crystal lattice, *i.e.*, an electron at a donor position and a hole at an acceptor position spatially separated by some distance,  $r$ , as shown schematically in Figure 7-4. The coulombic attraction between the recombining carriers is inversely proportional to  $r$  as given by the last term of Eq 7.11, and increases the energy of the photon emitted in a DAP recombination by effectively reducing the impurity ionization energies. Therefore, the energy of the photon emitted as a result of the DAP recombination is given by:

$$E_{\text{DAP}} = E_{\text{g}} - (E_{\text{D}} + E_{\text{A}}) + \frac{q^2}{4\pi\epsilon_r\epsilon_0 r}, \quad (7.11)$$

where  $E_g$  is the band gap energy,  $E_D$  is the donor ionization energy,  $E_A$  is the acceptor ionization energy,  $q$  is the elemental charge,  $\epsilon_r$  is the relative dielectric constant and  $\epsilon_0$  is the permittivity of free space.

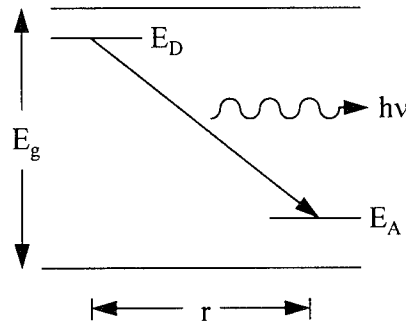


Figure 7-4. Schematic drawing of donor-acceptor pair radiative recombination. Donor-bound electrons and acceptor-bound holes are separated by some distance,  $r$ , in the crystal lattice. (Pankove, 1971:143)

Radiative transitions between pairs separated by a large  $r$  are less probable than those between pairs separated by a smaller  $r$ , *i.e.*, pairs separated by larger  $r$  have longer radiative lifetimes. Therefore, from a temporal point of view, the observed luminescence favors the nearer pairs. However, the number of possible pairs separated by any  $r$  increases as  $r$  increases, so from a spatial point of view, the observed luminescence favors the farther pairs. This competition causes the luminescence to peak at an energy associated with some intermediate separation,  $r$ , depending on the level of excitation (Pankove, 1971:143). At low excitation, even though the near pairs recombine at a relatively faster rate, the many more far pairs dominate the luminescence. The PL peak,

then, occurs at lower energies. As excitation is increased, far pair recombination is limited by longer lifetimes, and saturates. The rate of near pair recombination continues to increase since, with its shorter lifetime, it is not saturated by the increased rate of excitation. Thus, the PL peak position shifts to higher energies.

The assignment of peak  $E_{DAP1}$  as being due to DAP recombination with one impurity level associated with subpeak  $E_{DIH}$  implies another impurity level of opposite type exists at an energy of  $\sim 12$  meV from the band edge. However, no F-B peak was observed at this position (*i.e.*, at  $\sim 405$  meV at 4 K or at  $\sim 402$  meV at 32 K). Previously reported impurity levels near this energy have been assigned as acceptor levels in Ge- (14 meV) and Sn-doped (10 meV) bulk InAs (Guseva, 1975:591), and as donor levels in InAs epitaxy on GaAs substrate (14 meV) and on Si substrate (10 meV) (Grober, 1989:4079), and in homoepitaxy (10-14 meV) (Fang, 1990:7034).

The peak labeled  $E_{D2}$  in Figures 7-1 is located at  $390 \pm 0.7$  meV at temperatures 4-64 K before shifting to lower energies at higher temperatures (379 meV at 128 K) as shown in Figure 7-5. Since the band edge, labeled  $E_g$  in Figure 7-5 and determined from the absorption measurements, shifts to lower energies with increased temperature, peak  $E_{D2}$  shifts from  $\sim 27$  meV from the band edge at 4 K to  $\sim 21$  meV from the band edge at 64 K. Peak  $E_{D2}$  becomes the largest below-band-edge peak in the PL spectrum at the higher temperatures, since the other shallower peaks have decreased due to ionization ( $k_B T$  for 128 K is only 11 meV). A previously reported PL peak at 20-25 meV from the band edge



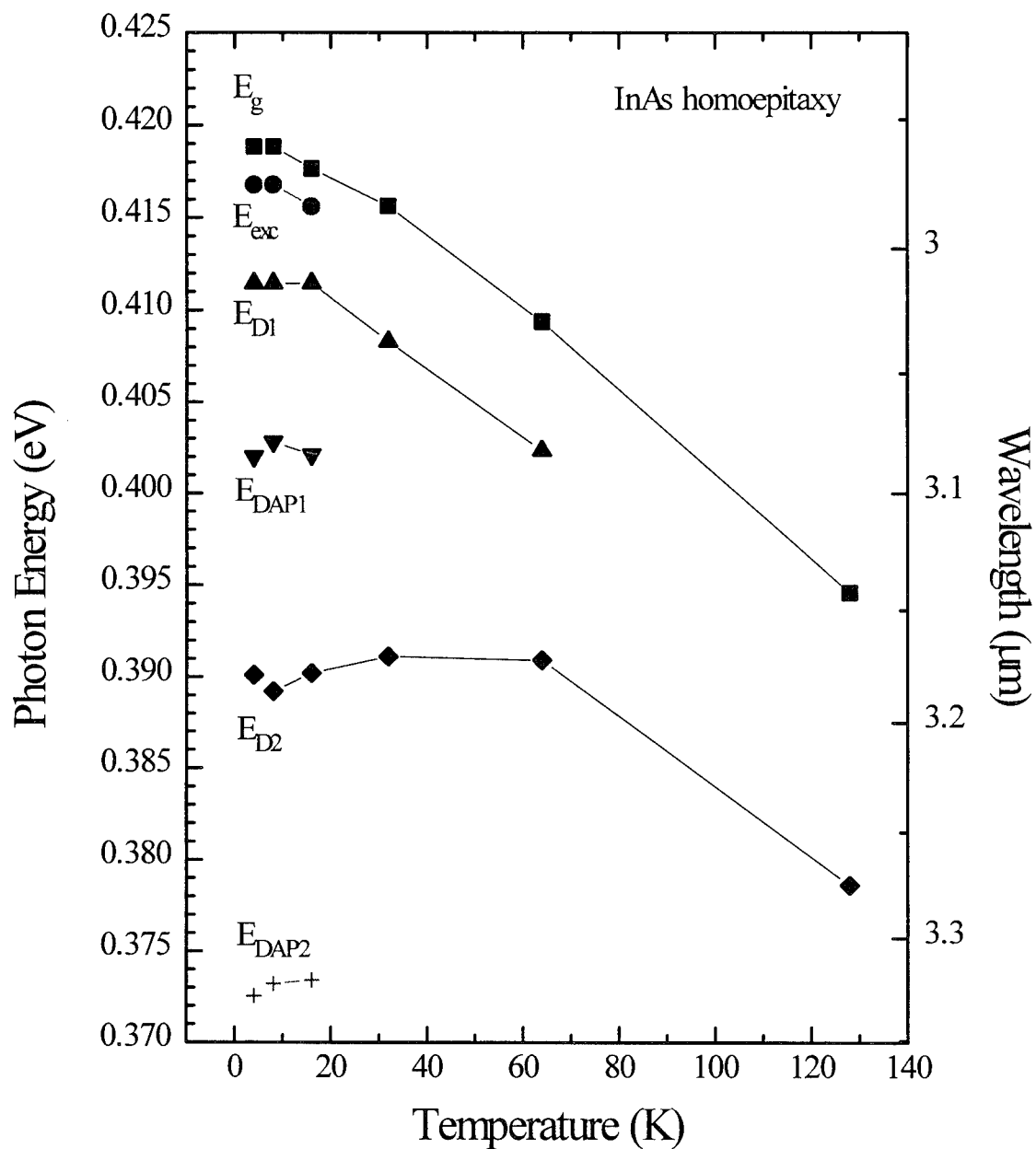


Figure 7-5. Photoluminescence peak positions as a function of temperature for homoepitaxial InAs. The PL spectrometer resolution is 0.8 meV.

in Sn-doped epitaxial InAs was assigned as a bound donor to free hole transition (Guseva, 1975:591).

Finally, the peak labeled  $E_{\text{DAP2}}$  was very weak and observed only at temperatures below 32 K. Again, since peak  $E_{\text{D1H}}$  also disappears due to ionization at  $\sim 32$  K, it is possible that peak  $E_{\text{DAP2}}$  is due to DAP recombination which involves the impurity level associated with  $E_{\text{D1H}}$ . However, because of the low intensity of peak  $E_{\text{DAP2}}$ , no peak shift with increased laser excitation power could be observed. Peak  $E_{\text{DAP2}}$  is located at  $373 \pm 0.6$  meV (or  $\sim 45$  meV from the band edge). Again, such a DAP transition would imply the existence of another impurity level of opposite type at  $\sim 42$  meV from the band edge (or a PL peak at  $\sim 376$  meV); this was not observed. These energy levels are deeper than any previously reported impurity levels for InAs. The deepest were at 35 meV and assigned as donor levels in: Te-doped epitaxy (Allaberenov, 1972a5:2050); undoped epitaxy on GaAs substrates (Grober, 1989:4079); and bulk InAs (Fang, 1990:7034).

In summary, the band edge peaks, either excitonic or band-to-band, were observed in PL experiments from an undoped InAs homoepitaxial sample grown by MBE, along with five peaks below the band edge. Three of these below-band-edge peaks were determined to be due to F-B recombination with the associated impurity levels of approximately 3, 7 and 21-27 meV from the band edge. The two shallower levels have not been previously reported for InAs PL, where the shallowest level is 10 meV, but a peak at 20-25 meV from the band edge has been for Sn-doped epitaxial InAs.

One of the other two PL peaks observed in these current experiments is believed to be due to DAP recombination since it shifts to higher energies with increased laser excitation power. Furthermore, the observed 3 meV impurity level is believed to be one of the impurity levels involved since the relatively strong DAP peak disappears with the ionization of this level. The remaining PL peak was observed at ~45 meV from the band edge which is significantly deeper than the deepest levels previous reported in InAs at 35 meV below the conduction band. This peak is also believed to be due to DAP recombination, with the 3 meV impurity level again involved since this peak also disappears with the ionization of the 3 meV level.

#### **InAs Heteroepitaxy on GaSb**

Similar to the InAs homoepitaxial sample, undoped InAs epitaxy grown by MBE on (100) n-GaSb substrate was also studied by PL and absorption. The PL spectra at 2 K from the heteroepitaxial InAs is shown in Figure 7-6 for three laser excitation powers. It is shown in Figure 7-6 that there are only three distinct peaks present. A comparison of the homoepitaxial and heteroepitaxial InAs spectra (Figures 7-1 and 7-6) shows the PL peaks of the heteroepitaxial sample have been broadened with linewidths of ~13 meV as compared to ~4 meV for the homoepitaxial sample. This linewidth broadening indicates the crystal quality for the heteroepitaxial sample is degraded, probably due to increased misfit dislocation densities resulting from the lattice mismatch of the epilayer with the GaSb substrate, where the mismatch is  $\Delta a/a = -0.617\%$ .

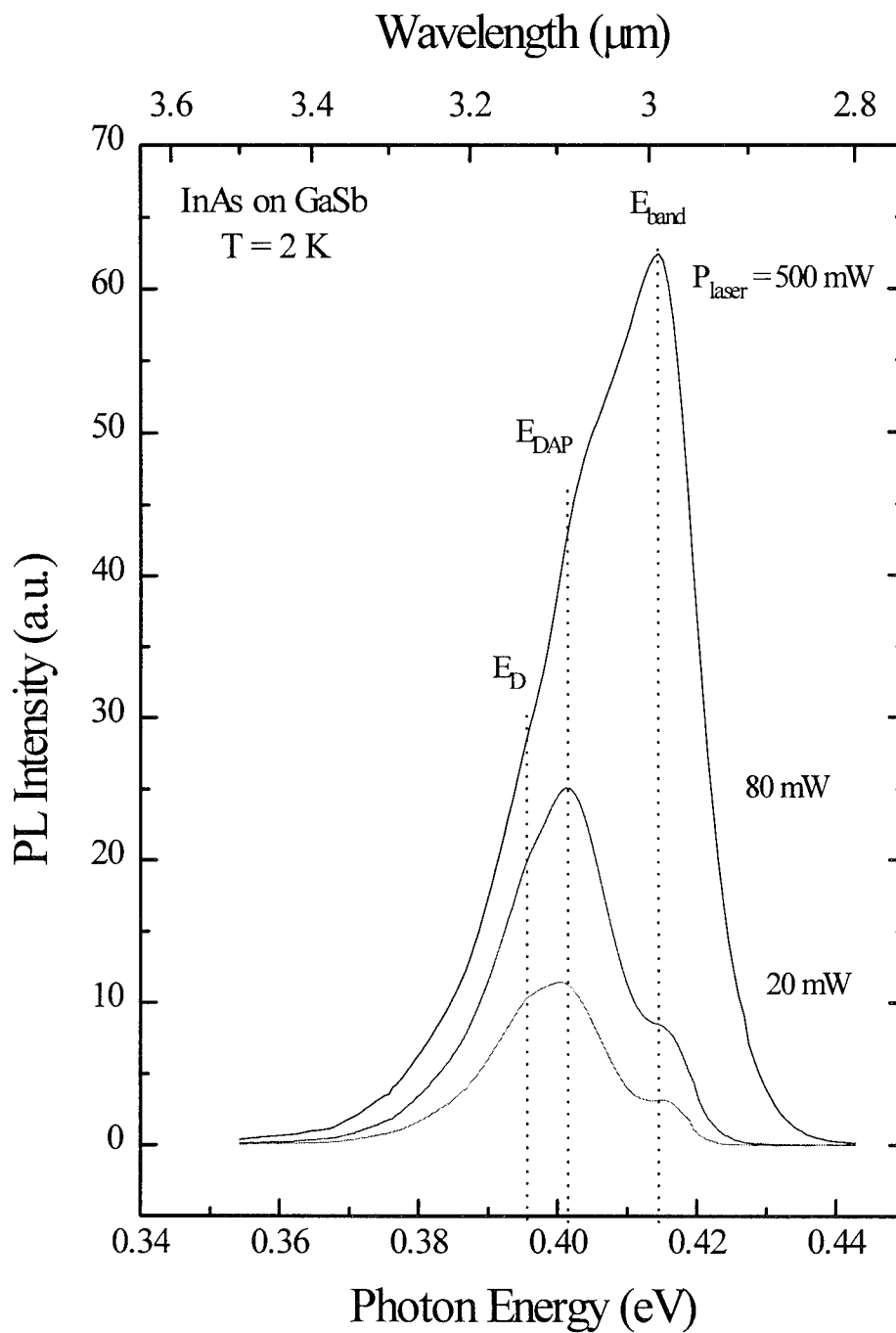


Figure 7-6. Low temperature photoluminescence spectra of MBE-grown InAs on n-GaSb substrate. The PL spectrometer resolution is 1.6 meV.

A comparison of the PL and absorption spectra for the InAs heteroepitaxial sample, as was done for the homoepitaxial InAs sample, identified the highest energy peak, labeled  $E_{\text{band}}$  in Figure 7-6, as being due to band-to-band recombination. Because of a high dislocation density due to the lattice mismatch, it is unlikely that any excitonic recombination would be observed as it was for the homoepitaxial sample; none was. Peak  $E_{\text{band}}$  is positioned at  $415 \pm 1.6$  meV at temperatures below 16 K, and is at most a few meV above the band edge due to its band-to-band nature, the low lattice temperature and its consistent position at low laser excitation powers. This position is compared to the excitonic band gap energies of  $417 \pm 0.8$  meV observed for the current InAs homoepitaxial sample at 4 K, and  $415.28 \pm 0.02$  meV for recently reported homoepitaxial InAs (Lacroix, 1995:1101).

As shown in Figure 7-6, at low laser excitation powers ( $< 160$  mW), peak  $E_{\text{band}}$  is relatively less intense than the two below-band-edge peaks. This indicates that as the two lower energy radiative transitions saturate with increased excitation, relatively more radiative transitions occur directly between the bands, probably due to the higher density of states. At temperatures above 32 K, the band edge peak is the dominant peak in the PL spectrum at all excitation levels.

The middle peak, labeled  $E_{\text{DAP}}$  in Figure 7-6, is positioned at an energy of  $400 \pm 1.5$  meV at low laser excitation powers (10 mW) and low temperatures ( $< 16$  K), and moves to higher energies with increased excitation powers at a rate of 2.8 meV/decade of excitation. This type of peak shift is indicative of DAP recombination

and implies the existence of impurity levels of opposite type at energies  $<15$  meV from the bands. The temperature dependencies of the heteroepitaxial PL peak positions are shown in Figure 7-7, along with that of the energy gap,  $E_g$ , as measured by the absorption experiment. As indicated symbolically in Figure 7-7, peak  $E_{DAP}$  is no longer observed at temperatures above 32 K.

The position of peak  $E_{DAP} \sim 15$  meV from the band edge is comparable to the position of the DAP peak,  $E_{DAP1}$ , in the InAs homoepitaxial sample. Also, the disappearance of peak  $E_{DAP}$  at temperatures above 32 K is comparable to the behavior of the homoepitaxial DAP peak. Thus, it is possible that a shallow level exists in the heteroepitaxial material, similar to the 3 meV level in the homoepitaxial material, which is unresolved in the heteroepitaxial PL spectra.

The position of the lowest energy peak, labeled  $E_D$  in Figure 7-6 and 7-7, is at an energy of  $395 \pm 1.5$  meV in the 2 K spectrum, which is  $\sim 20$  meV below the band edge, and is invariant with laser excitation power. This behavior is indicative of F-B recombination. This position is comparable to, though slightly shallower than, the F-B peak,  $E_{D2}$ , in the homoepitaxial PL spectra at 21-27 meV below the band edge. However, unlike the homoepitaxial peak  $E_{D2}$ , the heteroepitaxial peak  $E_D$  does not persist to higher temperatures. Impurity peaks previously reported at 20 meV from the band edge were assigned as due to bound donor to free hole transitions in Te-doped bulk (Allaberenov, 1972a5:2050) and Sn-doped bulk InAs, and free electron to bound acceptor transitions in Si-doped bulk InAs (Guseva, 1975:591).

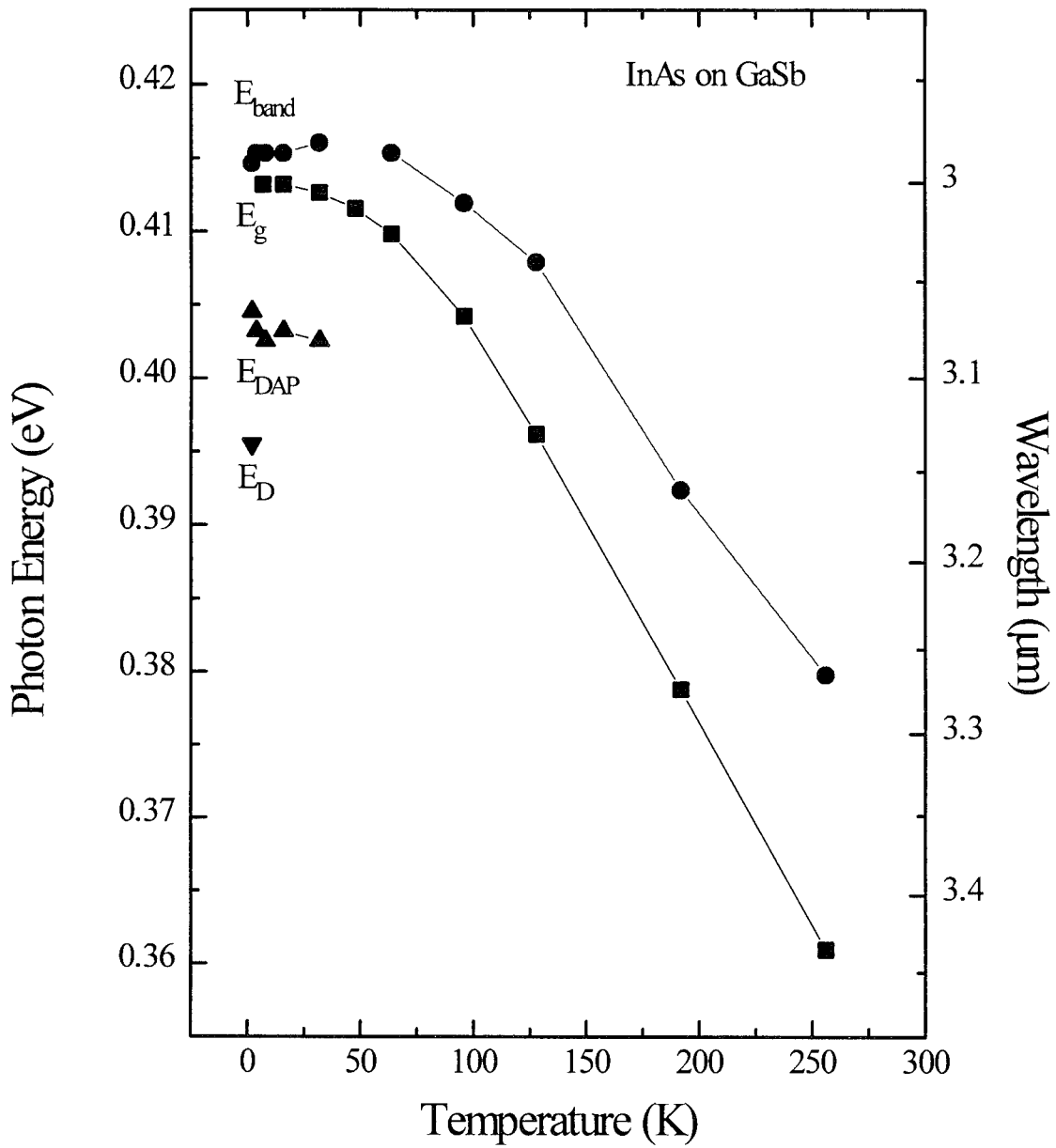


Figure 7-7. Photoluminescence peak positions as a function of temperature for MBE-grown InAs on n-GaSb substrate. The PL spectrometer resolution is 1.6 meV.

In summary, fewer peaks were observed in the PL spectra of heteroepitaxial InAs material grown by MBE on GaSb than in those of homoepitaxial InAs, and the linewidths of these peaks were broadened by ~4 times those of the homoepitaxial material. However, the positions and behavior of the two PL peaks observed below the band edge in the heteroepitaxial InAs were similar to peaks in the homoepitaxial spectra.

One heteroepitaxial peak was observed at ~15 meV below the band edge, shifted to higher energies with increased laser excitation power, and was no longer observed at temperatures above 32 K. This behavior is similar to that of a DAP peak in the homoepitaxial material which was associated with an observed 3 meV impurity level. This implies that it is possible that a similar shallow level, though unresolved, exists in the heteroepitaxial material, as well.

The second heteroepitaxial PL peak was observed at ~20 meV below the band edge and is believed to be due to a F-B transition. This position is slightly shallower than the F-B peak observed at 21-27 meV below the band edge in the homoepitaxial sample.

### **Undoped InAs<sub>1-x</sub>Sb<sub>x</sub>: Single-Peaked Spectra**

The main objective of this research was to assess the material quality of undoped MBE-grown InAs<sub>1-x</sub>Sb<sub>x</sub> at compositions nearly lattice-matched to (100) GaSb substrates ( $0.045 \leq x \leq 0.192$ ). With the InAs PL spectra in hand to reference peak position and linewidths, work on the main objective could be continued by making PL measurements on the undoped InAs<sub>1-x</sub>Sb<sub>x</sub> samples.



Twelve samples were studied as listed in Tables 4-1 and 4-2. The PL experiment for 11 of these 12 samples resulted in what is categorized here as a single peaked spectrum. Actually, a second peak was observed in spectra from several of these samples, but it was concluded this second peak was a phonon replica of the main peak, and not the result of a transition between bands or extrinsic levels. These “single-peaked” spectra are analyzed here.

**Spectra.** Temperature- and excitation-dependent PL experiments were performed on the nominally undoped  $\text{InAs}_{1-x}\text{Sb}_x$  epitaxial samples. A set of PL spectra for one sample at a single temperature and several laser excitation powers is shown in Figure 7-8. The single-peaked PL spectra of Figure 7-8 is very similar to that for the other ten samples at 4 K.

The spectra typically contained only one featureless peak. Spectra from seven of the samples also contained a much smaller peak  $27\text{-}29 \pm 0.5$  meV below the main peak, as shown in Figure 7-8, which has been assigned as an LO-phonon replica. The phonon dispersion relations for InAs and InSb were shown in Figure 2-7 where the energy of the LO-phonon at the  $\Gamma$ -point was 29.6 meV for InAs and 24.4 meV for InSb. A linear interpolation between these two binary points, as shown by Li in Figure 3-13 (Li, 1992:567), gives an estimate of  $\sim 29$  meV for the LO-phonon energy for the  $\text{InAs}_{1-x}\text{Sb}_x$  ternaries in the range of compositions in which the secondary peak was observed ( $0.045 \leq x \leq 0.096$ ).

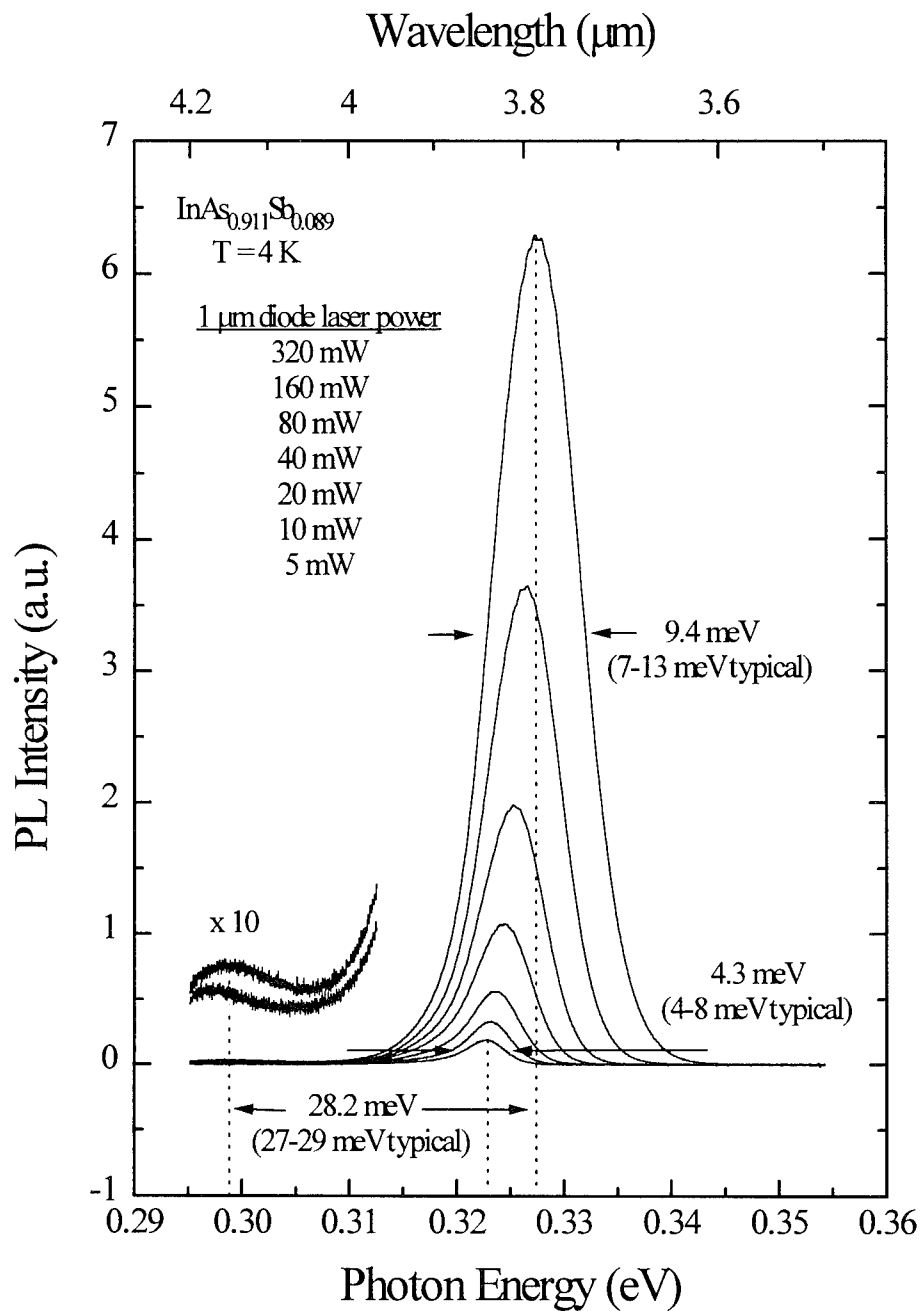


Figure 7-8. Typical low temperature photoluminescence spectra for MBE-grown  $\text{InAs}_{1-x}\text{Sb}_x$  on GaSb substrate. The LO-phonon replica appears in several samples at energies 27-29 meV below the main peak. The main peak shifts to higher energies with increased excitation. The PL spectrometer resolution is 0.5 meV.

Observation of the TO-phonon in  $\text{InAs}_{1-x}\text{Sb}_x$  at  $\sim 29$  meV by far-IR reflectivity has been reported (Lucovsky, 1970:1397), as were the InAs-like LO-phonon at  $\sim 30$  meV and TO-phonon at  $\sim 27$  meV by Raman scattering (Cherng, 1988:886; Li, 1992:567) as described in Chapter III, InAsSb Material Characterization. The observation of a phonon replica in PL measurements of  $\text{InAs}_{1-x}\text{Sb}_x$  has not been reported in the past (see Chapter III, InAsSb Material Characterization including Fang, 1990:7034; Yen, 1988a:489; Yen, 1988b:952; Elies, 1993:159; Mao, 1993:108). A summary of the LO-phonon energies measured for these seven samples is listed in Table 7-1.

Table 7-1. Photoluminescence characteristics of 11  $\text{InAs}_{1-x}\text{Sb}_x$  samples grown by MBE on GaSb substrates.  $h\nu_{\text{LO}}$  is the energy difference between the LO-phonon replica observed and the main PL peak.  $\text{FWHM}_{\text{min}}$  is the minimum linewidth observed for the main PL peak for that sample. The magnitude of the PL peak shift to higher energies with increased excitation power is given in meV/decade of excitation power.

Sample	x	$h\nu_{\text{LO}}$ (meV)	$\text{FWHM}_{\text{min}}$ (meV)	Peak Shift (meV/decade)
93-044	0.031	-	4.8	1.2
93-114	0.045	28.2	5.9	2.7
93-030	0.052	28.1	4.5	1.4
93-113	0.059	29.3	5.9	2.0
93-112	0.071	-	6.1	3.1
93-048	0.077	27.2	5.4	2.6
93-045	0.089	28.6	4.3	2.9
93-068	0.095	28.2	6.2	2.3
93-092	0.096	27.2	6.1	2.6
93-120	0.097	-	6.9	2.7
94-035	0.179	-	8.7	3.8

The linewidths of the main peaks in the single-peaked PL spectra from these 11 samples ranged between 4.3-8.7 meV at low excitations (5 mW), with the narrowest linewidth being for the lattice-matched sample,  $\text{InAs}_{0.911}\text{Sb}_{0.089}$ , and the largest being for the sample with the highest Sb content,  $\text{InAs}_{0.821}\text{Sb}_{0.179}$ . The narrowest linewidths previously reported for  $\text{InAs}_{1-x}\text{Sb}_x$  PL are: 5.15 meV for an impurity-related peak, and 5.76 meV for a band edge peak from MBE-grown  $\text{InAs}_{0.96}\text{Sb}_{0.04}$  on an InAs substrate (Yen, 1988a:489); and 22 meV (at 78 K) for LPE-grown  $\text{InAs}_{0.905}\text{Sb}_{0.095}$  on GaSb (Mao, 1993:108) (see Chapter III, Material Characterization). A summary of the linewidths measured for these current MBE-grown samples at low excitation powers is also given in Table 7-1.

The narrow linewidths measured for these 11 samples and the observation of the LO-phonon replicas in several of them indicate the quality of this material is very high in relation to the material on which previous PL results have been reported in the literature. However, additional structure in the PL spectrum was not observed as is expected for high quality material, and without additional structure, identification of the recombination mechanism responsible for the single luminescence peak is difficult.

As shown in Figure 7-8, the PL peak shifted to higher energies with increased excitation. The peak shift was nearly linear with respect to the log of the laser power for all the samples as shown in Figure 7-9, and the magnitudes of the peak shift ranged from 1.2-3.8 meV/decade of excitation at a PL temperature of 4 K. Coincidentally, the lowest shift occurred for the sample with the lowest Sb content ( $\text{InAs}_{0.969}\text{Sb}_{0.031}$ ) and the highest

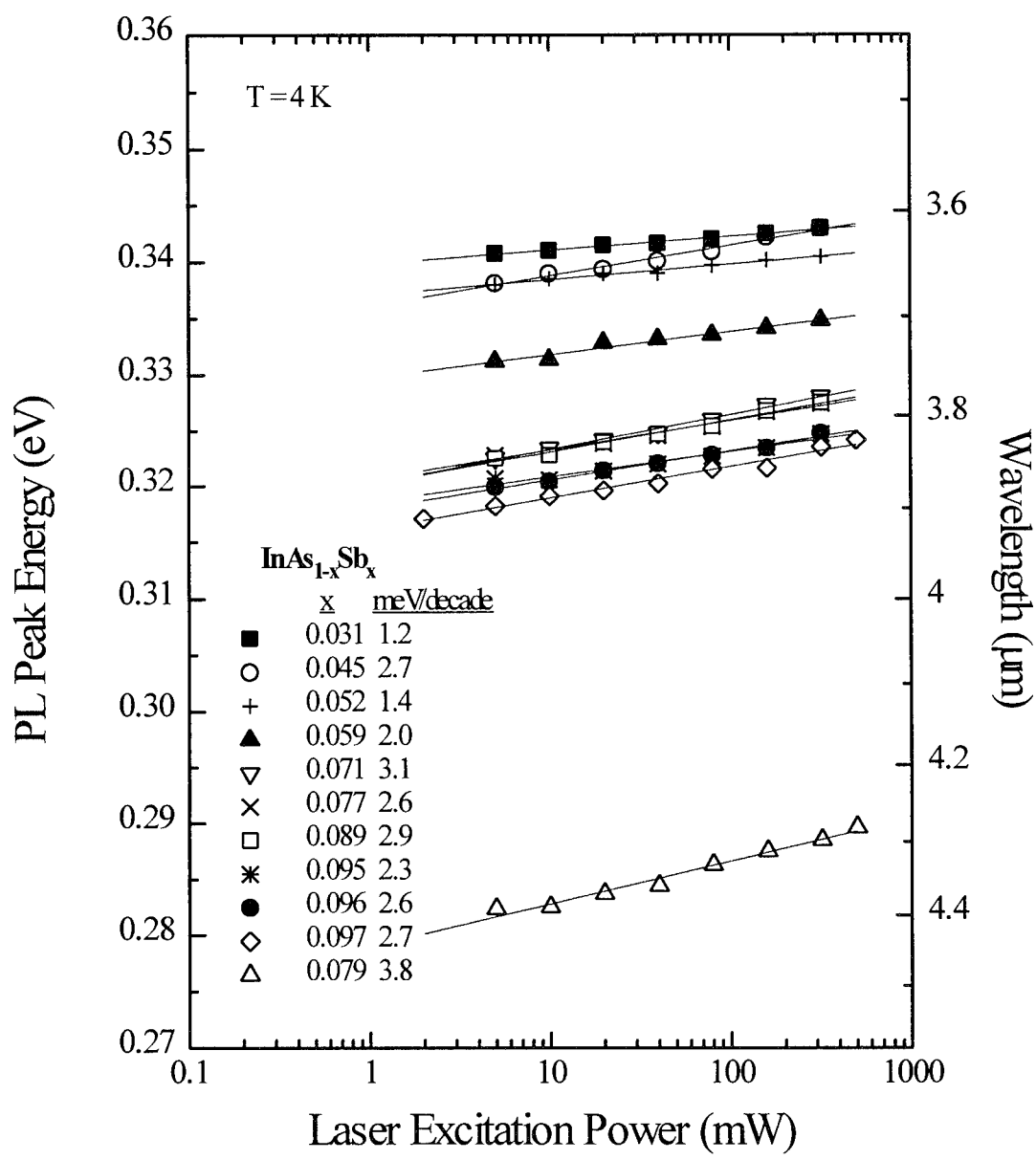


Figure 7-9. PL peak positions as a function of laser excitation power for 11 MBE-grown samples of InAs<sub>1-x</sub>Sb<sub>x</sub> on GaSb substrate at 4 K. The solid lines show the least squares linear fit to the data. The numbers in the legend show the magnitude of the peak shift for each sample in meV/decade of excitation power as given by the slope of the linear fit.

for the sample with the highest Sb content ( $\text{InAs}_{0.821}\text{Sb}_{0.179}$ ), but this trend did not hold for the intermediate samples. A summary of the magnitude of the 4 K peak shift for each sample is given in Table 7-1.

There are several radiative recombination mechanisms which result in a PL peak which shifts to higher energies as the excitation is increased: the donor-acceptor pair (DAP) as described in the InAs Homoepitaxy section above, alloy-broadened excitonic, band-to-band or band-to-band with additional broadening such as phase separation. Each of these mechanisms will now be analyzed.

The DAP recombination was described above and shown schematically in Figure 7-4, and the energy of the DAP transition was given by Eq (7.11). Because this transition involves two impurity levels whose energies lie within the energy gap, the DAP PL peak is positioned well below the band edge. Figure 7-10 shows a comparison of the PL and absorption spectra for the  $\text{InAs}_{0.911}\text{Sb}_{0.089}$  sample at several temperatures between 6 and 128 K. As shown in the figure, the PL peak is not below the band edge, but at or above the band edge for all the temperatures. Therefore, it is concluded the observed PL peak is not the result of a DAP transition. PL-absorption comparisons were made for all the samples with similar results.

**Alloy-Broadened Excitonic Recombination.** Since the comparison of PL and absorption data in Figure 7-10 showed the PL peaks to be near the band edge, the second recombination mechanism mentioned, alloy-broadened excitonic, is a possibility. Although excitonic transitions are slightly below the band edge, as shown for

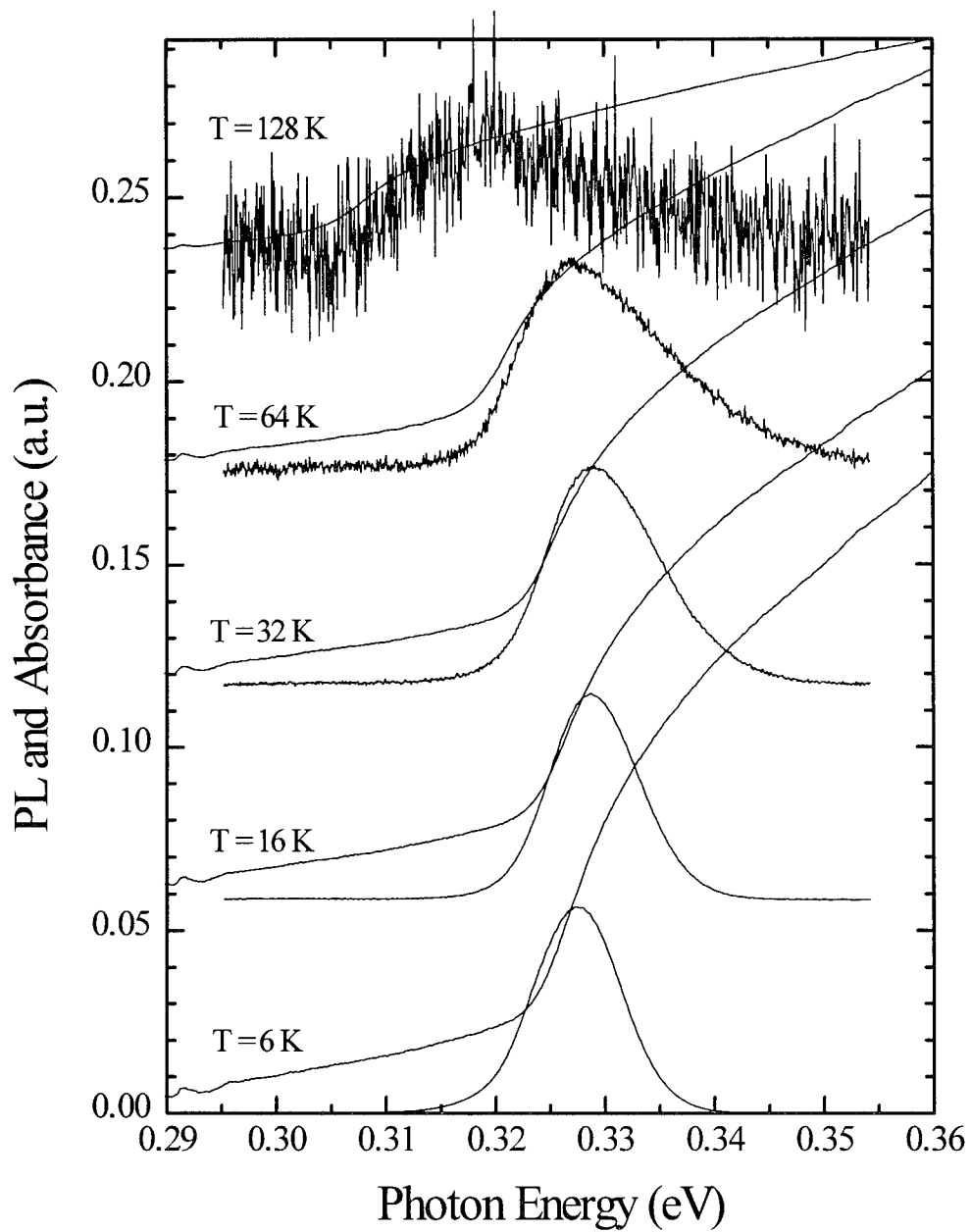


Figure 7-10. Comparison of photoluminescence and absorption spectra for MBE-grown  $\text{InAs}_{0.911}\text{Sb}_{0.089}$  on GaSb substrate shows the radiative recombination to be band-to-band. The PL spectrometer resolution is 0.5 meV.

homoepitaxial InAs in Figure 7-2, it is possible that these peaks are still excitonic if a broadening mechanism exists in the material which softens the rise of the absorption edge and broadens the excitonic PL peak. To determine whether or not these PL peaks are excitonic, the theoretical excitonic linewidth can be calculated. The theoretical linewidths can then be compared to the observed PL linewidths to determine if excitonic recombination is a reasonable assumption.

The lineshape for excitonic recombination is calculated based on a random anion distribution in the  $\text{InAs}_{1-x}\text{Sb}_x$  material as described by known ternary alloy exciton models (Singh, 1984:1075; Schubert, 1984:1075; Schubert, 1986:2991). This distribution accounts for the crystal's statistical compositional variation in real space, and thus, the statistical variation of the energy gap in real space, as well. Free carriers migrate to the lowest energy sites in the lattice in some migration time, where they recombine radiatively, emitting a low energy photon. At higher excitations, however, the radiative recombination lifetime of the carriers is much less than the migration time, so the carriers become distributed homogeneously in the crystal, and radiative recombination takes place from higher energy sites, as well, shifting the PL peak to higher energies.

The model for the recombination lineshape for this homogeneous distribution of carriers assumes a binomial distribution of Sb atoms within an excitonic volume,  $V_{\text{exc}}$ , given by:

$$V_{\text{exc}} = \frac{4}{3} \pi a_{\text{exc}}^3, \quad (7.12)$$



where  $a_{\text{exc}}$  is the excitonic radius given by the hydrogenic model as:

$$a_{\text{exc}} = \frac{\epsilon_r \epsilon_0 h^2}{4\pi^2 m_r q^2}. \quad (7.13)$$

The relative dielectric constant for  $\text{InAs}_{1-x}\text{Sb}_x$  is linearly interpolated from those of the binaries, InAs (Eq (7.2) and InSb (Madelung, 1991:147), as:

$$\epsilon_r(x) = 12.25 - 3.43 x. \quad (7.14)$$

The reduced effective mass was given in Eq (7.9) as:

$$\frac{1}{m_r} = \frac{1}{m_n} + \frac{1}{m_p}, \quad (7.9)$$

Here, the  $\text{InAs}_{1-x}\text{Sb}_x$  conduction band electron effective mass is taken from Rogalski as shown in Figure 3-12 to be (Rogalski, 1989:35):

$$m_n(x) = 0.0219 - 0.0338 x + 0.0206 x^2 + 0.00342 x^3 \quad (7.15)$$

The equivalent valence band hole effective mass,  $m_p$ , is derived from the effective masses of the heavy and light hole bands, which are interpolated from the valence band hole effective masses of the binaries, InAs (Eq (7.4)) and InSb (Madelung, 1991:142). The

heavy hole effective masses along the [111], [110] and [100] directions are

$$m_{ph111}(x) = 0.43 + 0.02 x, \quad (7.16a)$$

$$m_{ph110}(x) = 0.43 - 0.01 x, \quad (7.16b)$$

$$m_{ph100}(x) = 0.35 - 0.01 x, \quad (7.16c)$$

respectively. The equivalent heavy hole effective mass is then (McKelvey, 1986:301):

$$m_{ph} = (m_{ph111} m_{ph110} m_{ph100})^{1/3} \quad (7.17)$$

The light hole effective mass is also interpolated from the binaries (Eq (7.6) and (Madelung, 1991:142) as:

$$m_{pl}(x) = 0.026 - 0.0102 x \quad (7.18)$$

The equivalent effective mass of valence band holes was given in Eq (7.8) as:

$$m_p = (m_{ph}^{3/2} + m_{pl}^{3/2})^{2/3}. \quad (7.8)$$

The excitonic radius and volume of Eqs (7.12) and (7.13) are calculated using these results.

Returning to the model, the probability of finding  $n$  Sb atoms in  $V_{exc}$  of  $InAs_{1-x}Sb_x$  material is given by:

$$p(n) = \binom{KV_{exc}}{n} x^n (1-x)^{KV_{exc}-n}. \quad (7.19)$$

Here, there are  $KV_{exc}$  anions in the excitonic volume, since  $K$  is the density of anions in the zincblende lattice with lattice constant,  $a_0$ , given as:

$$K = 4a_0^{-3}. \quad (7.20)$$

The lattice constant,  $a_0$ , for  $InAs_{1-x}Sb_x$  is given by Vegard's law (Eq 4.8) and the lattice constant of the binaries (Eqs 2.4) as:

$$a_0(x) = 6.0583 + 0.42107 x \text{ \AA}. \quad (7.21)$$

The standard deviation of anions in the excitonic volume, given by:

$$\sigma = [KV_{exc} x(1 - x)]^{1/2}, \quad (7.22)$$

leads to the compositional standard deviation,

$$\sigma_x = \frac{\sigma}{KV_{exc}}. \quad (7.23)$$

Thus, the standard deviation of the energy gap is given by:

$$\sigma_E = \left| \frac{dE_g}{dx} \right| \sigma_x, \quad (7.24)$$

where the possible values for  $dE_g/dx$  were obtained from the compositional dependencies

of the energy gap as determined by the low temperature absorption data for these samples (Eqs (6.25), (6.26) and (6.27)), and are given by:

$$|dE_g/dx| = 0.3777 \quad (7.25a)$$

$$|dE_g/dx| = 1.037 - 1.716 x. \quad (7.25b)$$

Since Eq (7.25b) gives the larger value of  $dE_g/dx$  over the region of compositions considered ( $0.031 \leq x \leq 0.192$ ) and, thus, the larger linewidth, it was used for the calculations.

Because the variance,  $\sigma^2$ , is large (*i.e.*,  $KV_{exc}$  is large) for all the  $x$ -compositions studied, the binomial distribution can be approximated by a Gaussian distribution of the form,

$$f(x) = \frac{1}{\sigma(2\pi)^{1/2}} \exp\left[-\frac{1}{2} \left(\frac{x-\mu}{\sigma}\right)^2\right], \quad (7.26)$$

where  $\mu$  is the mean value and  $\sigma$  is the variance. The maximum value of the distribution occurs at the mean value, so the half maximum value is given by:

$$\frac{1}{2} = \exp\left[-\frac{1}{2} \left(\frac{x-\mu}{\sigma}\right)^2\right], \quad (7.27)$$

or, rearranging,

$$x - \mu = (\ln 4)^{1/2} \sigma \quad (7.28)$$

Thus, the full width at half maximum (FWHM) of the Gaussian distribution is related to the standard deviation of the energy gap from the binomial distribution by:

$$\text{FWHM} = 2.36 \sigma_E. \quad (7.29)$$

The excitonic linewidth was calculated for all 11  $\text{InAs}_{1-x}\text{Sb}_x$  samples using Eqs (7.12)-(7.29) and found to be 0.3 meV in all cases. This linewidth is very narrow compared to alloy-broadened excitonic linewidths of other ternaries (*e.g.*, several meV in InGaAs (Schubert, 1986:2991)) as a result of the very small effective masses in the  $\text{InAs}_{1-x}\text{Sb}_x$  material system (*e.g.*,  $m_n \cong 0.017\text{-}0.020$  and  $m_p \cong 0.41$ , compared to  $m_n \cong 0.07\text{-}0.15$  and  $m_p \cong 0.53\text{-}0.81$  for AlGaAs (Pavesi, 1994:4779)).

This calculated linewidth of 0.3 meV is over an order of magnitude narrower than the narrowest linewidth of 4.3 meV observed in the PL experiments. Furthermore, it has been shown in other material systems that a classical calculation of the excitonic linewidth such as this tends to overestimate the experimental linewidth, while a quantum mechanical approach would result in a decreased linewidth (Pavesi, 1994:4779). Therefore, from these results, it is concluded that the PL peaks observed are not alloy-broadened excitonic in nature.

**Band-to-Band Recombination.** The third possible radiative recombination mechanism suggested for the observed PL peak which shifts to higher energies with increases excitation is band-to-band recombination. As shown by the comparison of PL and absorption data in Figure 7-10, this appears to be a likely candidate.

The lineshape of band-to-band emission is determined by the densities of states and carrier distributions of each band. The joint density of states, assuming only direct transitions between parabolic bands, was given in Eq (6.7) as:

$$g(h\nu) d(h\nu) = \frac{(2m_r)^{3/2}}{2\pi^2 \hbar^2} \sqrt{h\nu - E_g} d(h\nu). \quad (6.7)$$

The emission probability is given by the product of the carrier occupation probabilities for each band (Saleh, 1991:581), *i.e.*,

$$f_c(h\nu) = f_n(E_c)[1-f_p(E_v)] \quad (7.30)$$

where  $h\nu$  is the transition energy ( $h\nu=E_c-E_v$ ), and  $f_n(E_c)$  and  $f_p(E_v)$  are the Fermi distributions for the conduction and valence bands, respectively, given by:

$$f_n(E_c) = \frac{1}{1 + \exp\left(\frac{E_c - E_F}{k_B T}\right)} \quad (7.31a)$$

$$1 - f_p(E_v) = \frac{1}{1 + \exp\left(\frac{E_F - E_v}{k_B T}\right)}. \quad (7.31b)$$

When the Fermi energy,  $E_F$ , lies within the energy gap at least several  $k_B T$  away from the band edges, the Boltzmann function may be used to approximate the exponential

tails of the Fermi function. Eqs (7.31) become:

$$f_n(E_c) \cong \exp\left[-\frac{(E_c - E_F)}{k_B T}\right] \quad (7.32a)$$

$$1 - f_p(E_v) \cong \exp\left[\frac{-(E_F - E_v)}{k_B T}\right]. \quad (7.32b)$$

Thus, the radiated spectrum for band-to-band recombination,  $I(h\nu)$ , which is given by the product of Eqs (6.7) and (7.30), is given by:

$$I(h\nu) \propto (h\nu - E_g)^{1/2} \exp\left[-\frac{(h\nu - E_g)}{k_B T}\right] \quad (7.33)$$

The low energy side of the band-to-band PL peak is primarily modeled by the square root term of Eq (7.33), as is the absorption edge as was shown by Eq (6.9). The comparison of PL and absorption data in Figure 7-10 shows the low energy side of the PL peak coincides with the absorption edge for all the temperatures shown. This is a clear indication of band-to-band recombination. This trend was consistent for all the samples as shown by the PL/absorption figures included in Appendix E.

Since it is likely that the radiative recombination mechanism in these PL experiments is band-to-band in nature, certain characteristics of the energy bands may be learned from the PL spectrum. For example, just as the low energy side of the PL peak was primarily given by the joint density of states (the square root term of Eq (7.33)), the high energy side is primarily given by the carrier distributions, *i.e.*, the emission

probability (the exponential term of Eq (7.33)). Thus, the temperature,  $T$ , of Eq (7.33) affects the shape and position of the PL peak. However, since Eq (7.33) describes carrier transitions, the temperature term may not pertain to the lattice temperature, as might be initially assumed, but to the effective carrier temperature,  $T_e$ , which is different than the lattice temperature in a non-equilibrium system such as the PL experiment.

Steady state PL can be used to measure the effective carrier temperature of the excited distribution (Lyon, 1986:121). The emission probability under the Boltzmann approximation is given from Eqs (7.30) and (7.32) as:

$$f_e(h\nu) = \exp\left[\frac{-(h\nu - E_g)}{k_B T_e}\right]. \quad (7.34)$$

If the PL spectra are plotted semi-logarithmically, as in Figure 7-11, the exponential nature of the high energy tail of the PL peak appears linear. The carrier temperature,  $T_e$ , is obtained from the slope of the high energy side of the peak plotted in this manner, defined here as  $\xi_e$ , and Eq (7.34) as:

$$T_e = \frac{-\log e}{k_B \xi_e}. \quad (7.35)$$

As shown in the legend of Figure 7-11, the effective carrier temperature obtained from this slope increases as expected for increased laser excitation power.

Knowledge of the effective carrier temperature at several excitation levels can lead to an understanding of the thermalization process at work (Lyon, 1986:121). To



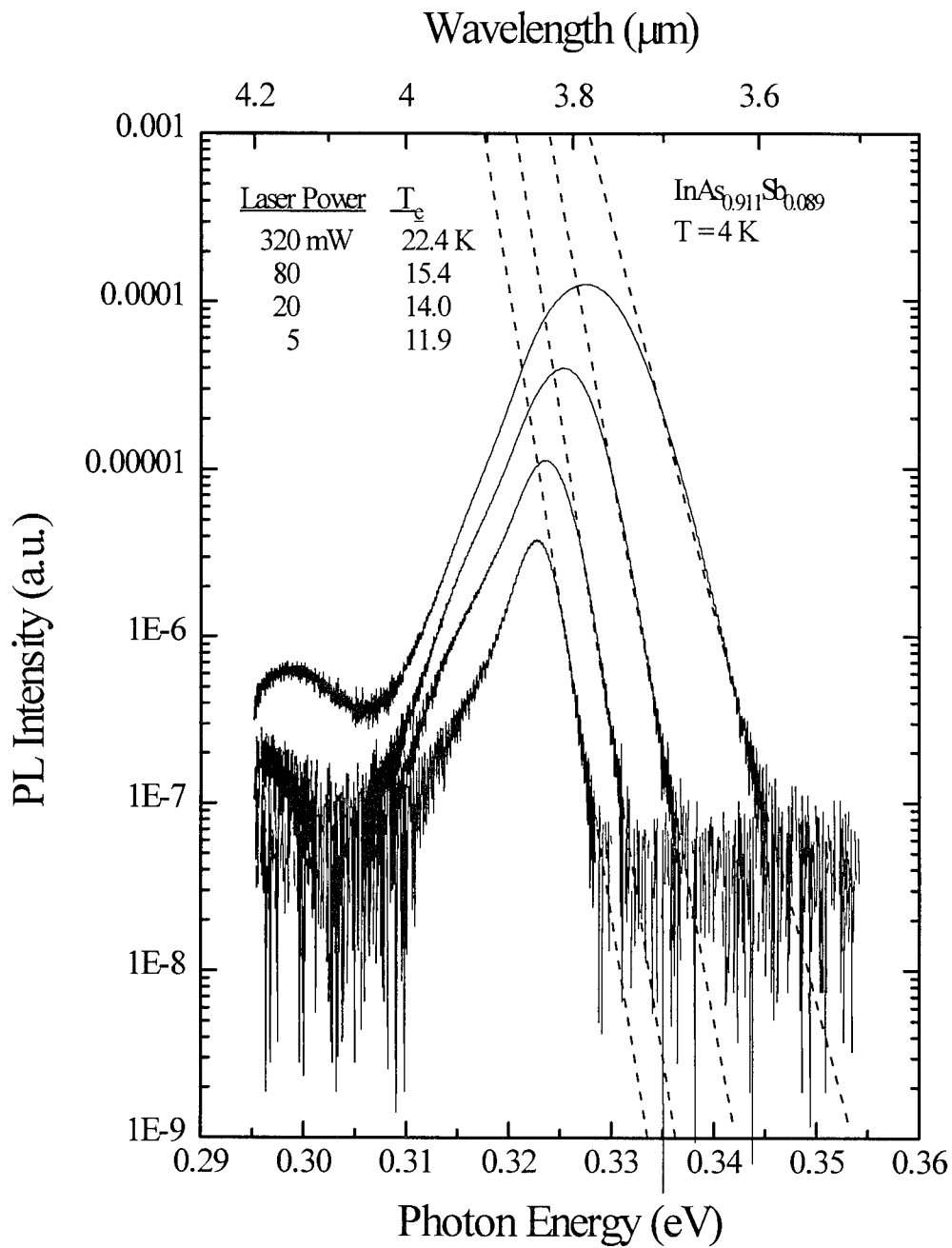


Figure 7-11. Effective carrier temperature,  $T_e$ , extracted from band-to-band PL peaks as shown. Dashed lines show the least squares linear fit to the high energy side of the peak.  $T_e$  is extracted from the slope of these lines using Eq (7.35). The PL spectrometer resolution is 0.5 meV.

review the possible thermalization or carrier cooling processes, the band structure of InAs shown in Figure 2-6 (included since the band structure of  $\text{InAs}_{1-x}\text{Sb}_x$  was unavailable, but assuming that of InAs is similar to it for  $x < 20\%$ ) is first considered. The vertical lines shown in Figure 2-6 joining the three valence bands with the conduction band near the  $\Gamma$ -point represent the absorption of  $1 \mu\text{m}$  ( $1.24 \text{ meV}$ ) radiation, *i.e.*, the laser radiation used in these PL experiments. Vertical transitions with this energy only occur in the regions of the bands near the  $\Gamma$ -point, which are approximately parabolic. Of the three valence bands, the majority of the excitation comes from the heavy hole band because of its higher density of states; and because the conduction band has a lower density of states, the majority of the excess kinetic energy is given to the conduction band electrons, as opposed to the free heavy holes. This kinetic energy must be lost for the carrier to reach thermal equilibrium with the lattice, *i.e.*, for the free carriers relax to the band edges.

Three processes of carrier thermalization which occur are shown schematically in Figure 7-12. In the first process, excited carriers thermalize among themselves (*i.e.*, scatter) until they reach a thermal distribution characterized by an effective carrier temperature, which is hotter than the lattice temperature. Thus, they are referred to as "hot carriers" and are not at thermal equilibrium with the lattice. Because of the differences in effective masses, electron-hole scattering is less likely than electron-electron scattering (Pavesi, 1994:4779).

Carrier-carrier interactions change neither the total energy nor the total momentum of the distribution, but they can cause a screening of the other thermalization

processes, *e.g.*, carrier-phonon scattering. Electron-phonon screening is more likely than hole-phonon screening since the higher effective mass of a hole means that hole-phonon scattering must involve a larger wave vector phonon; therefore, to screen hole-phonon interactions, a larger hole density is required (Lyon, 1986:121).

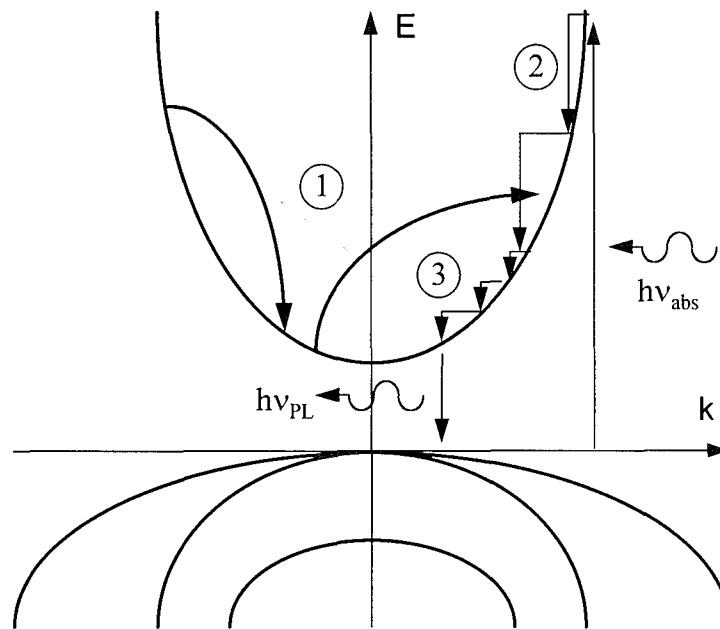


Figure 7-12. Schematic drawing of electron cooling processes: 1. Carrier-carrier interaction (scattering); 2. Optical phonon emission; and 3. Acoustic phonon emission.

The second and third thermalization processes shown schematically in Figure 7-12 are through phonon emission. Once the carrier distribution has thermalized among itself, the next step is thermalization with the lattice. The phonon dispersion relations for InAs and InSb were shown in Figure 2-7. Since the excitation was shown to occur near the  $\Gamma$ -point in Figure 2-6, the phonon dispersion must be considered there, as well. Near

the  $\Gamma$ -point, the energy of the acoustic phonons (LA and TA) is highly dependent on  $k$  and small, as shown in Figure 2-7. Therefore, emission of these acoustic phonons removes only a few meV of excess kinetic energy per phonon.

A much more efficient cooling process is the emission of optical phonons (LO and TO) whose energy is nearly independent of  $k$  near the  $\Gamma$ -point, and which removes  $\sim 29$  meV/phonon, as shown in Figure 2-7 and discussed above in the Spectra section. Also, the rate optical phonon emission is much faster than that of acoustic phonons; *e.g.*, in GaAs, the time for optical phonon emission is on the scale of femto- to pico-seconds while the time for acoustic phonon emission is on the scale of nonoseconds (Pavesi, 1994:4779). Carrier thermalization by optical phonon emission is efficient, but once the kinetic energy of the carrier is less than the LO-phonon energy, LO-phonons can no longer be emitted, and continued cooling must occur by acoustic phonon emission.

Alloy and defect scattering may be significant contributors to the phonon emission process, especially in a ternary material such as  $\text{InAs}_{1-x}\text{Sb}_x$ . However, their role is unclear at this time (Pavesi, 1994:4779).

A hot carrier must have at least as much kinetic energy as the phonon energy in order to emit such a phonon. The probability that a carrier has that much kinetic energy is given by (Lyon, 1986:121):

$$f(h\nu_{\text{ph}}) = \exp\left(\frac{-h\nu_{\text{ph}}}{k_B T_e}\right). \quad (7.36)$$

The energy loss rate of the carrier distribution due to phonon emission is the product of the phonon energy, the average phonon emission rate and the probability the carrier has that much energy, and is given by (Lyon, 1986:121):

$$\left\langle \frac{dE}{dt} \right\rangle_{\text{ph}}^e = \frac{-h\nu_{\text{ph}}}{\tau_{\text{ph}}} \exp\left(\frac{-h\nu_{\text{ph}}}{k_B T_e}\right), \quad (7.39)$$

where  $\tau_{\text{ph}}$  is used here as a simple phonon emission time averaged over the distribution, but is actually a complicated function dependent on each carrier's initial energy. In steady state, the power delivered to the carrier system must be equal to the sum of the luminescence power and the power dissipated to the lattice by phonon emission. Therefore, a relationship between the effective carrier temperature and the laser power can be derived from Eq (7.39) as:

$$\frac{1}{T_e} \sim \frac{-k_B}{h\nu_{\text{ph}} \log e} \log P_{\text{laser}} \quad (7.40)$$

where  $P_{\text{laser}}$  is the laser power.

Figure 7-11 showed how the effective carrier temperature for several laser excitation powers was extracted from the experimental PL data. A semi-logarithmic plot of inverse carrier temperature,  $1/T_e$ , versus pump intensity for a published GaAs experiment is shown in Figure 7-13. The solid line in Figure 7-13 shows the tangent to the curve over several decades of pump intensity. The phonon energy associated with the

primary carrier thermalization process over this range of pump intensity was extracted from the slope of this tangent, defined here as  $\xi_{ph}$ , using Eq (7.40) such that:

$$h\nu_{ph} = \frac{-k_B}{\xi_{ph} \log e}. \quad (7.41)$$

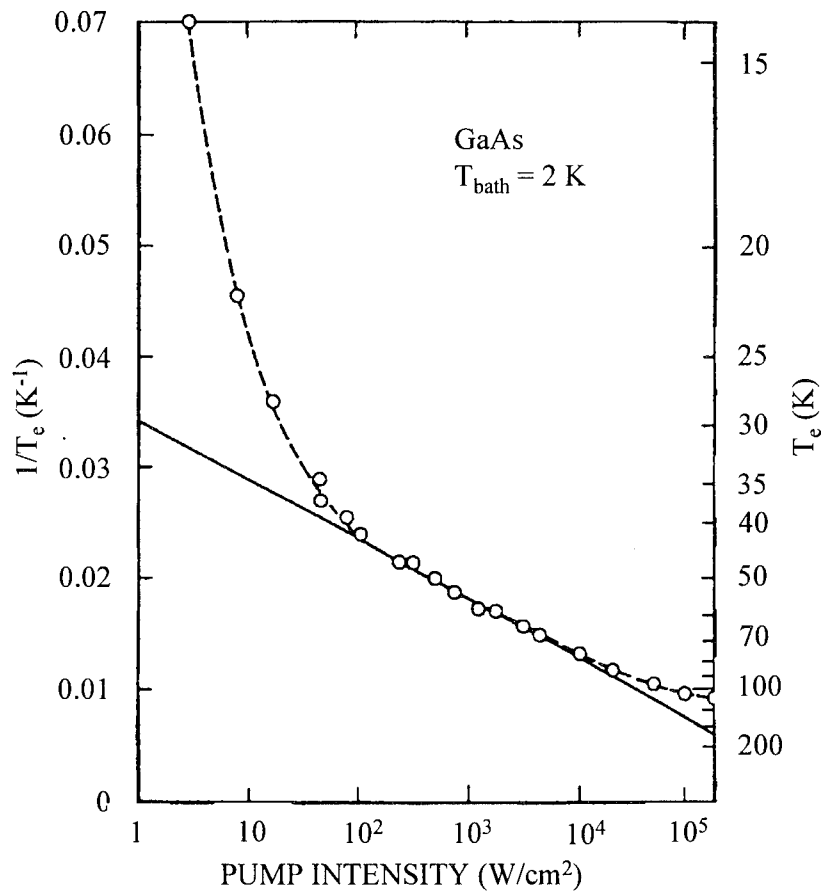


Figure 7-13. Inverse carrier temperature,  $1/T_c$ , as a function of excitation intensity for GaAs. The solid line has a slope of  $-k_B/h\nu_{LO}$  where  $h\nu_{LO}$  is the LO-phonon energy (36.7 meV). (Shah, 1978:43)

In Figure 7-13, the thermalization energy extracted from the tangential slope for these two decades of pump intensity was equal to the GaAs LO-phonon energy. This was expected since LO-phonon emission should be the dominant thermalization mechanism over a wide range of carrier temperatures as described above. At lower excitations, thus, lower carrier temperatures, the curve flattens to lower thermalization energies as the thermalization is no longer LO-phonon dominated, but becomes a mixture of optical and acoustic phonon emission (Lyon, 1986:121).

Plots of the inverse carrier temperatures, derived from the 4 K PL data of several of the  $\text{InAs}_{1-x}\text{Sb}_x$  samples studied here, as functions of laser excitation power are shown in Figure 7-14. The thermalization energies,  $h\nu_{\text{ph}}$ , derived using a linear fit of the data in this figure and the relationship of Eq (7.41), ranged between 9.3-14.5 meV as listed for each sample in Table 7-2. The optical phonon energies were shown earlier to be ~29 meV, and the acoustic phonon energies only a few meV, for these samples. Therefore, it is concluded that the 500 mW of excitation power from the InGaAs diode laser used for these experiments resulted in non-equilibrium carrier temperatures in the regime where carrier cooling was a mixture of optical- and acoustic-phonon emission. Higher excitation powers are needed to drive the system into the regime where the cooling is dominated by LO-phonon emission, only.

**Broadened Band-to-Band: Phase Separation.** From the comparisons of PL and absorption spectra as shown in Figure 7-10, it was concluded that the radiative transitions responsible for the observed PL peaks were band-to-band in nature. In this

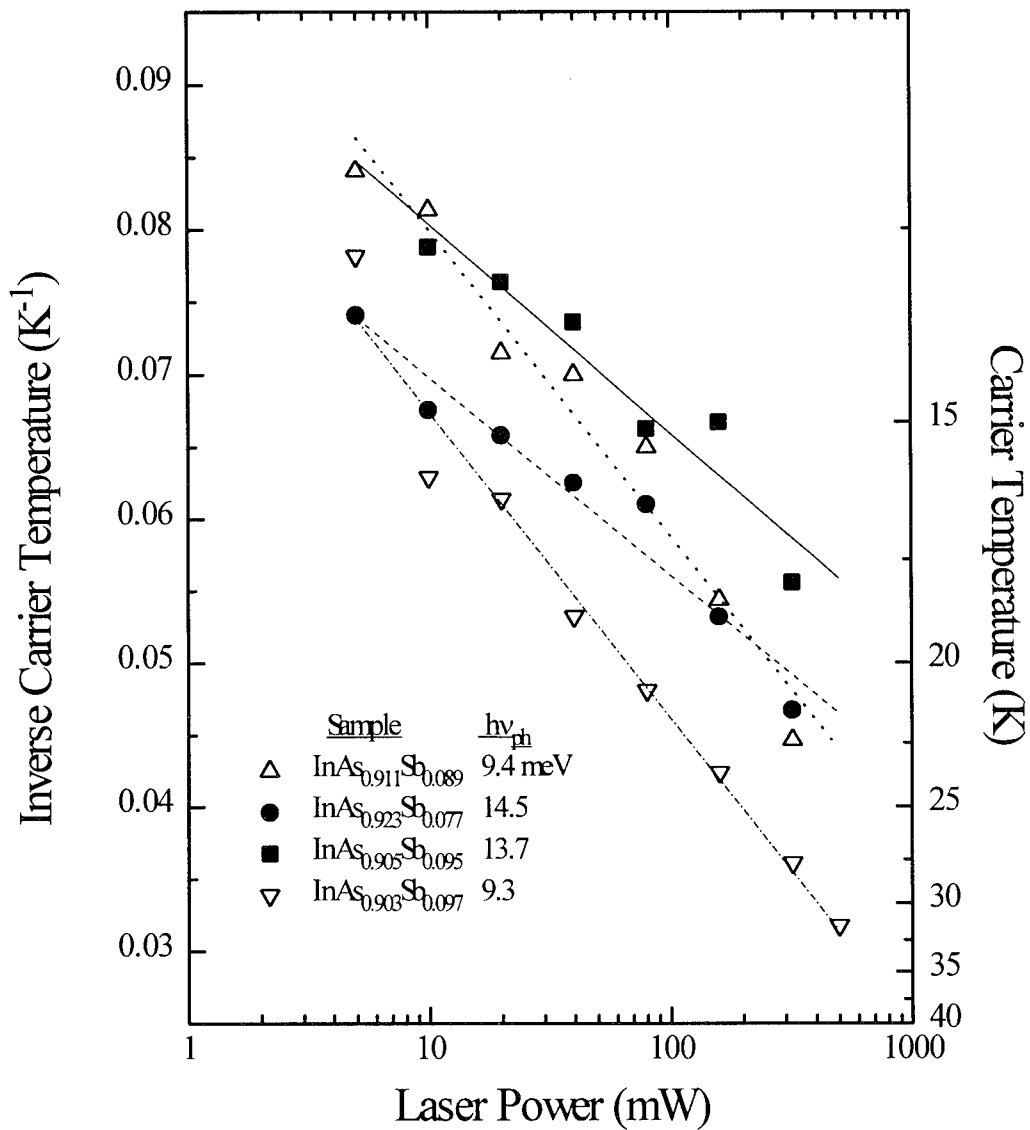


Figure 7-14. Inverse effective carrier temperatures,  $1/T_e$ , as a function of laser excitation power for several MBE-grown  $\text{InAs}_{1-x}\text{Sb}_x/\text{GaSb}$  samples. The lines show the least squares linear fit to the data. The energy of the carrier cooling mechanism,  $h\nu_{ph}$ , is extracted from the slopes of these lines using Eq (7.41).



Table 7-2. Photoluminescence characteristics of 11  $\text{InAs}_{1-x}\text{Sb}_x$  samples grown by MBE on GaSb substrates. The magnitude of the observed PL peak shift to higher energies with increased excitation power is given in meV/decade of excitation power.  $h\nu_{\text{ph}}$  is the quantized thermalization energy derived from the effective carrier temperatures. The magnitude of the PL peak shift to higher energies with increased excitation power calculated from the observed effective carrier temperatures is also given in meV/decade of excitation power.  $E_0$  refers to an empirical parameter having the dimensions of energy which describes band tailing effects.

Sample	x	Observed Peak Shift (meV/decade)	$h\nu_{\text{ph}}$ (meV)	Calculated Peak Shift (meV/decade)	$E_0$ (meV)
93-044	0.031	1.2	10.3	0.3	2.0
93-114	0.045	2.7	10.7	0.2	2.3
93-030	0.052	1.4	11.3	0.2	2.8
93-113	0.059	2.0	13.0	0.2	2.3
93-112	0.071	3.1	12.7	0.2	-
93-048	0.077	2.6	14.5	0.2	2.5
93-045	0.089	2.9	9.4-11.6	0.2	2.6
93-068	0.095	2.3	12.6-13.7	0.1	2.7
93-092	0.096	2.6	13.7	0.2	2.6
93-120	0.097	2.7	9.3-10.6	0.4	3.2
94-035	0.179	3.8	-	0.2	4.3

section, using the effective carrier temperatures,  $T_e$ , as extracted from the PL data in the previous section, it will be shown that the recombination is probably not a pure band-to-band transition, but is broadened by another mechanism. Phase separation, which was noted as a possible phenomenon existing in this material in Chapter VI, is suggested to be that mechanism here, as well.

The PL lineshape for band-to-band recombination was given by Eq (7.33). The shifting of the observed peaks to higher energies with increased laser excitation power, *e.g.*, as in Figure 7-8, is described by Eq (7.33) as an increase in the effective carrier

temperature,  $T_e$ . Since the effective temperatures were extracted from the semi-logarithmic plots of PL data as shown in Figure 7-11, an estimate of the magnitude of the peak shift can be made. These estimates should agree with the observed peak shift magnitudes if the band-to-band recombination is not broadened by another mechanism.

The theoretical band-to-band peak shift was calculated from the measured effective carrier temperatures at several laser excitation powers between 5 and 500 mW, and at a lattice temperature of 4 K for all the samples. These values are listed in Table 7-2 along with the observed peak shift magnitudes which were also listed in Table 7-1. A comparison of the calculated and observed values shows that, in all cases, the observed peak shift is at least four times as large as expected from a purely effective carrier temperature argument. Therefore, it is concluded that another peak-shifting mechanism, such as phase separation, is also involved in this recombination process.

The theory for an increased PL peak shift due to phase separation is similar to that given for alloy-broadened excitonic recombination above, but on a more macroscopic scale. In fact, alloy broadening theory and phase separation broadening theory become identical in the limit where the "cluster" size of the phase separated regions becomes one atomic radius (Singh, 1984:1075). Note that alloy broadening is an unlikely peak shift mechanism in this case since the maximum peak shift given by alloy broadening is equivalent to the sum of the peak shift calculated using the effective carrier temperatures, 0.1-0.4 meV/decade over two decades of laser excitation power as listed in Table 7-2, and

the excitonic linewidth calculated above to be 0.3 meV for this material. The observed peak shifts are well above this 1.1 meV maximum.

Phase separation is the material's compositional variation in real space, and thus, results in a variation of the energy gap in real space, as well. As described above, free carriers migrate to the lowest energy sites in the lattice in some migration time, where they recombine radiatively, emitting a low energy photon. At higher excitations, however, the radiative recombination lifetime of the carriers is much less than the migration time, so the carriers become distributed homogeneously in the crystal, and radiative recombination takes place from higher energy sites, as well, shifting the PL peak to higher energies. It is believed that the magnitude of the observed PL peak shift is due to a combination of the pure band-to-band peak shift as given by the increased effective carrier temperatures and a peak shift caused by phase separation, as described.

To summarize, the magnitudes of the shifts of the PL peaks to higher energies with increased laser excitation power that were observed in these MBE-grown  $\text{InAs}_{1-x}\text{Sb}_x$  epitaxial layers on GaSb substrates are larger than those given by a band-to-band peak shift due to increased effective carrier temperatures alone. Two broadening mechanisms, alloy and phase separation broadening, were considered since both are capable of increasing the magnitude of the peak shift, but alloy broadening was found to be an unlikely candidate since the magnitude of the total peak shift would still be too small. Therefore, phase separation in this material was found to be probable by PL measurements just as it had been from the absorption measurements of Chapter VI. Once

again, the existence of phase separation in this material cannot be disproved by the available characterization techniques.

**Band Tailing.** As in the previous section, since the radiative recombination in these MBE-grown  $\text{InAs}_{1-x}\text{Sb}_x$  samples is believed to be band-to-band in nature, the emitted PL spectrum is expected to behave in a certain way. Observed deviations from this expected behavior can be indications that other phenomena exist in this material, as well. In this section, such an observed deviation points to the existence of band tailing in this material.

The theoretical lineshape for band-to-band radiative recombination was given by Eq (7.33). Broadening mechanisms, such as the alloy or phase separation broadening described in the previous section, are typically Gaussian in shape as described in the Alloy-Broadened Excitonic Recombination section. The broadening of the band-to-band lineshape which results is given mathematically as the convolution of the unperturbed lineshape (Eq (7.33)) and the Gaussian broadening function:

$$I_{\text{br}}(h\nu) \propto \int_{x_1}^{x_2} \exp\left[-\frac{1}{2}\left(\frac{x - \mu}{\sigma}\right)^2\right] [h\nu - E_g(x)]^{1/2} \exp\left\{-\frac{[h\nu - E_g(x)]}{k_B T}\right\} dx, \quad (7.42)$$

where  $\mu$  is the center and  $\sigma$  is the standard deviation of the Gaussian function. Eqs (7.33) is plotted as a solid line in Figure 7-15, along with Eq (7.42) for two Gaussian widths,  $\sigma$ , as dotted lines, to be representative of band-to-band and broadened band-to-band PL peaks, respectively.

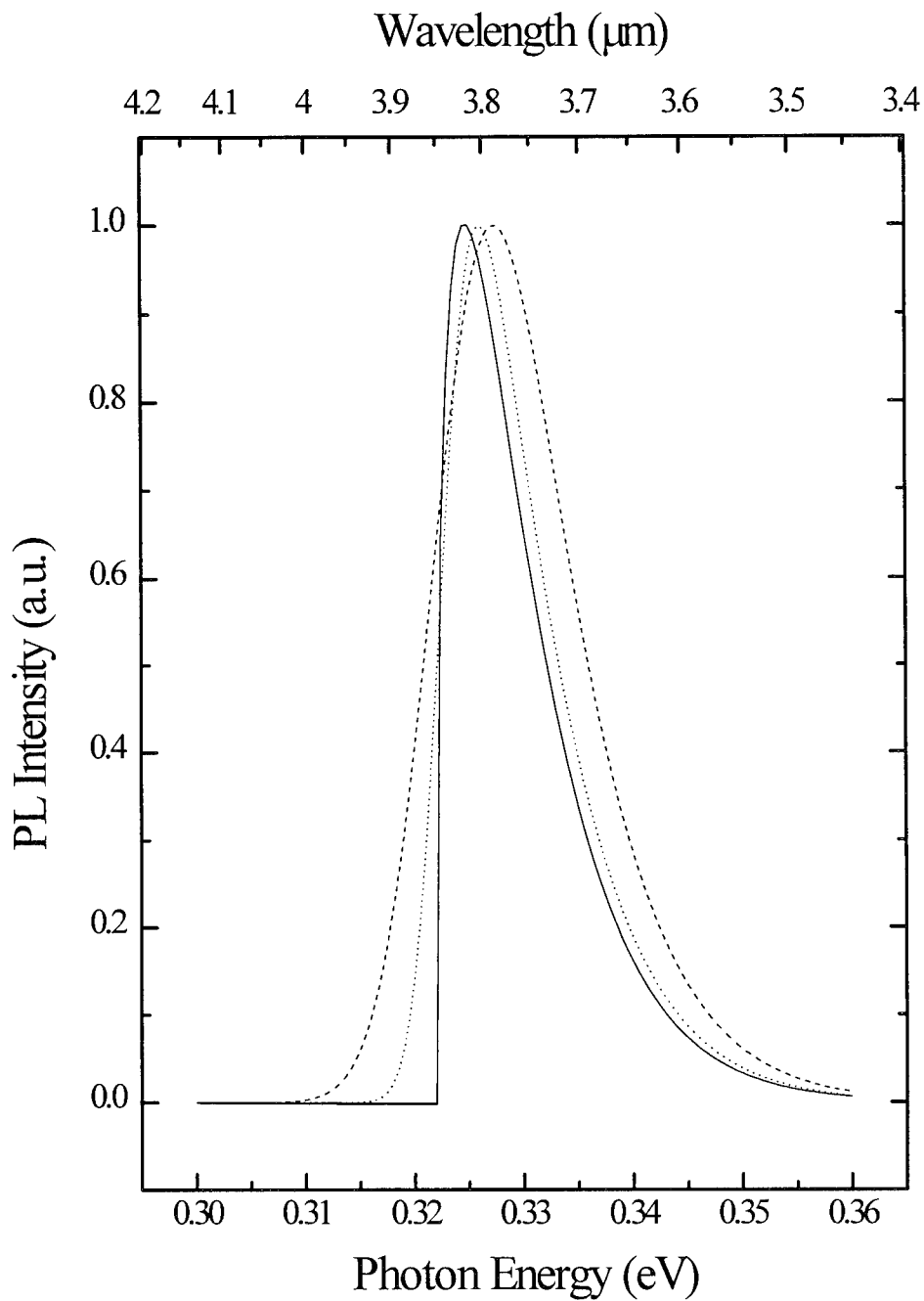


Figure 7-15. Theoretical band-to-band lineshape given by Eq (7.42), with (solid line) and without (dotted and dashed lines) Gaussian broadening. The broadening mechanism for the dotted line case has a narrower linewidth than that for the dashed line case.

It is shown by Figure 7-15 that for Gaussian broadening conditions, such as alloy or phase separation broadening, the rise of the low energy side of the PL peak is essentially given by the low energy side of the Gaussian exponential term of Eq (7.42), while the fall of the high energy side of the PL peak is essentially given either by the high energy side of the Gaussian exponential term or the band-to-band exponential term, whichever is a slower exponential. Therefore, the rise of the low energy side of a pure or broadened band-to-band PL peak can never be a slower exponential than that of the fall of the high energy side.

However, as shown by the experimental PL data for the MBE-grown  $\text{InAs}_{0.911}\text{Sb}_{0.089}$  sample at low temperatures and very low laser excitation powers (5 mW) in Figure 7-16, the exponential rise of the low energy side of the PL peak is indeed much slower than the fall of the high energy side. The very low laser excitation power was essential in making this observation. At low excitations, the effective carrier temperatures approach the lattice temperature, so the rate of fall of the exponential term of Eq (7.33), is greatly increased. At higher excitations, when the effective carrier temperatures are increased, the PL peaks appeared either more Gaussian in shape or as would be expected for band-to-band recombination. The phenomenon observed in the very low excitation spectra of these samples and shown in Figure 7-16 is believed to be due to band tailing in this epitaxial  $\text{InAs}_{1-x}\text{Sb}_x$  material.

Band tailing is a perturbation in real space in the density of states functions of each band typically due to sufficient impurity or defect concentrations, but also possibly

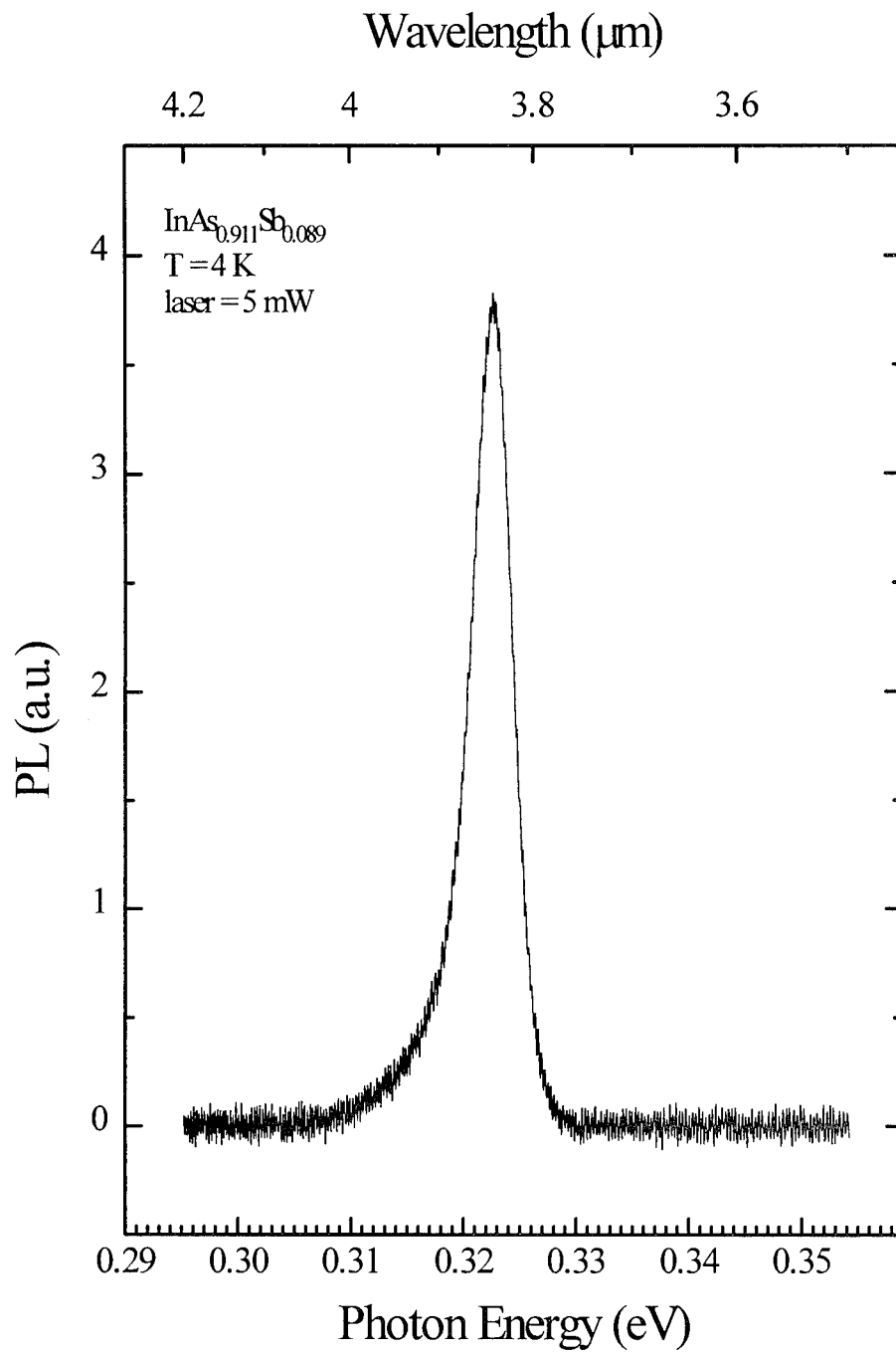


Figure 7-16. PL spectrum of sample InAs<sub>0.911</sub>Sb<sub>0.089</sub> showing effects of band tailing on the low energy side of the PL peak. The PL spectrometer resolution is 0.5 meV.

due to phase separation. As shown schematically in Figure 7-17 (a), the ionized donor exerts an attractive force on conduction band electrons and a repulsive force on valence band holes, shifting the local conduction and valence band edges to lower energies while the local energy gap still remains the same. Conversely, an acceptor would attract holes and repulse electrons for an analogous effect. The local concentration of the impurity or defect varies randomly throughout the crystal, affecting the magnitude of the local force on the bands, and causing the density of states function for each band to tail into the energy gap as shown schematically in Figure 7-17 (c) (Pankove, 1971:10). Figure 7-17 (b) shows a similar effect is caused by phase separation, but the variation of the local energy gap causes the tailing of the density of states function.

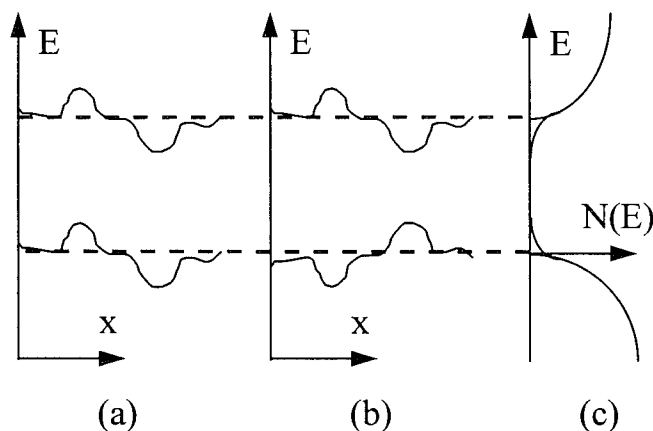


Figure 7-17. Band tailing effect on the density of states for each band as a result of (a) coulombic attraction between inhomogeneously distributed defects or impurities and free carriers (Pankove, 1971:11), and (b) phase separation of the material.



As a result of band tailing, the joint density of states function, which is normally given by Eq (6.7) and which primarily describes the low energy side of the PL peak, includes an exponential tail extending to lower energies described by:

$$g_{bt}(h\nu) d h\nu \propto \exp\left(\frac{h\nu}{E_0}\right) d h\nu, \quad (7.43)$$

where  $E_0$  is an empirical parameter having the dimension of energy and describing the distribution of states but not their energy assignment (Pankove, 1971:45). Figure 7-18 shows that, by plotting the PL spectra semi-logarithmically, a procedure similar to the one described above with Figure 7-11 for extracting the effective carrier temperatures may be used on the low energy side of the PL peaks to extract the  $E_0$  parameters from the data.  $E_0$  is obtained from the slope of the low energy side of the peak plotted in this manner, defined here as  $\xi_0$ , and Eq (7.43) as:

$$E_0 = \frac{\log e}{\xi_0} \quad (7.44)$$

The  $E_0$  values obtained from the PL spectra using Eq (7.44) are listed for each MBE-grown  $\text{InAs}_{1-x}\text{Sb}_x$  sample in Table 7-2. These  $E_0$  values ranged from 2.0-4.3 meV, with the largest value occurring for the sample with the highest Sb content,  $\text{InAs}_{0.821}\text{Sb}_{0.179}$ . As shown for the  $\text{InAs}_{0.911}\text{Sb}_{0.089}$  sample in Figure 7-18 and for each  $\text{InAs}_{1-x}\text{Sb}_x$  sample studied, the measured value of  $E_0$  was relatively independent of laser excitation power or sample lattice temperature. The variation of  $E_0$  was typically only a

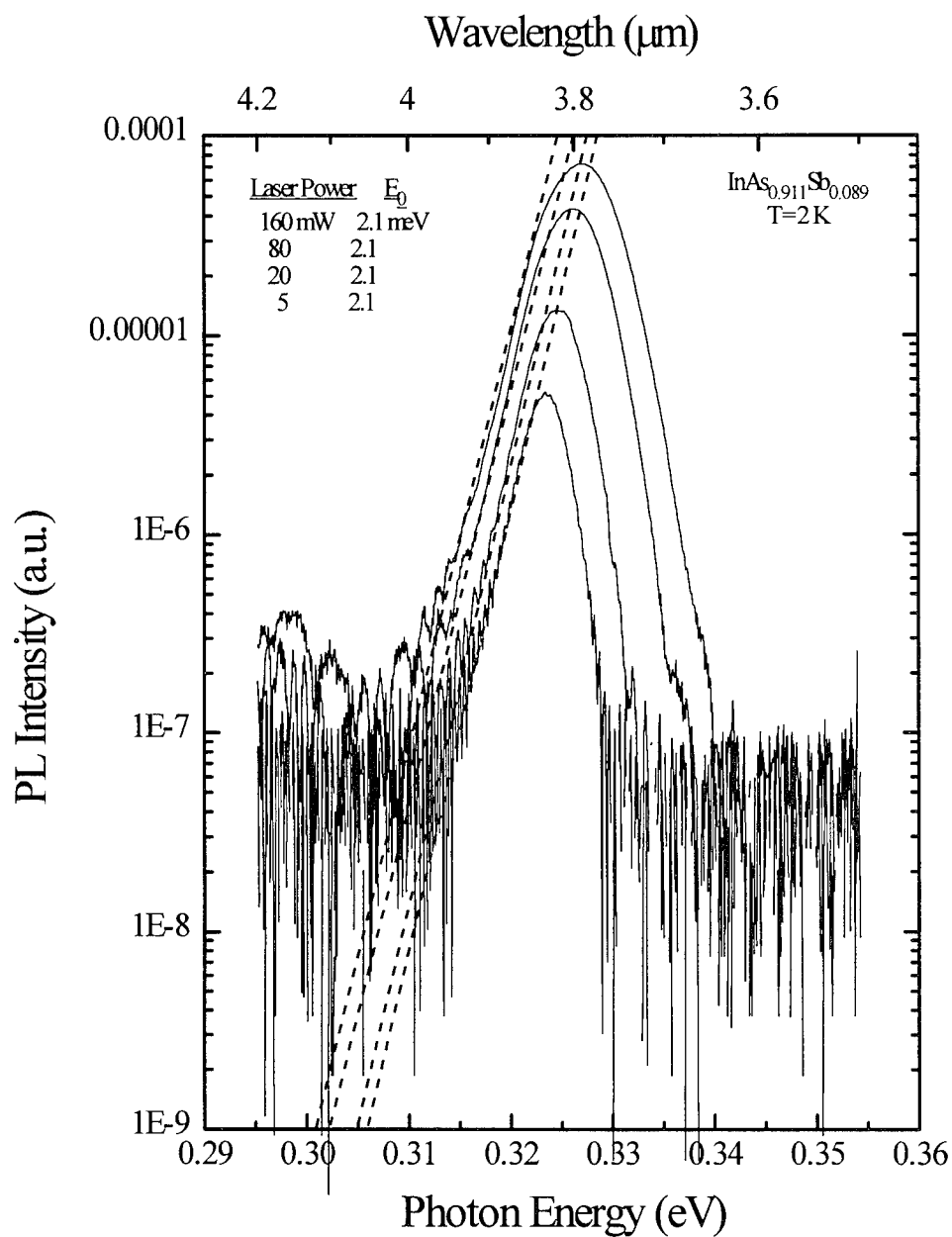


Figure 7-18. Empirical parameter with dimensions of energy describing band tailing effects on density of states,  $E_0$ , extracted from band-to-band photoluminescence peaks as shown. Dashed lines show the least squares linear fit to the low energy side of the peak.  $E_0$  is extracted from the slope of these lines using Eq (7.44). The PL spectrometer resolution is 0.5 meV.

few tenths of an meV at maximum, but excursions as large as 2 meV did occur in the InAs<sub>0.821</sub>Sb<sub>0.179</sub> sample, only.

The observation of band tailing in these MBE-grown undoped InAs<sub>1-x</sub>Sb<sub>x</sub> samples at compositions nearly lattice-matched to GaSb substrates directly addresses the primary objective of this research, which was to characterize this material. The observed band tailing is believed to be due to either a significant concentration of native or unintentional defect or impurity levels in this nominally undoped material, or to phase separation. The probability of both of these phenomena existing in these samples had already been suggested by other facets of this research. The impurity states were also observed from the free carrier analysis of the absorption experiment, and the phase separation from the compositional dependence of the energy gap obtained from the absorption experiment and from the peak shift behavior of the PL experiment. The observation of band tailing here gives further credibility to these suggestions.

### **Undoped InAs<sub>1-x</sub>Sb<sub>x</sub>: Multiple-Peaked Spectra**

The previous section reported and analyzed the PL results for the 11 MBE-grown InAs<sub>1-x</sub>Sb<sub>x</sub> samples on GaSb substrates with compositions  $0.031 \leq x \leq 0.179$  which were categorized as having “single-peaked spectra” because, aside from phonon replicas of the main peaks, only band-to-band recombination peaks were observed in the PL spectra. This section reports PL results for the final undoped, InAs<sub>0.808</sub>Sb<sub>0.192</sub>, which has a higher Sb content and larger lattice-mismatch with the GaSb substrate (+0.708%) than the

previous 11. However, it is distinguished from the other 11 here because it was the only undoped  $\text{InAs}_{1-x}\text{Sb}_x$  sample to show multiple peaks in its PL spectrum.

PL spectra for the  $\text{InAs}_{0.808}\text{Sb}_{0.192}$  sample at several different temperatures between 2 and 192 K are shown in Figure 7-19. As can be seen from the dotted lines in this figure, three peaks were distinguishable in the spectra. Only single-peaked PL spectra have been reported previously for  $\text{InAs}_{1-x}\text{Sb}_x$  grown on GaSb substrates (Elies, 1993:159; Mao, 1993:108), but separate band edge and impurity peaks were reported for  $\text{InAs}_{0.96}\text{Sb}_{0.04}$  and  $\text{InAs}_{0.87}\text{Sb}_{0.13}$  grown on InAs (Yen, 1988a:489) (see Chapter III, InAsSb Material Characterization).

The band edge position for this  $\text{InAs}_{0.808}\text{Sb}_{0.192}$  sample was determined by low temperature absorption measurements as reported in Chapter VI. As was done for the previous 11 samples, a comparison of the PL and absorption spectra at similar temperatures identified the highest energy peak, labeled  $E_{\text{band}}$  in Figure 7-19, as the result of band-to-band radiative recombination. As shown in the figure, peak  $E_{\text{band}}$  was not observed at temperatures below 32 K. At 32 K, the position of peak  $E_{\text{band}}$  was at  $278.0 \pm 0.6$  meV and the position of the absorption edge was at  $274.1 \pm 0.6$  meV, making the band-to-band peak  $\sim 1.0$ - $1.8 k_{\text{B}}T$  above the band edge, as expected.

The middle peak in Figure 7-19, labeled  $E_{\text{D}}$ , is positioned at an energy of  $272.0 \pm 0.6$  meV at 2 K, and at  $269.6 \pm 0.6$  meV at 32 K. At any set temperature, the position of  $E_{\text{D}}$  did not change with laser excitation power. This behavior, along with the position of  $E_{\text{D}}$ , is indicative of a F-B recombination. The position of the impurity level

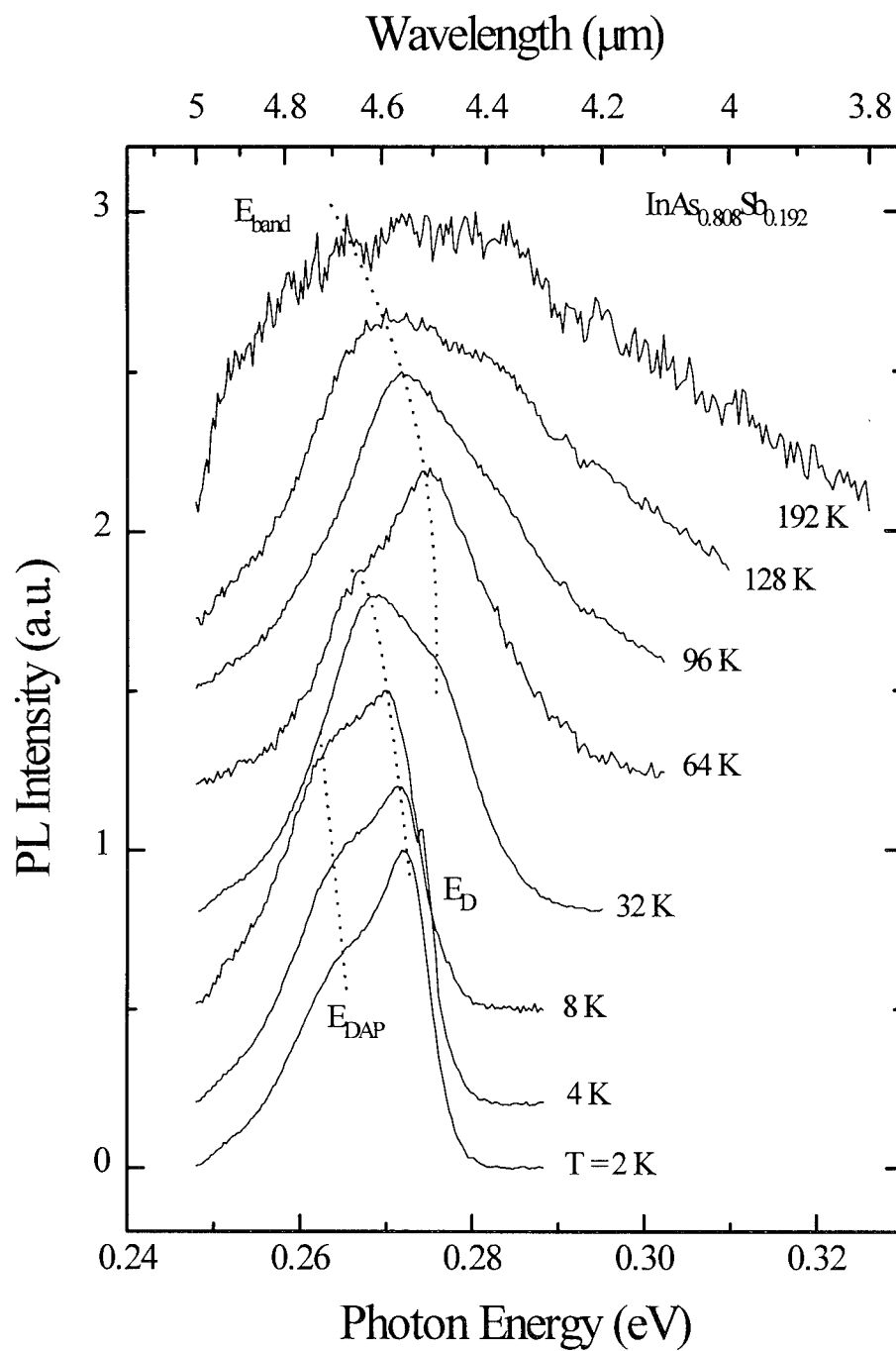


Figure 7-19. PL spectra of undoped  $\text{InAs}_{0.808}\text{Sb}_{0.192}$  sample showing three resolvable peaks. The PL spectrometer resolution is 0.6 meV.

corresponding to peak  $E_D$  is estimated to be 4-7 meV from the band edge from the PL data and absorption edge, and corroborated by the relative reduction of this peak in the PL spectra at temperatures above 32 K and disappearance at temperatures above 64 K ( $k_B T$  for 32 and 64 K is 2.8 and 5.5 meV, respectively). The position of this F-B peak is comparable to that of a F-B peak,  $E_{DIL}$ , observed in the InAs homoepitaxial sample (Figure 7-1).

The position of the lowest energy peak in Figure 7-19, labeled  $E_{DAP}$ , is at  $264.4 \pm 0.6$  meV at 2 K for low excitations and shifts to higher energies with increased laser excitation power at a rate of 4.0 meV/decade of excitation. This peak shift behavior and the location of this peak relative to the band edge are indicative of DAP recombination as described above in the InAs Homoepitaxy section. The position of peak  $E_{DAP}$  at 10-14 meV from the band edge is slightly lower than that observed for the DAP peaks in both the InAs homoepitaxial and heteroepitaxial samples ( $\sim 15$  meV from the band edge, Figures 7-1 and 7-6).

The implication assigning peak  $E_{DAP}$  as a DAP peak is that impurity levels of opposite type exist in this material at energies <10-14 meV from the band edge. If the impurity level associated with F-B peak  $E_D$  is assumed to also be involved in the DAP transition, than another (opposite-type) impurity level is expected to be of comparable energy. However, peak  $E_{DAP}$  is no longer observed at temperatures above 16 K, which typically indicates the ionization of one of the DAP impurity levels. Since  $k_B T$  for 16 K is <2 meV, and peak  $E_D$  persists to temperatures near 64 K, it is concluded the energy

level associated with peak  $E_D$  is not involved in the DAP transition. Note that not only is the position of peak  $E_{DAP}$  comparable to those of the DAP transitions in the homoepitaxial and heteroepitaxial InAs samples, but all three DAP peaks disappear from the PL spectra at fairly low temperatures, implying the existence of a very shallow impurity level. Also, the deeper impurity levels, which should be observable after the DAP peaks disappeared due to ionization, were never observed in any of the three.

To summarize the results for the  $\text{InAs}_{0.808}\text{Sb}_{0.192}$  sample, PL peaks below the band edge were observed for the first time in an  $\text{InAs}_{1-x}\text{Sb}_x$  material grown on GaSb. Two peaks were observed. One was identified as a F-B peak at a position of 4-7 meV below the band edge, which is a comparable position to that of a F-B peak observed in the homoepitaxial InAs material. The second was identified as a DAP peak because it shifted to higher energies with increased laser excitation power. This DAP peak was positioned at 10-14 meV from the band edge, which was again comparable to the positions of DAP peaks observed in both homoepitaxial and heteroepitaxial InAs. However, although the positions of these extrinsic levels have now been established, further identification of these levels is difficult because little has been reported about  $\text{InAs}_{1-x}\text{Sb}_x$  extrinsic levels in the literature.

### **Doped $\text{InAs}_{1-x}\text{Sb}_x$**

The PL results for the nominally undoped, MBE-grown  $\text{InAs}_{1-x}\text{Sb}_x$  material on GaSb substrates resulted in the observation of extrinsic peaks below the band edge which

could not be identified. Thus, although the establishment of the energy positions of these peaks is one step in achieving the objective of this research, which was to assess the quality of this material, the objective cannot be completely met until the nature of these peaks is known. Since very little has been reported in the literature about the extrinsic levels in  $\text{InAs}_{1-x}\text{Sb}_x$ , a PL study of intentionally doped material is called for in order to identify energy levels associated with specific impurities. To begin this task, the optical characterization of ion-implanted and epitaxially doped  $\text{InAs}_{1-x}\text{Sb}_x:\text{Be}$  was performed.

Beryllium was chosen simply because the ion-implantation of this element was available at the time of this study, as was the epitaxially doped material. Nominally undoped  $\text{InAs}_{1-x}\text{Sb}_x$  is natively n-type in conductivity as described in Chapter IV, Undoped Samples. Since Be is a group II element, it behaves as a single acceptor when substituted at a group III lattice site in the III-V zincblende structure. Therefore, the conductivity of  $\text{InAs}_{1-x}\text{Sb}_x$  was changed to p-type by doping with Be as described in Chapter IV, Doped Samples.

**Ion-Implanted  $\text{InAs}_{0.905}\text{Sb}_{0.095}:\text{Be}$ .** A description of the implantation and annealing parameters for the  $\text{InAs}_{0.905}\text{Sb}_{0.095}$  sample was given in Chapter IV, Doped Samples, and the luminescence of the unimplanted sample was described above in the Undoped  $\text{InAs}_{1-x}\text{Sb}_x$ : Single-Peaked Spectra section. (These spectra are shown in Appendix C.) As expected, no luminescence was observed from the implanted, unannealed material since the crystal lattice is severely damaged by the implantation process. Therefore, the implanted samples were annealed under a variety of conditions to



find the optimum annealing time and temperature, which would reconstruct the lattice sufficiently so as to return the band edge peak to the PL spectrum, and activate the dopant so as to produce an impurity peak.

No luminescence was observed from the samples which were rapid thermally annealed (RTA) at 450 and 550 °C for 10 sec. At an RTA temperature of 650 °C, band edge luminescence was beginning to be recovered for the implanted sample, but its intensity was greatly decreased from that of the unimplanted material. Therefore, it is concluded that RTA temperatures of 450, 550 or 650 °C for 10 sec. were not high enough to make the lattice recovery appreciable or activate the Be-dopant.

Other implanted samples were also conventionally annealed in an alloy furnace at a temperature of 550 °C for times of 4, 10 and 20 min. The PL spectra of the sample annealed for 4 min. was similar to that of the sample with an RTA temperature of 650 °C in that the band edge luminescence was being recovered, but was still much weaker than that of the unimplanted material, and no impurity peak was observed. In the PL spectra of the sample annealed for 10 min., not only was the band edge peak getting stronger, but an impurity peak below the band edge was emerging, as well. Finally, the 2 K PL spectra of the  $\text{InAs}_{0.905}\text{Sb}_{0.095}:\text{Be}$  sample annealed for 20 min. is shown in Figure 7-20 for several laser excitation powers. As is shown in the figure, although the luminescence intensity is still well below that of the unimplanted material, the band edge and impurity peaks are distinguishable and able to be studied.

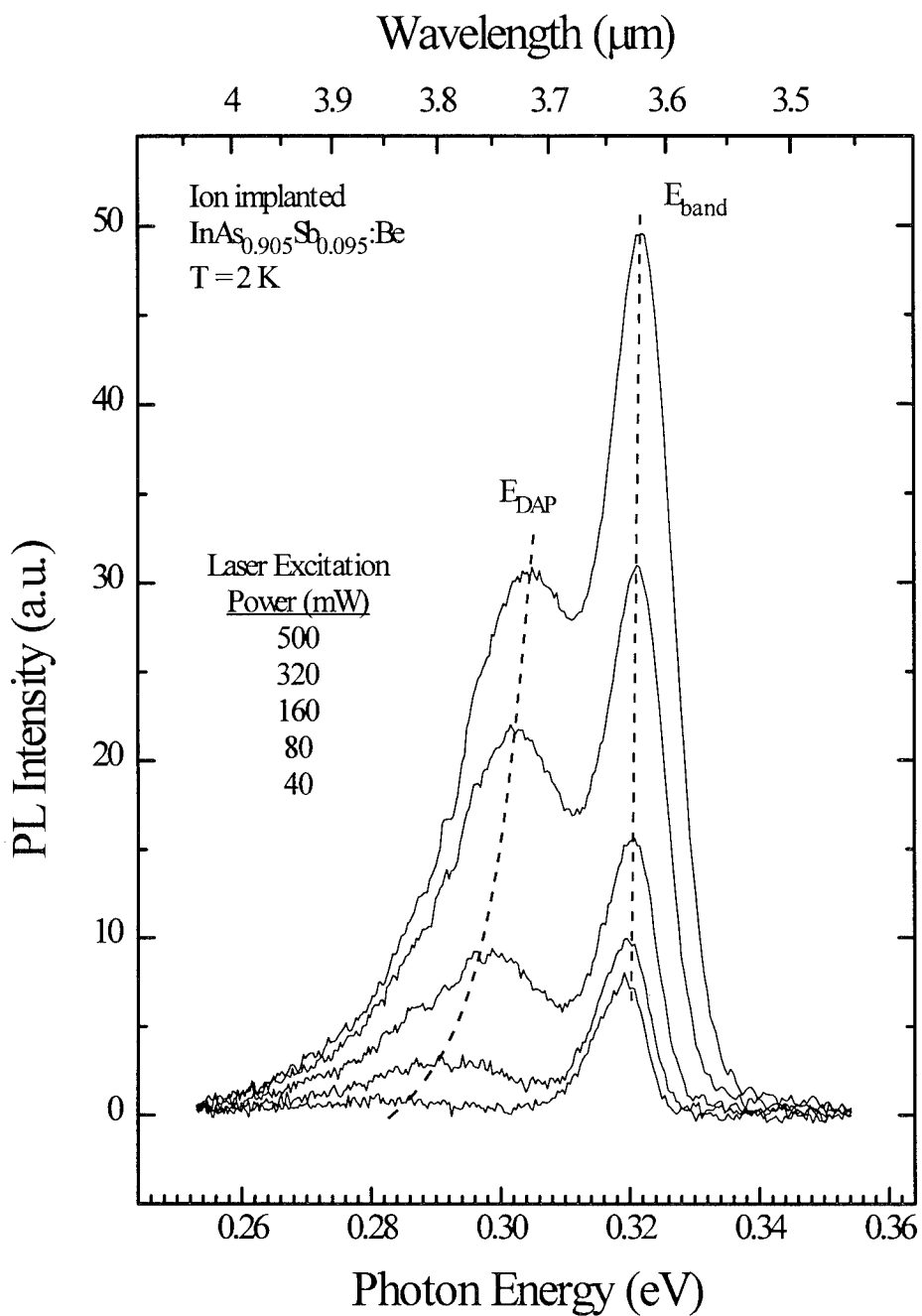


Figure 7-20. Low temperature PL spectra of Be-implanted MBE-grown  $\text{InAs}_{0.905}\text{Sb}_{0.095}$  on GaSb substrate. The PL spectrometer resolution is 0.9 meV.

The band edge peak, labeled  $E_{\text{band}}$  in Figure 7-20, is positioned at an energy of  $318 \pm 0.9$  meV at low laser excitation powers (40 mW), and shifts to a position of  $321 \pm 0.9$  meV at higher excitations (500 mW). Both the peak position and magnitude of the peak shift (2.7 meV/decade of laser excitation power) are comparable to those of the unimplanted control sample (sample 93-068 in Table 7-1), but the FWHM linewidth is slightly broadened (9.6 meV for an excitation of 320 mW as compared to 8.7 meV for the unimplanted sample).

The peak labeled  $E_{\text{DAP}}$  in Figure 7-20 is positioned at an energy of  $282 \pm 0.9$  meV at low laser excitation powers (40 mW), and shifts to a position of  $303 \pm 0.9$  meV at higher excitations (500 mW). The magnitude of this peak shift, 18.4 meV/decade of excitation, is much greater than that of the band edge peak. The position of peak  $E_{\text{DAP}}$  well below the band edge and its strong peak shifting behavior are indicative of a DAP transition.

As was the case in the above sections, the implication of assigning peak  $E_{\text{DAP}}$  as a DAP peak is that impurity levels of opposite type exist in the material at energies  $<36$  meV from the band edge. As shown in Figure 7-21, peak  $E_{\text{DAP}}$  persists in the PL spectra to a temperatures of  $\sim 64$  K. Since  $k_{\text{B}}T$  at 64 K is  $\sim 5.5$  meV, and if the disappearance of peak  $E_{\text{DAP}}$  is believed to be the result of the ionization of one of the impurity levels involved in the DAP transition, then one impurity level is expected to have an energy of  $\sim 6$  meV from the band edge. Since the implanted Be is an acceptor in this material, and

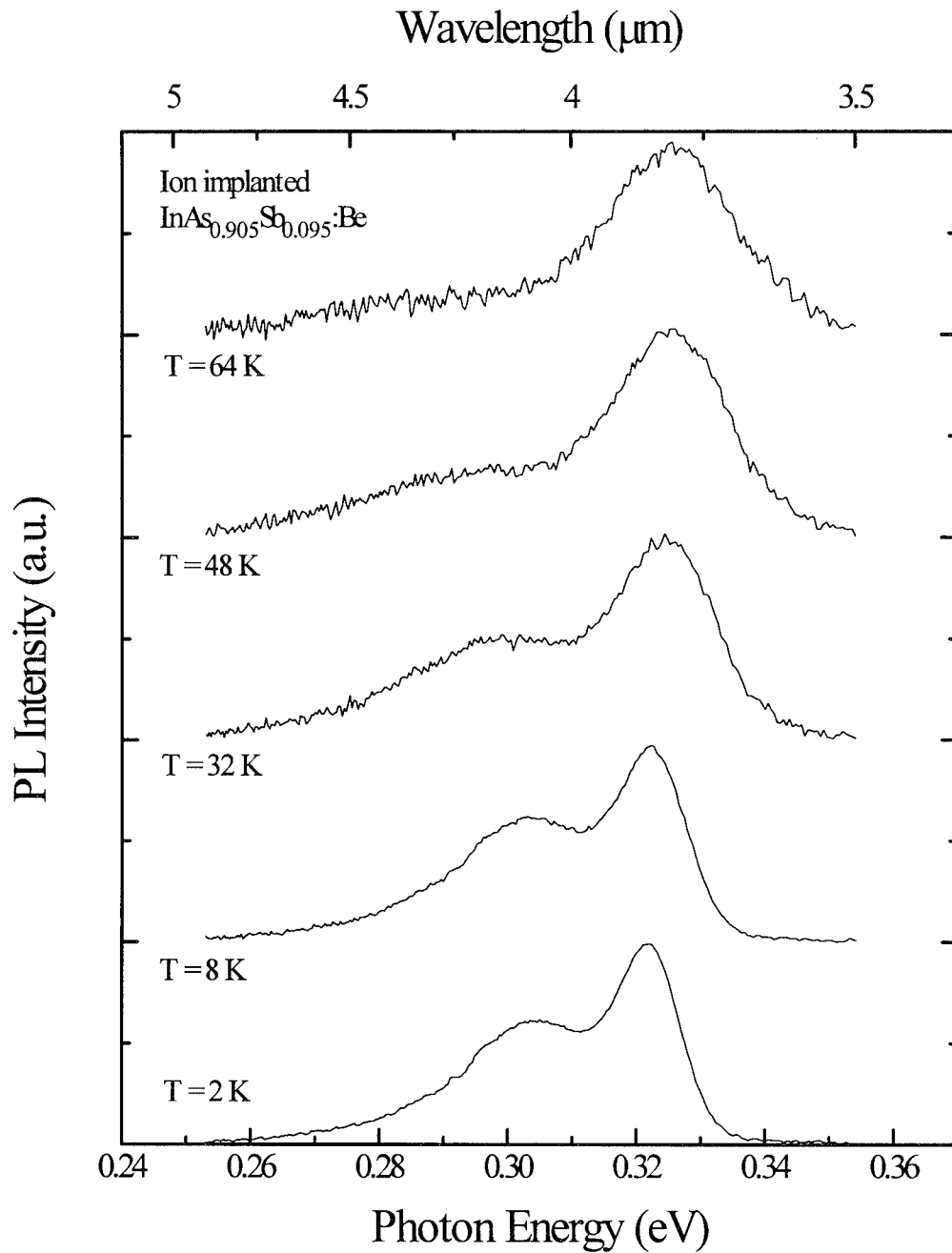


Figure 7-21. PL spectra for Be-implanted MBE-grown InAs<sub>0.905</sub>Sb<sub>0.095</sub> on GaSb substrate at several temperatures, showing the gradual ionization of the extrinsic peak. The PL spectrometer resolution is 0.9 meV.

acceptor levels are typically deeper than donor levels, it is believed this shallow level should be a donor level.

From the position of the peak  $E_{\text{DAP}}$  and assumption of the donor energy level above, the Be acceptor level in this ion implanted MBE-grown  $\text{InAs}_{0.905}\text{Sb}_{0.095}:\text{Be}$  sample is expected to be at an energy of:

$$E_{\text{A}} \cong 30 \text{ meV} \quad (\text{for ion implanted } \text{InAs}_{0.955}\text{Sb}_{0.045}:\text{Be}) \quad (7.45)$$

from the band edge. A F-B peak corresponding to this energy was not resolved in the PL spectra.

**Epitaxially Doped  $\text{InAs}_{0.955}\text{Sb}_{0.045}:\text{Be}$ .** An MBE-grown sample on GaSb substrate of composition  $\text{InAs}_{0.955}\text{Sb}_{0.045}$ , as determined by double crystal x-ray diffraction assuming full strain relaxation, was epitaxially doped with Be as described in Chapter IV, Doped Samples. The low temperature PL spectra for this sample is shown in Figure 7-22. As is shown in this figure, two peaks are resolved in the PL spectra.

The higher energy peak, labeled  $E_{\text{band}}$  in Figure 7-22, is positioned at an energy of  $327 \pm 0.9 \text{ meV}$ . The position and linewidth (11 meV) of this peak are invariant to changes in laser excitation power. A comparison of the PL and absorption spectra for this sample over temperatures 7 to 192 K is shown in Figure 7-23. This figure shows that peak  $E_{\text{band}}$  broadens and smoothly shifts to lower energies with increased temperature, indicating the radiative transition resulting in this peak remains the same over this

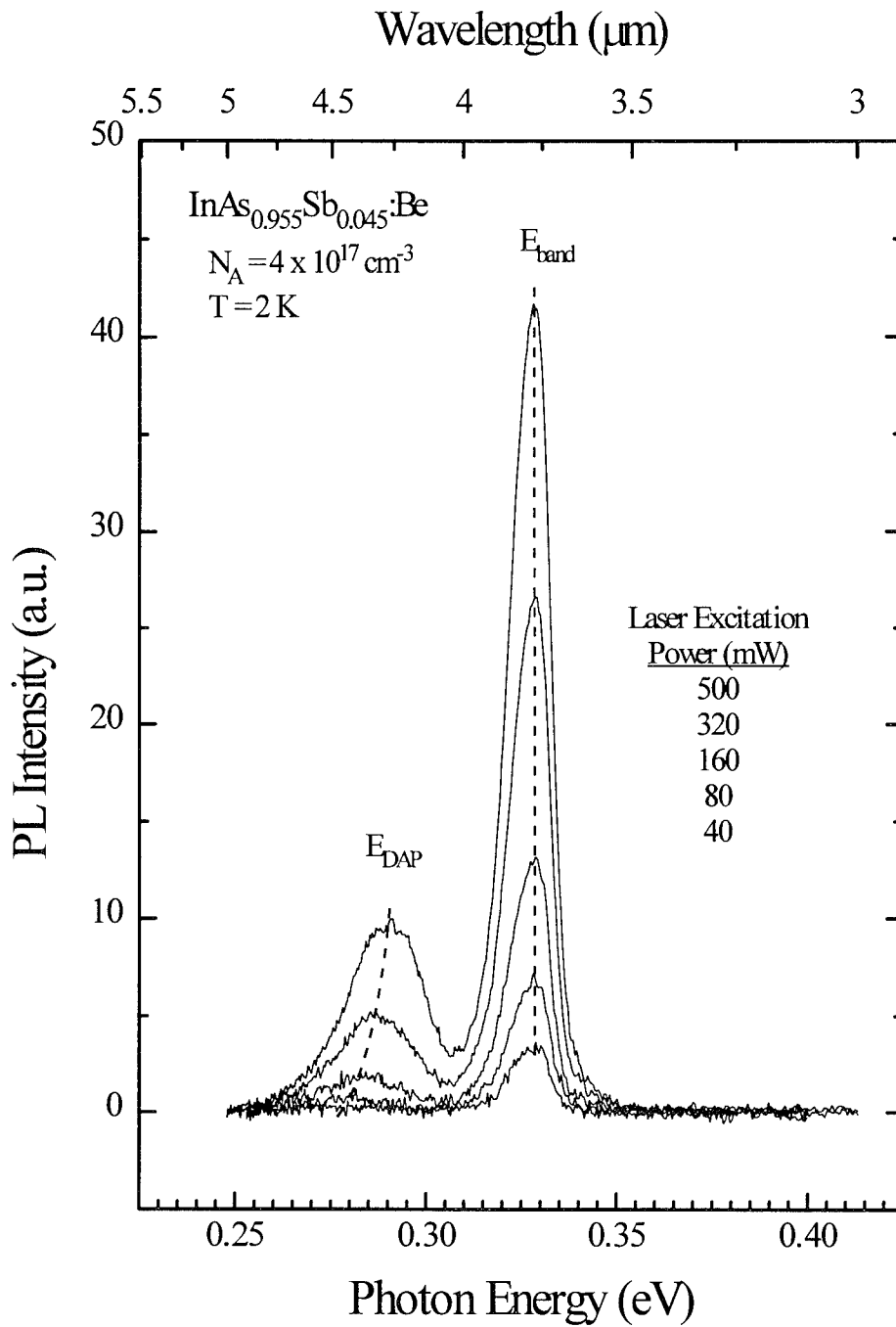


Figure 7-22. Low temperature PL spectra of p-type, Be-doped InAs<sub>0.955</sub>Sb<sub>0.045</sub> MBE-grown sample. The PL spectrometer resolution is 0.9 meV.

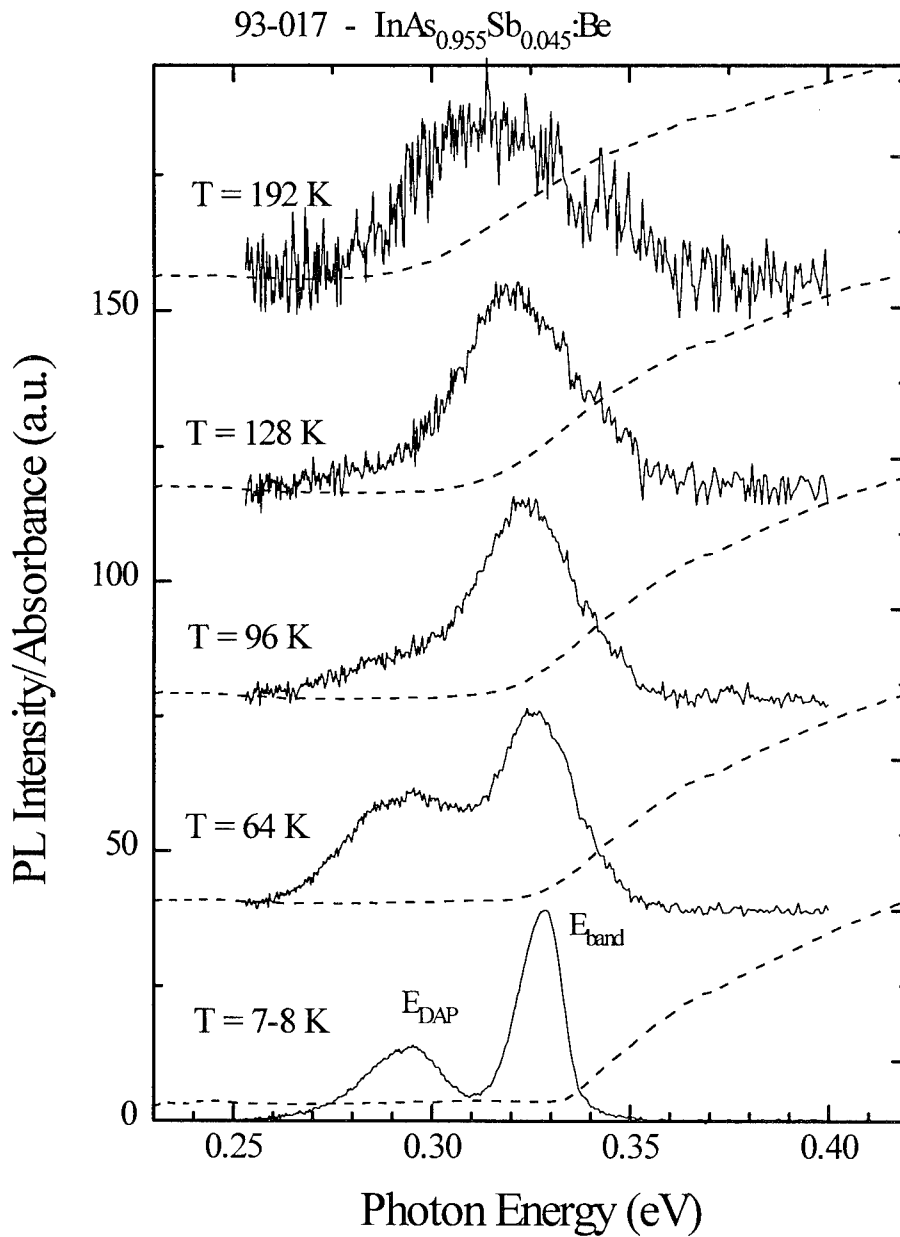


Figure 7-23. Comparison of PL (solid lines) and absorption (dashed lines) spectra for MBE-grown  $\text{InAs}_{0.955}\text{Sb}_{0.045}\text{:Be}$ . Peak  $E_{\text{band}}$  is due to band-to-band recombination. Peak  $E_{\text{DAP}}$  ionizes at  $\sim 96$  K. The PL spectrometer resolution is 0.9 meV; FTS absorption spectrometer resolution is 0.5 meV.

temperature range. Because of this, it is believed peak  $E_{\text{band}}$  results from band-to-band radiative recombination.

The luminescence signal for this epitaxially doped sample was very weak compared to those of the undoped material. Therefore, a significant excitation level was always required to observe the luminescence. Typically, PL peaks which have merged together due to broadening under high excitation conditions may be resolved at lower excitation levels. The use of this technique was not possible for this doped material. However, as shown in Figure 7-24, when peak  $E_{\text{band}}$  was studied further, it was found that this peak is not symmetric, but that it “bulges” to the low energy side.

A Gaussian fit to the high energy side of peak  $E_{\text{band}}$  is shown by a dotted line in Figure 7-24; the FWHM of this fit is 9 meV. The curve drawn by the dashed line in Figure 7-24 shows the difference between the original data and this Gaussian fit. The result is another nearly Gaussian peak 7-9 meV below the main peak, with a FWHM linewidth obtained from another Gaussian fit (as shown by the lower dotted line) of 7 meV. This double Gaussian fit of peak  $E_{\text{band}}$  was consistent over a range of excitation powers of 80-500 mW, and a range of temperatures of 2-8 K. At temperatures above 15 K, the two sub-peaks were no longer distinguishable by this method.

The higher energy subpeak of peak  $E_{\text{band}}$  is believed to be the true band-to-band recombination peak. The lower energy subpeak of peak  $E_{\text{band}}$  is assigned as a F-B transition because of its position 7-9 meV below the band edge.



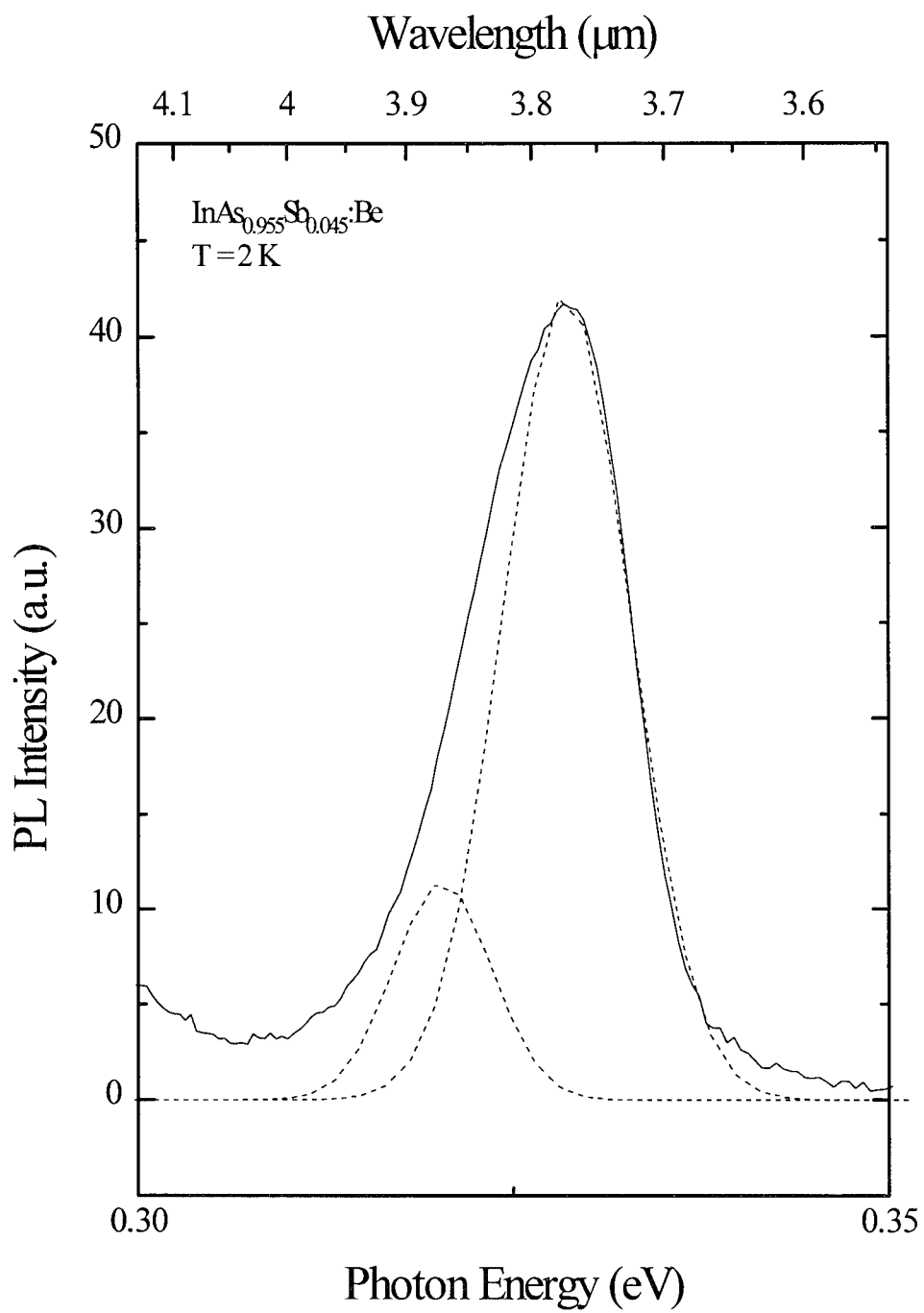


Figure 7-24. Double Gaussian fit of the higher energy peak of a low temperature  $\text{InAs}_{0.955}\text{Sb}_{0.045}\text{:Be}$  PL spectrum. The PL spectrometer resolution is 0.9 meV.

The peak labeled  $E_{\text{DAP}}$  in Figure 7-22 is positioned at an energy of  $278 \pm 0.9$  meV at low laser excitation powers (40 mW), and shifts to a position of  $290 \pm 0.9$  meV at higher excitations (500 mW). The magnitude of this shift was 11-15 meV/decade of laser power at temperatures below 16 K. Because of its position and strong peak shifting behavior, peak  $E_{\text{DAP}}$  is believed to be a DAP transition.

As mentioned several times above, the implication of assigning peak  $E_{\text{DAP}}$  as a DAP peak is that impurity levels of opposite type exist in the material at energies  $<49$  meV from the band edge. As shown in Figure 7-23, peak  $E_{\text{DAP}}$  persists in the PL spectra to a temperatures of  $\sim 96$  K. Since  $k_{\text{B}}T$  is 8.3 meV at 96 K, it is believed that the energy level 7-9 meV from the band edge associated with the F-B subpeak of peak  $E_{\text{DAP}}$  is also involved in the DAP transition. The ionization of this F-B subpeak at this temperature is reasonable and explains the disappearance of the DAP peak. Furthermore, it is believed that the energy level associated with the F-B subpeak of peak  $E_{\text{band}}$  is a donor level since the Be dopant should act as an acceptor in this material.

From the peak positions shown in Figures 7-22 and 7-24 and discussed above, the Be acceptor level in this epitaxially doped MBE-grown  $\text{InAs}_{0.955}\text{Sb}_{0.045}:\text{Be}$  sample is expected to be at an energy of:

$$E_{\text{A}} \cong 40 \text{ meV (for epitaxial } \text{InAs}_{0.955}\text{Sb}_{0.045}:\text{Be}) \quad (7.46)$$

from the band edge. A F-B peak corresponding to this energy was not resolved in the PL spectra.

**Conclusion.** The Be acceptor level in ion implanted, MBE-grown  $\text{InAs}_{0.905}\text{As}_{0.095}$  was determined to be  $\sim 30$  meV above the valence band. On the other hand, the Be acceptor level in epitaxially doped MBE-grown  $\text{InAs}_{0.955}\text{As}_{0.045}:\text{Be}$  was determined to be  $\sim 40$  meV above the valence band. This difference between the determined Be acceptor levels was not unexpected, since the crystal lattice was significantly damaged by the ion implantation and, therefore, the position of the Be atom in the lattice may be dissimilar for the two methods of doping.

Nevertheless, it can be concluded from this data that the Be acceptor energy in  $\text{InAs}_{1-x}\text{Sb}_x$  is probably  $>30$  meV. This fact is more important to the objective of this research than is making a conclusive statement regarding the exact Be acceptor level. No extrinsic PL levels were identified at energies this large in the nominally undoped  $\text{InAs}_{1-x}\text{Sb}_x$  spectra. Therefore, unintentional Be doping cannot be the reason for the existence of these observed PL peaks.

## Summary

MBE-grown  $\text{InAs}_{1-x}\text{Sb}_x$  on GaSb substrates was studied by PL to determine its material quality, and to identify any defect or impurity levels which exist. Since  $\text{InAs}_{1-x}\text{Sb}_x$  is relatively unstudied in the literature, InAs samples were also studied by PL to form a baseline against which the  $\text{InAs}_{1-x}\text{Sb}_x$  spectra could be compared.

PL measurements on an undoped homoepitaxial InAs sample resulted in the band edge peak, excitonic at low temperatures and band-to-band at higher temperatures, and

five peaks below the band edge. Three of these below-band-edge peaks were determined to be due to F-B recombination with associated extrinsic levels of approximately 3, 7 and 21-27 meV from the band edge. The other two PL peaks were observed at energies approximately 15 and 45 meV below the band edge, and are believed to be due to DAP recombination because of their peak shifting behavior. Furthermore, the observed 3 meV extrinsic level is believed to be one of the impurity levels involved in both DAP transitions since the DAP peaks disappear with the ionization of this level.

Only three PL peaks were resolved in the spectra of heteroepitaxial InAs material grown by MBE on GaSb, and the linewidths of these peaks were broadened by  $\sim 4$  times over those of the homoepitaxial material. However, the positions and behaviors of these peaks were comparable to those of the homoepitaxial spectra. One DAP peak at  $\sim 15$  meV below the band edge, was similar to a DAP peak in the homoepitaxial material, and implied the existence of a shallow level similar to the 3 meV level in the homoepitaxial material even though a PL peak at such a position could not be resolved. Another F-B peak at  $\sim 20$  meV below the band edge was slightly shallower than the F-B peak observed at 21-27 meV below the band edge in the homoepitaxial sample.

With the InAs baseline in hand, nominally undoped MBE-grown  $\text{InAs}_{1-x}\text{Sb}_x$  on GaSb substrates ( $0.031 \leq x \leq 0.192$ ) was studied. The narrow linewidths measured for these samples and the observation of the LO-phonon replicas in the PL spectra indicated that the quality of this material is very high in relation to the material on which PL results have been previously reported in the literature.

For the majority of the samples, only a single PL peak which shifted to higher energies with increased laser excitation power appeared in the spectra. A comparison of the PL spectra with absorption data showed the radiative recombination for these peaks was band-to-band, and since the nature of these peaks was known, further analyses could be done applying the physical principles established for band-to-band transitions.

One such analysis determined the effective carrier temperatures for the recombination, and established the peak shift rates that should be expected theoretically as a result of these temperatures. The observed peak shift rates, however, were larger than that given by the theory. Therefore, an additional broadening mechanism was suspected to exist in this material. Two broadening mechanisms, alloy and phase separation broadening, were considered since both could be responsible for the increased peak shift rate, but alloy broadening was determined to be unlikely since the magnitude of the total peak shift would still be too small. Therefore, phase separation in this material was found to be probable just as it had been from the absorption measurements of Chapter VI.

The observation of band tailing in these samples directly addresses the primary objective of this research, which was to characterize this material. The observed band tailing was believed to be due to either a significant concentration of native or unintentional defect or impurity levels in this nominally undoped material, or to phase separation. The possibility of both of these phenomena existing in this material had

already been suggested by other facets of this research, and the observation of band tailing here gave further credibility to these suggestions.

The remaining undoped sample,  $\text{InAs}_{0.808}\text{Sb}_{0.192}$ , differed from the other samples in that it produced additional peaks in its PL spectra below the band edge. As with the heteroepitaxial InAs sample, these extrinsic peaks were comparable to peaks observed from the homoepitaxial InAs material. One F-B peak was positioned 4-7 meV below the band edge, and another DAP peak was positioned 10-14 meV below the band edge. Although the positions of these extrinsic levels had been established, further identification of these levels was difficult because little has been reported about  $\text{InAs}_{1-x}\text{Sb}_x$  extrinsic levels in the literature.

To this end, the group II element, Be, was doped into  $\text{InAs}_{1-x}\text{Sb}_x$  material in an attempt to establish the acceptor level for this one impurity. Two methods of doping, ion implantation and epitaxial, were used, and the results differed between the two. The Be acceptor level in ion implanted  $\text{InAs}_{0.905}\text{As}_{0.095}$  was determined to be ~30 meV above the valence band, while that for epitaxially doped  $\text{InAs}_{0.955}\text{As}_{0.045}$  was determined to be ~40 meV above the valence band. Nevertheless, it was concluded from this data that the Be acceptor energy in  $\text{InAs}_{1-x}\text{Sb}_x$  is probably >30 meV, and this fact is more important to the objective of this research than is making a conclusive statement regarding the exact Be acceptor level. That is, no extrinsic PL peaks were observed at energies this large in the nominally undoped  $\text{InAs}_{1-x}\text{Sb}_x$  spectra. Therefore, unintentional Be doping cannot be

the reason for the existence of these observed peaks. For further identification of these peaks, other intentional dopants must be studied in  $\text{InAs}_{1-x}\text{Sb}_x$  in the future.

## VIII. Conclusions and Recommendations

### **Conclusions**

$\text{InAs}_{1-x}\text{Sb}_x$  is of much current interest in optoelectronic device development because it provides the lowest energy gap of the III-V semiconductors, corresponding to wavelengths in the mid-infrared (IR). This ternary has been studied since 1964 but there are surprisingly few reports in the literature on its basic material characterization, especially for epitaxially-grown samples. The two main reasons for this are: (1) much of the recent  $\text{InAs}_{1-x}\text{Sb}_x$  research has been device-oriented; and (2) high quality  $\text{InAs}_{1-x}\text{Sb}_x$  was difficult to grow in the past. The primary objective of this research, then, was to identify material parameters and assess the material quality of molecular beam epitaxially (MBE)-grown  $\text{InAs}_{1-x}\text{Sb}_x$  at compositions nearly lattice-matched to GaSb substrates, *i.e.*,  $-0.629\% \leq \Delta a/a \leq +0.708\%$ , where  $\Delta a/a$  is the lattice-mismatch between the  $\text{InAs}_{1-x}\text{Sb}_x$  and the GaSb, as it is grown for mid-IR semiconductor lasers devices.

The primary characterization technique to be used here was photoluminescence (PL). However, to accurately analyze the PL data, it was imperative to accurately know the energy gaps of these samples. The general energy gap positions for these compositions could be deduced from the few reports in the literature, but the accuracy of this data was questionable. Therefore, Fourier transform spectroscopic absorption measurements were first made on all the samples, at several temperatures between 6 and 295 K, to gain the band edge information. An empirical estimate of the absorption



coefficients for  $\text{InAs}_{1-x}\text{Sb}_x$  also resulted from these measurements. This provides useful device modeling parameters which have not been available previously from the literature.

The band edge absorption data for each composition gave the temperature dependence of the energy gap,  $E_g(T)$ , which was described very well by a commonly-used empirical relationship, the Varshni equation. A comparison to the few other  $\text{InAs}_{1-x}\text{Sb}_x$   $E_g(T)$  dependencies in the literature showed that the rate of change of the energy gap with temperature,  $dE_g/dT$ , was essentially the same for these current MBE-grown samples as for those previously reported, but their energy gap positions were generally lower for similar compositions.

When the compositional dependence of the energy gap,  $E_g(x)$ , over this composition range ( $0 \leq x \leq 0.192$ , corresponding to the lattice-mismatch range given above) was analyzed at any fixed temperature, it was found that not only were the energy gaps lower than previously reported values, but that the rate of change of the energy gap with composition,  $dE_g/dx$ , was also anomalous over this range. Three possibilities were introduced to explain this anomalous behavior: residual strain, Cu-Pt-type ordering, and phase separation in this material.

The existence of residual strain in this material was determined to be unlikely by theoretical analysis and experimental x-ray diffraction analysis. Ordering was, as well, since the observed anomalous  $dE_g/dx$  behavior was dissimilar to that predicted for this phenomenon. The third possibility, phase separation, was neither conclusively proven nor disproved by these measurements, but was shown to be a good explanation for phenomena observed in the PL experiments, as well.

One important corollary observation which impacted the objective of this research also resulted from these absorption measurements. A significant level of free carrier absorption existed in this epitaxial material at all temperatures. This indicated that a significant concentration of unintentional extrinsic levels in this material was probable.

With the energy gap information for each sample in hand, excitation- and temperature-dependent PL experiments were performed to further characterize the quality of the material. Once again, since little had been reported for  $\text{InAs}_{1-x}\text{Sb}_x$  in the literature, another baseline was deemed necessary for accurate analysis of the results. Therefore, PL spectra of homoepitaxial InAs and heteroepitaxial InAs/GaSb samples grown in the same MBE machine as the  $\text{InAs}_{1-x}\text{Sb}_x$  samples were studied.

Typically, a PL spectrum with many resolvable energy levels is indicative of high crystalline quality material; this was the case for both InAs samples. PL peaks from poorer materials are often broadened such that separate peaks are merged together and are no longer distinguishable. The PL spectra previously reported in the literature for  $\text{InAs}_{1-x}\text{Sb}_x$  have shown only a single peak. It was expected that the quality of this current  $\text{InAs}_{1-x}\text{Sb}_x$  material was high enough that multiple-peaked PL spectra would be observed, however, since the laser devices fabricated from this material have shown excellent operating characteristics; this was not the case.

The majority of the  $\text{InAs}_{1-x}\text{Sb}_x$  samples studied here produced only a single peak in their PL spectra, as their predecessors in the literature had. However, these peaks were narrower (as low as 4.3 meV linewidths) than any previously reported (a minimum of 5.15 meV), and the spectra also showed LO-phonon replicas of the main peak, which had

not been reported previously. These two observations indicate that this current material is of good quality in relation to that previously reported.

With only one peak in the PL spectrum, identification of a recombination mechanism for the PL peak was made by comparing the PL and absorption data for each sample. In all cases, it was found that these single peaks were band edge peaks. Further distinction between excitonic or band-to-band peaks was made through theoretical calculations, and the peak were determined to be band-to-band in nature. Since the nature of these peaks was known, other analyses applying physical relationships established for band-to-band transitions were performed.

One such analysis determined the effective temperature of the carriers recombining from the bands. The PL peak in these spectra shifted to higher energies with increased laser excitation power. This peak shift in pure band-to-band recombination is the result of band filling, which is described by this effective carrier temperature. The effective carrier temperatures extracted from the PL data were used to show that the rate and magnitude of the observed peak shift was greater than predicted from band filling alone. Therefore, another peak-shifting mechanism must also be present in this material.

Two possibilities were introduced: the random distribution of the ternary alloy or "alloy broadening" and, again, phase separation in this material. Theoretical analysis determined that alloy broadening would not produce a peak shift of the magnitude observed. Therefore, phase separation was again left as the likely candidate to explain an observed phenomenon.

Another analysis of the band-to-band peak determined band tailing existed in this material, which was the result of either phase separation or a significant concentration of unintentional extrinsic levels. Both these possibilities had been introduced earlier in this study.

The only  $\text{InAs}_{1-x}\text{Sb}_x$  sample to produce multiple peaks in its PL spectra was the one with the highest Sb content,  $\text{InAs}_{0.808}\text{Sb}_{0.192}$ . An extrinsic level was observed at 4-7 meV from the band edge, as was a donor-acceptor pair transition 10-14 meV below the band edge. Both these levels were comparable to similar levels observed in the InAs samples; however, identification of these levels was difficult because no information about the extrinsic levels in  $\text{InAs}_{1-x}\text{Sb}_x$  was available from the literature.

To establish one known extrinsic level in this material, the group II element, Be, was doped into  $\text{InAs}_{1-x}\text{Sb}_x$  by two doping methods, ion implantation and epitaxial doping. (Beryllium was selected only because of its availability at the time of this study.) Although the results for the Be acceptor level differed for each case (~30 meV above the valence band in the implanted material and ~40 meV in the epitaxially doped material), the conclusion was that the Be acceptor level in  $\text{InAs}_{1-x}\text{Sb}_x$  is >30 meV. Therefore, the extrinsic levels observed in the nominally undoped material were not the result of unintentional Be doping.

To summarize, the primary contributions made by this research to the development of mid-infrared semiconductor lasers are: the temperature- and compositional-dependencies of the energy gap for MBE-grown  $\text{InAs}_{1-x}\text{Sb}_x$  were established; the absorption coefficients for  $\text{InAs}_{1-x}\text{Sb}_x$  were measured for the first time;

and extrinsic levels in  $\text{InAs}_{1-x}\text{Sb}_x$ , including that of an intentional dopant, Be, were identified.

A secondary contribution is the analysis of the quality of the material being used for these devices. Although recent device performance is outstanding, further research directly pertaining to material issues may be warranted. This current research introduced the possibility of two unwanted phenomena existing in this material, unintentional extrinsic levels and phase separation, and substantiated these possibilities by several characterization techniques. Although phase separation may be avoided by changing the growth parameters for the material, the extrinsic levels may be native to the material and more difficult to eliminate. Samples grown specifically to examine these phenomena further are required to obtain conclusive results.

### **Recommendations**

The objective of this research was to characterize the MBE-grown  $\text{InAs}_{1-x}\text{Sb}_x$  material being used for mid-infrared semiconductor lasers. Follow-on research should address the issues raised here which were not resolved conclusively due to the limitations in characterization techniques or sample parameters imposed upon this current research.

One obvious next step is to extend the energy gap measurements of the MBE-grown  $\text{InAs}_{1-x}\text{Sb}_x$  samples to Sb compositions between 0-3.1%, and between 19.2-100%, to determine the compositional dependence of the energy gap over these ranges, as well. The dependence was shown in Chapter VI to be anomalous over the range studied.

Further insight into the anomaly will be gained by understanding the behavior beyond this range.

Another obvious step is to identify more impurity levels in  $\text{InAs}_{1-x}\text{Sb}_x$  using intentional doping as was done for Be in Chapter VII. No data of this type exists in the literature, and this type of knowledge is essential to identifying unintentional extrinsic levels observed in nominally undoped material.

Follow-on research on a larger scale should address the possibilities of phase separation, Cu-Pt ordering and residual strain in this material that were introduced in this current phase of the research. Although the ordering and strain were determined to be unlikely, all three should be studied in detail since: they have been shown to exist in this material; little has been quantified about them; and they all could impact device performance.

The current study focused on samples grown as test samples for laser structures. Future studies should dictate sample requirements determined specifically to study these phenomena. The degree of both phase separation and Cu-Pt ordering in this material has been shown to be related to the growth temperature of the sample. Therefore, analyses of samples grown over specific ranges of temperatures are required. Also, Cu-Pt ordering in  $\text{Ga}_{1-x}\text{In}_x\text{P}$  was studied through the use of oriented substrates (see Chapter IV for details). This should be considered for  $\text{InAs}_{1-x}\text{Sb}_x$ , as well.

Since intentional or residual strain is a real issue that impacts device performance, especially for quantum well (QW) devices, quantification of the critical (pseudomorphic) thickness at which strain relaxation begins is important. The use of theoretical analyses,

as done in this current research, gives the researcher a general idea of these thicknesses, but experimental results are needed to ground these models. Epilayer thicknesses below and above the calculated critical thickness for a given lattice-mismatch must be studied. Again, these samples must be grown specifically for this purpose.

Finally, this research concentrated on epitaxially-grown “bulk” samples. Clearly, the current structures of interest for mid-infrared optoelectronic devices are QWs. This research laid the ground work by identifying characteristics of MBE-grown material. This was essential before the material can be studied in an advanced structure. Although the study of QW samples is a logical next step, the parameter space, including QW/barrier compositions and interface treatments, QW thicknesses and strains, *etc.*, is quite large. Care should be taken to sufficiently limit the parameter space and to obtain a sufficient number of samples within this limitation to accurately characterize its impact on device performance.

## Bibliography

- Adachi, S., J. Appl. Phys. **61**, 4869 (1987).
- Akimova, I.V., A.E. Bochkarev, L.M. Dolginov, A.E. Drakin, L.V. Druzhinina, P.G. Eliseev, B.N. Sverdlov and V.A. Skripkin, Sov. Phys. Tech. Phys. **33**, 429 (1988).
- Allaberenov, O.A., N.V. Zotova, and D.N. Nasledov, Sov. Phys. Semicond. **5**, 2050 (1972a).
- Allaberenov, O.A., N.V. Zotova, and D.N. Nasledov, Sov. Phys. Semicond. **6**, 330 (1972b).
- Andrews, A.M., D.T. Chueng, E.R. Gertner and J.T. Longo, J. Vac. Sci. Technol. **13**, 961 (1976).
- Arias, J.M., M. Zandian, R. Zucca and J. Singh, Semicond. Sci. Technol. **8**, S255 (1993).
- Ashcroft, N.W. and N.D. Mermin, Solid State Physics, W.B. Saunders Co., Philadelphia, PA (1976).
- Aubin, M.J. and J.C. Woolley, Can. J. Phys. **46**, 1191 (1968).
- Basov, N.G., A.V. Dudenkova, A.I. Krasil'nikov, V.V. Nikitin, and K.P. Fedoseev, Sov. Phys. - Solid State **8**, 847 (1966).
- Bethea, C.G., M.Y. Yen, B.F. Levine, K.K. Choi and A.Y. Cho, Appl. Phys. Lett. **51**, 1431 (1987).
- Bethea, C.G., B.F. Levine, M.Y. Yen and A.Y. Cho, Appl. Phys. Lett. **53**, 291 (1988).
- Bochkarev, A.E., L.M. Dolginov, A.E. Drakin, L.V. Druzhinina, P.G. Eliseev and B.N. Sverdlov, Sov. J. Quant. Electron. **15**, 869 (1985).
- Bondar, S.A., V.N. Vigdorovich, G.P. Furmanov and S.G. Shutov, Sov. Phys. Tech. Phys. **27**, 215 (1982).
- Bube, R.H., *Electrons in Solids: An Introductory Survey*, Academic Press, Inc., San Diego, CA (1981).
- Bubulac, L.O., E.E. Barrowcliff, W.E. Tennant, J.G. Pasko, G. Williams, A.M. Andrews, D.T. Cheung, and E.R. Gertner, in *Gallium Arsenide and Related Compounds 1978*, C.M. Wolfe, ed., Inst. Phys. Conf. Ser. **45**, 519 (1979).



- Bubulac, L.O., A.M. Andrews, E.R. Gertner and D.T. Cheung, *Appl. Phys. Lett.* **36**, 734 (1980).
- Caneau, C., A.K. Srivastava, A.G. Dentai, J.L. Zyskind and M.A. Pollack, *Electron. Lett.* **21**, 815 (1985).
- Cherng, Y.T., K.Y. Ma and G.B. Stringfellow, *Appl. Phys. Lett.* **53**, 886 (1988).
- Chiang, P.K. and S.M. Bedair, *Appl. Phys. Lett.* **46**, 383 (1985).
- Chiu, T.H., W.T. Tsang and J.A. Ditzenberger, *J. Vac. Soc. Technol. B* **4**, 600 (1986).
- Choi, H.K., G.W. Turner, and Z.L. Liau, *Appl. Phys. Lett.* **65**, 2251 (1994).
- Chyi, J.I., S. Kalem, N.S. Kumar, C.W. Litton and H. Morkoc, *Appl. Phys. Lett.* **53**, 1092 (1988).
- Coderre, W.M. and J.C. Woolley, *Can. J. Phys.* **46**, 1207 (1968).
- Dawson, L.R., *J. Cryst. Growth* **98**, 220 (1989).
- Dean, P.J., *Prog. Crystal Growth Charact.* **5**, 89 (1982).
- Dixon, J.R. and J.M. Ellis, *Phys. Rev.* **123**, 1560 (1961).
- Dobbelaere, W., J. DeBoeck and G. Borghs, *Appl. Phys. Lett.* **55**, 1856 (1989).
- Eglash, S.J. and H.K. Choi, *Appl. Phys. Lett.* **64**, 833 (1994).
- ElAllali, M., C.B. Sorensen, and E. Veje, *Phys. Rev. B* **48**, 4398 (1993).
- Elies, S., A. Krier, I.R. Cleverley and K. Singer, *J. Phys. D: Appl. Phys.* **26**, 159 (1993).
- Esina, N.P., N.V. Sotova, A.A. Rogachev, N.M. Stus' and G.N. Talalakin, *Sov. Phys. Semicond.* **12**, 342 (1978).
- Fang, Z.M., K.Y. Ma, D.H. Jaw, R.M. Cohen, and G.B. Stringfellow, *J. Appl. Phys.* **67**, 7034 (1990).
- Ferguson, I.T., A.G. Norman, B.A. Joyce, T.Y. Seong, G.R. Booker, R.H. Thomas, C.C. Phillips, and R.A. Stradling, *Appl. Phys. Lett.* **59**, 3324 (1991a).
- Ferguson, I.T., A.G. Norman, T.Y. Seong, R.H. Thomas, C.C. Phillips, X.M. Zhang, R.A. Stradling, B.A. Joyce, and G.R. Booker, *Inst. Phys. Conf. Ser.* **120**, 395 (1991b).

- Gomyo, A., T. Suzuki and S. Iijima, Phys. Rev. Lett. **60**, 2645 (1988).
- Goodman, J.W., *Statistical Optics*, John Wiley & Sons, Inc., New York, NY (1985).
- Grober, R.D., H.D. Drew, J. Chyi, S. Kalem, and H. Morkoc, J. Appl. Phys. **65**, 4079 (1989).
- Guseva, M.I., N.V. Zotova, A.V. Koval', and D.N. Nasledov, Sov. Phys. Semicond. **9**, 591 (1975).
- Herman, M.A. and H. Sitter, *Molecular Beam Epitaxy, Fundamentals and Current Status*, Springer-Verlag, Berlin, Germany (1989).
- Jen, H.R., K.Y. Ma and G.B. Stringfellow, Appl. Phys. Lett. **54**, 1154 (1989).
- Kaneko, T., H. Asahi, Y. Itani, Y. Okuno and S. Gonda, J. Cryst. Growth **111**, 638 (1991).
- Kimball, G.E., J. Chem. Phys. **3**, 560 (1935).
- Kobayashi, N., Y. Horikoshi, and C. Uemura, Jpn. J. Appl. Phys. **19**, L30 (1980).
- Kuech, T.F., D.J. Wolford, E. Vuehoff, V. Deline, P.M. Potemski, and J. Bradley, J. Appl. Phys. **62**, 632 (1987).
- Kurtz, S.R., G.C. Osbourne, R.M. Biefeld and S.R. Lee, Appl. Phys. Lett. **53**, 216 (1988).
- Kurtz, S.R., L.R. Dawson, R.M. Biefeld, D.M. Follstaedt, and B.L. Doyle, Phys. Rev B **46**, 1909 (1992).
- Kurtz, S.R., R.M. Biefeld, L.R. Dawson, K.C. Baucom and A.J. Howard, Appl. Phys. Lett. **64**, 812 (1994).
- Lacroix, Y., S.P. Watkins, C.A. Tran and M.L. Thewalt, Appl. Phys. Lett. **66**, 1101 (1995).
- Le, H.Q., G.W. Turner, S.J. Eglash, H.K. Choi, and D.A. Coppeta, Appl. Phys. Lett. **64**, 152 (1994).
- Le, H.Q., J.M. Arias, M. Zandian, R. Zucca, and Y.-Z. Liu, Appl. Phys. Lett. **65**, 810 (1994).
- Lee, G.S., Y. Lo, Y.F. Lin, S.M. Bedair and W.D. Laidig, Appl. Phys. Lett. **47**, 1219 (1985).

- Li, Y.B., S.S. Dosanjh, I.T. Ferguson, A.G. Norman, A.G. de Oliviera, R.A. Stradling and R. Zallen, *Semicond. Sci. Technol.* **7**, 567 (1992).
- Liau, Z.L. and H.K. Choi, *Appl. Phys. Lett.* **64**, 3219 (1994).
- Logothetidis, S., M.Cardona, and M. Garriga, *Phys. Rev. B* **43**, 11950 (1991).
- Lucovsky, G. and M.F. Chen, *Solid State Comm.* **8**, 1397 (1970).
- Lyon, S.A., *J. Luminescence* **35**, 121 (1986).
- Madelung, O., ed., *Semiconductors: group IV elements and group III-V compounds*, Springer-Verlag, Berlin, Germany (1991).
- Mani, H., A. Joullie, G. Boussier, E. Tournie, F. Pitard, A.-M. Joullie, and C. Alibert, *Electron. Lett.* **24**, 1542, 1988.
- Mao, Y. and A. Krier, *J. Cryst. Growth* **133**, 108 (1993).
- Martinelli, R.U., R.E. Enstrom, R. Menna and P. York, *Development of 2-D GSE Laser Arrays Operating at 3.3 to 3.5  $\mu\text{m}$* , USAF Final Report # PL-TR-91-1048 -- Vol. II (1991).
- McKelvey, J.P., *Solid State and Semiconductor Physics*, Robert E. Kreiger, Inc., Malabar, FL (1966).
- Mielenz, K.D., *J. Opt. Soc. Am.* **57**, 66 (1967).
- Microcal Software, Inc., *Origin version 3.5 Reference Manual*, Northampton, MA.
- Mohammed, K., F. Capasso, R.A. Logan, J.P. vanderZiel and A.L. Hutchinson, *Electron. Lett.* **22**, 215 (1986).
- O'Donnell, K.P. and X. Chen, *Appl. Phys. Lett.* **58**, 2924 (1991).
- Pancove, J.I., *Optical Processes in Semiconductors*, Dover Publications, Inc., New York, NY (1971).
- Partin, D.L., *IEEE JQE* **24**, 1716 (1988).
- Pavesi, L. and M. Guzzi, *J. Appl. Phys.* **75**, 4779 (1994).
- Potter, R.F. and G.G. Kretschmar, *Infrared Phys.* **4**, 57 (1964).

- Press, W.H., B.P. Flannery, S.A. Teukolsky, and W.T. Vetterling, *Numerical Recipes in C, The Art of Scientific Computing*, Cambridge University Press, New York, NY (1988).
- Rogalski, A. and Z. Orman, *Infrared Phys.* **25**, 551 (1985).
- Rogalski, A., *Prog. Quant. Electr.* **13**, 191 (1989a).
- Rogalski, A. and K. Jozwikowski, *Infrared Phys.* **29**, 35 (1989b).
- Saleh, B.E.A. and M.C. Teich, *Fundamentals of Photonics*, John Wiley & Sons, Inc., New York, NY (1991).
- Schubert, E.F., E.O. Gobel, Y. Horikoshi, K. Ploog, and H.J. Quessier, *Phys. Rev. B* **30**, 813 (1984).
- Schubert, E.F. and W.T. Tsang, *Phys. Rev. B* **34**, 2991 (1986).
- Seong, T.Y., A.G. Norman, J.L. Hutchison, I.T. Ferguson, G.R. Booker, R.A. Stradling, and B.A. Joyce, *Inst. Phys. Conf. Ser.* **117**, 485 (1991).
- Shah, J., *Solid St. Electron.* **21**, 43 (1978).
- Shah, M., M.O. Manasreh, R. Kaspi, M.Y. Yen, B.A. Philips, M. Skowronski and J. Shinar, *Mat. Res. Soc. Symp. Proc.* **325**, 449 (1994).
- Singh, J. and K.K. Bajaj, *Appl. Phys. Lett.* **44**, 1075 (1984).
- Srivastava, A.K., J.L. Zyskind, R.M. Lum, B.V. Dutt and J.K. Klingert, *Appl. Phys. Lett.* **49**, 41 (1986).
- Stradling, R.A., *Semicond. Sci. Technol.* **6**, C52 (1991).
- Stringfellow, G.B. and P.E. Greene, *J. Phys. Chem. Solids* **30**, 1779 (1969).
- Stringfellow, G.B. and P.E. Greene, *J. Electrochem. Soc.* **118**, 805 (1971).
- Stringfellow, G.B., *J. Cryst. Growth* **98**, 108 (1989).
- Suzuki, T. and A. Gomyo, *J. Cryst. Growth* **93**, 396 (1988).
- Swaminathan, V., M.D. Sturge, and J.L. Zilko, *J. Appl. Phys.* **52**, 6306 (1981).
- Sze, S.M., *Semiconductor Devices, Physics and Technology*, John Wiley & Sons, Inc., New York, NY (1985).

- Thomas, M.B. and J.C. Woolley, *Can. J. Phys.* **49**, 2052 (1971).
- Tsang, W.T., T.H. Chiu, D.W. Kisker and J.A. Ditzenberger, *Appl. Phys. Lett.* **46**, 283 (1985).
- Turner, G.W., H.K. Choi, D.R. Calawa, J.V. Pantano, and J.W. Chludzinski, *J. Vac. Sci. Technol. B* **12**, 1266 (1994).
- Turner, G.W., H.K. Choi and H.Q. Le, *J. Vac. Sci. Technol. B* **13**, 699 (1995).
- Urbach, F., *Phys. Rev.* **92**, 1324 (1953).
- vanderZiel, J.P., R.A. Logan, R.M. Mikulyak and A.A. Ballman, *IEEE JQE* **QE-21**, 1827, (1985).
- vanTongerloo, E.H. and J.C. Woolley, *Can. J. Phys.* **46**, 1199 (1968).
- Varshni, Y.P., *Physica* **34**, 149 (1967).
- Vishnubhatla, S.S., B. Eyglunent and J.C. Woolley, *Can. J. Phys.* **47**, 1661 (1969).
- Warren, B.E., *X-Ray Diffraction*, Addison-Wesley Publ. Co., Reading, MA (1969).
- Wei, S.-H. and A. Zunger, *Appl. Phys. Lett.* **58**, 2684 (1991).
- Wolfe, W.L. and G.J. Zissis, ed., *The Infrared Handbook (revised edition)*, The Infrared Information Analysis Center, Environmental Research Institute of Michigan, 5-88 (1989).
- Woolley, J.C. and J.A. Evans, *Proc. Phys. Soc.* **78**, 354 (1961).
- Woolley, J.C. and J. Warner, *J. Electrochem. Soc.* **111**, 1142 (1964a).
- Woolley, J.C. and J. Warner, *Can. J. Phys.* **42**, 1879 (1964b).
- Woolley, J.C. and A.G. Thompson, *Can. J. Phys.* **42**, 2030 (1964c).
- Yen, M.Y., B.F. Levine, C.G. Bethea, K.K. Choi and A.Y. Cho, *Appl. Phys. Lett.* **50**, 927 (1987).
- Yen, M.Y., R. People, K.W. Wecht and A.Y. Cho, *Appl. Phys. Lett.* **52**, 489 (1988a).
- Yen, M.Y., R. People and K.W. Wecht, *J. Appl. Phys.* **64**, 952 (1988b).
- Yen, M.Y., *J. Appl. Phys.* **64**, 3306 (1988c).

## Vita

Maj Michael A. Marciniak was born on 20 February 1957 in Milwaukee, WI. He graduated from Thomas More High School in Milwaukee in 1977, and attended St Joseph's College in Rensselaer, IN on a Trustee's Academic Scholarship where he received the Bachelor of Science degree in Mathematics-Physics in 1981. He received his USAF commission upon graduation from Officer's Training School, Lackland AFB, TX in 1981, and entered the undergraduate engineering conversion program at the University of Missouri - Columbia where he graduated Cum Laude with the Bachelor of Science in Electrical Engineering degree in 1983. From 1984 to 1986, he was assigned to the Air Force Electronic Warfare Center, Kelly AFB, TX where he served as Communications Systems Analysis Engineer and Chief, Electro-Optics/Infrared Technology Section. He was assigned to the Air Force Institute of Technology (AFIT), Wright-Patterson AFB, OH in 1986, and received the Master of Science in Electrical Engineering degree (with Electro-Optics emphasis) in 1987. From 1988 to 1992, he was assigned to the Phillips Laboratory, Kirtland AFB, NM where he served as Electro-Optics Systems Engineer and Chief, Single-Device Laser Development. In 1992, he returned to AFIT to pursue the Doctor of Philosophy degree (with Solid State Physics specialty).

~~Permanent Address: [REDACTED]~~

~~[REDACTED]~~

REPORT DOCUMENTATION PAGE			Form Approved OMB No. 0704-0188	
Public reporting burden for this collection of information is estimated to average 1 hour per response, including the time for reviewing instructions, searching existing data sources, gathering and maintaining the data needed, and completing and reviewing the collection of information. Send comments regarding this burden estimate or any other aspect of this collection of information, including suggestions for reducing this burden, to Washington Headquarters Services, Directorate for Information Operations and Reports, 1215 Jefferson Davis Highway, Suite 1204, Arlington, VA 22202-4302, and to the Office of Management and Budget, Paperwork Reduction Project (0704-0188), Washington, DC 20503.				
1. AGENCY USE ONLY (Leave blank)	2. REPORT DATE September 1995	3. REPORT TYPE AND DATES COVERED PhD Dissertation		
4. TITLE AND SUBTITLE Optical Characterization of Indium Arsenide Antimonide Semiconductors Grown by Molecular Beam Epitaxy			5. FUNDING NUMBERS	
6. AUTHOR(S) Michael A. Marciniak, Major, USAF				
7. PERFORMING ORGANIZATION NAME(S) AND ADDRESS(ES) Robert L. Hengehold AFIT/ENP 2950 P St Wright-Patterson AFB, OH 45433-7765			8. PERFORMING ORGANIZATION REPORT NUMBER AFIT/DS/ENP/95-03	
9. SPONSORING / MONITORING AGENCY NAME(S) AND ADDRESS(ES) Nicholas R. Pchelkin PL/LIDA 3550 Aberdeen Av SE Kirtland AFB, NM 87117-5000			10. SPONSORING / MONITORING AGENCY REPORT NUMBER	
11. SUPPLEMENTARY NOTES				
12a. DISTRIBUTION / AVAILABILITY STATEMENT Approved for public release; distribution unlimited			12b. DISTRIBUTION CODE	
13. ABSTRACT (Maximum 200 words) <p>The material parameters and crystalline quality of undoped, MBE-grown <math>\text{InAs}_{1-x}\text{Sb}_x</math> nearly lattice-matched to (100) GaSb (<math>-0.617\% \leq \Delta a/a \leq +0.708\%</math>) similar to material used for mid-infrared semiconductor lasers were determined by optical characterization. Absorption measurements at temperatures between 6-295 K determined the energy gap and wavelength-dependent absorption coefficient for each sample. The compositional dependence of the energy gap was anomalous when compared to previously reported data, suggesting phase separation existed in the material. The samples were also studied by temperature- and excitation-dependent photoluminescence (PL), which, for the majority of cases, showed only a single band-edge peak, identified by comparison with the absorption data. PL linewidths as narrow as 4.3 meV and LO-phonon replicas indicated high material quality, but the shift of the PL peak to higher energies with increased excitation was greater than expected from band filling alone, and underscored the likelihood of phase separation. Extrinsic PL peaks were also observed from one undoped sample, and identified a F-B transition at 4-7 meV and a DAP transition at 10-14 meV below the band edge. Characterization of <math>\text{InAs}_{1-x}\text{Sb}_x:\text{Be}</math> identified the Be acceptor energy as <math>&gt;30</math> meV above the valence band.</p>				
14. SUBJECT TERMS absorption, absorption coefficient, beryllium, InAs, InAsSb, MBE, phase separation, photoluminescence			15. NUMBER OF PAGES 262	
			16. PRICE CODE	
17. SECURITY CLASSIFICATION OF REPORT UNCLASSIFIED	18. SECURITY CLASSIFICATION OF THIS PAGE UNCLASSIFIED	19. SECURITY CLASSIFICATION OF ABSTRACT UNCLASSIFIED	20. LIMITATION OF ABSTRACT UL	

## GENERAL INSTRUCTIONS FOR COMPLETING SF 298

The Report Documentation Page (RDP) is used in announcing and cataloging reports. It is important that this information be consistent with the rest of the report, particularly the cover and title page. Instructions for filling in each block of the form follow. It is important to *stay within the lines* to meet *optical scanning requirements*.

**Block 1. Agency Use Only (Leave blank).**

**Block 2. Report Date.** Full publication date including day, month, and year, if available (e.g. 1 Jan 88). Must cite at least the year.

**Block 3. Type of Report and Dates Covered.** State whether report is interim, final, etc. If applicable, enter inclusive report dates (e.g. 10 Jun 87 - 30 Jun 88).

**Block 4. Title and Subtitle.** A title is taken from the part of the report that provides the most meaningful and complete information. When a report is prepared in more than one volume, repeat the primary title, add volume number, and include subtitle for the specific volume. On classified documents enter the title classification in parentheses.

**Block 5. Funding Numbers.** To include contract and grant numbers; may include program element number(s), project number(s), task number(s), and work unit number(s). Use the following labels:

C - Contract	PR - Project
G - Grant	TA - Task
PE - Program Element	WU - Work Unit Accession No.

**Block 6. Author(s).** Name(s) of person(s) responsible for writing the report, performing the research, or credited with the content of the report. If editor or compiler, this should follow the name(s).

**Block 7. Performing Organization Name(s) and Address(es).** Self-explanatory.

**Block 8. Performing Organization Report Number.** Enter the unique alphanumeric report number(s) assigned by the organization performing the report.

**Block 9. Sponsoring/Monitoring Agency Name(s) and Address(es).** Self-explanatory.

**Block 10. Sponsoring/Monitoring Agency Report Number.** (If known)

**Block 11. Supplementary Notes.** Enter information not included elsewhere such as: Prepared in cooperation with...; Trans. of...; To be published in.... When a report is revised, include a statement whether the new report supersedes or supplements the older report.

**Block 12a. Distribution/Availability Statement.** Denotes public availability or limitations. Cite any availability to the public. Enter additional limitations or special markings in all capitals (e.g. NOFORN, REL, ITAR).

DOD - See DoDD 5230.24, "Distribution Statements on Technical Documents."  
DOE - See authorities.  
NASA - See Handbook NHB 2200.2.  
NTIS - Leave blank.

**Block 12b. Distribution Code.**

DOD - Leave blank.  
DOE - Enter DOE distribution categories from the Standard Distribution for Unclassified Scientific and Technical Reports.  
NASA - Leave blank.  
NTIS - Leave blank.

**Block 13. Abstract.** Include a brief (*Maximum 200 words*) factual summary of the most significant information contained in the report.

**Block 14. Subject Terms.** Keywords or phrases identifying major subjects in the report.

**Block 15. Number of Pages.** Enter the total number of pages.

**Block 16. Price Code.** Enter appropriate price code (*NTIS only*).

**Blocks 17. - 19. Security Classifications.** Self-explanatory. Enter U.S. Security Classification in accordance with U.S. Security Regulations (i.e., UNCLASSIFIED). If form contains classified information, stamp classification on the top and bottom of the page.

**Block 20. Limitation of Abstract.** This block must be completed to assign a limitation to the abstract. Enter either UL (unlimited) or SAR (same as report). An entry in this block is necessary if the abstract is to be limited. If blank, the abstract is assumed to be unlimited.